

INFORMATION TO USERS

This manuscript has been reproduced from the microfilm master. UMI films the text directly from the original or copy submitted. Thus, some thesis and dissertation copies are in typewriter face, while others may be from any type of computer printer.

The quality of this reproduction is dependent upon the quality of the copy submitted. Broken or indistinct print, colored or poor quality illustrations and photographs, print bleedthrough, substandard margins, and improper alignment can adversely affect reproduction.

In the unlikely event that the author did not send UMI a complete manuscript and there are missing pages, these will be noted. Also, if unauthorized copyright material had to be removed, a note will indicate the deletion.

Oversize materials (e.g., maps, drawings, charts) are reproduced by sectioning the original, beginning at the upper left-hand corner and continuing from left to right in equal sections with small overlaps.

**ProQuest Information and Learning
300 North Zeeb Road, Ann Arbor, MI 48106-1346 USA
800-521-0600**

UMI[®]

PHASE EQUILIBRIA IN THE $\text{AlN-Al}_2\text{O}_3\text{-Y}_2\text{O}_3$ SYSTEM

- *UTILITY IN ALN PROCESSING*

by

Mamoun Medraj

Department of Mining and Metallurgical Engineering
McGill University
Montreal, Canada

A thesis submitted to the
Faculty of Graduate Studies and Research
in partial fulfillment of the requirements for the degree of
Doctor of Philosophy

© Mamoun Medraj, 2001.



**National Library
of Canada**

**Acquisitions and
Bibliographic Services**

**385 Wellington Street
Ottawa ON K1A 0N4
Canada**

**Bibliothèque nationale
du Canada**

**Acquisitions et
services bibliographiques**

**385, rue Wellington
Ottawa ON K1A 0N4
Canada**

Your file Votre référence

Our file Notre référence

The author has granted a non-exclusive licence allowing the National Library of Canada to reproduce, loan, distribute or sell copies of this thesis in microform, paper or electronic formats.

L'auteur a accordé une licence non exclusive permettant à la Bibliothèque nationale du Canada de reproduire, prêter, distribuer ou vendre des copies de cette thèse sous la forme de microfiche/film, de reproduction sur papier ou sur format électronique.

The author retains ownership of the copyright in this thesis. Neither the thesis nor substantial extracts from it may be printed or otherwise reproduced without the author's permission.

L'auteur conserve la propriété du droit d'auteur qui protège cette thèse. Ni la thèse ni des extraits substantiels de celle-ci ne doivent être imprimés ou autrement reproduits sans son autorisation.

0-612-75659-9

Canada

ABSTRACT

The importance of aluminum nitride (AlN) stems from its application in microelectronics as a substrate material due to its high thermal conductivity, high electrical resistance, mechanical strength and hardness, thermal durability and chemical stability. Ytria (Y_2O_3) is the best additive for AlN sintering, which undergoes densification through a liquid phase mechanism. The surface oxide, Al_2O_3 , reacts with the oxide additive, Y_2O_3 , to form a Y-Al-O-N liquid that promotes particle rearrangement and densification. Construction of the phase relations in this multicomponent system is becoming essential for further development of AlN.

Binary diagrams of Al_2O_3 - Y_2O_3 , AlN- Al_2O_3 , and AlN- Y_2O_3 were thermodynamically modeled in this work. The obtained Gibbs free energies of the components, stoichiometric phases and solution parameters were used for the calculation of the isothermal sections and liquidus surface of the AlN- Al_2O_3 - Y_2O_3 system. Phase evolutions, melting and solidifications in the Al_2O_3 - Y_2O_3 phase diagram were investigated using x-ray diffraction and *in situ* high temperature neutron diffractometry. The phase diagram of AlN- Y_2O_3 system was established and verified experimentally. The predicted ternary phase diagram for AlN- Al_2O_3 - Y_2O_3 was also verified experimentally using *in situ* high temperature neutron diffractometry and it has been constructed for the first time in this work.

A self-consistent thermodynamic database including all the phases in the AlN- Al_2O_3 - Y_2O_3 system was developed during the course of this project. This database was used to explain the experimental results of AlN sintering. It has been found that the samples with high densities had lower liquid formation temperatures, and low thermal conductivity was related to the residual Al_2O_3 and high YAP (Al_2O_3 , Y_2O_3) content.

RÉSUMÉ

L'importance du nitrure d'aluminium (AlN) provient des applications dans le domaine de la micro-electronique; étant une matière utiliser comme substrat dû à sa haute conductivité thermique, haute résistance électrique, force mécanique et dureté, durabilité thermique et stabilité chimique. L'oxyde d'yttrium (Y_2O_3) est le meilleur additif pour le frittage de AlN, et il a été montré que AlN se densifie par un mécanisme en phase liquide où l'oxyde de surface, Al_2O_3 , réagit avec l'additif, Y_2O_3 , formant un de composition Y-Al-O-N liquide qui favorise le réarrangement des particules et la densification. La construction des relations de phases dans ce système a plusieurs composés devient essentiel pour le développement future de l'AlN.

Les diagrammes binaires Al_2O_3 - Y_2O_3 , AlN- Al_2O_3 , et AlN- Y_2O_3 ont été modélisés thermodynamiquement. Les valeurs obtenues de l'énergie Gibbs des composants, les phases stoechiométriques et les paramètres de la solution ont été utilisés pour le calcul des sections isothermales et les *liquidus* du système d'AlN- Al_2O_3 - Y_2O_3 . L'évolution des phases, les liquéfactions et les solidifications dans le diagramme de phases Al_2O_3 - Y_2O_3 a été enquêté par l'utilisation de la diffraction des rayons X et la diffraction à haute température de neutron *en situ*. Le diagramme de la phase de système AlN- Y_2O_3 a été établi et vérifié expérimentalement. Le diagramme ternaire de phases prédit a été vérifié expérimentalement par l'utilisation de la diffraction à haute température de neutron *en situ*. Le diagramme ternaire de phases AlN- Al_2O_3 - Y_2O_3 a été construit pour la première fois dans cette recherche.

Une base de données thermodynamiques auto-compatible incluant toutes les phases du système AlN- Al_2O_3 - Y_2O_3 a été développé au cours de ce projet. Cette base de données a été utilisée pour expliquer les résultats expérimentaux du frittage de l'AlN. On a trouvé que les échantillons possédant une grande densification ont une basse température de formation de liquide, et que la faible conductivité thermique est dû à la quantité résiduelle d' Al_2O_3 et de la haute teneur en YAP.

ACKNOWLEDGEMENTS

I owe a sincere gratitude to Prof. Robin. A. L. Drew and Prof. W.T. Thompson for their invaluable guidance and advice which was of paramount importance in making this thesis possible.

I would like to express special thanks and appreciation to Dr. Robert Hammond of Neutron Program for Materials Research (NPMR-NRC) in Chalk River for his help in the neutron diffraction experimental work and data analysis and the useful discussions and conversations throughout the course of this research. I appreciate the opportunity provided by (NPMR-NRC) to conduct the unique high temperature *in situ* neutron diffraction experiments. Sincere thanks also go to Mike Watson for the design of the furnace and setting up the experiments.

My thanks to all the members of the ceramics and composites materials group for the valuable discussions and for providing stimulating atmosphere for creative thinking. Also I would like to thank the technical personnel of the Metallurgical Engineering Department at McGill University for their help.

Acknowledgements are due to the Natural Science and Engineering Research Council (NSERC) for its financial support, through the Strategic Project Program, which kept this research work going.

Sincere thanks to all my friends, brothers and sisters for their encouragement and continuous support. I do not think I could ever pay back my parents for their endless love and support. Finally, many special uncountable thanks to Andrea, for her continuous encouragement and enormous patience with my crankiness during the writing of this thesis.

TABLE OF CONTENTS

ABSTRACT	i
RÉSUMÉ	ii
ACKNOWLEDGMENTS	iii
TABLE OF CONTENTS	iv
LIST OF FIGURES	viii
LIST OF TABLES	xiv
NOMENCLATURE	xvii

Chapter 1

1 INTRODUCTION	1
1.1 Applications of Aluminum Nitride	2
1.2 Major Obstacles to Commercialization of AlN	4

Chapter 2

2 LITERATURE SURVEY	5
2.1 Crystal Structure of AlN	5
2.2 Properties of Aluminum Nitride	6
2.2.1 Thermal Conductivity	6
2.2.2 Mechanical Properties	9
2.2.3 Electrical Properties	10
2.3 Sintering Additives	10
2.4 Sintering Mechanism of AlN	13
2.5 Ternary AlN-Al ₂ O ₃ -Y ₂ O ₃ Phase Diagram	15
2.6 Al ₂ O ₃ - Y ₂ O ₃ System	15
2.7 AlN - Y ₂ O ₃ System	21
2.8 AlN - Al ₂ O ₃ System	22

Chapter 3

3 THE AIM OF THIS WORK	27
------------------------------	----

Chapter 4

4	REVIEW OF CHEMICAL THERMODYNAMIC CALCULATIONS FOR ASSESSMENT OF PHASE EQUILIBRIA	29
4.1	Introduction	29
4.2	Theory	33
4.2.1	Margules Equations for Representation of Excess Properties ...	36
4.2.2	Determination of the Coefficients	38
4.2.3	Higher Component Systems	39

Chapter 5

5	METHODOLOGY OF THERMODYNAMIC MODELING OF AlN-Al ₂ O ₃ -Y ₂ O ₃ PHASE EQUILIBRIA	41
5.1	Mathematical Expressions for the Thermodynamic Properties	42
5.1.1	Al ₂ O ₃ - Y ₂ O ₃ Phase Diagram	42
5.1.2	AlN - Al ₂ O ₃ Phase Diagram	44
5.1.3	AlN - Y ₂ O ₃ Phase Diagram	45
5.2	The Validity of the Models	46
5.3	Thermodynamic Model for the Spinel Phase	52
5.4	Database for AlN-Al ₂ O ₃ -Y ₂ O ₃ System	58
5.4.1	Stoichiometric Compounds	58
5.4.2	Liquid Phases	63
5.4.3	Al ₂ O ₃ -AlN Spinel	64

Chapter 6

6	RESULTS And DISCUSSION OF THERMODYNAMIC ANALYSIS	66
6.1	Al ₂ O ₃ - Y ₂ O ₃ Phase Diagram	67
6.2	AlN - Al ₂ O ₃ Phase Diagram	68
6.3	AlN - Y ₂ O ₃ Phase Diagram	71
6.4	Isothermal Sections of AlN-Al ₂ O ₃ -Y ₂ O ₃ System	74
6.5	Liquidus Projection of AlN - Al ₂ O ₃ - Y ₂ O ₃ System	81

6.6	Phase Assemblage Diagrams	82
6.7	Thermodynamics of AlN Sintering	83

Chapter 7

7	MATERIALS, EQUIPMENT AND PROCEDURES	92
7.1	Materials	92
7.1.1	AlN Powder	92
7.1.2	Al ₂ O ₃ Powder	93
7.1.3	Y ₂ O ₃ Powder	94
7.2	Equipment	95
7.2.1	X-ray Diffractometry	95
7.2.2	Neutron Diffractometer	96
7.3	Experimental Procedures	99
7.3.1	X-ray Diffraction Experiments	99
7.3.2	Neutron Diffraction Experiments	101

Chapter 8

8	PHASE EVOLUTION IN Al ₂ O ₃ -Y ₂ O ₃ AND AlN-Y ₂ O ₃ SYSTEMS	104
8.1	X-ray Diffraction of Al ₂ O ₃ -Y ₂ O ₃ System	104
8.2	Neutron Diffraction Results	112
8.2.1	Neutron Diffraction Results of Al ₂ O ₃ -Y ₂ O ₃ Phase Diagram ...	116
8.2.2	Neutron Diffraction Results of AlN-Y ₂ O ₃ Phase Diagram ...	133

Chapter 9

9	HIGH TEMPERATURE NEUTRON DIFFRACTION OF AlN-Al ₂ O ₃ -Y ₂ O ₃ TERNARY SYSTEM	137
9.1	Composition 1	139
9.2	Composition 2	145
9.3	Composition 3	150
9.4	Composition 4	154
9.5	Composition 5	157

Chapter 10

10	CONCLUSIONS, ORIGINAL CONTRIBUTIONS TO KNOWLEDGE AND SUGGESTIONS FOR FUTURE WORK	163
10.1	Conclusions	163
10.2	Contributions to Original Knowledge	166
10.3	Suggestions For Future Work	167
REFERENCES		168
APPENDIX A		181
A-1 Neutron Diffraction Pattern Calculation of Al_2O_3		181
A-2 Neutron Diffraction Pattern Calculation of Y_2O_3		183
A-3 Neutron Diffraction Pattern Calculation of YAG		185
A-4 Neutron Diffraction Pattern Calculation of YAP		187
A-5 Neutron Diffraction Pattern Calculation of YAM		189
A-6 Neutron Diffraction Pattern Calculation of Spinel		191
APPENDIX B		193
B-1 Differential Thermal Analysis of YAG		193
B-2 Differential Thermal Analysis of YAP		194
B-3 Differential Thermal Analysis of YAM		194

LIST OF FIGURES

Chapter 1

Figure 1-1: Thermal conductivity versus temperature for AlN [11].....	3
---	---

Chapter 2

Figure 2-1: (a) The crystal structure of AlN [19]. (b) Wurtzite structure of AlN [14]. ...	5
Figure 2-2: Variation of thermal conductivity of AlN as a function of Y_2O_3 content...	12
Figure 2-3: Schematic diagram of AlN sintering.....	13
Figure 2-4: (a) TEM Micrograph of fracture surface of sintered AlN without Y_2O_3 [19] (b) BS-SEM micrograph of commercial AlN substrates sintered with addition of Y_2O_3	14
Figure 2-5: The experimental phase diagram of Y_2O_3 - Al_2O_3 System [47].	16
Figure 2-6: Chronological development of the Al_2O_3 - Y_2O_3 phase diagram; (a) Schneider et al. (1961), (b) Olds and Otto (1961), (c) Toropov et al. (1969), (d) Mizuno and Naguche (1967), (e) Abell et al. (1974) and (f) Mah and Petry (1992).....	19
Figure 2-7: Al_2O_3 - Y_2O_3 phase diagram, after Warshaw and Roy 1959, [55].....	20
Figure 2-8: Calculated $AlO_{1.5}$ - $YO_{1.5}$ phase diagram by Jin and Chen [45].	21
Figure 2-9: Y_2O_3 -AlN calculated phase diagram by; Kaufman et al. [62].	21
Figure 2-10: The phase diagram of AlN- Al_2O_3 system [23].	22
Figure 2-11: Calculated phase diagram of binary Al_2O_3 -AlN system [65].	25

Chapter 4

Figure 4-1: Hypothetical phase diagram and associated DTA curves [83].	31
Figure 4-2: The assessed excess Gibbs energies of the constituent subsystems are for extrapolation to a higher component system [72].	40

Chapter 5

Figure 5-1: Gibbs energy of Al_2O_3 - Y_2O_3 system at 2000K (1727°C).....	46
Figure 5-2: Gibbs energy of Al_2O_3 - Y_2O_3 system at 2213K (1940°C).....	47
Figure 5-3: Gibbs energy of Al_2O_3 - Y_2O_3 system at 2400K (2127°C).....	48
Figure 5-4: Al_2O_3 - Y_2O_3 calculated phase diagram from the mathematical model.....	49

Figure 5-5: The experimental phase diagram of Y_2O_3 - Al_2O_3 System [47].	50
Figure 5-6: Calculated Al_2O_3 – AlN phase diagram from the mathematical model.	51
Figure 5-7: Calculated AlN - Y_2O_3 phase diagram from the mathematical model.	52
Figure 5-8: Schematic Gibbs energy-composition diagrams show; (a) Spinel as stoichiometric compound, (b) spinel as non-stoichiometric phase.	52
Figure 5-9: Optimized phase diagram [65].	53
Figure 5-10: Gibbs energy for the liquid and spinel of AlN- Al_2O_3 system.	56
Figure 5-11: Gibbs energy for the liquid and spinel of AlN- Al_2O_3 system at (a) 2373K (2100°C) and (b) 2200K (1923°C)	57

Chapter 6

Figure 6-1: Calculated Y_2O_3 - Al_2O_3 phase diagram with experimental data from the literature.	67
Figure 6-2: Calculated Al_2O_3 -AlN phase diagram and comparison with experimental data from the literature.	68
Figure 6-3: Calculated AlN- Al_2O_3 phase diagram at $P_{tot} = 1.0$ atm illustrating AlN decomposition.	70
Figure 6-4: Calculated AlN- Al_2O_3 phase diagram at $P_{tot} = 0.1$ atm showing AlN decomposition.	71
Figure 6-5: Calculated AlN- Y_2O_3 phase diagram.	72
Figure 6-6: Calculated AlN- Y_2O_3 phase diagram at $P_{tot} = 1.0$ atm showing AlN decomposition.	73
Figure 6-7: Calculated AlN- Y_2O_3 phase diagram illustrating AlN decomposition.	74
Figure 6-8: Isothermal Section at 2500°C.	75
Figure 6-9: Isothermal Section at 2000°C.	76
Figure 6-10: Isothermal Section at 1900°C.	77
Figure 6-11: Isothermal Section at 1800°C.	78
Figure 6-12: Isothermal Section at 1700°C.	80
Figure 6-13: Liquidus projection for AlN- Al_2O_3 - Y_2O_3 system.	81
Figure 6-14: Phase assemblage of (7 mol% AlN, 60 mol% Y_2O_3 , 33 mol% Al_2O_3) composition.	82

Figure 6-15: Relative density of the four compositions as a function of sintering temperature [106].	84
Figure 6-16: X-ray powder diffraction patterns of AlN for four compositions, G: YAG, P: YAP and *: YAM [106].	84
Figure 6-17: Predicted phase assemblage of composition I.	85
Figure 6-18: Phase assemblage of composition II.	86
Figure 6-19: Phase assemblage of composition III.	87
Figure 6-20: Phase assemblage of composition IV.	87
Figure 6-21: Variation in thermal conductivity with composition.	88
Figure 6-22: X-ray diffractogram of 5 wt% Y_2O_3 -added AlN sample sintered at 1900°C for 1 h [108].	89
Figure 6-23: Phase assemblage of 5 wt% Y_2O_3 -added AlN sample.	89
Figure 6-24: X-ray diffraction pattern of 4 wt% Y_2O_3 -added AlN sample sintered at 1800°C for 3 h.	90
Figure 6-25: Phase assemblage of 4 wt% Y_2O_3 -added AlN sample.	91

Chapter 7

Figure 7-1: SEM micrograph of as received AlN powder.	93
Figure 7-2: SEM micrograph of Al_2O_3 powder (a) x500 and (b) x2500.	94
Figure 7-3: SEM micrograph of as received Y_2O_3 powder (a) x3300 (b) x17000.	95
Figure 7-4: X-ray Diffractometer configuration.	96
Figure 7-5: Neutron Diffractometer, C2, Chalk River Laboratories, $2\theta_m$: Scattering from monochromatic to select wavelength, $2\theta_s$: Scattering from sample.	97
Figure 7-6: High temperature vacuum furnace, Chalk River Laboratories.	98
Figure 7-7: Detailed drawing of the circled parts in Figure 7-6; (1) sample capsule, (2) molybdenum sample support and (3) molybdenum pencil tube.	98
Figure 7-8: Flow diagram showing X-ray diffraction experimental procedure.	99
Figure 7-9: Calculated Al_2O_3 - Y_2O_3 phase diagram and the different nine investigated compositions.	100
Figure 7-10: AlN- Al_2O_3 - Y_2O_3 composition triangle with samples studied by neutron diffractometry.	101

Figure 7-11: Sealed Mo container used to conduct the neutron diffraction experiments at high temperature.	102
Figure 7-12: Heating and cooling cycle for neutron diffraction experiments.	103

Chapter 8

Figure 8-1: XRD patterns of sample 2 (YAM).	105
Figure 8-2: XRD patterns of sample 4 (YAP).	106
Figure 8-3: XRD patterns of YAP phase before and after heat treatment.	107
Figure 8-4: XRD patterns of sample 6 (YAG).	108
Figure 8-5: XRD patterns of sample 9 (hyper E1).	109
Figure 8-6: XRD patterns of sample 8 (E1).	109
Figure 8-7: XRD patterns of sample 7 (hypo E1).	110
Figure 8-8: XRD patterns of sample 5 (E2).	111
Figure 8-9: XRD patterns of sample 3 (E3).	111
Figure 8-10: XRD patterns of sample 1 (E4).	112
Figure 8-11: (a) Wurtizite structure of AlN. (b) Perspective view of the atoms arrangements of AlN.	113
Figure 8-12: Calculated neutron diffraction pattern for AlN.	115
Figure 8-13: Neutron diffractogram of the furnace and a sample.	115
Figure 8-14: Neutron diffractogram of the blank furnace.	116
Figure 8-15: Neutron diffractogram after subtracting the pattern of the blank furnace.	116
Figure 8-16: Neutron diffractograms during heating of E1 composition.	118
Figure 8-17: Neutron diffractograms during cooling of E1 composition.	119
Figure 8-18: Neutron diffractograms during heating of YAG composition.	121
Figure 8-19: Neutron diffractograms during cooling of YAG composition.	122
Figure 8-20: Neutron diffractograms during heating of E2 composition.	123
Figure 8-21: Neutron diffractograms during cooling of E2 composition.	125
Figure 8-22: Neutron diffractograms during heating of YAP composition.	127
Figure 8-23: Neutron diffractograms during cooling of YAP composition.	128
Figure 8-24: Neutron diffractograms of heating of YAM composition.	130

Figure 8-25: Neutron diffractograms during cooling of YAM composition.	131
Figure 8-26: Calculated AlN-Y ₂ O ₃ phase diagram with the investigated sample.	133
Figure 8-27: Neutron diffractograms during heating of AlN-Y ₂ O ₃ eutectic composition.	135
Figure 8-28: Neutron diffractograms during cooling of AlN-Y ₂ O ₃ eutectic composition.	136

Chapter 9

Figure 9-1: AlN-Al ₂ O ₃ -Y ₂ O ₃ isothermal sections at different temperatures with the five investigated ternary compositions.	138
Figure 9-2: Neutron diffractograms during heating of composition 1 (12 mol% AlN, 74 mol% Al ₂ O ₃ and 14 mol% Y ₂ O ₃).	141
Figure 9-3: Neutron diffractograms during cooling of (12 mol% AlN, 74 mol% Al ₂ O ₃ and 14 mol% Y ₂ O ₃) composition.	143
Figure 9-4: Phase assemblage diagram of (12 mol% AlN, 74 mol% Al ₂ O ₃ and 14 mol% Y ₂ O ₃) composition.	144
Figure 9-5: Neutron diffractograms during heating of (17.5 mol% AlN 64 mol% Al ₂ O ₃ and 18.5 mol% Y ₂ O ₃) composition.	146
Figure 9-6: Neutron diffractograms during cooling of (17.5 mol% AlN 64 mol% Al ₂ O ₃ and 18.5 mol% Y ₂ O ₃) composition.	148
Figure 9-7: Phase assemblage diagram of (17.5 mol% AlN 64 mol% Al ₂ O ₃ and 18.5 mol% Y ₂ O ₃) composition.	149
Figure 9-8: Neutron diffractograms during heating of (24 mol% AlN 70 mol% Al ₂ O ₃ and 6 mol% Y ₂ O ₃) composition.	151
Figure 9-9: Neutron diffractograms during cooling of (24 mol% AlN 70 mol% Al ₂ O ₃ and 6 mol% Y ₂ O ₃) composition.	152
Figure 9-10: Phase assemblage diagram of (24 mol% AlN 70 mol% Al ₂ O ₃ and 6 mol% Y ₂ O ₃) composition.	154
Figure 9-11: Neutron diffractograms during heating of (7 mol% AlN 33 mol% Al ₂ O ₃ and 60 mol% Y ₂ O ₃) composition.	155

Figure 9-12: Phase assemblage diagram of composition 4 (7 mol% AlN 33 mol% Al ₂ O ₃ and 60 mol% Y ₂ O ₃).	156
Figure 9-13: Neutron diffractograms during heating of (33 mol% AlN 20 mol% Al ₂ O ₃ and 47 mol% Y ₂ O ₃) composition.....	158
Figure 9-14: Neutron diffractograms during cooling of (33 mol% AlN 20 mol% Al ₂ O ₃ and 47 mol% Y ₂ O ₃) composition.....	160
Figure 9-15: Phase assemblage diagram of (33 mol% AlN 20 mol% Al ₂ O ₃ and 47 mol% Y ₂ O ₃) composition	161

APPENDIX A

Figure A-1: (a) Al ₂ O ₃ unit cell, (b) (001) projection.	181
Figure A-2: Calculated neutron diffraction pattern for Al ₂ O ₃	182
Figure A-3: (a) Y ₂ O ₃ unit cell, (b) (001) projection.	181
Figure A-4: Calculated neutron diffraction pattern for Y ₂ O ₃	184
Figure A-5: (a) YAG unit cell (b) (001) projection.	185
Figure A-6: Calculated neutron diffraction pattern for YAG.	186
Figure A-7: (a) YAP unit cell, (b) (001) projection.....	187
Figure A-8: Calculated neutron diffraction pattern for YAP.....	188
Figure A-9: (a) YAM unit cell, (b) (001) projection.	189
Figure A-10: Calculated neutron diffraction pattern for YAM.	190
Figure A-11: Calculated neutron diffraction pattern for spinel when $a = 7.9526(5)$	192

APPENDIX B

Figure B-1: DTA traces of cooling and heating of YAG phase.	193
Figure B-2: DTA traces of heating of YAP phase.....	194
Figure B-3: DTA traces of cooling and heating of YAM phase.....	194

LIST OF TABLES

Chapter 2

Table 2-1: Thermal conductivity of AlN and other materials used in the electronic industry.	8
Table 2-2: Mechanical properties of AlN and other ceramics used for electronic substrates and packaging.....	9
Table 2-3: Electrical properties of AlN and other ceramics used for substrates and packages.	10
Table 2-4: Melting points, stability and structure of the phases in the Al_2O_3 - Y_2O_3 system [43].	17
Table 2-5: Melting temperature in the Al_2O_3 - Y_2O_3 system.....	18
Table 2-6: Properties of spinel.....	25

Chapter 5

Table 5-1: The data and the mathematical model of Al_2O_3 - Y_2O_3 binary system.....	43
Table 5-2: Gibbs energy of fusion of the solid compounds when solid Al_2O_3 and solid Y_2O_3 are the reference state	44
Table 5-3: The input and the mathematical model of Al_2O_3 - AlN binary system.....	45
Table 5-4: The data and the mathematical model of AlN - Y_2O_3 binary system.....	46
Table 5-5: Thermodynamic properties of Al_2O_3 and Y_2O_3	59
Table 5-6: Gibbs energy of formation of the stoichiometric compounds in Al_2O_3 - Y_2O_3 system.	60
Table 5-7: Thermodynamic properties of the stoichiometric compounds in Al_2O_3 - Y_2O_3 system.	61
Table 5-8: Thermodynamic properties of AlN.	62
Table 5-9: Gibbs energy of formation of the stoichiometric	62
Table 5-10: Thermodynamic properties of the stoichiometric compounds in AlN - Al_2O_3 system	62
Table 5-11: Thermodynamic data for liquid AlN- Al_2O_3 - Y_2O_3 system.	63
Table 5-12: Binary excess mixing terms.	64
Table 5-13 Thermodynamic data for spiel phase.....	65

Table 5-14: Binary excess mixing terms for spinel solution.	65
--	----

Chapter 6

Table 6-1: Amount of Y_2O_3 additive in each sample.	83
---	----

Chapter 7

Table 7-1: Chemical analysis of AlN powder.....	92
Table 7-2: Chemical analysis of Al_2O_3 powder.....	93
Table 7-3: Chemical composition of Y_2O_3 powder.	94
Table 7-4: Chemical composition and the expected phases of the studied samples.....	99
Table 7-5: Chemical composition of the samples studied by neutron diffractometry....	102

Chapter 8

Table 8-1: Crystal Structure data of AlN [1,14,115].	114
Table 8-2: Atoms positions in the unit cell of AlN [1,14,118].	114
Table 8-3: Summary of phase evolution for the Al_2O_3 - Y_2O_3 system.	132

Chapter 9

Table 9-1: The chemical composition of the studied samples.	137
--	-----

Appendix A

Table A-1: Crystal Structure data of Al_2O_3 [122,123,124].....	182
Table A-2: Atoms positions in the unit cell of Al_2O_3 [122]	182
Table A-3: Crystal Structure data of Y_2O_3 [48,109,124,128].....	183
Table A-4: Atoms positions in the unit cell of Y_2O_3 [109].....	184
Table A-5: Crystal Structure data of YAG [41,46,60].....	185
Table A-6: Atoms positions in the unit cell of YAG [129].	186
Table A-7: Crystal Structure data of YAP [41,103,132,133].	187
Table A-8: Atoms positions in the unit cell of YAP [133].	188

Table A-9: Crystal Structure data of YAM [51,53,132,134].....	189
Table A-10: Atoms positions in the unit cell of YAM [53].....	190
Table A-11: Crystal Structure data of spinel [64,68,115].....	191
Table A-12: Atoms positions in the unit cell of spinel [68,115].	191

NOMENCLATURE

k	Thermal conductivity
CTE	Coefficient of thermal expansion
q	Heat flux per unit time per unit area
T	Temperature
G	Gibbs energy of the system under consideration
H	Enthalpy
S	Entropy
C_p	Heat capacity
n_i	Number of moles of phase i
G_i	Gibbs energy of phase i
P	Number of phases
R	Gas constant
W	Any thermodynamic property like G , H or S
W_A^E	Integral excess thermodynamic property of component A
$a(s)$	The activity of that species on the solidus with respect to the liquid standard state
$a(liq)$	The activity of that species on the liquidus with respect to the liquid standard state
θ	Diffraction angle
λ	Wavelength
d	Lattice spacing

Chapter 1:

INTRODUCTION

The use of ceramics can be traced back to early civilizations when clay pots were used to keep food. After the discovery of fire, early humans used firing to improve the quality of the clay. The importance of ceramics increased significantly in the twentieth century for industrial applications involving the design and development of electrical systems. Ceramics have become the main stream form of electronic packaging. Their importance is directly related to their good electrical insulation, mechanical strength, thermal and chemical stability and durability. Aluminum nitride, AlN, is one of the most promising ceramic materials due to its excellent physical properties such as high thermal conductivity and high electrical resistivity, which are increasingly important in modern industrial and consumer applications, such as electronic packaging and microelectronics [1,2,3].

According to the United States Advanced Ceramic Association (USACA), there are currently twelve Japanese companies involved in AlN powder or component manufacturing, whereas in the USA only eight companies are involved in production and/or research and development [4], with one being in Canada. Moreover, a joint project involving both government and industry in Japan and United States has been established to determine the effects of microstructure and grain boundary chemistry on the strength of AlN substrates. This collaboration between Japan and the United States represents one of the first formal joint venture of both government and commercial enterprises in these two countries [5].

Numerous research programs are aimed at providing the technological base for the high volume production of AlN packaging at a cost comparable to alumina, Al_2O_3 . Currently, alumina is the dominant material used in ceramic packaging with an annual worldwide market for co-fired Al_2O_3 packaging of two billion dollars. AlN is also the most promising substrate alternative, due to its high thermal conductivity which is approximately 20 times better than that of alumina.

1.1 Applications of Aluminum Nitride

Aluminum nitride is an electrical insulator and a good thermal conductor. This combination of properties makes it a suitable material for packaging electronic devices, since there is no loss in the electrical signal and, at the same time, the heat generated can be dissipated efficiently [6].

Diamond and cubic boron nitride are theoretically superior to other ceramic materials with regards to their high thermal conductivity, but they are very expensive and processes for manufacturing practical parts have not yet been achieved. In addition, beryllium oxide, BeO, has a theoretical thermal conductivity of 370 W/m.K and a practical value of approximately 260 W/m.K, but it has a relatively high coefficient of thermal expansion, CTE, ($8 \times 10^{-6}/^\circ\text{C}$) compared with silicon ($3.2 \times 10^{-6}/^\circ\text{C}$) [7,8]. Although it is toxic, it is still being used [7]. On the other hand, AlN is a non-hazardous, synthetic ceramic material that can offer similar functionality as BeO [9] and experiments from Miyashiro showed that BeO can be replaced by AlN without any circuit pattern changes [7].

Therefore AlN is a very promising material for electronic substrate applications, due to its intrinsic properties such as a low dielectric constant and electrical resistivity, good mechanical properties, a coefficient of thermal expansion near that of silicon and high thermal conductivity [7,9]. Moreover, the temperature dependent difference in the thermal expansion coefficient between AlN and Si is very small. This is considered as a major advantage for high power semiconductor substrates and packages and for large silicon chips

[7,10]. Moreover, the co-firing approach enables the creation of sophisticated AlN packages with up to twelve layers of ceramic and metal [9].

Nipko *et al.* mentioned that AlN has a phonon Density-of-State similar to those of BeO and SiC, and its thermal conductivity peaks at ~ 45 K can be seen in Figure 1-1. It was found that AlN possesses the microscopic and macroscopic properties that are desirable for wide-bandgap semiconducting devices capable of operating at elevated temperatures [11].

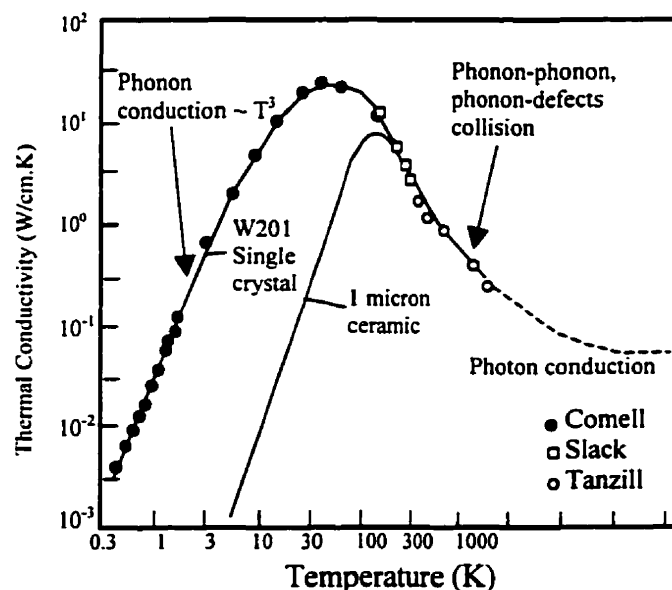


Figure 1-1: Thermal conductivity versus temperature for AlN [11].

Conventionally, Al_2O_3 has been used as an electronic substrate due to its good mechanical properties as well as low manufacturing costs. But due to its low thermal conductivity ($\sim 20 \text{ W/m.K}$) at room temperature and high CTE ($7.2 \times 10^{-6}/^\circ\text{C}$) compared with that of silicon ($3.2 \times 10^{-6}/^\circ\text{C}$) alumina is adequate to dissipate the heat of simple modules. However it is not adequate for the newer modules with a high circuit density [7,8,12]. Hence Miyashiro *et al.* proposed that AlN can replace alumina because of its high thermal conductivity [7]. Furthermore, its dielectric constant is no more than that of alumina and the thermal expansion coefficient ($4.2 \times 10^{-6}/^\circ\text{C}$) matches that of silicon [3].

Recently, a higher frequency band has been introduced for telecommunication systems such as mobile cellular phones and broadcasting satellites due to the increasing volume of information and communication media. Since AlN films exhibit piezoelectric behaviour with high velocity, AlN has drawn attention as a piezoelectric material for high frequency acoustic wave devices [13]. Furthermore, because of this property, AlN has also been used in thin-film microwave acoustic resonator applications [14].

AlN substrates are more translucent when their purity is increased, resulting in higher thermal conductivity. This is not a problem for general use, but in the case of packages for Large-Scale Integrated (LSI) memories, light from outside the package must be avoided because the devices are light sensitive [7]. However in other areas, this transparent property when combined with its wear resistance make AlN attractive for some electro-optic applications [4].

1.2 Major obstacles to commercialization of AlN

The single most important obstacle in the commercialisation of AlN is the cost, since the cost of most AlN powders in the market is four to ten times that of electronic grade alumina [4, 16].

Another obstacle is the reputation for poor lot-to-lot reproducibility both in thermal conductivity and the adhesion of metallization layers [4]. As a result, only directly bonded copper substrates and metallized substrates are currently on the market because there are still several production problems to be solved [7].

Chapter 2:

LITERATURE SURVEY

2.1 Crystal structure of AlN

Aluminum nitride is a tetrahedrally coordinated III-V compound which crystallizes at ambient conditions in the hexagonal, wurtzite structure [14,17-19]. However at a high pressure of 16-17 GPa and at 1673-1873K, it undergoes a first order phase transition to the rock salt, cubic structure.

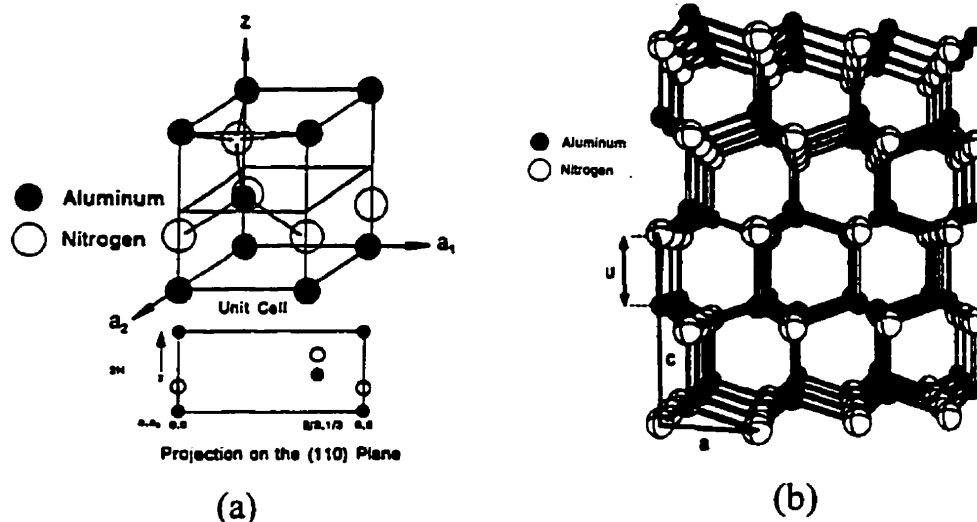


Figure 2-1: (a) The crystal structure of AlN [19]. (b) Wurtzite structure of AlN [14].

According to Jackson *et al.* and Ruiz *et al.*, [1,14], the wurtzite structure (shown in Figure 2-1) has cell dimensions of $a = 3.11(2)\text{\AA}$, $c = 4.98(2)\text{\AA}$, and the internal

coordinate $u = 0.382(1)\text{\AA}$. The careful determination of the AlN lattice parameters has been proposed as a means of obtaining quantitative information about the oxygen concentration in the AlN lattice, and its thermal conductivity. A reduction in the c lattice parameter has been shown to accompany higher oxygen concentration and lower thermal conductivity of the AlN grains [20]. Even though several investigators have focused on relating thermal conductivity of AlN to *lattice oxygen* concentration, Grigoriev *et al.* [21] mentioned that the investigation of grain-boundary purity is an equally important factor affecting thermal conductivity. Also, Tsuge *et al.* [22] related the oxygen contents in synthesized AlN in the formation of the spinel phase. As the spinel content increases with greater oxygen impurity in the starting powder there was a correlation to the thermal conductivity drop in the sintered nitride. Moreover, McCauley *et al.* [23] concluded that minor additions of nitrogen or oxygen to Al_2O_3 and AlN, respectively, result in a variety of modulated structures based on either AlN or spinel. It is also interesting to note that pure AlN does not form polytypic structures, whereas small oxygen additions result in several polytype-like structures which will be discussed further in section 2.8.

Although AlN crystallizes in the hexagonal wurtzite structure, which is the only stable phase at ambient pressure, the growth of single crystals is difficult primarily due to the high melting temperature and the decomposition of the material at temperatures approaching the melting point. Only small single crystals in the order of millimetres have been prepared thus far [11].

2.2 Properties of Aluminum Nitride

2.2.1 Thermal Conductivity

Thermal conduction is the phenomenon by which heat is transported from high to low temperature regions of a substance. The property that characterizes the ability of a material to transfer heat is the thermal conductivity and it is defined in terms of the Fourier equation:

$$q = -k \frac{dT}{dx} \quad \text{..... 2-1}$$

where q denotes the heat flux per unit time per unit area, k is the thermal conductivity, and dT/dx is the temperature gradient through the conducting medium.

Heat is transported in solid materials by both lattice vibration waves, or phonons, and free electrons. At high temperatures, radiation conductivity becomes important. Thus total conductivity is the sum of the three contributions,

$$k = k_l + k_e + k_r \quad \text{..... 2-2}$$

where k_l , k_e and k_r represent the lattice vibration, electron and radiation thermal conductivities, respectively. In dense ceramic materials, the phonons are primarily responsible for thermal conduction, i.e. k_e is much smaller than k_l [12,24].

Extensive research is under way to increase the thermal conductivity of sintered AlN and to improve their lot-to-lot reproducibility. High thermal conductivity is the main attribute of AlN, and is the driving force behind its development as a packaging material. The principle behind this is that a high thermally conductive substrates obviates the necessity of external cooling and facilitates the development of packages with a high chip density [1].

The theoretical thermal conductivity of 319 W/m.K [20,25-28] has not been attained although values above 280 W/m.K have been reported [28]. According to other investigators this theoretical value has only been measured on single crystals. Knowing that compounds with the wurtzite structure have two different principal thermal conductivities in directions parallel and perpendicular to the c-axis, these values do not differ by more than 20%, and the value given is an average [29]. A thermal conductivity of 230 W/m.K has been achieved by an annealing process developed by Taiyo Yuden Company (Gumma, Japan) [4], while the highest thermal conductivity of sintered AlN reported in the literature is 260 W/m.K [4,20,26,30].

Table 2-1: Thermal conductivity of AlN and other materials used in the electronic industry.

Reference	Thermal conductivity 25°C (W/m.K)						
	AlN		Al ₂ O ₃	BeO		SiC	Si
	experimental	theoretical		experimental	theoretical		
Ref. 19	160	320	20	260	370	270	==
Ref. 7	70-270		20	250-300		==	120
Ref. 10	170-260		20	260		==	==
Ref. 26	no additives	4wt% Y ₂ O ₃	==	==		==	==
	114	194					

Kuramoto *et al.* mentioned that the thermal conductivity of AlN ceramics is very sensitive to both metallic and oxygen impurities. As little as 200ppm of silicon, iron or magnesium significantly reduces the conductivity, suggesting that these metals diffuse into the AlN lattice during processing or sintering [10].

The heat carrier in AlN is the phonon. Phonon scattering may occur due to impurities or lattice imperfections and decrease thermal conductivity. The most harmful impurity has been found to be oxygen. This is a result of the relatively high oxygen levels in the starting AlN powder, the high solubility of oxygen in the AlN lattice and the powder's susceptibility to oxidation and hydrolysis. Dissolved oxygen ions in AlN occupy the nitrogen sites, and they generate aluminum vacancies to compensate for the electric charge imbalance [26,28,30]. The thermal conductivity of AlN depends on the sintering conditions, temperature and holding time, as well as, the amount of sintering additive [25,30].

Most of the recent work on high thermal conductivity AlN ceramics has focused on reducing the oxygen levels in solution in the AlN lattice [26].

At low temperatures the major limitation of heat conduction by phonons is scattering by external boundaries (e. g., domain size of a powder or sample dimensions of a single crystal). This gives rise to a $\sim T^3$ behavior of the thermal conductivity at low temperatures. In a typical log-log plot (Figure 1-1) the thermal conductivity increases linearly, reaching a maximum at a characteristic temperature (T_0), and then decreases

with increasing temperature as phonon-phonon and phonon-defect scattering become the dominant processes [11].

2.2.2 Mechanical Properties

Aluminum nitride has excellent ballistic impact resistance, which has provoked substantial attention for its potential structural applications despite its relatively low fracture toughness and strength [32]. The mechanical properties of AlN and other ceramic materials used in the electronic industry are summarized in Table 2-2. It can be noticed that AlN is stronger than Al_2O_3 which is used in standard applications.

Table 2-2: Mechanical properties of AlN and other ceramics used for electronic substrates and packaging.

Flexure strength (MPa)				
Reference	AlN	Al_2O_3	BeO	SiC
Ref. 19	340-490	304-314	245	==
Ref. 7	300-500	240-260	170-230	450
Ref. 10	320-350	300	200	==
Ref. 26	No additives	4wt% Y_2O_3		
	240	353	==	==
Vickers Hardness (GPa)				
Ref. 19	12	12	23-27	==
Ref. 10	11	25	12	==
Ref. 35	12	19	12	24
Bulk modulus of AlN (GPa)				
Reference	Measured value		Theoretical	
Ref. 14	202-237		228-231	

Experimental work conducted by Chen *et al.* showed that the highest compressive strength of sintered aluminum nitride was 5.4 GPa [33].

2.2.3 Electrical Properties

Aluminum nitride is an electrical insulator [6]. Electrical resistivity of AlN, formed by nitrogen implantation into aluminum, increased with increasing implanted dose, which was found experimentally to be about 1.4×10^{12} to $2 \times 10^{12} \Omega\text{cm}$ [34].

The Raman piezo-spectroscopic behaviour of AlN has been studied for two materials prepared with and without sintering aids, by Muraki *et al.*. The values of the slope, that is, the uniaxial piezo-spectroscopic coefficients are different, whereas the stress-free frequency is the same for the samples prepared with and without sintering aids. This indicates that there is no major dissolution of the sintering aid inside the AlN lattice. This is consistent with their TEM observations, which show that the sintering aid tends to remain in triple pockets among the grains [6].

Table 2-3: Electrical properties of AlN and other ceramics used for substrates and packages.

Item	Reference	AlN	Al ₂ O ₃	BeO	SiC
Volume resistivity (Ωcm)	[7,19]	$>10^{14}$	$>10^{14}$	$>10^{14}$	$>10^{14}$
Dielectric strength (kV/cm)	[7]	140-170	100	100	7
	[10,19,35]	150	150	100	7
Dielectric constant (1MHz)	[7]	8.8	8.5	6.5	40
	[10,35]	8.9	9.4	7.0	42

2.3 Sintering additives

In general because of its poor sinterability, AlN is densified using typical sintering aids, such as rare earth compounds (Y_2O_3 , YF_3 , $\text{Y}_3\text{Al}_5\text{O}_{12}$) and alkaline earth compounds (CaO , CaCO_3) [27,36].

Aluminum nitride is a covalently bonded solid with an associated low diffusivity which would be expected to lead to poor sinterability. However AlN powder, when exposed to air, always contains a protective surface oxide in addition to dissolved oxygen

in the lattice. Hence it is possible to densify AlN directly as a result of Al-O-N liquid formation at temperatures $> 1850^{\circ}\text{C}$. However, this liquid wets the AlN grains and is not effective in eliminating lattice oxygen, which invariably results in low thermal conductivity values.

In the case of additives, it has been hypothesized that the AlN densifies rapidly by a transient liquid phase mechanism [1], where the surface Al_2O_3 reacts with the oxide additives to form the initial M-Al-O-N liquid (M = metal) that promotes particle rearrangement and densification [2,10,27]. For example, from the experimental work of Jackson *et al.*, densification of AlN- Y_2O_3 at 1850°C for 1 minute had a tendency to confirm this hypothesis. They inferred from the micrographs that after a few seconds, the liquid, that originally was wetting the AlN grains, had become quickly nonwetting with changes in concentration [1]. According to De Baranda *et al.*, the effects of additives were:

- the formation of liquid phase at high temperatures, which promoted densification via liquid-phase sintering.
- the reduction of the impurity levels in the AlN grains by incorporating them into the liquid [10,26,28].

The liquid effectively prevents oxygen atoms from diffusing into AlN grains during sintering and thus prevents the decrease in thermal conductivity [10]. According to Dumitrescu and Sundman, Al_2O_3 is considered a basic oxide, assuming that it would easily give up its oxygen [37]. The sintering aid for AlN should react with the surface Al_2O_3 . Moreover the quantity of this additive should be sufficient to consume all existing Al_2O_3 in order to purify AlN grains and to have AlN-AlN surface contact.

Hence the addition of sintering aids has a dual purpose; it aids in densification and enhances the thermal conductivity by controlling the grain boundary microstructure. The role of additives in enhancing thermal conductivity can be understood, when considering the effect of various parameters on thermal conductivity, particularly the role of impurities. From a thermodynamic point of view, the greater the affinity of an additive

for Al_2O_3 , the greater the degree of purification of the AlN lattice during sintering and/or annealing [1].

According to Kuramoto *et al.*, AlN sintered without an aid had a thermal conductivity of 124 W/m.K. They also studied the sintering behaviour of AlN using calcium aluminate ($3\text{CaO} \cdot \text{Al}_2\text{O}_3$) as sintering aid. They concluded that a translucent and higher thermal conductivity (175 W/m.K) AlN ceramic can be produced from high-purity raw powder using this sintering aid by normal sintering in N_2 at 1800°C [10].

Kasori and Ueno have shown that Y_2O_3 was a better additive for thermal conductivity enhancement than YAG ($\text{Y}_3\text{Al}_5\text{O}_{12}$), although YAG has been used as a sintering aid for AlN, but without any thermal conductivity improvement (90-110 W/m.K). On the other hand, a value of 245 W/m.K was achieved using Y_2O_3 and by annealing it in a carbon-reducing atmosphere at 1850°C for 100 h [30]. Also it was concluded by More *et al.*, that Y_2O_3 was an excellent additive for AlN, when compared with other rare-earth additives such as; Sm_2O_3 , Lu_2O_3 , Ce_2O_3 , Nd_2O_3 and Pr_6O_{11} [1].

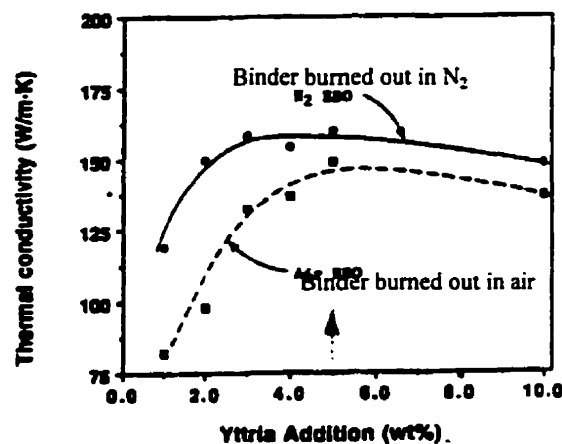


Figure 2-2: Variation of thermal conductivity of AlN as a function of Y_2O_3 content.

De Baranda *et al.*, studied the effects of Y_2O_3 over the range of 1.0 to 10.0 wt%. Figure 2-2 shows that the thermal conductivity increases with increasing Y_2O_3 doping, goes through a maximum at about 3 to 5 wt% Y_2O_3 and then slowly decreases with increasing Y_2O_3 doping [28]. This is consistent with the observations of More *et al.*, in that the thermal conductivity of the AlN ceramic increases as the Y_2O_3 content increases

and then decreases after 5 wt% Y_2O_3 because of the increasing volume fraction of yttrium aluminate volume at the grain boundaries [1].

Hirano *et al.*, studied the effect of Y_2O_3 on sinterability, thermal conductivity and microstructure of AlN, and showed that addition of 3 wt% Y_2O_3 was required to achieve a fully densified AlN body by sintering at 1750°C for 2 h., while material with only 1.5 wt% Y_2O_3 did not reach its theoretical density. They also found that Y_2O_3 enhanced the thermal conductivity of AlN [25].

It is becoming clear that an understanding of the phase equilibria of the ternary AlN- Al_2O_3 - Y_2O_3 system is essential for further development of the AlN ceramic materials, because phase diagrams (*even if based on estimated data*) can illustrate the phase relations and phase stability under different sintering conditions.

2.4 Sintering Mechanism of AlN

Sintering of AlN with the addition of Y_2O_3 occurs in the presence of a liquid phase. According to Kingery the classical liquid-phase sintering must satisfy three requirements:

1. formation of a liquid phase, even though it is metastable at the sintering temperature.
2. Solubility of the solid phase in the liquid.
3. Wetting of the solid by the liquid [38].

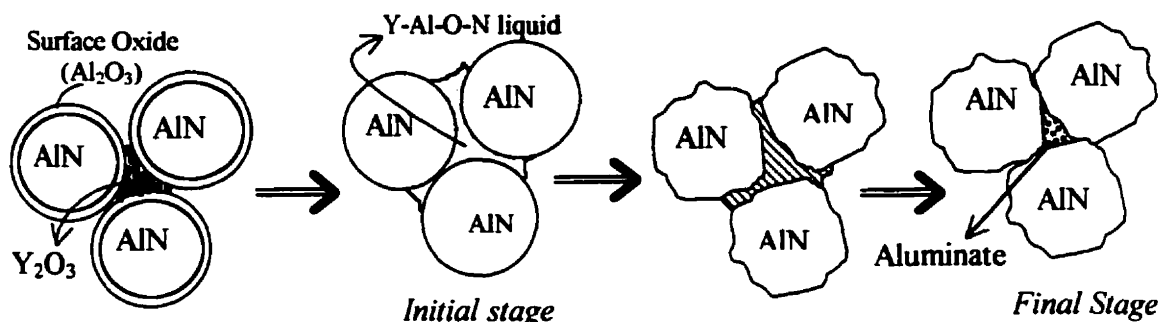


Figure 2-3: Schematic diagram of AlN sintering.

Figure 2-3 illustrates a model for AlN sintering, where the interaction between Y_2O_3 and the surface oxide of AlN powder leads to the formation of a liquid during sintering. When the liquid first forms, it tends to completely coat the surface of the solid particles. At later stages this liquid becomes nonwetting and migrates to the triple points prior to solidification. Chen *et al.* observed that the distribution of the secondary phase changed from good to nonwetting with increasing sintering time [39].

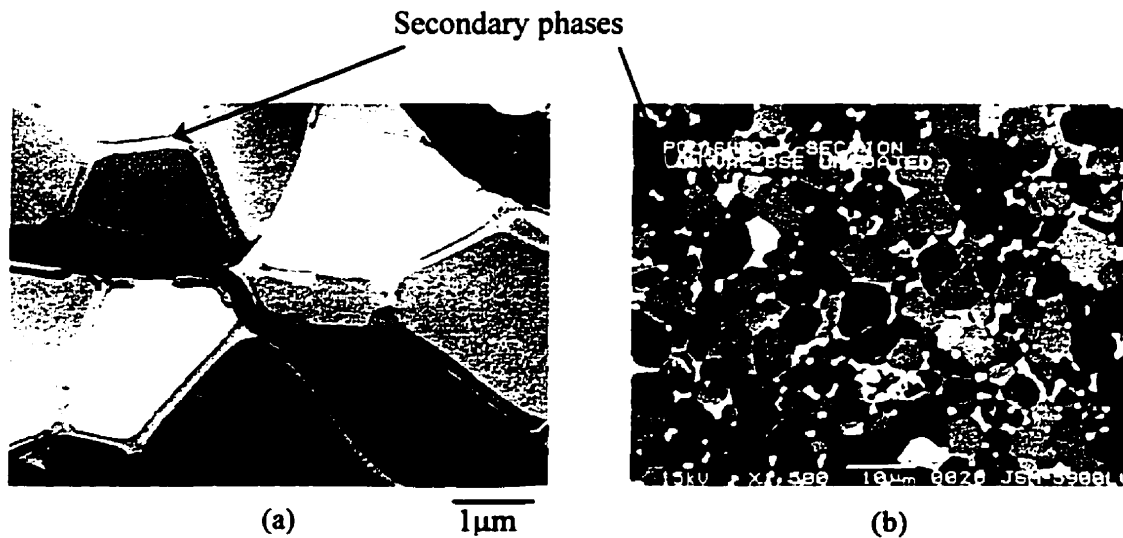


Figure 2-4: (a) TEM Micrograph of fracture surface of sintered AlN without Y_2O_3 [19]
(b) BS-SEM micrograph of commercial AlN substrates sintered with addition of Y_2O_3 .

This can be easily observed by comparing Figure 2-4(a) with 2-4(b). Figure 2-4(a) shows an AlN microstructure sintered without Y_2O_3 and displays a secondary phase film entirely coating the AlN grains. In contrast, Figure 2-4 (b) shows the microstructure of sintered AlN containing Y_2O_3 addition as the sintering aid. With the introduction of Y_2O_3 , the secondary phase is segregated to the triple points and adjacent AlN particles are intimately connected without any physical barrier.

The amount of liquid and the phase formation at a selected sintering temperature can be predicted using phase equilibrium diagrams. Hence one can clearly see the importance of a detailed and complete study of the ternary AlN- Al_2O_3 - Y_2O_3 phase equilibria.

2.5 Ternary AlN-Al₂O₃-Y₂O₃ Phase Diagram

To date, there is little information on the ternary AlN-Al₂O₃-sintering additives system [27]. To calculate reliable ternary, quaternary, and higher order metallic and ceramic phase diagrams, we need a thermodynamic description of the binary phase diagrams and a thermodynamic model that can extrapolate binary data into ternary and higher-order systems [40]. This is commonly done for metals where the thermodynamic data are more readily available. For ceramic systems, thermodynamic data are very sparse. Furthermore measurements are very difficult considering the high temperatures involved.

The effect of Al₂O₃ additions on the phase reaction of the AlN- Y₂O₃ system at high temperatures of 1900°C and 1950°C was investigated by Kim *et al.* For the AlN-3wt% Y₂O₃ system, Al₂O₃.2Y₂O₃ (the YAM phase) having the lowest Al₂O₃ content of yttrium aluminates was identified. And in the AlN-10wt% Y₂O₃ system, unreacted Y₂O₃ was detected in addition to YAM, because the Y₂O₃ was in excess amounts [27].

In a ternary system (A-B-C), the other binary systems (A-B), (A-C) and (B-C) contribute similarly to the thermodynamic properties of the ternary component system [40]. In our case they are (AlN-Al₂O₃), (AlN-Y₂O₃) and (Al₂O₃-Y₂O₃) respectively.

2.6 Al₂O₃-Y₂O₃ System

The significance of this phase diagram comes from the importance of alumina and yttria for liquid phase sintering of covalently bonded ceramics, such as AlN, Si₃N₄ and SiC.

According to the literature review of Gröbner *et al.*, there are three aluminate compounds in this system; Ytria Alumina Garnet (YAG), Ytria Alumina Perovskite (YAP) and Ytria Alumina Monoclinic (YAM) [41]. The published stability and melting temperatures of these phases are reported and are summarized in Table 2-4. These

compounds are of considerable interest as solid-state laser materials [41-43]. Recent studies show that YAG and the Al_2O_3 -YAG eutectic are potential candidate materials for reinforcement fibers in ceramic and intermetallic composites used in structural applications [44,45], because YAG and Al_2O_3 do not react with each other, they have a low thermal expansion mismatch and YAG has a lower and less anisotropic creep rate than Al_2O_3 [46].

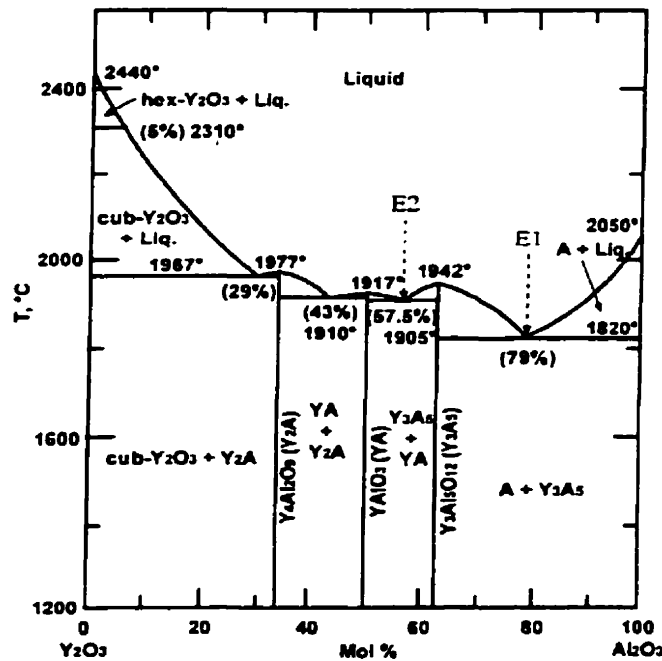


Figure 2-5: The experimental phase diagram of Y_2O_3 - Al_2O_3 System [47].

YAG adopts the cubic garnet structure, YAP has an orthorhombic distorted perovskite structure and YAM has monoclinic structure [42,43]. It can be seen from the experimental phase diagram (Figure 2-5) that Y_2O_3 has two forms: the low temperature form which crystallizes in the cubic c-type structure with $a = 10.604 \text{ \AA}$ and the high temperature hexagonal phase with $a = 3.81 \text{ \AA}$ and $c = 6.08 \text{ \AA}$. The transition temperature was determined by Foex and Traverse in 1966 to be 2573K (2300°C) and in 1985 by Mizuno as 2614K (2341°C) [48].

Since YAG has been found to produce translucent ceramics, it is used for high pressure sodium lamp envelopes due to its better properties when compared to the earlier used alumina ceramics [41]. And since it has a cubic structure, there are no birefringence effects and the thermal expansion is isotropic. This, coupled with its refractive nature and other useful properties, makes it an advanced ceramic for applications in electronic, optical and magneto-optic devices [49].

YAlO_3 (YAP) is an excellent material for gain media, scintillators and acousto-optics. Single crystal YAP can be grown by the Czochralski technique or by vertical directional solidification [50]. Yamane *et al.* [51,52,53] studied the phase transition of $\text{Y}_4\text{Al}_2\text{O}_9$ (YAM) by high temperature Differential Scanning Calorimetry (DSC), high temperature X-ray powder diffraction and high temperature dilatometry. They detected an enthalpy and a volume change around 1400°C , which is an indication of a phase transition. The phase transition showed thermal hysteresis with a width of 78°C and characteristics of martensitic phase transition. Their powder diffraction experiments also showed no difference in the diffraction patterns of the high temperature or the room temperature phases [42,43,51]. YAG is the only unambiguously stable phase in the system according to Abell *et al.* [42].

Cockayne [43] reviewed this system and reported the melting points and the stability ranges for the end and stoichiometric compounds that occur in this system. These data are summarized in Table 2-4.

Table 2-4: Melting points, stability and structure of the phases in the Al_2O_3 - Y_2O_3 system [43].

Compound	Melting Point	Stability range	Structure of room temperature phase.
Al_2O_3	2050	T_{melt} to room temp.	Rhombohedral
YAG	1970	T_{melt} to room temp.	Cubic (garnet)
YAP	1870	T_{melt} to room temp.	Orthorhombic (perovskite)
YAM	1930	T_{melt} to 1000°C .	Monoclinic
Y_2O_3	2400	T_{melt} to room temp.	Cubic

Also Gröbner *et al.* [41] reported the measured melting temperature by different researchers for the stoichiometric compounds in this system. These values are summarized in Table 2-5.

Table 2-5: Melting temperature in the Al_2O_3 - Y_2O_3 system.

Researcher	Melting Temperature K		
	YAG	YAP	YAM
Warshaw [55]	2243	=	2303
Toropov [56]	2203	2143	2293
Abell [42]	2243	2148	2203
Caslavsky [57]	2213	2189	=
Bondar [58]	2223	2213	2293
Adylov [41] (cited)	2215	2190	2250
Gröbner [41](calculated)	2213	2184	2299

A mutual solubility of Y_2O_3 in Al_2O_3 mentioned by Mizuno and Naguchi (1967), Figure 2-6(d), could not be verified by other researchers. Whereas Goldberg stated that there is almost no solubility of Y_2O_3 in Al_2O_3 [41].

Lo and Tseng [59] studied the phase evolution of YAG, YAP and YAM synthesized by a modified sol-gel method and they used X-ray diffractometry to determine the crystalline phases. They could obtain synthesized high-purity YAG and YAM phases, but they concluded that YAP is a result of reaction between YAG and YAM, where residual amounts were left even after heat treatment. The temperature range and holding time used in this study are 650°C to 1500°C and 6 min. to 40 h respectively.

Gervais *et al.* [60] studied the solidification process of liquid YAG and YAP by differential thermal analysis. They found that the crystallization of melts of YAG and YAP depend on their liquidus temperature and critical temperatures and these were evident in the liquid. Cooling from these critical temperatures or above was shown to lead to a stable or metastable solidification path, respectively. They concluded their study by referring to the difficulties in the growth of single crystals of both YAG and YAP and related this behaviour to the discrepancies in the published Al_2O_3 - Y_2O_3 phase diagrams.

Cockayne [43] reviewed the chronological development of the $\text{Al}_2\text{O}_3\text{-Y}_2\text{O}_3$ phase diagram, Figure 2-6(a) to Figure 2-6(e). Part (f) of this figure was published in 1992 by Mah and Petry after Cockayne's 1985 paper.

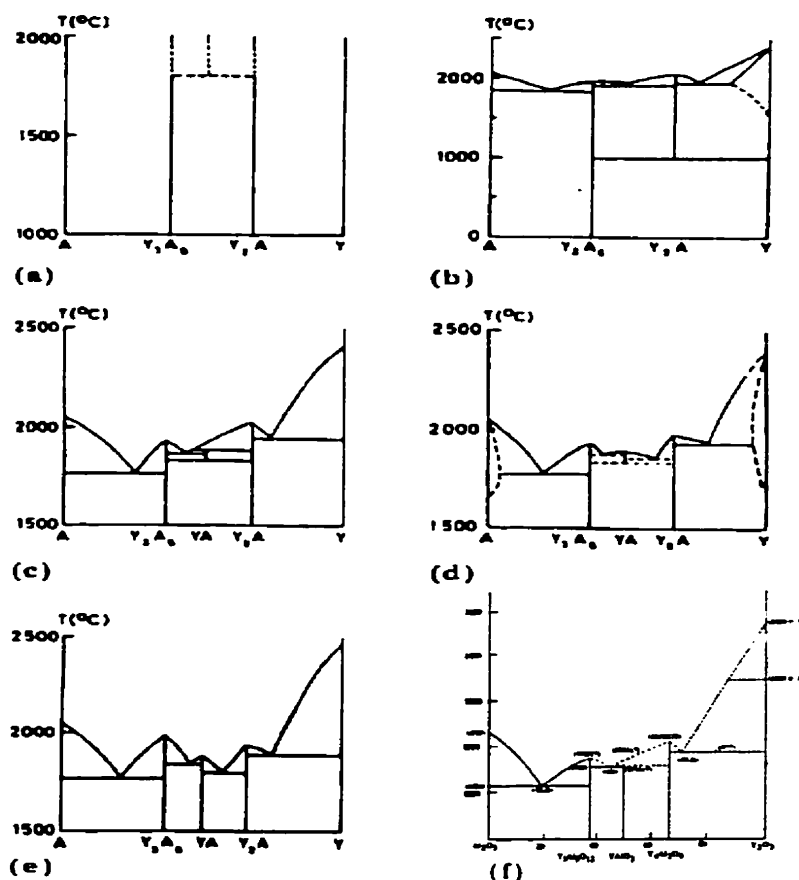


Figure 2-6: Chronological development of the $\text{Al}_2\text{O}_3\text{-Y}_2\text{O}_3$ phase diagram; (a) Schneider *et al.* (1961), (b) Olds and Otto (1961), (c) Toropov *et al.* (1969), (d) Mizuno and Naguche (1967), (e) Abell *et al.* (1974) and (f) Mah and Petry (1992).

Cockayne reported that the first $\text{Al}_2\text{O}_3\text{-Y}_2\text{O}_3$ phase diagram was published by Schneider *et al.* in 1961. However an earlier paper published by Warshaw and Roy [55] in 1959 was found. In this paper Warshaw and Roy, who were the first to study phase

equilibria in this system, considered YAP as a thermodynamically metastable compound and did not include it in their phase diagram. However, they indicated the liquidus in this phase diagram with a dashed line [50,55]. Their phase diagram, Figure 2-7, was measured using X-ray analysis and melting observations. It can be seen that this figure is a better estimation for the Al_2O_3 - Y_2O_3 phase diagram than that of Schneider (1961) and Ods and Otto (1969), if they are all compared with the most recent experimental phase diagram shown in Figure 2-5.

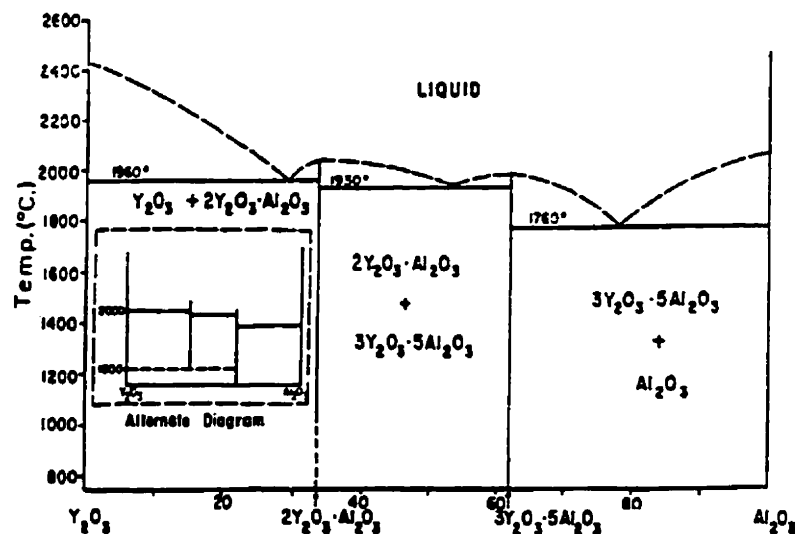


Figure 2-7: Al_2O_3 - Y_2O_3 phase diagram, after Warshaw and Roy 1959, [55].

The first estimate of thermodynamic functions in this system was published by Kaufman *et al.* [62]. While, Gröbner *et al.* [41] optimized the system using all available experimental data in the literature, Jin and Chen [45] modeled the Al_2O_3 - Y_2O_3 phase diagram using Kaufman estimating methods. Their published phase diagram is shown in Figure 2-8.

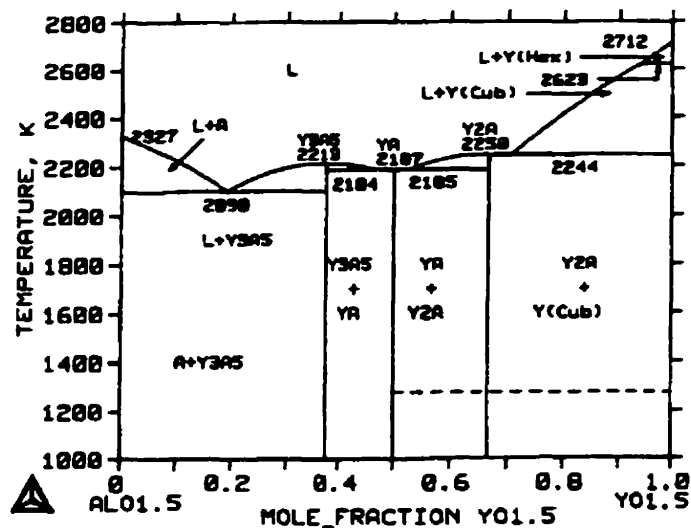


Figure 2-8: Calculated $\text{AlO}_{1.5}$ - $\text{YO}_{1.5}$ phase diagram by Jin and Chen [45].

2.7 AlN - Y_2O_3 System

No effort has been made thus far in analyzing the entire system experimentally. Kaufman *et al.* [62] published a thermodynamic estimation for this phase diagram and they reported that a simple eutectic system describes the equilibria between the various phases, as shown in Figure 2-9.

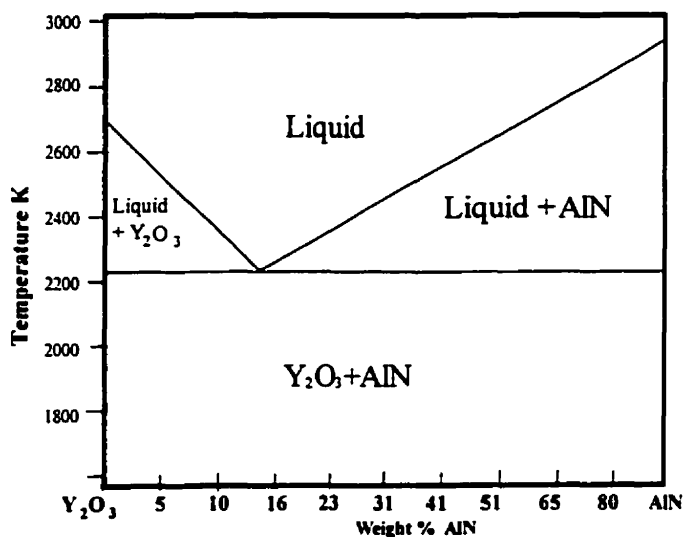


Figure 2-9: Y_2O_3 -AlN calculated phase diagram by; Kaufman *et al.* [62].

2.8 AlN - Al₂O₃ System

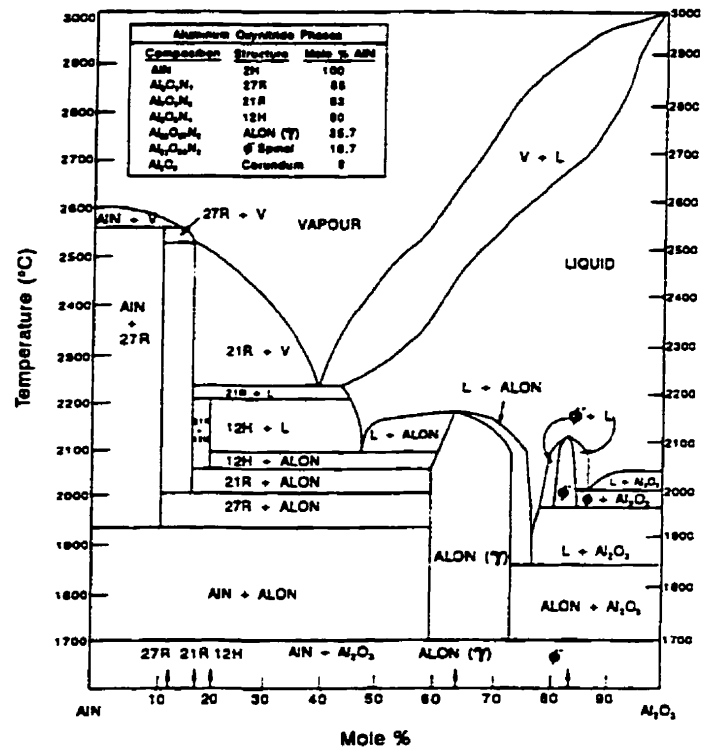


Figure 2-10: The phase diagram of AlN-Al₂O₃ system [23].

In general, knowledge of the AlN-Al₂O₃ phase equilibria is based on that of the Al-N-O-Si quaternary system, because it includes the formation of SiAlON compounds, which exhibit good properties for a wide range of applications [63]. The interest of these compounds started in the United Kingdom in the early 1960s [64].

The phase diagram of AlN - Al₂O₃ system was studied by several authors [23, 63-71]. McCauley and Corbin [23] published an experimental estimation for this system shown in Figure 2-10. Qui and Metselaar [65] reviewed the contradictory information obtained previously, reinvestigated the system and published an optimized phase diagram shown in Figure 2-11.

The first phase diagram for this system was reported by Lejus in 1964. Six phases were identified including a phase designated 'X' which encompassed all compositions for the polytype phases [64].

The phases which form in the AlN - Al₂O₃ system can be separated into two groups depending on their basic crystallographic structure. One group is based on polytypes of the wurtzite structure and the other is based on the spinel structure [64].

McCauley and Corbin constructed an isobaric condensed phase diagram in the region of stability of cubic aluminum oxynitride spinel (AlON) in the binary Al₂O₃-AlN system. The phase equilibria were deduced primarily from various analytical measurements and microstructural observations (Figure 2-10). They reported that cubic aluminum oxynitride spinel melts incongruently at about 2050°C and is compositionally centered at 35.7 mol% AlN, which is equivalent to the stoichiometric composition of Al₂₃O₂₇N₅ or 5AlN.9Al₂O₃ [66]. They published an experimental phase diagram for the AlN-Al₂O₃ system and they listed seven phases [23, 37,66]:

- AlN with the wurtzite structure.
- Al₉O₃N₇ with 27R AlN polytype structure.
- Al₇O₃N₅ with 21R AlN polytype structure.
- Al₆O₃N₄ with 12H AlN polytype structure.
- Al₂₃O₂₇N₅ with an AlON spinel structure.
- Al₂₂O₃₃N₂ with a Φ -spinel structure.
- Al₂O₃ with a corundum structure.

The polytypes are layer super structures based on AlN hexagonal wurtzite structure with large repeat distances along the c-axis. The first polytype of the AlN-Al₂O₃ system is 21R and was formed by Adams *et al.* in 1962 with a chemical composition of 66 mol% AlN. This is in addition to the fact that they reported an important solubility of Al₂O₃ in AlN of up to 17 mol% [63,64]. In the notation of Ramsdell-Parthé (1964), polytypes with the formula Al_nO₃N_{n-2} in the AlN-Al₂O₃ system were denoted as 2nH (n is even) or 3nR (n is odd). The H polytypes have the P6₃mc space group and the R

polytypes have the $R\bar{3}m$ space group. Sakai (1978) found the phases 27R, 16H, 21R, and 12H in the Al-N-O ternary system [63].

Since Yamaguchi and Yanadigida found a new spinel phase in 1959 (the γ -phase of aluminum oxynitride synthesized from Al_2O_3 and AlN) many investigations have been conducted on its optical, mechanical and chemical properties. This phase has been referred to in several ways, e.g. γ -alon, γ -ALON, AlON, alon and spinel. The latter one will be used in the present work for the solid solution region in the Al_2O_3 -AlN system and will be centered around the composition $5AlN.9Al_2O_3$, which has a spinel structure.

Spinel has been an attractive ceramic material for refractories in the ferrous and non ferrous industries and for protective windows in optical systems due to its chemical stability and transparency at high temperature [67,68]. Goursat *et al.* determined by neutron diffraction the crystal structure of spinel to be $Fd\bar{3}m$ spinel [64] with vacancies in the octahedral positions [69].

Although a considerable number of articles on spinel have been published the thermodynamics of spinel are still not very well known. In the first place there is some disagreement about the temperature at which spinel can be formed. Secondly, the proper formula for spinel, which is not a stoichiometric compound, creates some difficulty as to how the reactions should be balanced. Willems *et al.* reported that values determined by other researchers for the temperature necessary for the formation of spinel is above 1500-1700°C [69].

In the experimental work of Willems *et al.*, neutron and X-ray diffraction experiments were performed on spinel powders with compositions corresponding to 67.3, 73 and 77.5 mol% Al_2O_3 . Neutron diffraction yielded approximately the same lattice parameters for the spinel phase as X-ray diffraction. The measured lattice parameters were 7.953 Å, 7.944 Å and 7.938 Å for spinel with a composition of 67.5, 73 and 77.5 mol% Al_2O_3 , respectively [68].

Corbin *et al.* [23] determined the basic properties of spinel using pressureless sintering, forming nearly pore free single phase samples. Their results are summarized in Table 2-6.

Table 2-6: Properties of spinel.

Knoop (100) hardness		1800 kg/mm ²
Elastic Modulus		3.3×10^5 MPa
4-point bend strength	at room temperature	306 MPa
	at 1000°C	267 MPa
	at 1200°C	190 MPa
Thermal expansion coefficient		7×10^{-6} /°C

According to Corbin [64], this material has been processed into fully dense transparent material and shows promising mechanical and optical properties suitable for infrared and visible window applications.

The stability of the spinel phase is well described and all other compounds except $\text{Al}_{22}\text{N}_{33}\text{O}_2$ with a Φ -spinel structure are included in the new evaluation (1997) of the $\text{AlN-Al}_2\text{O}_3$ system, by Qiu and R. Metselaar [65].

Figure 2-11 shows the calculated phase diagram of the binary $\text{AlN-Al}_2\text{O}_3$ system, by Qiu and Metselaar, The interaction parameters for the liquid were evaluated by applying the ionic liquid model using the Thermo-Calc program, whereas the thermodynamic descriptions of the ternary compounds are from the work of Dumitrescu and Sundman, where they used the substitutional model for the liquid [37,65].

The phase relations were also calculated by Dorner *et al.* in 1981 and Kaufman in 1979 using thermodynamic data. Both investigations used a 25 mol% AlN for the composition of spinel phase. The resulting calculated phase diagrams had spinel as the only stable intermediate phase in the system [64]. On the other hand, Hillert and Jonsson in 1992 included a 27R stoichiometric phase in their calculations in addition to considering the non-stoichiometry of the spinel phase. They reported that 27R and spinel melt congruently at 2998K (2725°C) and 2436K (2163°C) respectively [70].

Tabary and Servant [71] published a calculated AlN-Al₂O₃ phase diagram recently (1998). In their calculation the Gibbs energy of formation of the solution and compound phases in this system were derived from an optimization procedure using all the available experimental thermodynamic and phase diagram data. They used the sub-lattice model for the compounds which exhibit a range of non-stoichiometry and the Redlich-Kister polynomial for the solution phases.

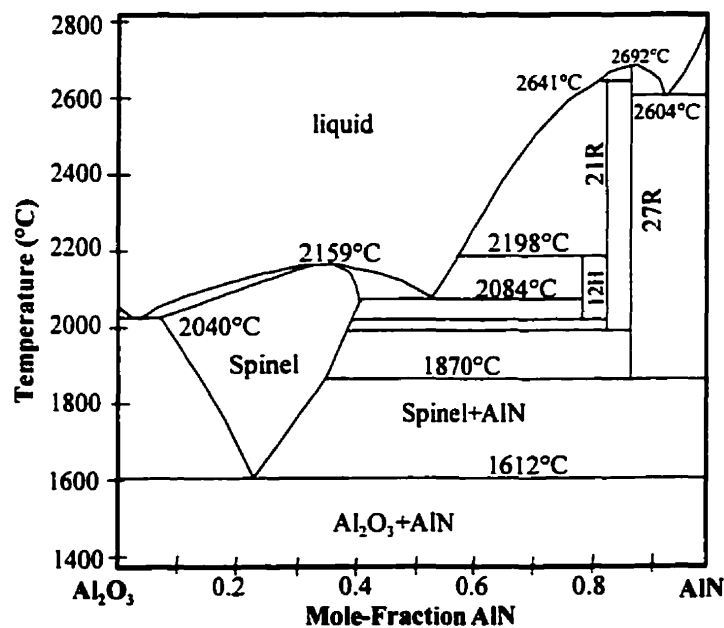


Figure 2-11: Calculated phase diagram of binary Al₂O₃-AlN system [65].

Chapter 3:

THE AIM OF THIS WORK

Aluminum nitride substrates are of interest for applications in electronic packaging because of several advantageous properties they possess. Yttrium oxide is the best sintering additive to produce high density thermally conductive AlN.

The phase diagram of the ternary AlN-Al₂O₃-Y₂O₃ is essential in understanding the reactions which take place and for further development of AlN ceramic, because the diagram can illustrate the phase relations and phase stability under different conditions.

To date no effort has been made to analyze the entire AlN-Al₂O₃-Y₂O₃ system and to construct the phase relationships. A first attempt to investigate this ternary system and to construct the ternary phase diagram will be done during the course of this work.

This work will include:

- ♦ formulation of the appropriate thermodynamic model to reassess AlN-Al₂O₃ and Al₂O₃-Y₂O₃ phase diagrams and, using the developed model, the unknown AlN-Y₂O₃ phase equilibrium will be predicted.
- ♦ Investigation of the phase development and phase stability in the Al₂O₃-Y₂O₃ phase diagram using room temperature X-ray diffraction. Since alumina and yttria are important for liquid phase sintering of AlN, the need to understand the phase relationships in the Al₂O₃-Y₂O₃ system becomes more urgent. So special focus will be placed on the Al₂O₃-Y₂O₃ binary phase diagram in this research.

-
- ◆ *In situ* study of the development and stability of the phases in the Al_2O_3 - Y_2O_3 and AlN - Y_2O_3 systems using high temperature neutron diffraction.
 - ◆ Verification of the thermodynamic predictions with experimental data.
 - ◆ Construction of the ternary AlN - Al_2O_3 - Y_2O_3 phase diagram using binary data.
 - ◆ Experimental verification of the predicted ternary phase diagram using high temperature neutron diffraction.
 - ◆ Application of the modeled phase diagrams for the sintering of AlN .

Chapter 4:

REVIEW OF CHEMICAL THERMODYNAMIC CALCULATIONS FOR ASSESSMENT OF PHASE EQUILIBRIA

4.1 Introduction

The state of a two-component material at constant pressure can be presented in the well-known graphical form of temperature-composition isobaric binary phase diagram. For three-component materials, an additional dimension is necessary for a complete representation. Therefore, ternary systems are usually presented by a series of isothermal sections or projections using the Gibbs triangle to represent composition. For systems with more than three components, the graphical representation of the phase diagram in a useful form becomes not only a challenging task, but is also limited by the lack of sufficient experimental information. However, the difficulty of graphically representing systems with many components is irrelevant for the calculation of phase equilibrium. Such calculations can be customized for the materials problem of interest [72] and can be presented in tabular form for a particular condition of overall composition, temperature and pressure.

While it is only due to modern developments in modeling and computational technology that have made development of likely multicomponent phase equilibria a realistic possibility, the correlation between thermodynamics and phase equilibria was established more than a century ago by Josiah Willard Gibbs, whose groundbreaking

work has been summarized by Hertz [73]. It is now universally recognized that Gibbs invented a new science, that we now call "*chemical thermodynamics*", when he published his three papers in the Transactions of the Connecticut Academy. At first two papers were published in 1873, "Graphical Methods in the Thermodynamics of Fluids" [74] and "Representation by Surfaces of the Thermodynamic Properties and Substances" [75]. But the most important contribution of Gibbs in the field of phenomenological thermodynamics is "On the Equilibrium of Heterogeneous Substances" [76]. The first part was published in 1876 and the second part of this work [77] was published in 1878 [73,78]. However, it took many years for this work to be discovered and its full implication to be appreciated. This delay may have been partially due to the mathematical form of this work, but was probably also due to the fact that the Transactions of the Connecticut Academy did not have a large international readership, particularly in Europe. The method used by Gibbs was always mathematical modeling, which gives his work a degree of universality that persists to this day [73].

Even though the mathematical foundation was laid, more than 30 years passed before J.J. van Laar published his mathematical synthesis of hypothetical binary systems [79]. To describe the solution phases, van Laar used concentration dependent terms that Hildebrand [80] called regular solutions. More than 40 years then passed before J.L. Meijering [81] published his calculations of miscibility gaps in ternary and quaternary solutions. Shortly afterward, Meijering applied this method to the thermodynamic analysis of the Cr-Cu-Ni system [82]. Simultaneously, Kaufman and Cohen applied thermodynamic calculations in the analysis of the martensitic transformation in the Fe-Ni system. Kaufman continued his work on the calculation of phase diagrams, including the dependency pressure. In 1970, Kaufman and Bernstein summarized the general features of the calculation of phase diagrams and introduced the concept of "lattice stability" [72].

Another important paper on the calculation of phase equilibria was published in the 1950s. In his paper, Kikuchi described a method to treat order/disorder phenomena. This method later became known as the cluster variation method (CVM) and is extensively used in conjunction with first-principle calculations [72].

Differential thermal analysis is a commonly used method to determine the location of phase boundaries. Figure 4-1 shows a hypothetical binary phase diagram and the DTA curves that would be expected for several compositions within the system. The endothermic melting and solid1-solid2 first-order transformations during heating are clearly evident [83].

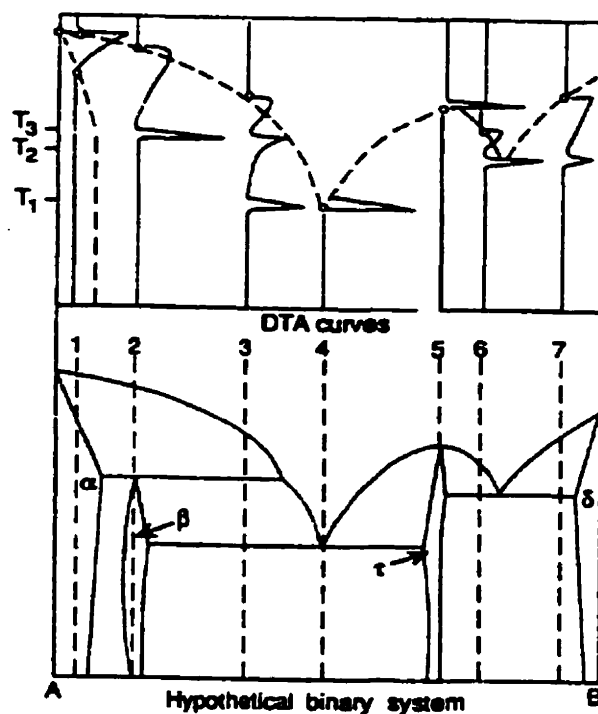


Figure 4-1: Hypothetical phase diagram and associated DTA curves [83].

This experimental determination of phase diagrams is a time-consuming and costly task, especially when it involves high temperatures. This becomes even more pronounced as the number of components increases. The calculation of phase diagrams reduces the effort required to determine equilibrium conditions in a multicomponent system and focuses experimental work on critical regions. A preliminary phase diagram can be obtained from extrapolation of the thermodynamic functions of constituent subsystems. This preliminary diagram can be used to identify composition and temperature regimes with limited experimental effort [72,84,85].

The most reliable phase diagrams are developed when all experimental data are taken into account and if thermodynamic consistency exists between all thermodynamic functions of the different phases and the phase diagram. If these functions are presented analytically they can be extrapolated for systems with one additional component. If the analytical representation always uses the same formalisms, all the information can be contained in a set of coefficients and is, therefore, easily stored [85].

A system is at equilibrium when its Gibbs energy is at a minimum. If we could calculate the Gibbs energy of all the possible phases of a system at a specified temperature as a function of composition, it would be a simple matter to select that phase or combination of phases, which provides the lowest value of Gibbs energy for that system. By definition these would be the equilibrium phases for the system at that temperature. By repetition of these calculations for the number of temperatures, the phase boundaries of the system can be determined and the phase diagram can be constructed [86].

Since phase relations in ceramics involve comparison at the same pressure for each phase, the Gibbs energy is used as the stability criterion. The appropriate equation is:

$$G = H - TS \quad \text{..... 4-1}$$

Where G is the Gibbs energy of the system under consideration, H is the enthalpy, S is the entropy and T is the absolute temperature in degrees Kelvin [87].

The absolute values of the thermodynamic quantities are usually not known, but the changes in these quantities can be determined, by using the following expression:

$$\Delta G = \Delta H - T\Delta S \quad \text{..... 4-2}$$

where the change in Gibbs energy of the system can be related to changes in enthalpy and entropy [86,88].

In order to determine the Gibbs energy change for the reaction at some other temperature, the following equations are used:

$$H = H_{298}^{\circ} + \int_{298}^T C_p dT \quad \text{J/mol}$$

$$S = S_{298}^{\circ} + \int_{298}^T \frac{C_p}{T} dT \quad \text{J/mol.K} \quad [89,90] \quad \dots\dots\dots 4-3$$

It is necessary to know the heat capacity as a function of temperature for each of the reactants and products in order to calculate the changes in the enthalpy and entropy [86]. This is usually given by an empirical series, equation 4-4, in which two to three terms generally suffice.

$$C_p = a + bT + cT^{-2} + dT^{-1} + eT^{-3} + fT^2 \quad [89,90] \quad \dots\dots\dots 4-4$$

4.2 Theory

For the calculation of phase equilibria in a multicomponent system, it is necessary to minimize the total Gibbs energy, G , of all the phases that take part in this equilibrium where n_i is the number of moles of phase i , G_i is the Gibbs energy of phase i and p is the number of phases.

$$G = \sum_{i=1}^p n_i G_i \quad \dots\dots\dots 4-5$$

A thermodynamic description of a system requires the knowledge of thermodynamic functions for each phase. There are various models to describe the temperature, pressure, and concentration dependencies of the Gibbs-energy functions of the different phases. The contributions to the Gibbs energy of a phase ϕ can be written as

$$G^{\phi} = G_T^{\phi}(T, x) + G_p^{\phi}(P, T, x) + G_m^{\phi}(T_c, \beta_o, T, x) \quad \dots\dots\dots 4-6$$

where $G_T^{\phi}(T, x)$ is the contribution of temperature and composition to the Gibbs energy, $G_p^{\phi}(P, T, x)$ is the contribution of the pressure, and $G_m^{\phi}(T_c, \beta_o, T, x)$ is the magnetic contribution of the Curie or Néel temperature (T_c) and the average magnetic moment per atom (β_o) [72].

For multicomponent systems, it is useful to distinguish three contributions from the concentration dependency to the Gibbs energy of a phase, G^ϕ :

$$G^\phi = G^\circ + G^{ideal} + G^E \quad \text{..... 4-7}$$

The first term, G° , corresponds to the Gibbs energy of a mechanical mixture of the constituents of the phase; the second term, G^{ideal} , corresponds to the entropy of mixing for an ideal solution, and the third term, G^E , is the so-called excess term [72,84,91]. Since Hildebrand [80] introduced the term *regular solution* to describe interactions of different elements in a random solution, a series of models have been proposed for phases that deviate from this regularity (i.e., show a strong compositional variation in their thermodynamic properties) to describe the excess Gibbs energy. For example, an ionic liquid model or associate model, among others, have been proposed for liquid phases. For ordered solid phases, Wagner and Schottky introduced the concept of defects on the crystal lattice in order to describe deviations from stoichiometry.

A description of order/disorder transformations was proposed by Bragg and Williams. Since then, many other models have been proposed. Today, the most commonly used models are those for stoichiometric phases, regular solution-type models for disordered phases, and sublattice models for ordered phases having a range of solubility or exhibiting an order/disorder transformation [72].

The Gibbs energy of a binary stoichiometric phase is given by:

$$G^\phi = x_A^\circ G_A^\circ + x_B^\circ G_B^\circ + \Delta G^f \quad \text{..... 4-8}$$

where x_A° and x_B° are mole fractions of elements A and B and are given by the stoichiometry of the compound, G_A° and G_B° are the respective reference states of elements A and B, and ΔG^f is the Gibbs energy of formation. The first two terms correspond to G° , and the third term corresponds to G^E in Equation 4-7. G^{ideal} of Equation 4-7 is zero for a stoichiometric phase, since there is no random mixing [72].

Binary solution phases, such as liquid and disordered solid solutions, are described as random mixtures of the components by a regular-solution type model:

$$G^o = x_A G_A^o + x_B G_B^o + RT \{x_A \ln x_A + x_B \ln x_B\} + x_A x_B \sum_{j=1}^M k_j (x_A - x_B)^j \quad \text{..... 4-9}$$

where x_A and x_B are the mole fractions, and G_A^o and G_B^o are the reference states of elements A and B, respectively. The first two terms correspond to G^o and the third term corresponds to G^{ideal} in Equation 4-7. The k_j of the fourth term are coefficients of the excess Gibbs energy term, G^E , in Equation 4-7. The sum of the terms $(x_A - x_B)^j$ is the so-called Redlich-Kister polynomial, which is the most commonly used polynomial in regular-solution type descriptions, and M is the number of coefficients. Redlich-Kister polynomial can be represented as:

$$k_j = A_j + B_j T + C_j T \ln(T) + D_j T^2 + E_j T^3 + F_j T^3 \quad \text{..... 4-10}$$

If the first term A_j is non zero, then K_j is constant and the solution is termed "regular" [91,92].

The coefficients k_j may be written as linear functions of temperature, T:

$$k_j = h_j - TS_j \quad \text{..... 4-11}$$

Hence the integral molar enthalpy of mixing and excess entropy of mixing, assumed independent of temperature, are given in terms of the coefficients h_j and S_j as;

$$\Delta h = \sum_{j=1}^M h_j x_A^j (1 - x_A)^j \quad \text{..... 4-12}$$

$$S^E = \sum_{j=1}^M S_j x_A^j (1 - x_A)^j \quad \text{..... 4-13}$$

where M is the total number of such coefficients [93,94]. Although other polynomials have been used in the past, in most cases they can be converted to Redlich-Kister polynomials [72].

Since liquids have no long-range order and, since a detailed knowledge of the short-range order is usually lacking, liquid models cannot be as structure-based as is the

case for solids. On the other hand, models should be as physically realistic as possible and should conform to what is known about the structure of liquids, otherwise the models will not extrapolate properly and will not be useful in the prediction of multicomponent solution properties [95]. Let us consider a hypothetical system:



The Gibbs energy, of this hypothetical system, for the liquid phase with a variable composition can be represented with an equation of the type:

$$\Delta G = \{(1-X)RT \ln(1-X) + XRT \ln(X)\} + [(1-X)X(a+bX)] \quad \dots\dots\dots 4-15$$

where R is the gas constant, T is the absolute temperature and X is the atom fraction of A; a and b are empirical constants. The leading term within the braces gives the Gibbs energy for the ideal mixing and the following term in square brackets provides the excess Gibbs energy [96].

The most complex and general model is the sublattice model frequently used to describe ordered binary solution phases. The basic premise for this model is that a sublattice is assigned for each distinct site in the crystal structure. This can be applied only when there is a clear understanding of the distribution of ions within the structure.

4.2.1 Margules equations for representation of excess properties

Any integral excess thermodynamic property, W_A^E , or of component B, W_B^E , in the binary system A-B, may be expressed as a simple power series expansion of the mole fraction [97]:

$$W^E = X_A X_B (q_0 + q_1 X_B + q_2 X_B^2 + \dots) \quad \dots\dots\dots 4-16$$

$$W_A^E = X_B^2 (a_0 + a_1 X_B + a_2 X_B^2 + \dots) \quad \dots\dots\dots 4-17$$

$$W_B^E = X_A^2 (b_0 + b_1 X_B + b_2 X_B^2 + \dots) \quad \dots\dots\dots 4-18$$

Where X_A and X_B are the mole fractions, and W is any thermodynamic property such as G, H or S. Excess properties are preferable in such series expansions because they are well-behaved in the dilute regions. For example, $W_A^E = 0$ when $X_B = 0$, and Raoult's law;

$W_A^E = RT \ln \gamma_A \rightarrow 0$ as $x_A \rightarrow 1$, which implies that; $\frac{dW_A^E}{dx_B} \rightarrow 0$ as $x_B \rightarrow 0$, is obeyed [91.98].

The thermodynamic relationships between the coefficients of equations 4-16 to 4-18 are derived using the Gibbs-Duhem equation, which may take the form;

$$x_A \frac{dW_A^E}{dx_B} + x_B \frac{dW_B^E}{dx_A} = 0 \quad \dots\dots\dots 4-19$$

These recursive relations for coefficients in equations 4-16 to 4-17 are;

$$b_n = (n+1)q_n \quad \dots\dots\dots 4-20$$

$$a_n = (n+1)(q_n - q_{n+1}) \quad \dots\dots\dots 4-21$$

$$a_n = b_n - \frac{n+1}{n+2} b_{n+1} \quad \dots\dots\dots 4-22$$

Thus, if values of any one of the properties W^E , W_A^E or W_B^E are known at various compositions, a least squares regression analysis will provide the coefficients a_n , b_n or q_n of the measured property. Thus the behaviour of all three thermodynamic properties over the composition range in question is defined [91.92,97].

For example, for a system where one coefficient is sufficient to describe the measured property (i.e. $n = 0$):

$$a_0 = b_0 = q_0 \quad \dots\dots\dots 4-23$$

If relative molar enthalpy can be described by one coefficient then we speak of a regular-solution [91.92] and the following equations can be written;

$$\Delta h = q_0 x_A x_B \quad \dots\dots\dots 4-24$$

$$\Delta h_A = q_0 x_B^2 \quad \dots\dots\dots 4-25$$

$$\Delta h_B = q_0 x_A^2 \quad \dots\dots\dots 4-26$$

If two coefficients are enough to describe Δh then the solution is called sub-regular [97], and from equation 4-16 the following equation is derived:

$$\Delta h = X_A X_B (q_0 + q_1 X_B) \quad \dots\dots\dots 4-27$$

and so, the following can be derived from equations 4-17, 4-18, 4-20 and 4-21:

$$\Delta h_A = X_B^2 (q_o + 2q_1 X_B) \quad \dots\dots\dots 4-28$$

$$\Delta h_B = X_A^2 ((q_o - q_1) + 2q_1 X_B) \quad \dots\dots\dots 4-29$$

By applying the same analogy, excess Gibbs energy expression can be written as:

$$G^E = X_A X_B (q_o + q_1 X_B + q_2 X_B^2) \quad \dots\dots\dots 4-30$$

Then the partial free Gibbs energy expressions are;

$$G_A^E = X_B^2 (((q_o - q_1) + 2q_1 - 2q_2) X_B + 3q_2 X_B^2) \quad \dots\dots\dots 4-31$$

$$G_B^E = X_A^2 (q_o + 2q_1 X_B + 3q_2 X_B^2) \quad \dots\dots\dots 4-32$$

4.2.2 Determination of the coefficients

From the condition that the Gibbs energy at thermodynamic equilibrium reveals a minimum for a given temperature, pressure, and composition, J.W. Gibbs derived the well-known equilibrium conditions that the chemical potential, μ_n^o , of each component, n, is the same in all phases:

$$\begin{aligned} \mu_1 &= \mu_1^* = \dots\dots\dots = \mu_1^o \\ \mu_2 &= \mu_2^* = \dots\dots\dots = \mu_2^o \\ &\vdots \\ &\vdots \\ \mu_n &= \mu_n^* = \dots\dots\dots = \mu_n^o \end{aligned} \quad \dots\dots\dots 4-33$$

The chemical potentials are in effect partial molar Gibbs energies and related to the Gibbs energy by the well-known equation:

$$G = \sum_{i=1}^n \mu_i x_i \quad \dots\dots\dots 4-34$$

Equation 4-33 results in n nonlinear equations that can be used in numerical calculations to minimize the Gibbs energy. These nonlinear equations can be solved numerically by such methods as the Newton-Raphson technique [72].

The coefficients of the Gibbs energy functions are determined from experimental data for each system. In order to obtain an optimized set of coefficients, it is desirable to take into account all types of experimental data (e.g., phase diagram, chemical potential, and enthalpy data). The coefficients can be determined from the experimental data by a trial-and-error method or using mathematical methods. The trial-and-error method is only feasible if few different data types are available. This method becomes increasingly cumbersome as the number of components and/or the number of data types increases. In this case, mathematical methods, such as the least squares method of Gauss, the Marquardt method, or Bayesian estimation method, are more efficient. The determination of the coefficients is frequently called assessment or optimization of a system [72,85].

4.2.3 Higher component systems

A higher number of components system can be calculated from thermodynamic extrapolation of the thermodynamic excess quantities of the constituent subsystems. Several methods exist to determine the weighted terms used in such an extrapolation formula. Hillert [84] analyzed various extrapolation methods and recommended the use of Muggianu's method since it can easily be generalized. The Gibbs energy of a ternary-solution phase determined by extrapolation of the binary energies using Muggianu's method is given by;

$$G^{\phi} = X_A G_A^o + X_B G_B^o + X_C G_C^o + RT \{X_A \ln X_A + X_B \ln X_B + X_C \ln X_C\} + \\ X_A X_B \sum_{j=1}^{M_{AB}} k_j^{AB} (X_A - X_B)^j + X_A X_C \sum_{j=1}^{M_{AC}} k_j^{AC} (X_A - X_C)^j + X_B X_C \sum_{j=1}^{M_{BC}} k_j^{BC} (X_B - X_C)^j \quad \dots 4-35$$

where the parameters k_j have the same values as in Equation 4-9 for each of the binary systems. If necessary, a ternary term $X_A X_B X_C G^{ABC}(T, X)$ can be added in order to describe the contribution of three element interactions to the Gibbs energy.

The usual strategy for assessment of a multicomponent system is shown in Figure 4-2. First, the thermodynamic descriptions of the constituent binary systems are derived. Thermodynamic extrapolation methods are then used to extend the thermodynamic functions of the binaries into ternary and higher order systems. The results of such

extrapolations can then be used to design critical experiments. The results of the experiments are compared to the extrapolation, and if necessary, interaction functions are added to the thermodynamic description of the higher order system. As mentioned previously, the coefficients of the interaction functions are optimized on the basis of these data. In principle, this strategy is followed until all 2, 3,... n constituent systems of an n-component system have been assessed. However, experience has shown that in most cases no corrections or very minor corrections are necessary or justified for reasonable prediction of quaternary or higher component systems.

Once the binary sub-systems have been analysed by a coupled thermodynamic/phase diagram analysis, the phase diagram of a ternary or quaternary system can usually be developed with reasonable validity. Hence, in order to minimize the experimental work, one should concentrate on re-measuring regions of the binary diagrams where required. The ternaries and quaternaries can then be recalculated [94].

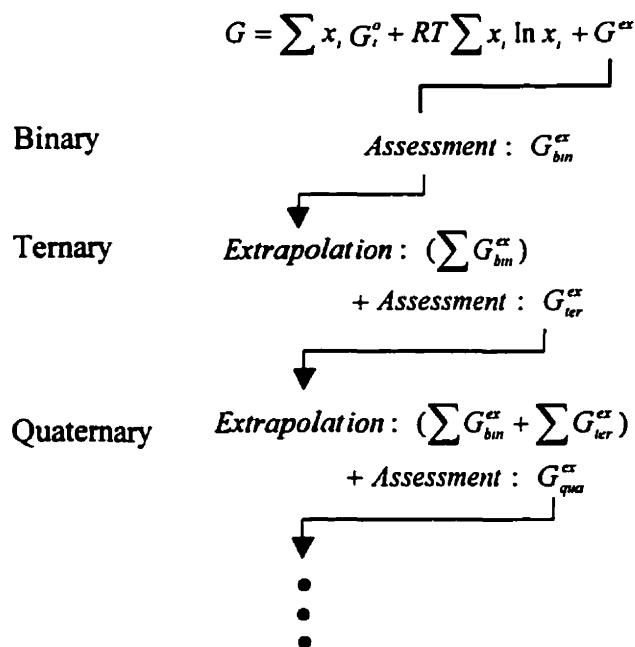


Figure 4-2: The assessed excess Gibbs energies of the constituent subsystems are for extrapolation to a higher component system [72].

Chapter 5:

METHODOLOGY OF THERMODYNAMIC MODELING OF AIN- Al_2O_3 - Y_2O_3 PHASE EQUILIBRIA

For storage and manipulation of data of binary and multicomponent system using computers, it is essential to have simple and general methods of representing the thermodynamic solution properties mathematically as a function of composition and temperature [92]. Thermodynamic property data, such as activity data, can aid in the evaluation of the phase diagram, and phase diagram measurements can be used to deduce thermodynamic properties [99]. All calculations were performed with the aid of the F*A*C*T program [91].

Generally speaking, there will always exist some difference in thermodynamic properties between actual and ideal solution behaviour depending on the premises for the *ideal* mixing. Since there was no strong basis for selection of the ideal Gibbs energy of mixing term based upon experimental knowledge of the structure of the solution phases, the choice was made to base it on the mole fraction of component oxides or nitrides in all three sub-system solution phases. The excess Gibbs energy function was then adjusted accordingly to provide the Gibbs energy of the solution phase to fit the known phase diagram. Success in this endeavour and justification of this modeling approach was judged on the basis of being able to represent the binary phase diagrams as well as current experimental understanding allows and further that not more than a few adjustable parameters in the expression of the excess Gibbs energy be needed. Li *et al.* [88] earlier analyzed the phase diagrams of Al_2O_3 - SiO_2 - R_2O_3 (where R= Nd, Sm) system

using the same methodology. Also Fang *et al.* [100] used this approach to study 13 binary systems of the form A₂CO₃-AX or A₂SO₄-AX (where A = Li, Na, K; X = Cl, F, NO₃, OH) and to calculate their binary phase diagrams.

5.1 Mathematical expressions for the thermodynamic properties

5.1.1 Al₂O₃ - Y₂O₃ phase diagram

The experimental phase diagram in Figure 2-5 and the Gibbs energies of fusion of the two pure components are the only data used in the optimization analysis. Gibbs energy of fusion and melting points of the pure components, Al₂O₃ and Y₂O₃ were taken from references 41,47 and 91. Mathematical expressions of Gibbs energy for the different phases were generated using regression methods. Since the standard Gibbs energy of fusion of a species is given by:

$$\Delta G (\text{fusion}) = -RT \ln (a(\text{liq}) / a(\text{s})) \quad \dots\dots\dots 5-1$$

where $a(\text{s})$ and $a(\text{liq})$ are the activities of that species on the solidus and liquidus with respect to the solid and liquid standard states respectively, $a(\text{liq})$ can be calculated from equation 5-1 if $a(\text{s})$ as well as $\Delta G (\text{fusion})$ at the same temperature are known.

So the experimental liquidus curves of this system are the source of thermodynamic data for the liquid and for the stoichiometric compounds. The phase diagram data, particularly the eutectic points, have been given heavy weighting factors. Since the Gibbs energies of fusion of the three stoichiometric phases are unknown they are not a source of thermodynamic data. However, the liquidus surface is used as (temperature, composition) data points to deduce Gibbs energy of fusion expressions for these compounds from the derived expressions for the liquid.

Basically, polynomial expressions of the form of equation 5-2 were obtained.

$$\Delta G = a + bT + CT^2 + dT^3 + eT^4 + F \cdot T \cdot \ln(T) + G/T \quad \dots\dots\dots 5-2$$

These polynomial expressions represent the excess Gibbs energy for the liquid phase, and/or the Gibbs energy of fusion in the case of stoichiometric compounds.

$$\Delta G = RT (X_A \ln (X_A) + X_B \ln (X_B)) + G^E \quad \dots\dots\dots 5-3$$

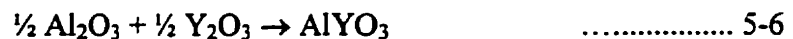
$$G^E = H^E - TS^E \quad \dots\dots\dots 5-4$$

In equation 5-2 only two coefficients, a and b, were calculated, because the number of coefficients must be less than or equal to the number of data points. The input data and the mathematical expressions calculated for the Al₂O₃ - Y₂O₃ binary system are listed in Table 5-1.

Table 5-1: The data and the mathematical model of Al₂O₃ - Y₂O₃ binary system.

Input data	
Al ₂ O ₃	Y ₂ O ₃
$\Delta G_M^\circ = 87111.0 - 37.847T$	$\Delta G_M^\circ = 101840.0 - 38.0T$
(temperature, composition) points from the experimental phase diagram (Figure 2-5)	
Mathematical model for the different phases	
Liquid Phase:	
Gibbs energy of mixing	
$\Delta G_L^{MIX} = RT(X_A \ln X_A + X_B \ln X_B) + G^E$	
$G^E = X_{Al_2O_3} X_{Y_2O_3} (-115270) + X_{Al_2O_3}^2 X_{Y_2O_3} (18454)$	
Solid Phases	
YAG	$\Delta G = -74133 + 17.0T$
YAP	$\Delta G = -76364.8 + 17.0T$
YAM	$\Delta G = -81158.7 + 20.0T$
Y ₂ O ₃ (high)	$\Delta G = -68908.0 + 25.35T$

The output values shown in the table above are used when the liquid phase is the reference state. Calculating these expressions when another phase is considered as reference state is also possible. For example, if the solid phase of Al₂O₃ and Y₂O₃ is set to be the arbitrary zero (reference state) then ΔG of fusion of YAP can be calculated as:



and ΔG of reaction 5-6 can be expressed as;

$$\begin{aligned}\Delta G &= \Delta G^f(\text{AlYO}_3) - \frac{1}{2} (\Delta G^f(\text{Al}_2\text{O}_3)) - \frac{1}{2} (\Delta G^f(\text{Y}_2\text{O}_3)) \\ &= -76364.8 + 17T - \frac{1}{2} (0.0) - \frac{1}{2} (0.0) \dots\dots\dots 5-7\end{aligned}$$

The zeros in the right hand side of equation 5-7 are the Gibbs energy of the reference phase. The Gibbs energy of the reference phase may be assigned any value but it is easier to select zero for all temperatures. Substitution of $\Delta G^f(\text{Al}_2\text{O}_3)$ and $\Delta G^f(\text{Y}_2\text{O}_3)$ from Table 5-1 results in:

$$\Rightarrow \Delta G^f(\text{AlYO}_3) = 18514.5 - 20.925T \dots\dots\dots 5-8$$

Equation 5-8 represents ΔG^f of YAP when the reference state is the solid Al₂O₃ and Y₂O₃. Gibbs energies of fusion for the other compounds in the system were calculated using solid Al₂O₃ and Y₂O₃ as the reference state. These values are summarized in Table 5-2.

Table 5-2: Gibbs energy of fusion of the solid compounds when solid Al₂O₃ and solid Y₂O₃ are the reference state

Solid phase	Gibbs energy
Y ₂ O ₃ (BCC)	$\Delta G = 101840.0 - 38.0 T$
Al ₂ O ₃	$\Delta G = 87918.6 - 37.85$
YAG	$\Delta G = 19006.125 - 20.906T$
YAP	$\Delta G = 18514.5 - 20.925T$
YAM	$\Delta G = 16040.83 - 17.95T$
Y ₂ O ₃ (HCP)	$\Delta G = 32932 - 12.66T$

5.1.2 AlN – Al₂O₃ phase diagram

So far we have mathematical expressions for the phases in Al₂O₃ – Y₂O₃ and the same procedure was followed for the Al₂O₃ – AlN system. The phase diagram in Figure 2-11 and Gibbs energy of fusion of the two pure components were used to model this phase diagram. Gibbs energy of fusion and the hypothetical melting point of AlN are taken from reference [62]. The input data and the mathematical model for this system are shown in Table 5-3.

Table 5-3: The input and the mathematical model of Al₂O₃ - AlN binary system.

Data	
Al ₂ O ₃	AlN
$\Delta G_M^0 = 87111.0 - 37.847T$	$\Delta G_M^0 = 70557.8 - 23.0T$
(temperature, composition) points from the optimized phase diagram (Figure 2-11)	
Mathematical model	
Liquid Phase:	
Gibbs energy of mixing	
$\Delta G_L^{MIX} = RT(X_A \ln X_A + X_B \ln X_B) + G^E$	
$G^E = X_{Al_2O_3} X_{AlN} (-45961) + X_{Al_2O_3}^2 X_{AlN} (25119)$	
Solid Phases	
27R	$\Delta G = -49000 + 12.25T$
21R	$\Delta G = -42950 + 9.428T$
12H	$\Delta G = -40500 + 8.3T$
Spinel {(Al ₂ O ₃) ₂ (AlN)}	$\Delta G = -33784 + 5.185T$

It can be seen from Table 5-3 that the four intermediate compounds were assumed to be stoichiometric. The spinel phase will be treated as non-stoichiometric later.

5.1.3 AlN - Y₂O₃ phase diagram

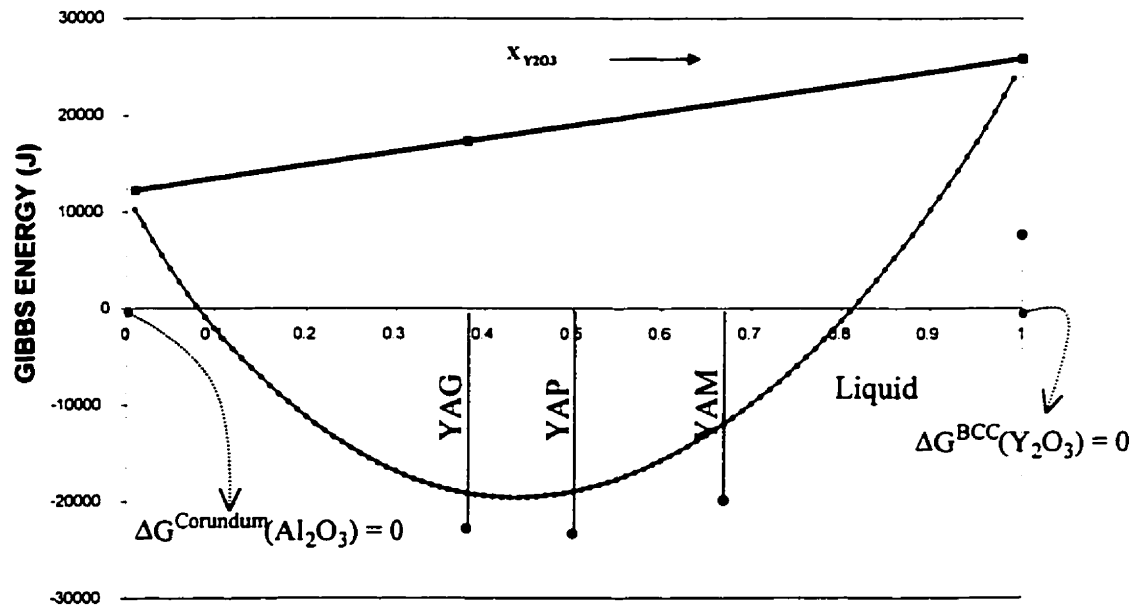
In the case of the AlN - Y₂O₃, it was mentioned earlier there is no experimental phase diagram available for this system in the literature. So this system will be predicted using the Gibbs energy of fusion of the two pure components, AlN and Y₂O₃, which were already used to calculate the other two binary systems, in addition to the reported eutectic point at 14.5 wt% AlN by Kaufman *et al.* [62]. Mathematical expressions for the liquid phase of this system was obtained following the same procedure and is shown in Table 5-4.

Table 5-4: The data and the mathematical model of AlN - Y₂O₃ binary system.

Input	
Y ₂ O ₃	AlN
$\Delta G_M^\circ = 101840 - 38.0T$	$\Delta G_M^\circ = 70557.8 - 23.0T$
The eutectic point at 48 mol% AlN and 2215K	
Output	
Liquid Phase:	
Gibbs energy of mixing	
$\Delta G_L^{MIX} = RT(X_A \ln X_A + X_B \ln X_B) + G^E$	
$G^E = X_{AlN} X_{Y_2O_3} (-57164) + X_{AlN} X_{Y_2O_3}^2 (36945)$	

5.2 The validity of the models

From the expressions for the Gibbs energy of each phase as a function of temperature and composition and by determining the lowest common tangents to the Gibbs energy–composition curves, a graphical presentation of the binary phase diagram can be generated. By comparing these diagrams with the experimental phase diagrams the mathematical models can be examined.

Figure 5-1: Gibbs energy of Al₂O₃ - Y₂O₃ system at 2000K (1727°C)

In Figure 5-1 the Gibbs energy for the solid compounds were plotted relative to the base line. In this case solid Al_2O_3 and Y_2O_3 (BCC) were treated as the base line and given a relative reference level Gibbs energy of zero Joules. This diagram was calculated at 2000 K (1727°C), where the Gibbs energy of the solid phases were more negative than the liquid phase. Stable phases at this temperature can be determined using the lowest common tangent technique. Combining several Gibbs energy–composition isothermal sections, which cover the desired temperature range, generated a graphical representation of the mathematical model. In order to explain this technique two other isotherms at 2213K (1940°C) and 2400K (2177°C) will be shown.

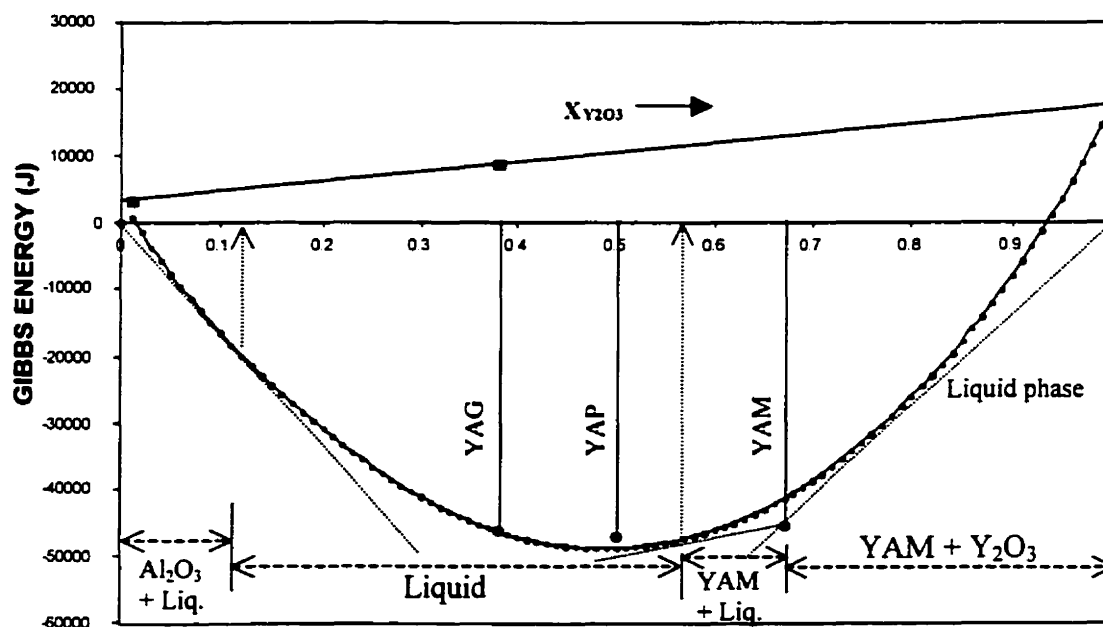


Figure 5-2: Gibbs energy of $\text{Al}_2\text{O}_3 - \text{Y}_2\text{O}_3$ system at 2213K (1940°C)

Figure 5-2 was computed at the fusion temperature of Yttrium Aluminum Garnet (YAG), 2213K (1940°C). It can be seen that YAG is in equilibrium with the liquid, YAP is more positive than the liquid (no solid YAP is expected) and YAM is more negative than the liquid (solid YAM exists at this temperature). The lowest common tangents

show that, at this temperature, from pure Al_2O_3 to 88 mol% Al_2O_3 , a mixture of liquid and solid Al_2O_3 is found. From 88 to 43 mol% Al_2O_3 liquid is formed. Between 43 mol% Al_2O_3 and YAM a mixture of liquid and YAM existed. From YAM to pure Y_2O_3 a mixture of YAM and Y_2O_3 (BCC) was found.

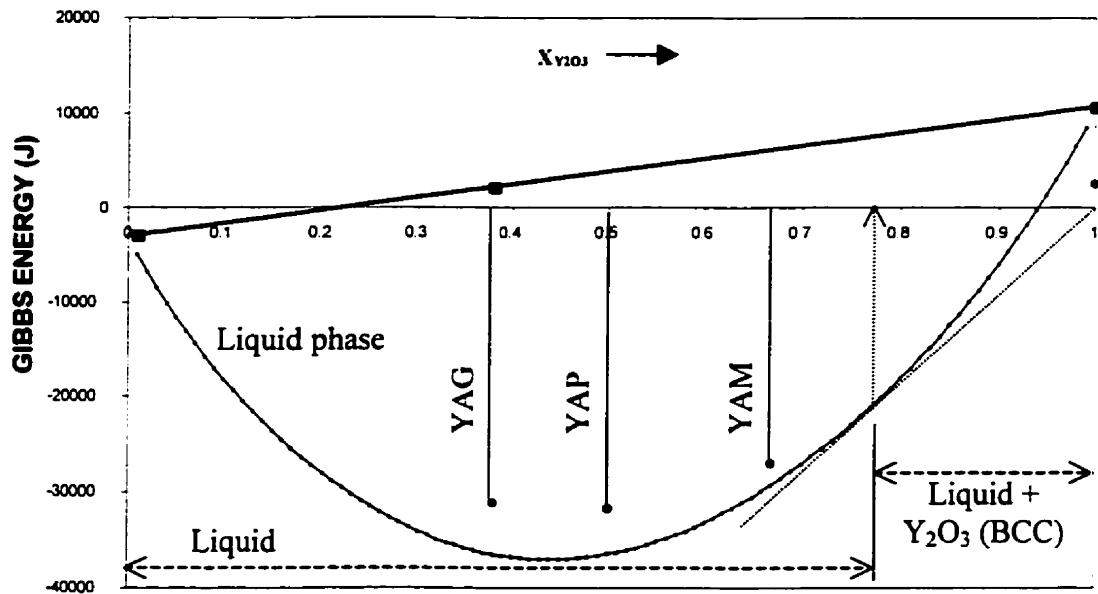


Figure 5-3: Gibbs energy of $\text{Al}_2\text{O}_3 - \text{Y}_2\text{O}_3$ system at 2400K (2127°C)

In Figure 5-3 the three stoichiometric compounds have more positive G than the liquid. Y_2O_3 (BCC) has a greater negative G than the liquid while Al_2O_3 has a lesser negative G than the liquid. Hence, the only solid at this temperature is Y_2O_3 (BCC) and by drawing a tangent line from Y_2O_3 (BCC) to the liquidus the phase boundary was found to be 22.5 mol% Al_2O_3 . The liquid region is from 22.5 mol% to 100 mol% Al_2O_3 while the other region is a mixture of liquid and Y_2O_3 (BCC), between pure Y_2O_3 (BCC) and 22.5 mol% Al_2O_3 .

Tracing of the Gibbs energy-composition will give the stable species at different temperatures, enabling the construction of the phase equilibria of the system. Figure 5-4 shows the calculated $\text{Al}_2\text{O}_3\text{-Y}_2\text{O}_3$ phase diagram using ΔG° of formation of $\alpha\text{-Al}_2\text{O}_3$

(corundum) and bcc Y_2O_3 equal to zero. An identical phase diagram was obtained for this system when the arbitrary zero was assumed to be liquid Al_2O_3 and liquid Y_2O_3 .

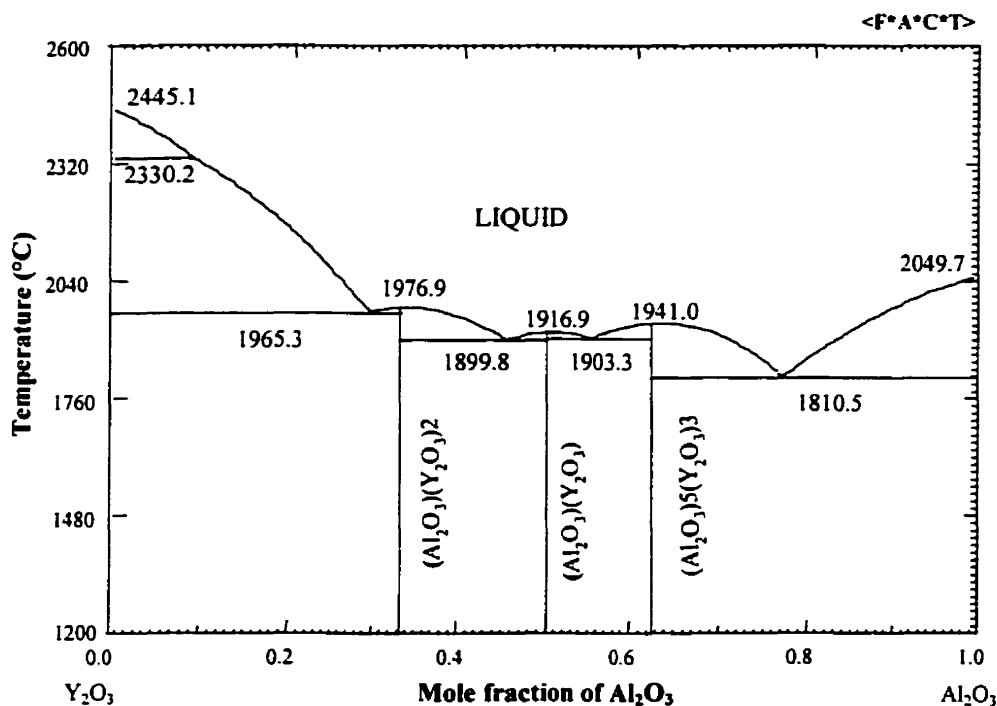


Figure 5-4: Al_2O_3 - Y_2O_3 calculated phase diagram from the mathematical model.

Comparing this diagram with the experimental one shown in Figure 5-5, indicates reasonable consistent values for both the composition and temperature of all the phases and the critical points of this system.

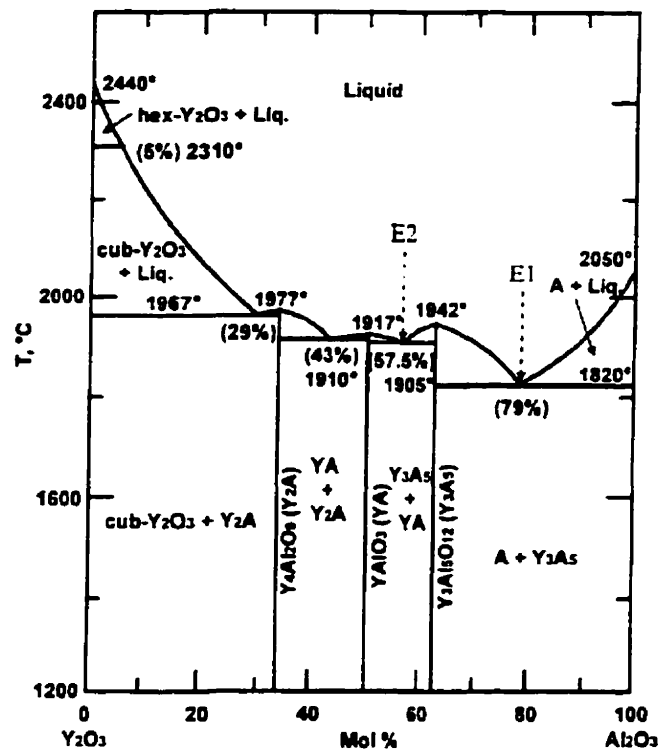


Figure 5-5: The experimental phase diagram of $\text{Y}_2\text{O}_3\text{-Al}_2\text{O}_3$ System [47].

The mathematical model in Table 5-3 for $\text{Al}_2\text{O}_3\text{-AlN}$ system generates the phase diagram shown in Figure 5-6. It can be seen that spinel appears as a stoichiometric compound with a $2\text{Al}_2\text{O}_3\cdot\text{AlN}$ stoichiometry. Calculation of the mathematical model which describes the spinel phase as a non-stoichiometric compound will be shown in the next section. Comparing the other compounds and critical points of this diagram with the phase diagram shown in Figure 2-11 indicates that the thermodynamic model describes the $\text{Al}_2\text{O}_3\text{-AlN}$ system reasonably well.

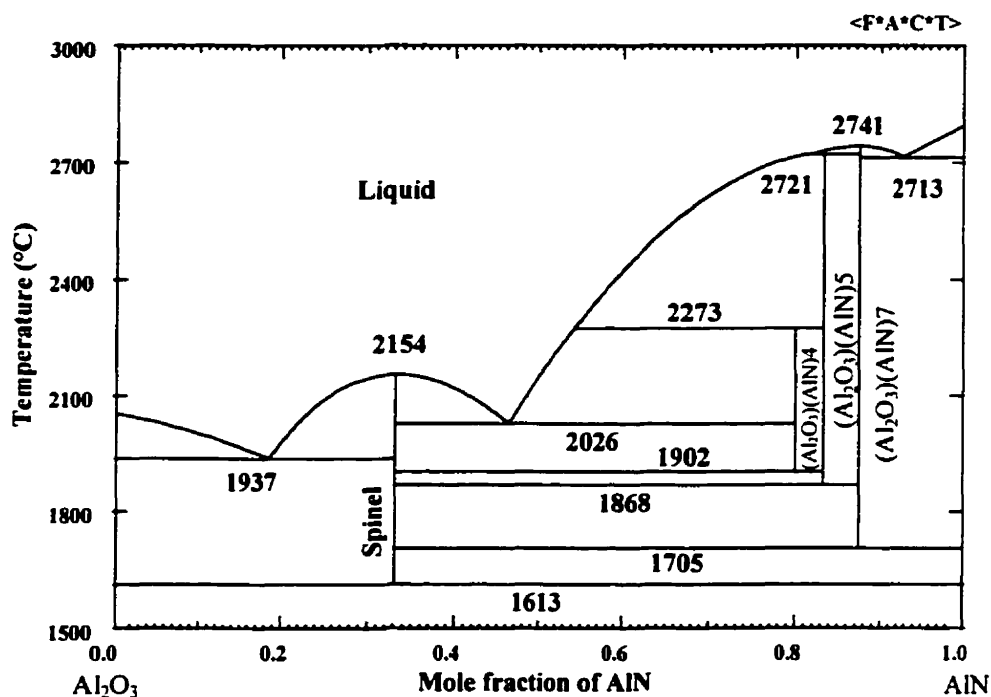


Figure 5-6: Calculated Al_2O_3 – AlN phase diagram from the mathematical model.

As for the last binary $\text{AlN} - \text{Y}_2\text{O}_3$, it can be seen from Figure 5-7 that the thermodynamic model reproduced the reported eutectic point of this system at 48.5 mol% AlN . Also the phase transformation of Y_2O_3 from BCC to HCP at around 2320°C is consistent with the transformation temperature in the literature.

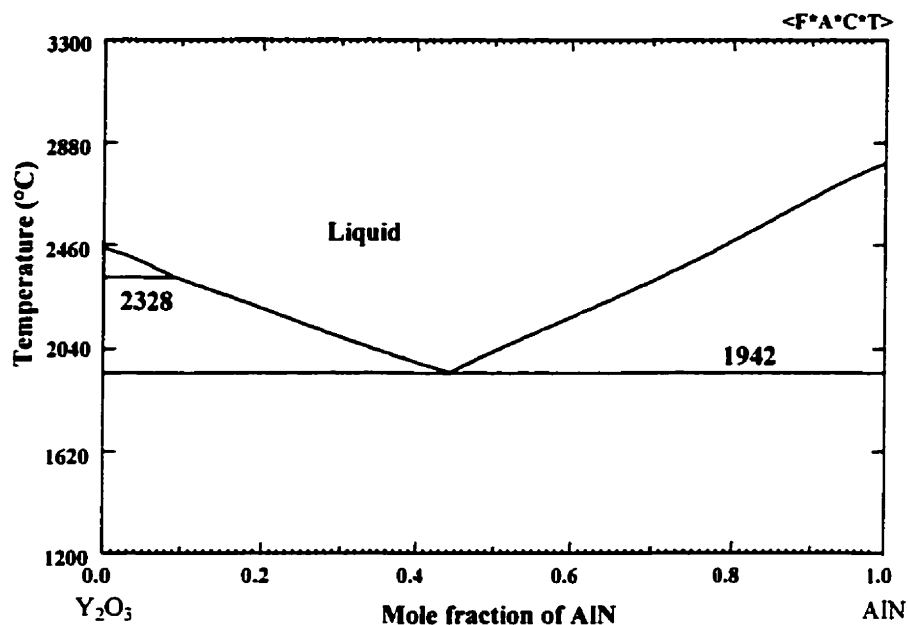


Figure 5-7: Calculated $\text{AlN}-\text{Y}_2\text{O}_3$ phase diagram from the mathematical model.

5.3 Thermodynamic model for the spinel phase

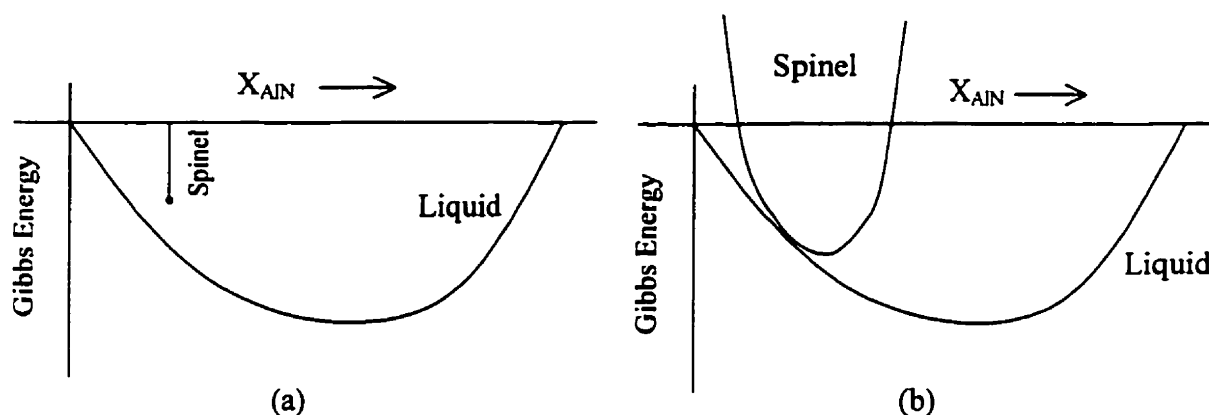


Figure 5-8: Schematic Gibbs energy-composition diagrams show; (a) Spinel as stoichiometric compound, (b) spinel as non-stoichiometric phase

In order to model the spinel phase a mathematical expression for the spinel Gibbs energy-composition curve, Figure 5-8 (b), as a function of temperature and composition is required. To do so the optimized phase diagram in Figure 5-9 was referred to as a source of thermodynamic data.

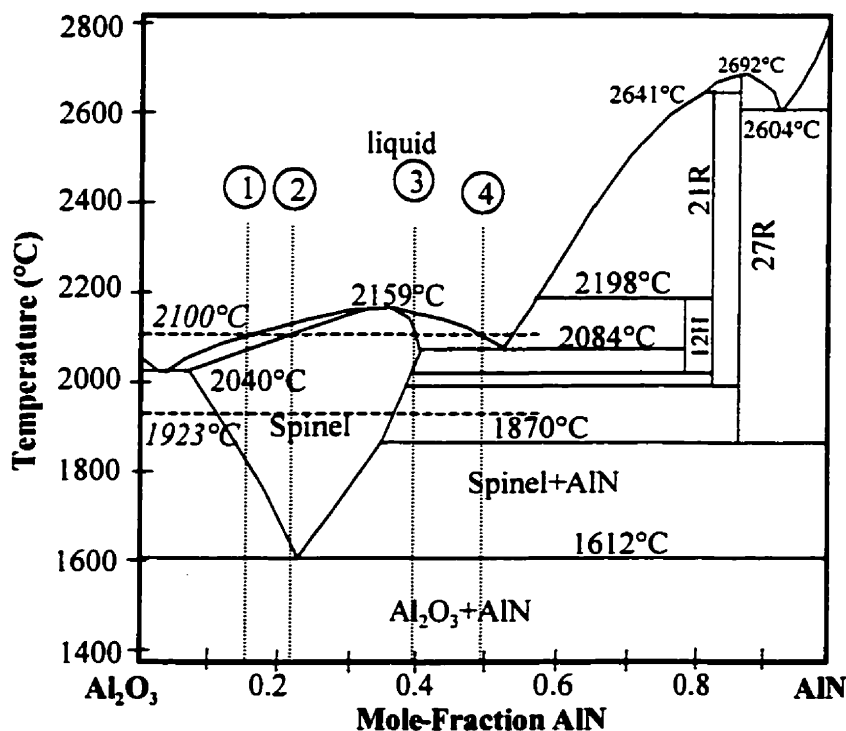


Figure 5-9: Optimized phase diagram [65].

The first estimation for the spinel phase was done using the tie line at 2373K (2100°C) shown in Figure 5-9. There are four intersection points and these points must satisfy the free Gibbs energy equations for the liquid and spinel phases. Since the liquid phase has already been calculated the empirical constants of the spinel Gibbs energy expression can be found.

Recall the excess Gibbs energy of the liquid phase of the $\text{AlN-Al}_2\text{O}_3$ system; $G^E = X_{\text{Al}_2\text{O}_3} X_{\text{AlN}} [-45961 + 25119 X_{\text{AlN}}]$. From the known excess Gibbs energy of the liquid

phase, partial excess Gibbs energies of Al₂O₃ and AlN can be calculated along their respective liquidus lines via equations 4-31 and 4-32, respectively:

$$\bar{G}_{Al_2O_3}^L = RT \ln X_{Al_2O_3}^L + X_{AlN}^2 (-45961) + X_{AlN}^2 X_{Al_2O_3} (2 \times 25119) \quad \dots\dots\dots 5-9$$

$$\bar{G}_{AlN}^L = RT \ln X_{AlN}^L + X_{Al_2O_3}^2 (-45961 - 25119) + X_{Al_2O_3}^3 (2 \times 25119) \quad \dots\dots\dots 5-10$$

(At 2100°C $X_{AlN}^L = 0.148$ and $X_{AlN}^C = 0.222$ points 1 and 2 respectively, Figure 5-9)

Substitute in equations 5-9 and 5-10 to find;

$$\bar{G}_{Al_2O_3}^L = -3229.17 \text{ J/mol} \quad \dots\dots\dots 5-11$$

$$\bar{G}_{AlN}^L = -49059.8 \text{ J/mol} \quad \dots\dots\dots 5-12$$

(At 2100°C $X_{AlN}^L = 0.5$ and $X_{AlN}^C = 0.4$, points 3 and 4 respectively, Figure 5-9)

Substitute in equations 5-9 and 5-10 to find;

$$\bar{G}_{Al_2O_3}^L = -18885.7 \text{ J/mol} \quad \dots\dots\dots 5-13$$

$$\bar{G}_{AlN}^L = -32815.0 \text{ J/mol} \quad \dots\dots\dots 5-14$$

Now the model for the spinel phase using equation 4-32 can be derived as the following:

$$\bar{G}_{Al_2O_3}^C = G_{Al_2O_3}^o + RT \ln X_{Al_2O_3}^C + X_{AlN}^2 (p_o) + X_{AlN}^2 X_{Al_2O_3} (2 \times p_1) \quad \dots\dots\dots 5-15$$

From the equilibrium at point 1 of Figure 5-9:

$$\bar{G}_{Al_2O_3}^C = \bar{G}_{Al_2O_3}^L = -3229.17 \text{ J/mol} \quad \dots\dots\dots 5-16$$

Assume that the relative lattice stability Gibbs energy of Al₂O₃ is:

$$G_{Al_2O_3}^o = a + 10T \quad \dots\dots\dots 5-17$$

Substitute $T = 2373\text{K}$, $X_{AlN}^C = 0.222$, $G_{Al_2O_3}^o$ and $G_{Al_2O_3}^C$ in equation 5-15:

$$-22006.63 = a + 0.04928 p_o + 0.076686 p_1 \quad \dots\dots\dots 5-18$$

At point 2 in Figure 5-9:

$$\bar{G}_{AlN}^C = G_{AlN}^o + RT \ln X_{AlN}^C + X_{AlN}^2 (p_o - p_1) + X_{Al_2O_3}^3 (2 \times p_1) \quad \text{..... 5-19}$$

From the equilibrium at this point

$$\bar{G}_{AlN}^C = \bar{G}_{AlN}^L = -49059.8 \text{ J/mol} \quad \text{..... 5-20}$$

Assume that the relative lattice stability Gibbs energy of AlN is:

$$G_{AlN}^o = c + 10T \quad \text{..... 5-21}$$

Substitute T = 2373K, $X_{AlN}^C = 0.222$, G_{AlN}^o and G_{AlN}^C in equation 5-19;

$$-43095.93 = c + 0.04928 p_o + 0.8925 p_1 \quad \text{..... 5-22}$$

At point 3, Figure 5-9;

$$\bar{G}_{Al_2O_3}^C = \bar{G}_{Al_2O_3}^L = -18885.7 \text{ J/mol} \quad \text{..... 5-23}$$

Substitute T = 2373K, $X_{AlN}^C = 0.4$, $G_{Al_2O_3}^o = a + 10T$, and $G_{Al_2O_3}^C$ in equation 5-15;

$$-32537.1 = a + 0.16 p_o + 0.192 p_1 \quad \text{..... 5-24}$$

At point 4, Figure 5-9;

$$\bar{G}_{AlN}^C = \bar{G}_{AlN}^L = -32815.0 \text{ J/mol} \quad \text{..... 5-25}$$

Substitute T = 2373K, $X_{AlN}^C = 0.4$, $G_{AlN}^o = c + 10T$ and G_{AlN}^C in equation 5-19

$$-38467.39 = c + 0.16 p_o + 0.272 p_1 \quad \text{..... 5-26}$$

Solving 4-52, 4-56, 4-58 and 4-60 for p_o , p_1 , a and c simultaneously gives $p_o = -39997.9$, $p_1 = -33867.8$, $a = -17159.8$ and $c = -13730.9$. Substitute for a and c in equations 5-17 and 5-21:

$$G_{Al_2O_3}^o = -17159.8 + 10T \quad \text{..... 5-27}$$

$$G_{AlN}^o = -13730.9 + 10T \quad \text{..... 5-28}$$

The output of the first trail for modeling spinel phase is shown in Figure 5-10. It can be seen that the spinel phase has a greater negative Gibbs energy than the liquid in

the range of 52 mol% to 75 mol% AlN. This indicates that the initial assumptions should be modified until spinel can be presented in the right range.

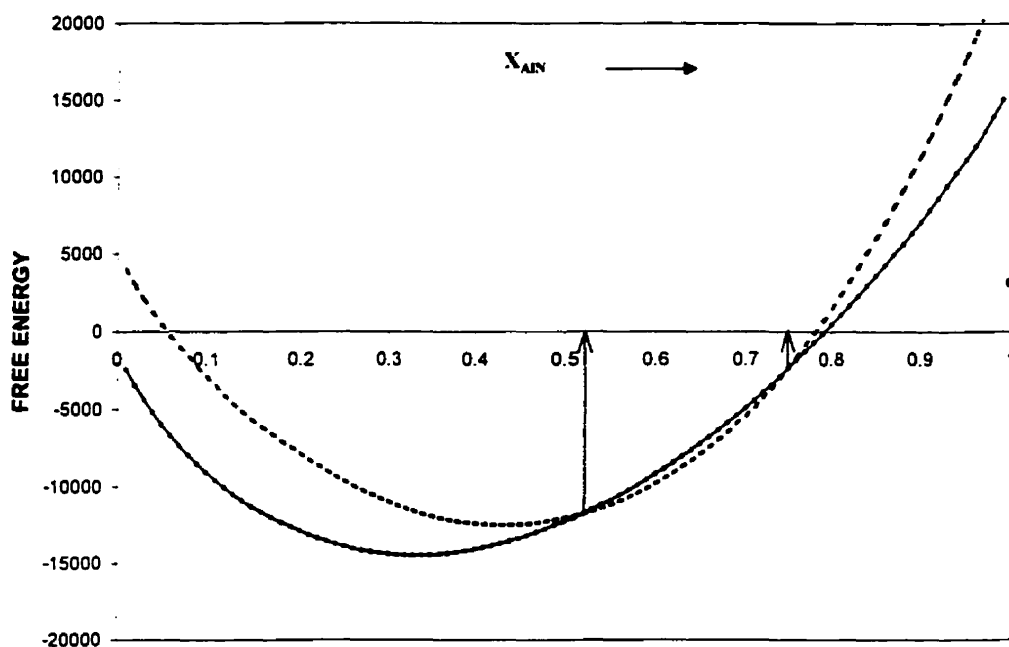


Figure 5-10: Gibbs energy for the liquid and spinel of AlN-Al₂O₃ system.

Several trials were attempted when p_o and p_I were assumed to be temperature independent. These trials did not lead to the correct homogeneity region of the spinel phase. Then p_o and p_I were assumed to have a linear relation with temperature, (i.e. $p_o = d + eT$ and $p_I = f + gT$). The same procedure was repeated to evaluate; d, e, f, g , ($\Delta G^\circ_{\text{AlN}} = \Delta H^\circ_{\text{AlN}} - \Delta S^\circ_{\text{AlN}}T$) and ($\Delta G^\circ_{\text{Al}_2\text{O}_3} = \Delta H^\circ_{\text{Al}_2\text{O}_3} - \Delta S^\circ_{\text{Al}_2\text{O}_3}T$). To determine these eight constants from the four equations of the Gibbs energy of mixing of the liquid and spinel phases, four constants were assumed and four were calculated by solving the four resulting equations. When the mathematical model gave close results to the optimized phase diagram, as in Figure 5-9, these constants were tuned in order to make the model as close as possible to the experimental results of the homogeneity region of the spinel phase in the AlN-Al₂O₃ system reported by Willems *et al.* [101]. The set of constants that gave the best agreement is:

$$p_o = -171499 + 38 T \quad \dots\dots\dots 5-29$$

$$p_l = 438695.08 - 151.17 T \quad \dots\dots\dots 5-30$$

$$\Delta G^\circ_{\text{Al}_2\text{O}_3} = 64500.48 - 25.85 T \quad \dots\dots\dots 5-31$$

$$\Delta G^\circ_{\text{AlN}} = 52500.15 - 13.36 T \quad \dots\dots\dots 5-32$$

Graphical presentation of the liquid phase and the resulting Gibbs energy-composition of the spinel phase at different temperatures is shown in figure 5-11.

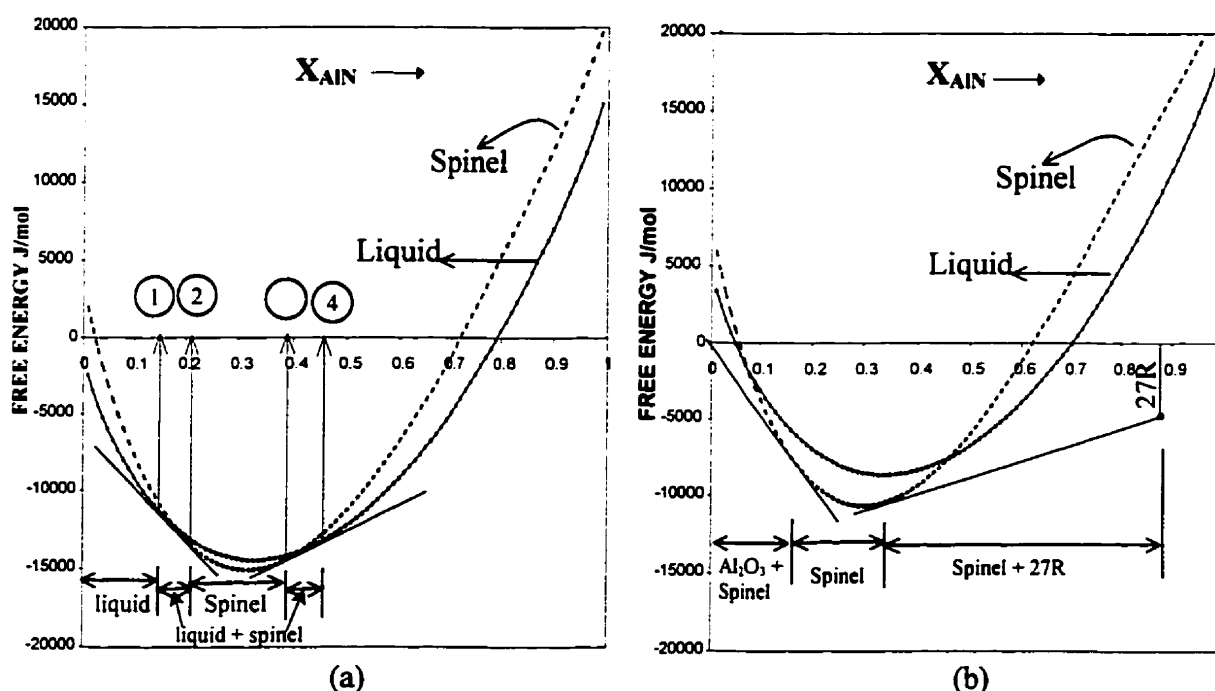


Figure 5-11: Gibbs energy for the liquid and spinel of $\text{AlN-Al}_2\text{O}_3$ system at (a) 2373K (2100°C) and (b) 2200K (1923°C)

It can be seen from Figure 5-11 (a) that the resulting mathematical model for the spinel phase gave close values for AlN concentration at points 1, 2, 3 and 4, which correspond to points 1, 2, 3 and 4 of Figure 5-9. Additional energy-composition section at 2200K (1923°C) is shown in Figure 5-11 (b). This section shows good agreement with the tie line at 2200K (1923°C) in Figure 5-9.

5.4 Database for $\text{AlN-Al}_2\text{O}_3\text{-Y}_2\text{O}_3$ system

There is an increasing demand for the development of thermodynamic databases, which are practically useful. A simple model is preferable to one which is unnecessarily complex and is based on speculation about the ionic structure of the phases. The trick is to identify the line between necessary and unnecessary complexity.

5.4.1 Stoichiometric compounds

5.4.1.1 Stoichiometric compounds in $\text{Al}_2\text{O}_3\text{-Y}_2\text{O}_3$

In order to establish a thermodynamic database for new compounds, the standard enthalpy of formation *from the elements* ΔH_{298}° and standard entropy S_{298}° at 298.15K and the heat capacity at constant pressure must be known. These values are essential to calculate the thermodynamic properties at 1 atm. pressure, represented by the following equations.

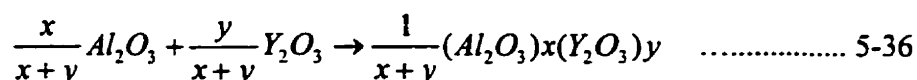
$$H_{T,P} = \Delta H_{298}^\circ + \int_{298}^T C_p dT \quad \dots\dots\dots 5-33$$

$$S_{T,P} = S_{298}^\circ + \int_{298}^T \frac{C_p}{T} dT \quad \dots\dots\dots 5-34$$

$$C_p = a + bT + cT^{-2} + dT^2 + eT^i + fT^j + gT^k \quad \dots\dots\dots 5-35$$

ΔH_{298}° , S_{298}° and C_p were calculated from the standard properties of Al_2O_3 and Y_2O_3 and from Gibbs energy of formation from the component oxides established by phase diagram modeling.

The reaction to form the stoichiometric compounds in the $\text{Al}_2\text{O}_3\text{-Y}_2\text{O}_3$ system can be summarized by the following equation:



What is known about these reactions is the Gibbs energy of formation in the form $\Delta G = \Delta H - T\Delta S$, from the phase diagram modeling. This expression will be referred to as $\Delta G = a + bT$ to distinguish these values from the standard values of ΔH and ΔS . The expressions in Table 5-1 are based on 1 mole of the component oxide as opposed to 1 mole of compound $(\text{Al}_2\text{O}_3)_x (\text{Y}_2\text{O}_3)_y$. So in order to have the enthalpy change per mole of compound, ΔH should be multiplied by $(x + y)$ while ΔS multiplied by $(x + y)$ is the entropy change per mole of compound.

Enthalpy change of formation of a compound at 298K is given by:

$$\Delta H_{(\text{Al}_2\text{O}_3)_x (\text{Y}_2\text{O}_3)_y}^\circ = a(x + y) + x(\Delta H_{\text{Al}_2\text{O}_3}^\circ) + y(\Delta H_{\text{Y}_2\text{O}_3}^\circ) \quad \dots\dots\dots 5-37$$

Absolute entropy at 298K is calculated by:

$$S_{(\text{Al}_2\text{O}_3)_x (\text{Y}_2\text{O}_3)_y}^\circ = -b(x + y) + x(S_{\text{Al}_2\text{O}_3}^\circ) + y(S_{\text{Y}_2\text{O}_3}^\circ) \quad \dots\dots\dots 5-38$$

Where ΔH° and S° are the standard values at 298K.

When the enthalpy and entropy of formation are independent of temperature, the heat capacity difference between reactants and products must be zero. Therefore for self-consistency, the C_p expression must be:

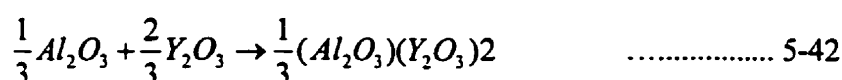
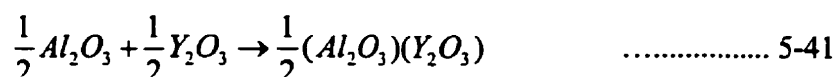
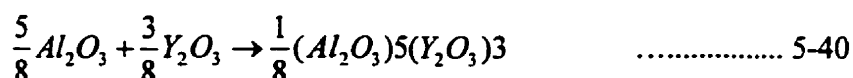
$$C_{p_{(\text{Al}_2\text{O}_3)_x (\text{Y}_2\text{O}_3)_y}} = x(C_{p_{\text{Al}_2\text{O}_3}}) + y(C_{p_{\text{Y}_2\text{O}_3}}) \quad \dots\dots\dots 5-39$$

The absolute enthalpy changes, entropies and C_p 's of Al_2O_3 and Y_2O_3 in their standard conditions at 298K are tabulated in Table 5-5.

Table 5-5: Thermodynamic properties of Al_2O_3 and Y_2O_3 .

Reference phase	ΔH_{298}° (J)	S_{298}° (J/K)	C_p (J/K)
Al_2O_3 (S4)	-1675700.00	50.82	$155.018 + 3861363T^{-2} + 828.3869T^{-1/2} + 409083646T^{-3}$
Y_2O_3 (S2)	-1913286.01	82.75	131.796

The stoichiometric compounds in Al₂O₃ - Y₂O₃ system form according to the following chemical equations:



Equation 5-40 represents the formation of the YAG compound, where x = 5 and y = 3. Equation 5-41 is for the YAP compound, where x = 1 and y = 1. Equation 5-42 is for the YAM compound, where x = 1 and y = 2, wherein the transformation of Y₂O₃ can be described as: $Y_2O_3^{HCP} \leftrightarrow Y_2O_3^{BCC}$ or as: $Y_2O_3(S1) \rightleftharpoons Y_2O_3(S2)$ where x = 0 and y = 1.

Gibbs energy of formation for the stoichiometric compounds resulted from the phase diagram modeling are shown in Table 5-6.

Table 5-6: Gibbs energy of formation of the stoichiometric compounds in Al₂O₃-Y₂O₃ system.

Compound	$\Delta G = a + bT$
YAG	-74133.0 + 17T
YAP	-76364.8 + 17T
YAM	-81158.7+20T
Y ₂ O ₃ (BCC)	-68908+25.35T

Using equations 5-37 to 5-39 the thermodynamic properties of the stoichiometric compounds in Al₂O₃ - Y₂O₃ system can be calculated. These properties are shown in Table 5-7.

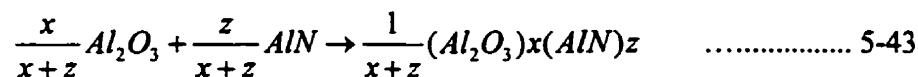
Table 5-7: Thermodynamic properties of the stoichiometric compounds in Al₂O₃-Y₂O₃ system.

Compound	ΔH°_{298} (J)	S°_{298} (J/K)	C_p (J/K)
YAG	-14711422.0	366.34	$1170.478 - 19306815T^{-2} - 4141.93T^{-1/2} + 2045418230 T^{-3}$
YAP	-3741715.6	99.56	$286.814 - 3861363T^{-2} - 828.3869T^{-1/2} + 409083646 T^{-3}$
YAM	-5745748.1	156.31	$418.61 - 3861363T^{-2} - 828.3869T^{-1/2} + 409083646 T^{-3}$
Y ₂ O ₃ (Sl)	-1982194.0	57.40	131.796

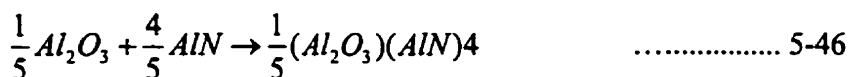
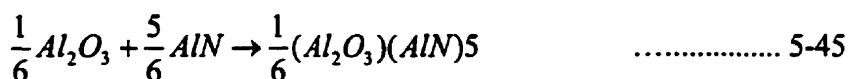
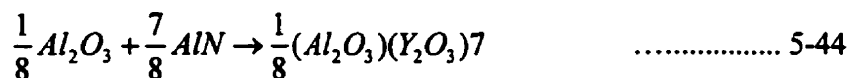
Table 5-7 represents the input necessary to establish the database of the stoichiometric compounds in the Al₂O₃ - Y₂O₃ binary system. The same steps were followed for the stoichiometric compounds in the Al₂O₃ - AlN binary system.

5.4.1.2 Stoichiometric compounds in AlN - Al₂O₃ system

The reaction of formation of the stoichiometric compounds in the AlN - Al₂O₃ system can be described in the following chemical equation:



The stoichiometric compounds in the AlN - Al₂O₃ binary system form according to the following equations:



Equation 5-44 represents the formation of 27R, where $x = 1$ and $z = 7$. Equation 5-45 is for the formation of 21R, where $x = 1$ and $z = 5$, and equation 5-46 is for the formation of 12H compound, where $x = 1$ and $z = 4$.

In order to calculate the thermodynamic properties of these compounds the absolute enthalpy changes, entropy and Cp of Al₂O₃ are taken from the F*A*C*T database and are shown in Table 5-5. These values for AlN are shown in Table 5-8.

Table 5-8: Thermodynamic properties of AlN.

Reference phase	ΔH°_{298} (J)	S°_{298} (J/K)	Cp (J/K)
AlN (S1)	-317984	20.142	$50.4165 - 1665496.46T^{-2} + 7861.955T^{-1} + 232.265T^{-1/2} + 300647796 T^{-3}$

The Gibbs energy of formation of these stoichiometric compounds resulting from the phase diagram model are shown in Table 5-9.

Table 5-9: Gibbs energy of formation of the stoichiometric compounds in AlN-Al₂O₃ system.

Compound	$\Delta G = a + bT$
27R	$27542.45 - 14.486 T$
21R	$35587.33 - 18.221 T$
12H	$39633.24 - 20.278 T$

It can be seen that equations 5-37 to 5-39 can be easily modified to suit the compounds in the AlN-Al₂O₃ system by replacing y with z and Y₂O₃ with AlN, respectively. The thermodynamic properties of 27R, 21R and 12H can be calculated using the modified 5-37 to 5-39 equations. These properties are shown in Table 5-10.

Table 5-10: Thermodynamic properties of the stoichiometric compounds in AlN - Al₂O₃ system

Compound	ΔH°_{298} (J)	S°_{298} (J/K)	Cp (J/K)
27R	-3681248.4	307.702	$507.93 - 15519838.24T^{-2} - 55027 T^{-1} + 797.468 T^{-1/2} + 2513618218 T^{-3}$
21R	-3052096.02	238.446	$407.101 - 4694110.32T^{-2} - 39309.78 T^{-1} + 332.938 T^{-1/2} + 1912322626 T^{-3}$
12H	-2749469.8	232.778	$356.685 - 10523348.85T^{-2} - 31447.82T^{-1} + 100.673 T^{-1/2} + 1611674830 T^{-3}$

Table 5-10 represents the input necessary to establish the database of the stoichiometric compounds in the Al₂O₃ - AlN binary system.

5.4.2 Liquid phases

The storage, retrieval and manipulation of thermodynamic data with the aid of the computer require accurate analytical representation of the thermodynamic properties of the solutions. Values of the standard Gibbs energies, G° , of each component are entered and stored in the solution database along with parameters which define the Gibbs energy of mixing according to the Kohler/Toop polynomial model.

Table 5-11 Thermodynamic data for liquid AlN-Al₂O₃-Y₂O₃ system.

Component	Component No.	G°
AlN	1	G° of AlN (S1) from [91] + $\Delta G^\circ_{\text{fusion}}$ Where $\Delta G^\circ_{\text{fusion}} = 70557.8 - 23.0055 T$
Al ₂ O ₃	2	G° of Al ₂ O ₃ (S4) from [91] + $\Delta G^\circ_{\text{fusion}}$ Where $\Delta G^\circ_{\text{fusion}} = 87918.58 - 37.847 T$
Y ₂ O ₃	3	G° of Y ₂ O ₃ (S2) from [91] + $\Delta G^\circ_{\text{fusion}}$ Where $\Delta G^\circ_{\text{fusion}} = 68908.00 - 25.340 T$

The Gibbs energy of the pure liquid components is expressed relative to the solid phases so that the addition of a Gibbs energy of melting equation is consistent with the binary diagram model discussed previously. As shown in Table 5-11, the AlN G° of S1 is taken from the F*A*C*T database and $\Delta G^\circ_{\text{fusion}}$ of (AlN) is added to obtain G° of AlN. This will cause all the parameters for G° of S1 AlN to be copied into the solution database then the expression of $\Delta G^\circ_{\text{fusion}}$ will be added. The same thing goes for Al₂O₃ and Y₂O₃ except that they have different reference phases, and when this solution database is subsequently read to calculate for the equilibrium, G° for each pure component will be taken from the values stored in the solution database.

Binary terms of the polynomial expansion for G^E were entered as Redlich-Kister or Legendre polynomials due to their simplicity and the fact that their functional form is consistent with the empirical observations of the solution's behavior [97]. The J'th Redlich-Kister polynomial term in the binary system M-N is defined as: $X_M X_N P_J (X_N - X_M)^J$ or in a more general form as:

$$G^E = X_M^I X_N^J (A + BT + CT \ln T) \quad \dots\dots\dots 5-47$$

In Table 5-12, the G^E terms for the AlN-Al₂O₃-Y₂O₃ system are given as Redlich-Kister polynomials, where M and N are defined by the component number as shown in Table 5-11.

Table 5-12: Binary excess mixing terms.

Parameter	M	N	I	J	A	B	C
1	1	2	1	1	-40061.00	0.0	0.0
2	1	2	2	1	29119.00	0.0	0.0
3	1	3	1	1	-57164.00	0.0	0.0
4	1	3	2	1	36945.00	0.0	0.0
5	2	3	1	1	-167230.00	0.0	0.0
6	2	3	1	2	-39366.00	0.0	0.0

5.4.3 Al₂O₃-AlN spinel

Values of the standard Gibbs energy, G° , for AlN and Al₂O₃ components summarized in Table 5-13 are entered and stored in the solution database with parameters that define the Gibbs energy of mixing according to the Kohler/Toop polynomial model, as shown in Table 5-14.

Table 5-13 Thermodynamic data for spinel phase.

Component	Component No.	G°
AlN	1	G° of AlN (S1) from [91] + $\Delta G^\circ_{\text{fusion}}$ Where $\Delta G^\circ_{\text{fusion}} = 52500.15 - 13.355 T$
Al ₂ O ₃	2	G° of Al ₂ O ₃ (S4) from [91] + $\Delta G^\circ_{\text{fusion}}$ Where $\Delta G^\circ_{\text{fusion}} = 64500.48 - 25.847 T$

Table 5-14: Binary excess mixing terms for spinel solution.

Parameter	M	N	I	J	A	B	C
1	1	2	1	1	-171499.0	38.00	0.0
2	1	2	2	1	438695.1	-151.17	0.0

The self-consistent thermodynamic database developed in this way is used for interpolation purposes in order to develop the phase equilibria in the AlN-Al₂O₃-Y₂O₃ ternary system.

Chapter 6:

RESULTS AND DISCUSSION OF THERMODYNAMIC ANALYSIS

In a thermodynamic optimization of a binary system, all available thermodynamic and phase equilibrium data are critically evaluated simultaneously in order to obtain one set of model equations for the Gibbs energy for all the phases as a function of temperature and composition. From these equations, all of the thermodynamic properties and the phase diagrams can be generated. In this way, the data are rendered consistent with thermodynamic principles [89,99].

Modeling the thermodynamic properties of solutions permits a consistent means of smoothing, interpolating and extrapolating data. Phase diagrams are a form of thermodynamic data since they present the conditions for minimum Gibbs energy of the system in terms of the phases present for a given overall composition, temperature and pressure.

At a specified temperature and pressure the most stable product(s) is the one that is associated with the lowest Gibbs energy. The products of the reaction are either solution phases or stoichiometric phases. So if the existence of a particular phase does not assist in minimizing G , it will be dropped in the course of successive iterations. By repeating this computation for a matrix of compositions and temperatures, a ternary phase diagram can be constructed.

6.1 Al_2O_3 - Y_2O_3 phase diagram.

The calculated phase diagram of the Al_2O_3 - Y_2O_3 system is shown in Figure 6-1. This diagram was calculated from the database built for the $\text{AlN-Al}_2\text{O}_3$ - Y_2O_3 system. Agreement between the calculated Al_2O_3 - Y_2O_3 phase diagram and measured liquidus and other critical points is shown in this figure. The calculated eutectic composition and temperature agree very well with the experimental values from the literature. This indicates that the polynomial representation of the thermodynamic properties is capable of reproducing the measured phase diagram within experimental error limits, even when the measurements are very precise.

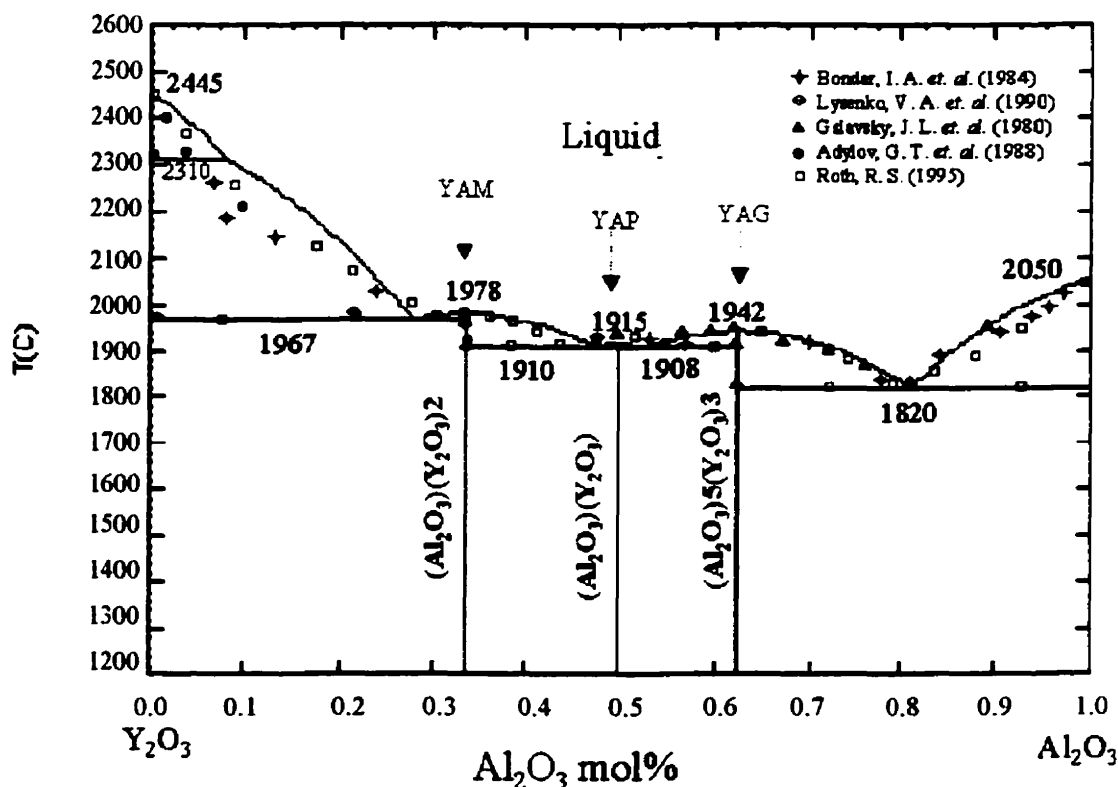


Figure 6-1: Calculated Y_2O_3 - Al_2O_3 phase diagram with experimental data from the literature.

The melting point of pure Al_2O_3 , 2054°C , reported by Gervais *et al.* [60] agrees very well with the value resulted from the present model, 2050°C . Likewise, the measured melting point of pure Y_2O_3 , $2439 \pm 12^\circ\text{C}$ and $2500 \pm 50^\circ\text{C}$, reported by [102] and [44], respectively, agrees very well with the value that resulted from the present model at 2445°C . The transition temperature of Y_2O_3 was determined by Foex and Traverse to be 2300°C and by Misuno *et al.* as 2341°C . This is consistent with the calculated transition temperature, 2310°C , shown in Figure 6-1. Mah and Petry [44] determined the eutectic composition and temperature between Y_2O_3 and YAM to be (29.5 mol% Al_2O_3 , 70.5 mol% Y_2O_3) and 1977°C respectively. Comparing this result with the corresponding eutectic point in Figure 6-1, 28 mol% Al_2O_3 and 1967°C provides good agreement.

6.2 $\text{AlN} - \text{Al}_2\text{O}_3$ phase diagram.

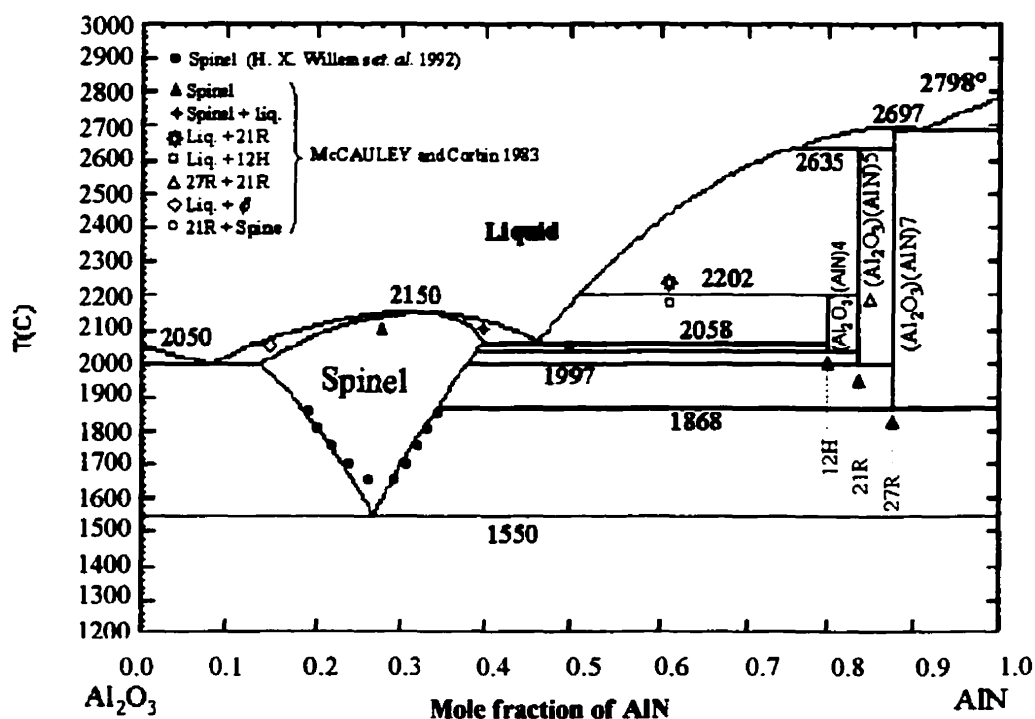


Figure 6-2: Calculated Al_2O_3 - AlN phase diagram and comparison with experimental data from the literature.

The optimized phase diagram for the AlN-Al₂O₃ system in relation to the experimental data from the literature is shown in Figure 6-2. Since experimental data are rarely self-consistent, a decision as to which data one wishes to emphasize is inescapable. The most recent experimental results for AlN-Al₂O₃ were chosen for these purposes. The present analysis is in excellent agreement with the experimental results from the literature.

The resultant melting point of pure AlN agrees very well with the hypothetical melting temperature of AlN, 2794°C, reported by [70] and $2797 \pm 100^\circ\text{C}$ reported by [104]. Spinel was reported to melt congruently at 2165°C in one atmosphere of nitrogen [64,71]. Ish-Shalom observed that at 1580°C, spinel and AlN are formed by carbothermal reduction of aluminum oxide in nitrogen [69]. However, Lejus mentioned that at temperatures below 1600°C, spinel decomposes into AlN and Al₂O₃. According to the experimental results of Yawei *et al.* [105], samples with a high content of the spinel could be produced below 1550°C if processing parameters, for instance heating rate and nitrogen flow rate, are carefully controlled. These results agree with what Ish-Shalom [69] found. Dumitrescu and Sundman [37] reported that the homogeneity region of spinel phase varies with temperature. For instance, at 1850°C, spinel is stable between 66 mol% Al₂O₃ and 81 mol% Al₂O₃. This region becomes smaller at lower temperatures and below 1690°C spinel is not stable. Also, Willems *et al.* [69] studied the stability of spinel phase using carbothermal reduction of alumina and reaction sintering of AlN-Al₂O₃ mixtures, shown in Figure 6-2. It can be seen that they agree very well with the current calculations. The 27R, 21R and 12H compounds have been considered in this calculation and the assessment shows good agreement when compared with Metselaar's phase diagram shown in Figure 2-11.

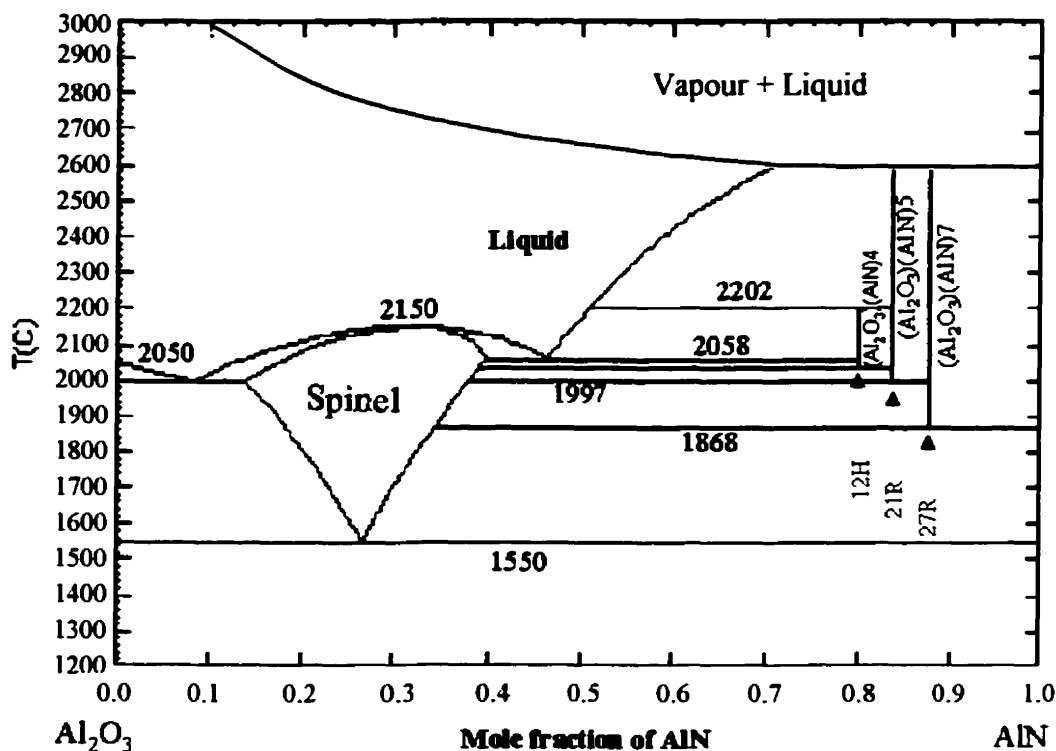


Figure 6-3: Calculated AlN-Al₂O₃ phase diagram at $P_{tot} = 1.0$ atm illustrating AlN decomposition.

Figure 6-3 was calculated at $P_{N_2} + P_{Al} = 1$ atm. It can be seen that AlN decomposes at 2600°C. However, this temperature decreases to 2200°C when the total pressure decreases to 0.1 atm. (Figure 6-4). Kaufman *et al.* [62] reported that AlN decomposes into Al and N₂ at one atmosphere above 2577°C. This generally agrees with the diagram in Figure 6-3. On the other hand, D'ychkov reported that the heating of AlN at atmospheric pressure results in intensive dissociation and complete destruction of the sample at 2400-2700K [104], which is lower than the decomposition temperature resulted from the current assessment.

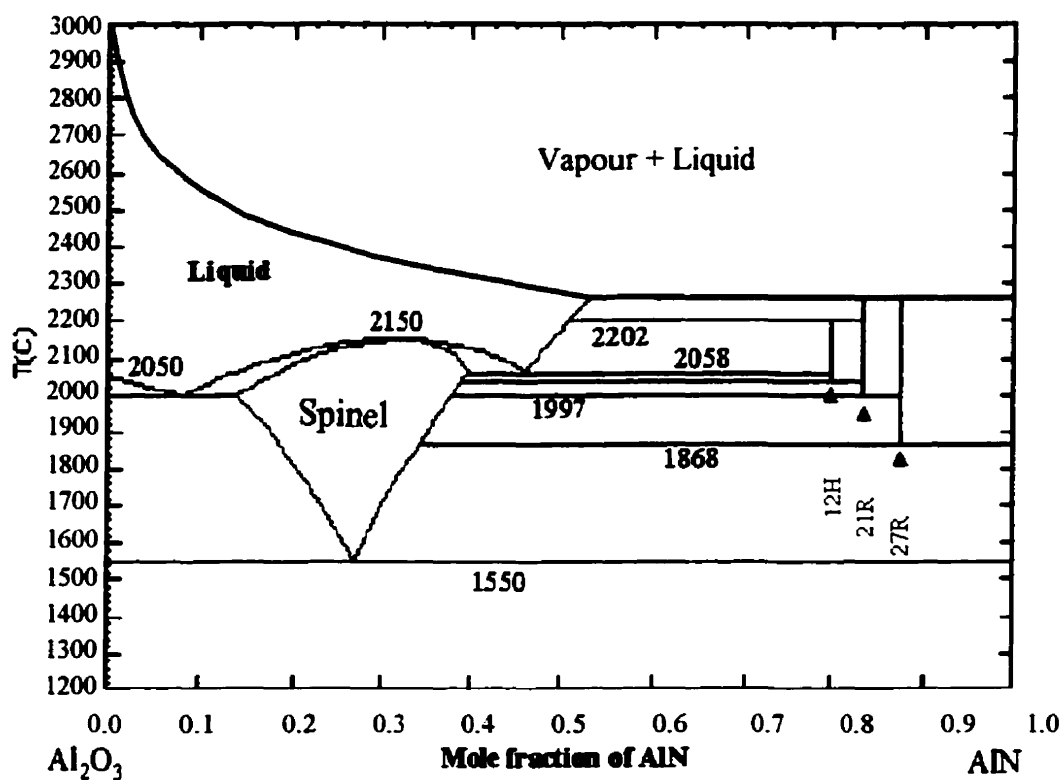


Figure 6-4: Calculated AlN-Al₂O₃ phase diagram at $P_{\text{tot}} = 0.1 \text{ atm}$ showing AlN decomposition.

The vapour phase was incorporated in Figures 6-3 and 6-4 at different pressures to emphasize its importance on the stability of AlN, but no studies were conducted to determine either the composition or pressure of the vapour phase in this system.

6.3 AlN - Y₂O₃ phase diagram.

The AlN-Y₂O₃ phase diagram is a simple eutectic type. The calculated equilibrium phase diagram is shown in Figure 6-5.

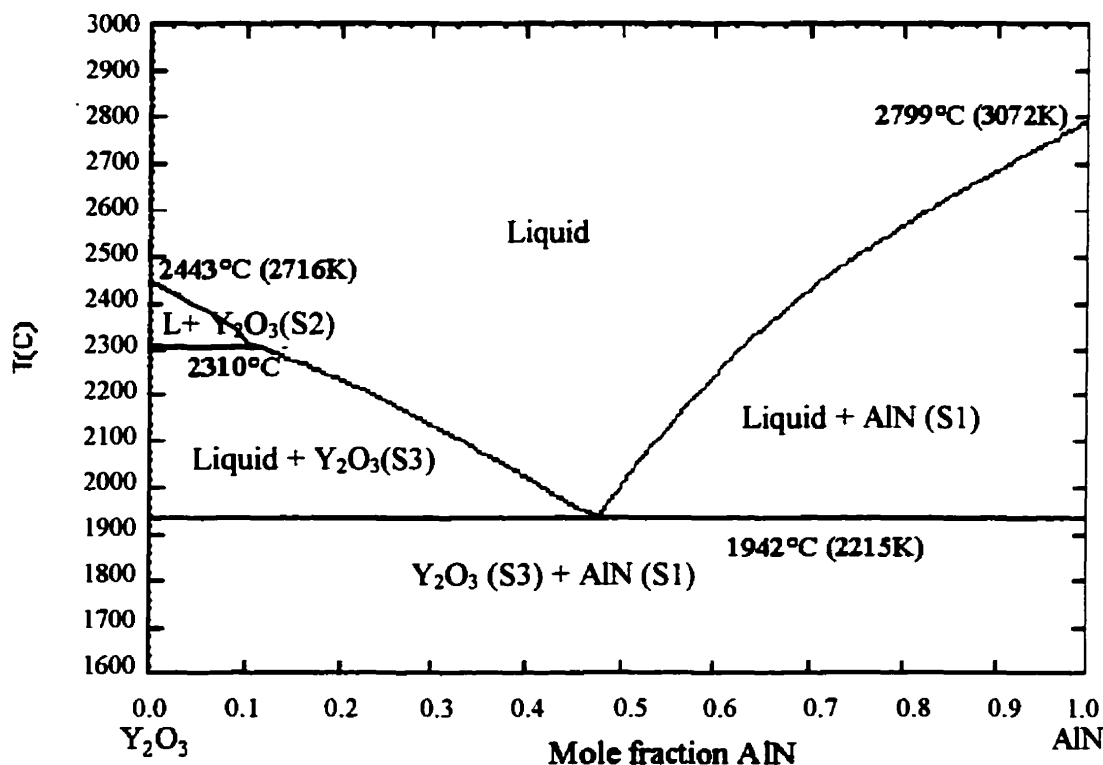


Figure 6-5: Calculated AlN-Y₂O₃ phase diagram.

In the optimization of the AlN-Y₂O₃ system, a high weighting factor was applied to the eutectic point. This choice was made on the basis that the eutectic temperature and composition are the only thermodynamic data available in the literature for this binary system. The same Gibbs energy of fusion for Y₂O₃ and AlN, which were used in optimizing the other two phase diagrams, were utilized in modeling the AlN-Y₂O₃ system.

Figure 6-5 shows that the eutectic point is at $X_{\text{AlN}} = 47 \text{ mol\%}$ and 1942°C, which is very close to what Kaufman *et al.* [62] reported (i.e. $X_{\text{AlN}} = 48.3 \text{ mol\%}$ and 1942°C, for the eutectic composition and temperature, respectively). However, comparing the current assessment of this phase diagram with Kaufman's diagram (Figure 2-9) reveals two

improvements: the melting points of the pure components are closer to the values reported in the literature and the phase transformation of Y_2O_3 from BCC to HCP at 2310°C .

As stated before, experimental information on this system is not available in the literature. Hence, this system will be studied using *in situ* high temperature neutron diffractometry in the course of this research.

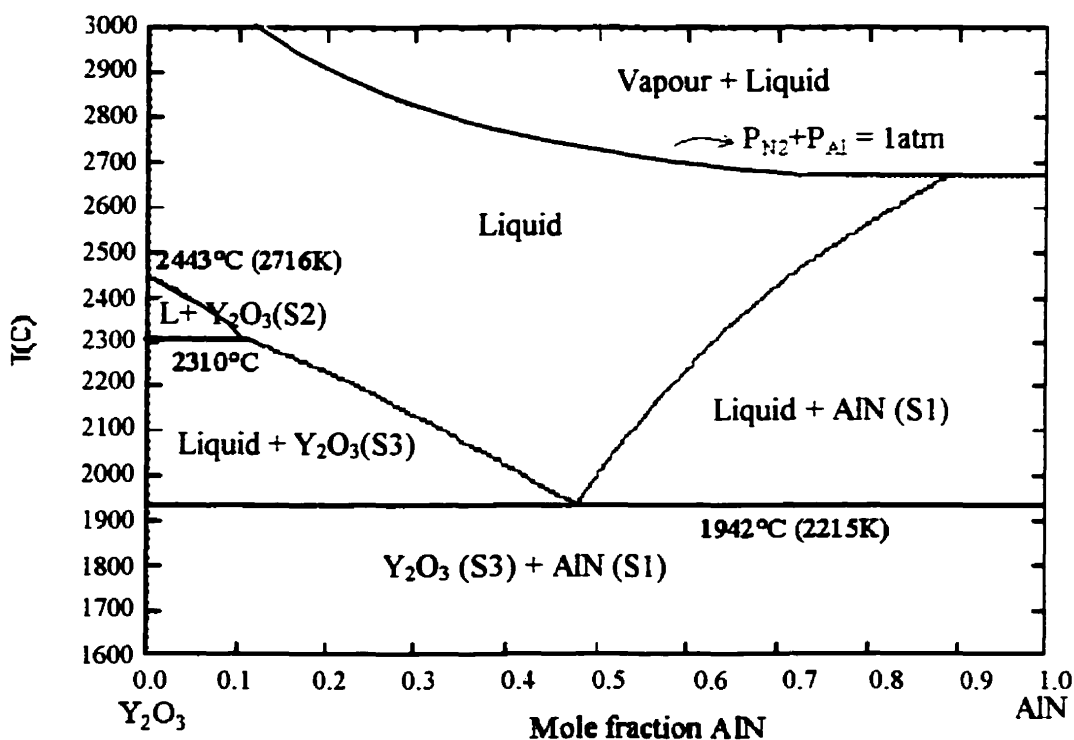


Figure 6-6: Calculated AlN - Y_2O_3 phase diagram at $P_{tot} = 1.0 \text{ atm}$ showing AlN decomposition.

Calculated AlN - Y_2O_3 phase diagrams illustrating AlN decomposition at different total pressures are presented in Figure 6-6 and 6-7.

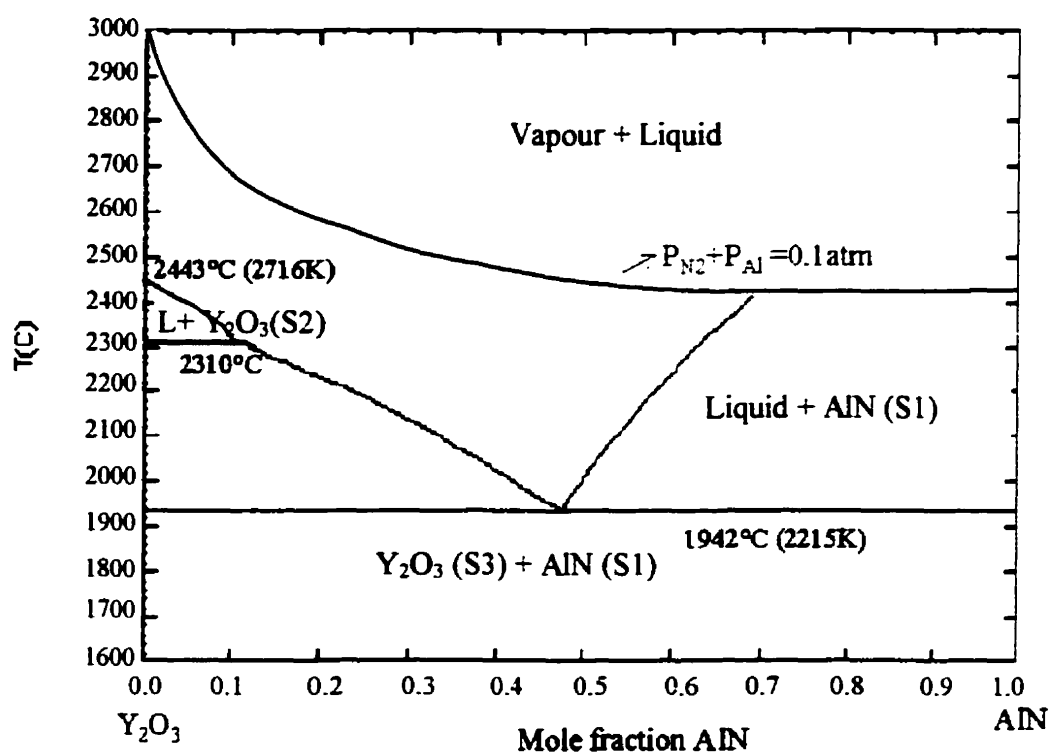


Figure 6-7: Calculated $\text{AlN-Y}_2\text{O}_3$ phase diagram illustrating AlN decomposition at $P_{\text{tot}} = 0.1 \text{ atm}$.

6.4 Isothermal sections of $\text{AlN-Al}_2\text{O}_3\text{-Y}_2\text{O}_3$ system.

Isothermal sections are directly calculated from the constructed database for $\text{AlN-Al}_2\text{O}_3\text{-Y}_2\text{O}_3$ system. That is, after choosing the desired temperature, the composition of the phases in equilibrium was determined and plotted on the ternary Gibbs triangle by Triplot program. Then the phase boundaries were drawn by connecting these points by hand.

The ternary phase diagrams were calculated by assuming the ternary parameters to be zero, and taking all the thermodynamic data stated for the binary phases into consideration. The calculated isothermal sections of the $\text{AlN-Al}_2\text{O}_3\text{-Y}_2\text{O}_3$ system are given in Figures 6-8 to 6-12.

At high temperature, prior to solidification, the whole concentration triangle is composed of a homogeneous melt, and obviously no phase boundaries exist. 2500°C is below the temperature at which the primary crystallization of AlN sets in but is still above the melting point of both other two components. This isothermal section shows that beside the region of homogeneous melt, heterogeneous regions of the primary crystallization of AlN and AlN-based polytypes exist in equilibrium with the liquid phase. In addition, two small three-phase areas of L+27R+AlN and L+21R+27R are found. The regions of the melt and two solids are the result of the binary eutectic crystallization of AlN and 27R according to:



and of the binary peritectic crystallization of 27R and 21R which occurs according to:

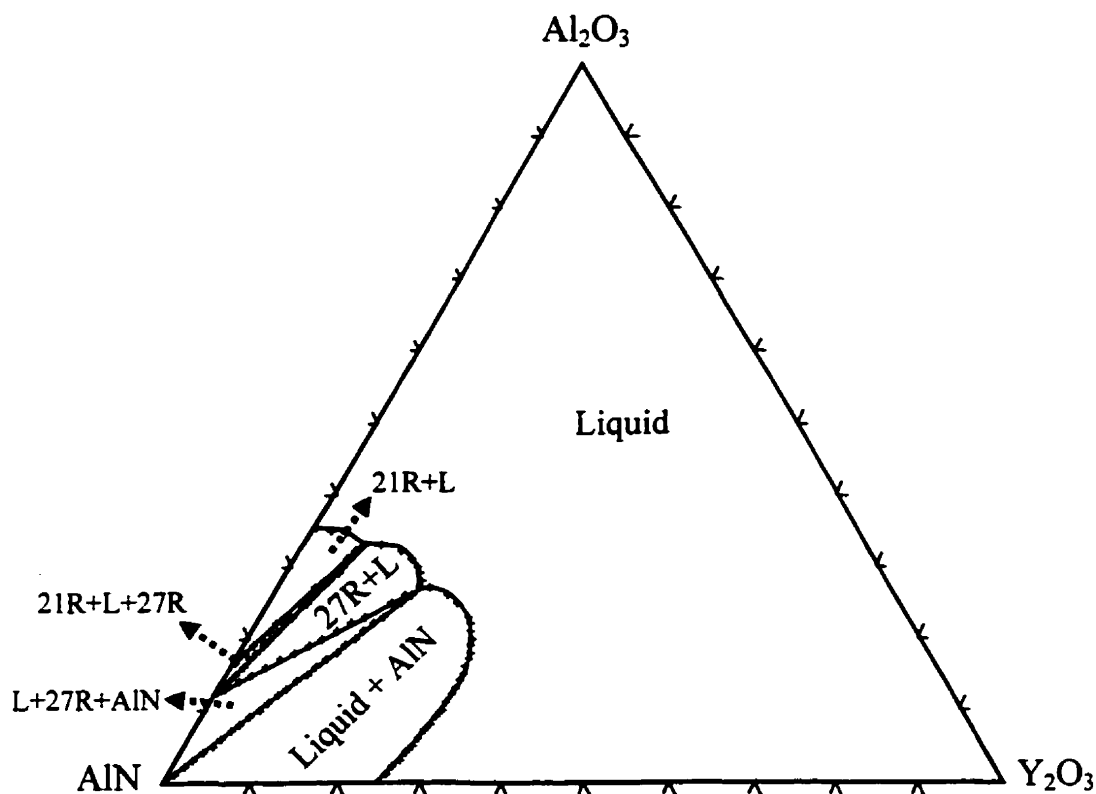


Figure 6-8: Isothermal Section at 2500°C.

By cooling from 2500°C to 2000°C, further primary solidification of different phases takes place, and instead of three, there are five regions of primary solidification in which the crystalline types, AlN, Y_2O_3 , 27R, spinel and Al_2O_3 occur in equilibrium with the liquid phase.

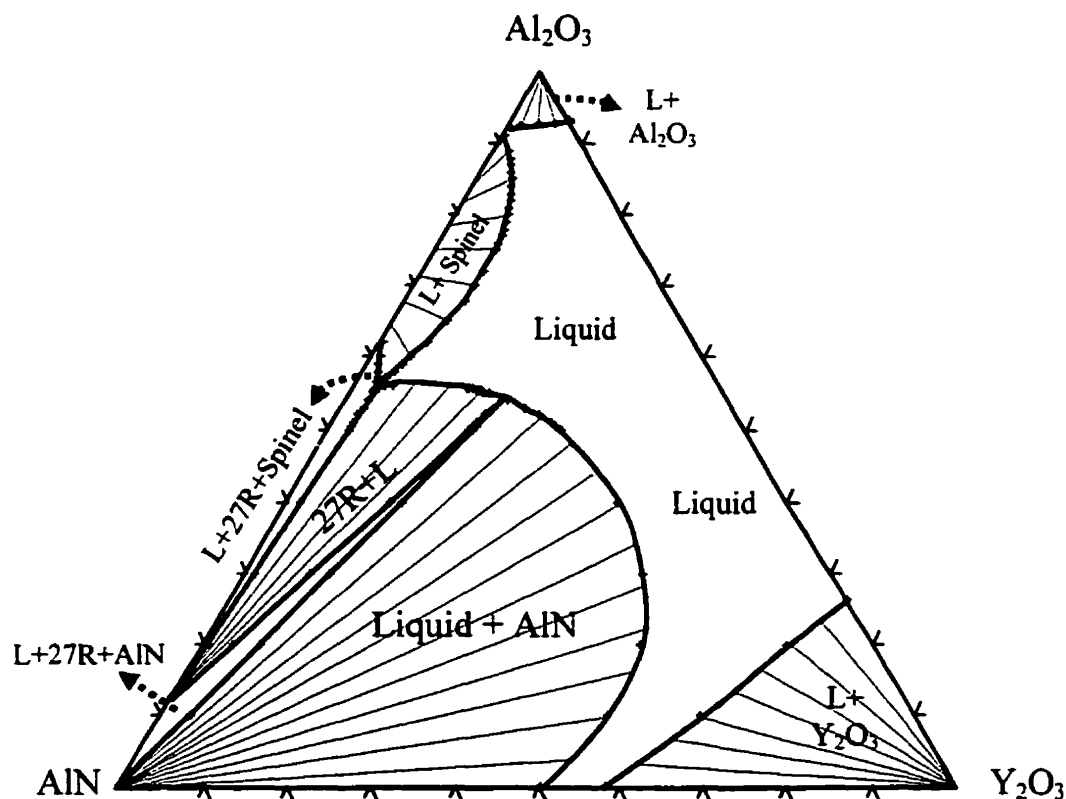


Figure 6-9: Isothermal Section at 2000°C.

It is self-evident that in the isothermal sections the lines separating regions of primary (i.e. L + a crystalline phase) and binary eutectic crystalline (i.e. L + two crystalline phases) must appear as straight lines, since they represent intersections of a horizontal plane (isothermal section) with a surface which was generated through the motion of a horizontal line, (the eutectic tie line).

In Figure 6-9 tie lines are drawn in the two-phase region. It can be noticed that they rotate gradually from the orientation of bounding tie lines. The information regarding the compositions and proportional amounts of the conjugate phases for a particular composition can be obtained by the tie line that passes through the composition point, since along the tie line the two phases have a fixed composition but different proportions.

Two binary eutectic points have been encountered by cooling to 2000°C, these are;

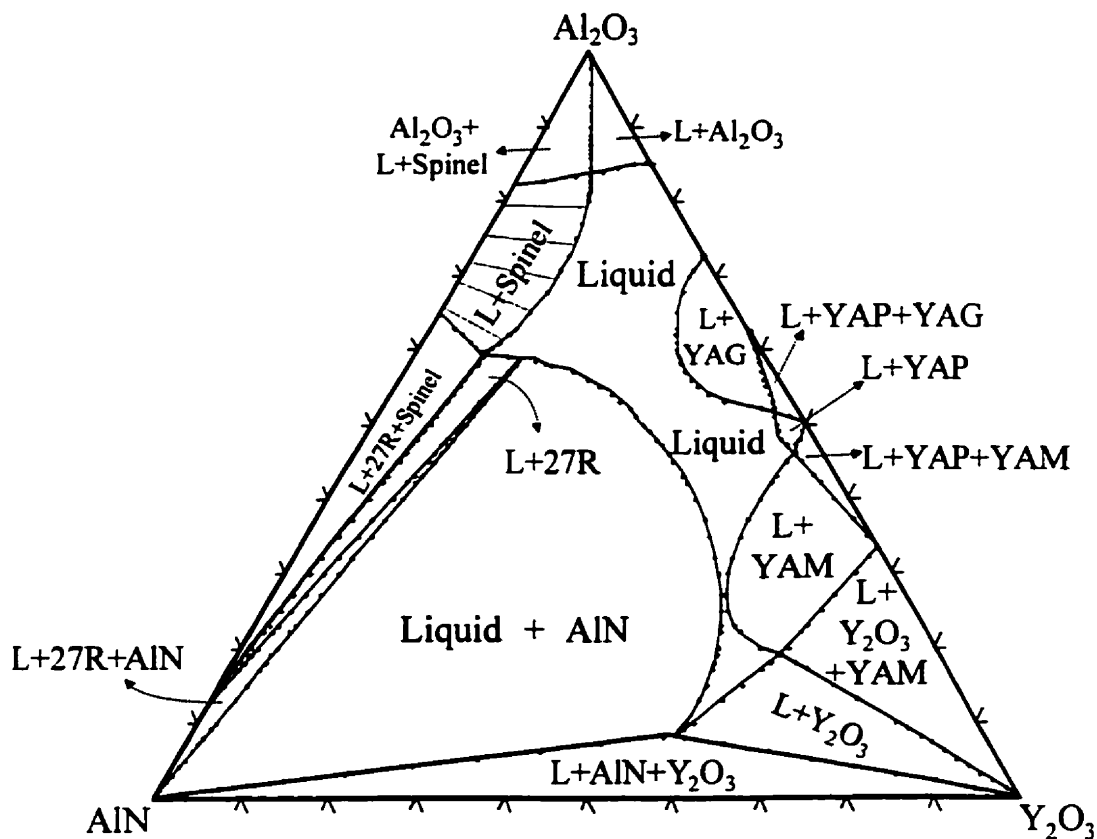


Figure 6-10: Isothermal Section at 1900°C.

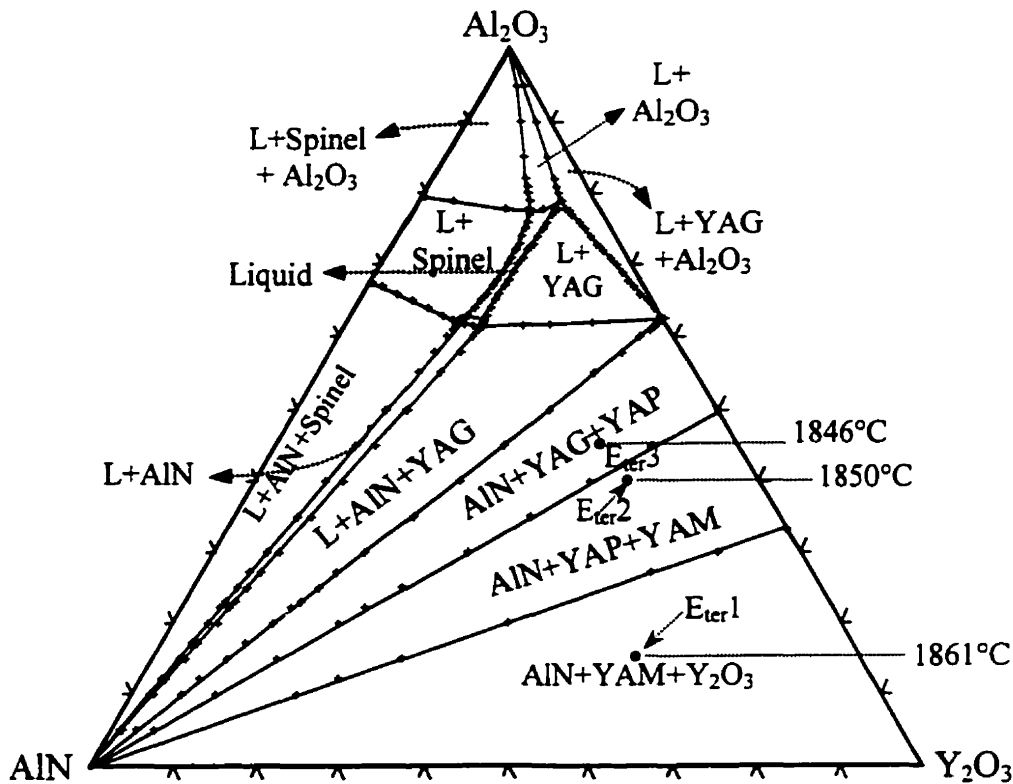
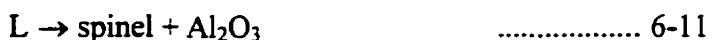
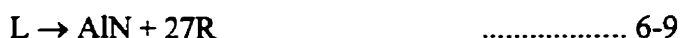


Figure 6-11: Isothermal Section at 1800°C.

At 1800°C the isothermal section can be seen in Figure 6-11. It can be seen that the region of the melt shrinks, however at this temperature the liquid is still in equilibrium with the other phases in the two and three phase regions. At this temperature, the eutectic point between Al_2O_3 and YAG has been encountered as can be seen from the region of $\text{L}+\text{YAG}+\text{Al}_2\text{O}_3$, and is a result of the following eutectic reaction;



Also, there are still regions of primary solidification of AlN , YAG, spinel, and Al_2O_3 in equilibrium with the melt. Figure 6-11 shows three regions of three-solid-phases. These indicate that three ternary eutectic points have been encountered upon cooling to this temperature, and they are results of the following reactions:



The first ternary eutectic point has a composition of 27.48 mol% AlN , 14.52 mol% Al_2O_3 , 58 mol% Y_2O_3 and occurs at 1861°C. Whereas, the second ternary eutectic point has a composition of 16 mol% AlN , 40 mol% Al_2O_3 , 44 mol% Y_2O_3 and occurs at 1850°C, and the third one has a composition of 16.1 mol% AlN , 45.4 mol% Al_2O_3 , 35.5 mol% Y_2O_3 and occurs at 1846°C.

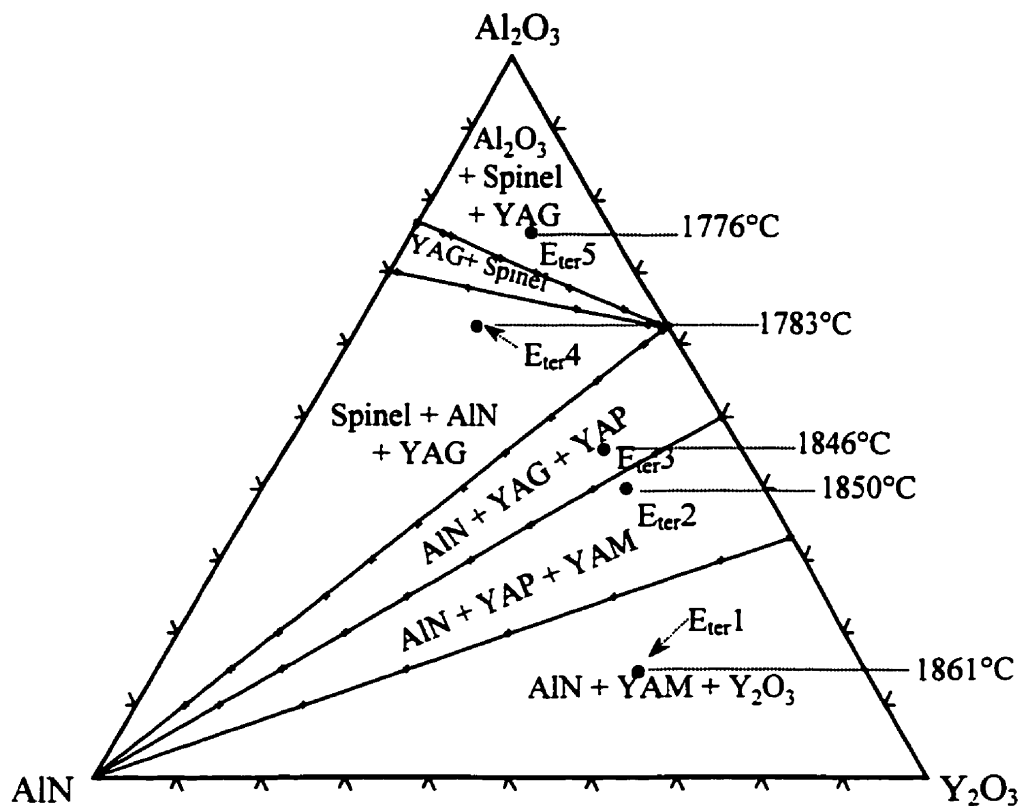


Figure 6-12: Isothermal Section at 1700°C.

A later stage of solidification is shown in Figure 6-12, where there is no residual liquid. At this temperature, there are five three-crystalline-phases regions and one two-crystalline-phases region. This means that there are two other ternary eutectic points that have been encountered upon cooling to 1700°C. They occur at 1783°C and 1776°C according to the following reactions:



6.5 Liquidus projection of AlN - Al₂O₃ - Y₂O₃ system.

Figure 6-13 shows projection of the equilibrium liquidus surface of the AlN-Al₂O₃-Y₂O₃ system. This diagram is calculated by using the F*A*C*T system with the optimized models for the binary systems. The arrows on the dotted boundary lines show directions of falling liquidus temperatures. As solidification proceeds by precipitation of primary phases, the composition of the liquid changes progressively, and this change is represented by a path on the liquidus projection, occurring in a direction representing a lowering of the temperature on the liquidus surface.

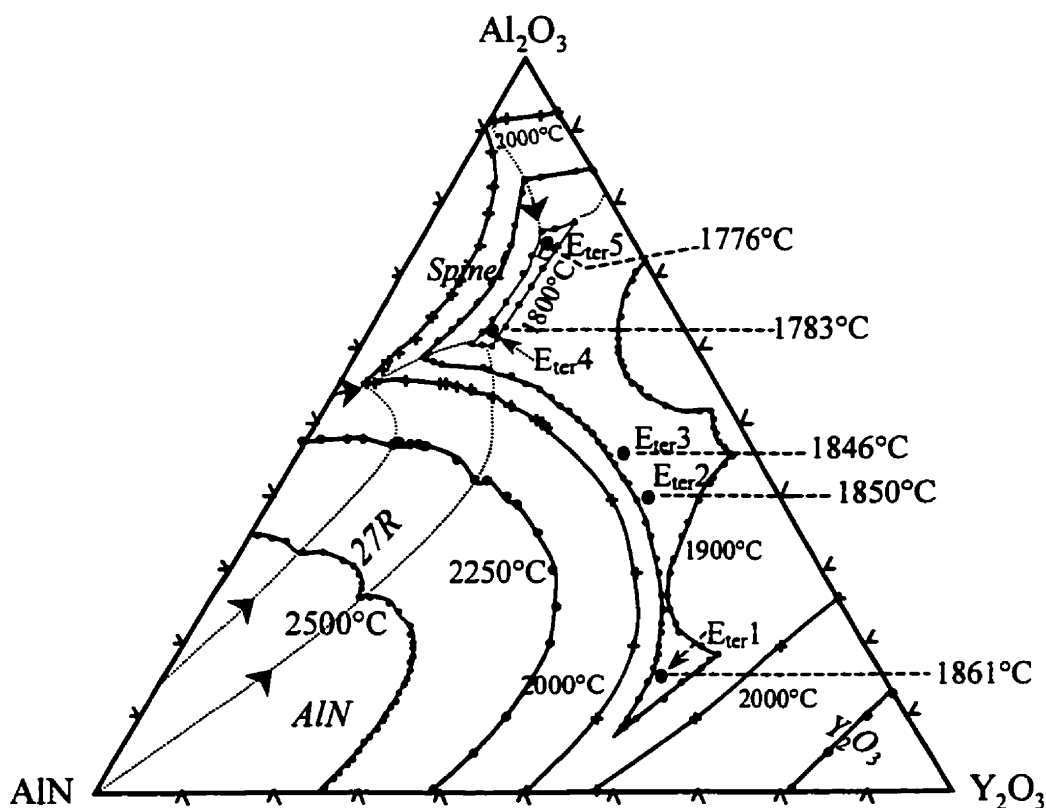


Figure 6-13: Liquidus projection for AlN-Al₂O₃-Y₂O₃ system.

On each liquidus surface, the liquid is in equilibrium with one solid phase, thus only one solid phase is marked in each area. Figure 6-13 shows also the five ternary eutectic points and their temperatures.

6.6 Phase assemblage diagrams

As shown in the discussion section of the ternary isothermal diagrams, these diagrams show the phases in equilibrium and their composition at various temperatures. However, they do not show the relative amount of each phase and the formation and/or decomposition temperature of these phases. For this purpose, relative mass versus temperature is calculated from the database and will be compared with the experimental results in the following sections. In order to explain the benefit of these diagrams an example will be demonstrated in this section.

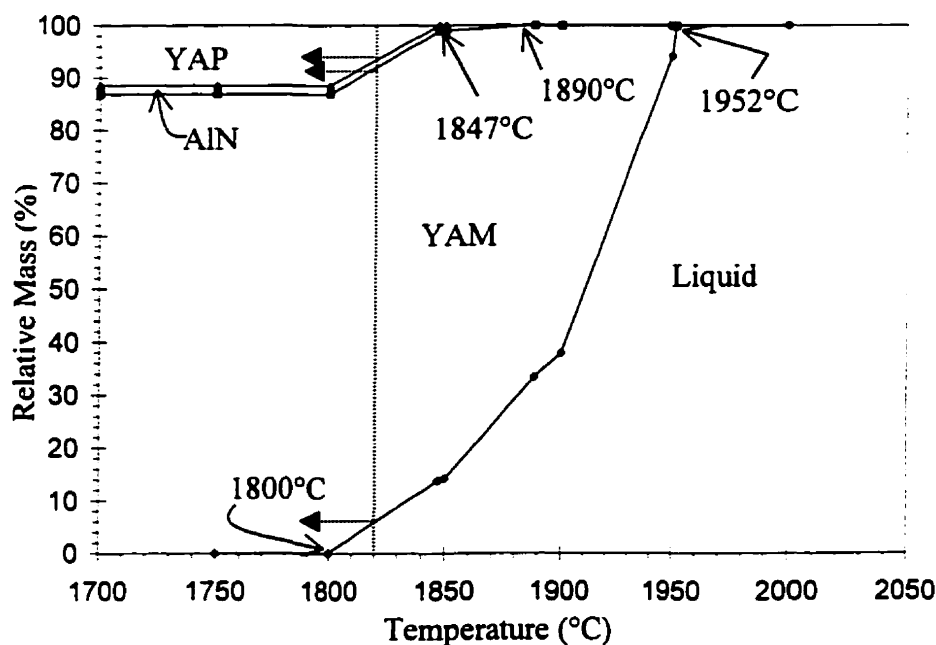


Figure 6-14: Phase assemblage of (7 mol% AlN, 60 mol% Y_2O_3 , 33 mol% Al_2O_3) composition.

Figure 6-14 is calculated for a sample composed of 7 mol% AlN, 60 mol% Y_2O_3 and 33 mol% Al_2O_3 . The proportion of different phases at any working temperature can easily be read from this figure. For instance, at 1820°C, 100 g of the overall material consists of 8 g of liquid, 85 g of YAM, 2 g of AlN and 5 g of YAP. It can be seen from this figure that YAM is the first solid to precipitate in this sample upon cooling. It starts precipitating at 1952°C, whereas AlN and YAP phases start to precipitate at 1890°C and

1847°C respectively. This figure also gives the phase proportions of this sample at room temperature after solidification. One more important point can be noticed from this figure that the proportion of solids does not increase rapidly with decreasing temperature. This means that this composition is not sensitive to small changes in operating temperature.

6.7 Thermodynamics of AlN sintering

The sintering of AlN with an additive is usually performed at 1450-2000°C for 1-6 hours under N₂ atmosphere. Nitrogen gas prevents AlN from decomposition and oxidation. In this section, the thermodynamic calculations of the AlN-Al₂O₃-Y₂O₃ system and the experimental work of Drew *et al.* [106] on the effect of Y₂O₃ content and sintering conditions on the densification, secondary phase evolution and thermal conductivity of AlN will be compared. The compositions used in their study are shown in Table 6-1.

Table 6-1: Amount of Y₂O₃ additive in each sample.

Composition	Y ₂ O ₃ Content (wt%)	AlN content (wt%)
I	1.36	98.64
II	3.04	96.96
III	3.47	96.53
IV	7.59	92.41

The amount of Al₂O₃ in each sample was calculated according to the following chemical equation:



assuming that all the oxygen in AlN powder is present in the form of Al₂O₃. The total oxygen level in the AlN powder was analysed after milling and drying by ELKEM Metals in Niagara Falls (New York) using a TC136 LECO EF100 electrode furnace and associated analyser.

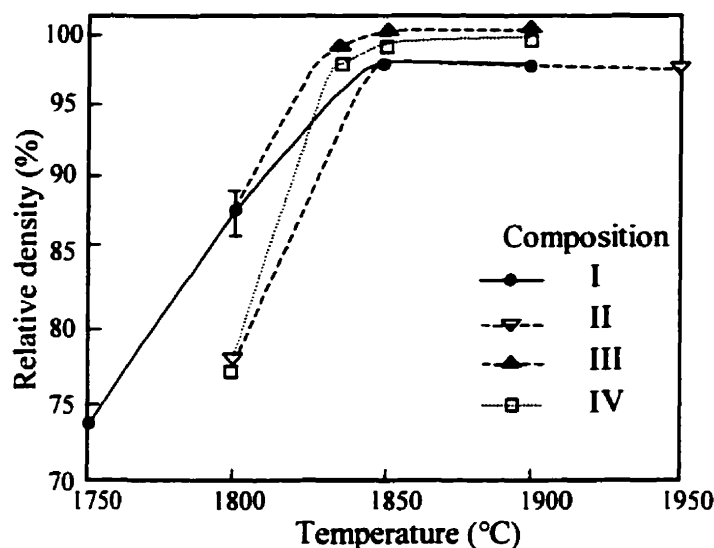


Figure 6-15: Relative density of the four compositions as a function of sintering temperature [106].

Figure 6-16 is taken from the same reference [106]. It gives the X-ray powder diffraction patterns for the four compositions after sintering at 1900°C for one hour. Each composition shows strong peaks associated with AlN in addition to minor peaks associated with the secondary grain boundary phase. These results agree very well with the thermodynamic calculations presented in Figures 6-17 to 6-20.

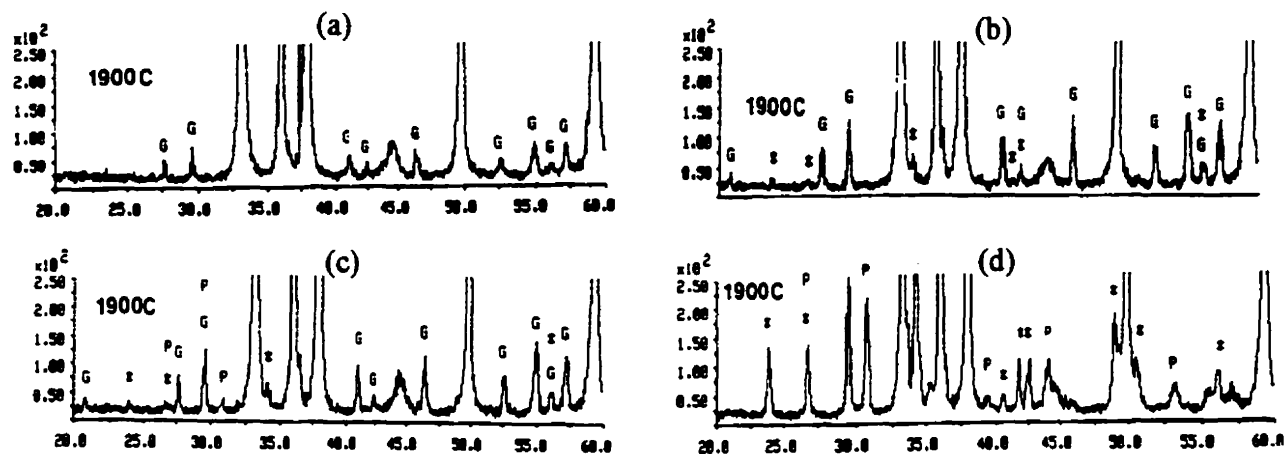


Figure 6-16: X-ray powder diffraction patterns of AlN for four compositions, G: YAG, P: YAP and *: YAM [106].

Figure 6-15 shows that all compositions reach complete densification after sintering at $>1850^{\circ}\text{C}$ for one hour. This can be explained by the phase assemblage diagrams, Figures 6-17 to 6-20. These figures show that all compositions would have formed liquid at this temperature. Also, Figure 6-15 shows that composition I reached higher density than the other samples sintered at 1800°C , and this can be explained by referring to Figure 6-17. This figure indicates that this composition starts forming liquid at 1782°C , whereas a higher temperature ($\sim 1850^{\circ}\text{C}$) is required for the other compositions to form liquid.

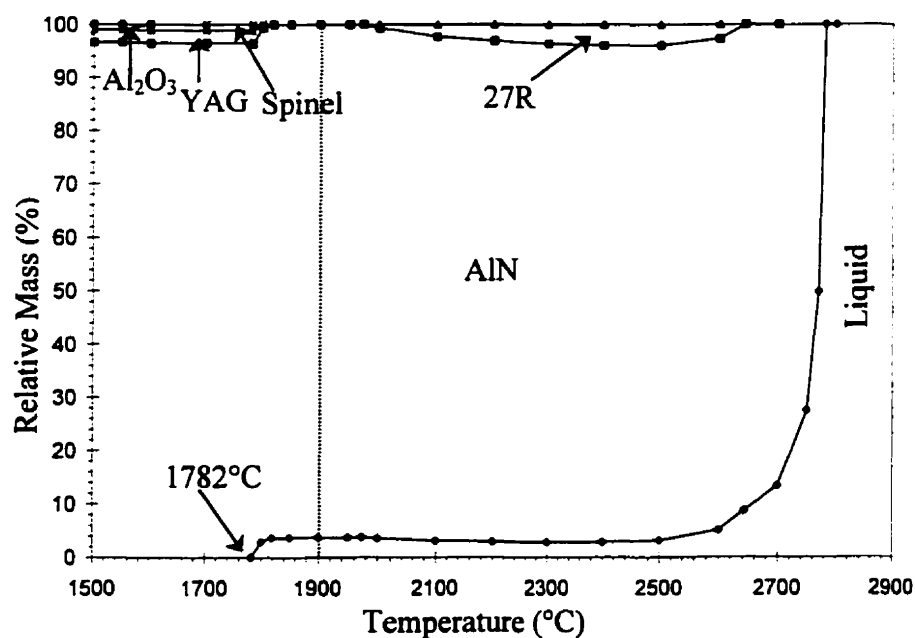


Figure 6-17: Predicted phase assemblage of composition I.

Figure 6-17 shows, that at room temperature, composition I is composed of 96.64 wt% AlN with 2.38 wt% YAG and 0.976 wt% Al_2O_3 . The X-ray diffraction analysis at room temperature in Figure 6-16(a) showed peaks for AlN and YAG phases only. Al_2O_3 peaks were not detected because the amount of residual Al_2O_3 is very small and below

the detection limit of the equipment. Moreover, Al_2O_3 occurs as a surface layer on AlN grains. Because of this surface layer and residual spinel, thermal conductivity is very low for this sample, as can be seen in Figure 6-21. This means that the amount of added Y_2O_3 was insufficient to fully react with residual Al_2O_3 and to purify the AlN and to complete the oxygen removal from both the lattice and the surface.

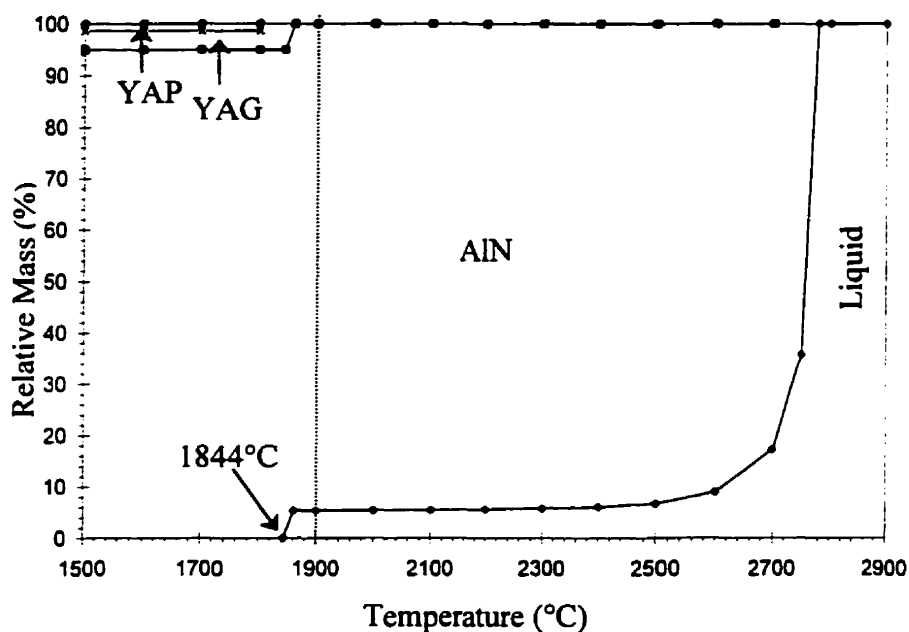


Figure 6-18: Phase assemblage of composition II.

Figure 6-18 shows that the room temperature composition II consists of 94.96 wt% AlN , 3.65 wt% YAG and 1.39 wt% YAP . In this sample there is more YAG than YAP at room temperature. This agrees with the X-ray pattern shown in Figure 6-16(b) where YAG peaks are stronger than those of YAP phase.

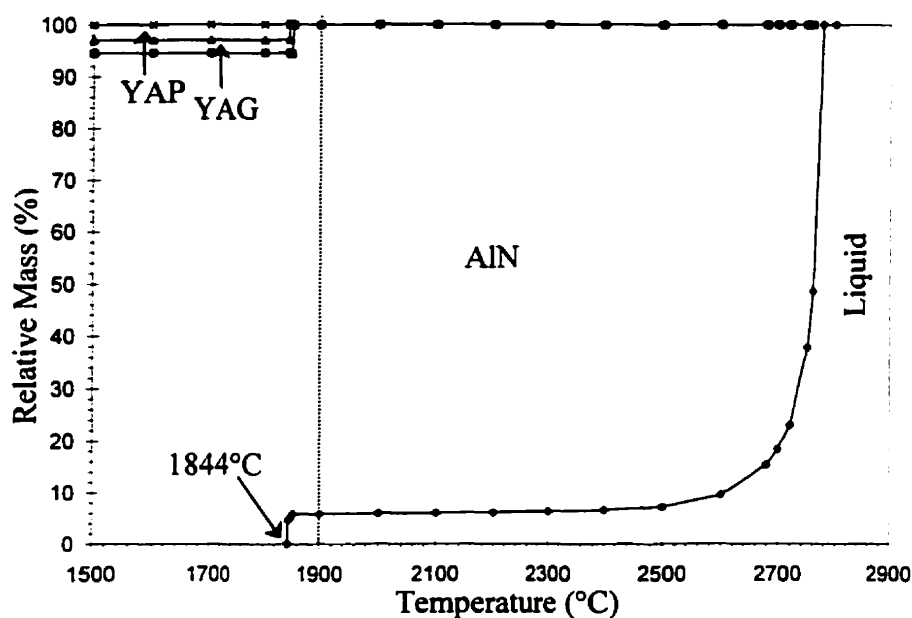


Figure 6-19: Phase assemblage of composition III.

Figure 6-19 indicates that composition III has a similar phase assemblage to composition II with a difference in the relative amount of each phase. At room temperature composition III consists of 94.53 wt% AlN, 2.52 wt% YAG and 2.95 wt% YAP. This corresponds well with the X-ray pattern for this sample shown in Figure 6-16(c).

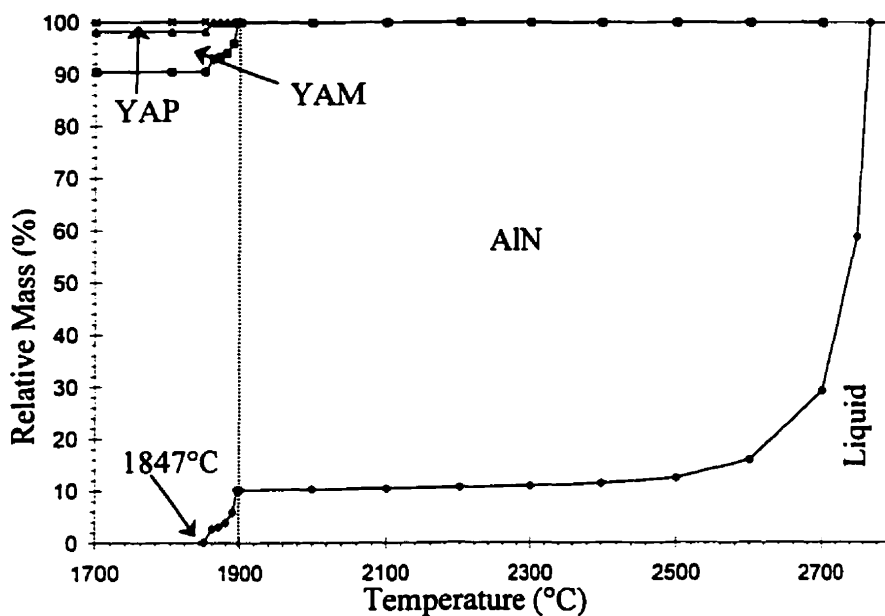


Figure 6-20: Phase assemblage of composition IV.

Figure 6-20 shows the phase assemblage for composition IV and at room temperature this sample is composed of 90.41 wt% AlN, 7.75 wt% YAM and 1.84 wt% YAP. This sample has more YAM than YAP, which agrees with Figure 5-16(d), where the diffraction peaks for YAM were stronger than for YAP.

Figure 6-21 is taken from reference [19]. It shows the trend in thermal conductivity for the four compositions along with their relative densities. Compositions II, III and IV have higher thermal conductivity than composition I because the oxide layer was completely reacted and consumed to produce YAG, YAP and YAM as secondary phases.

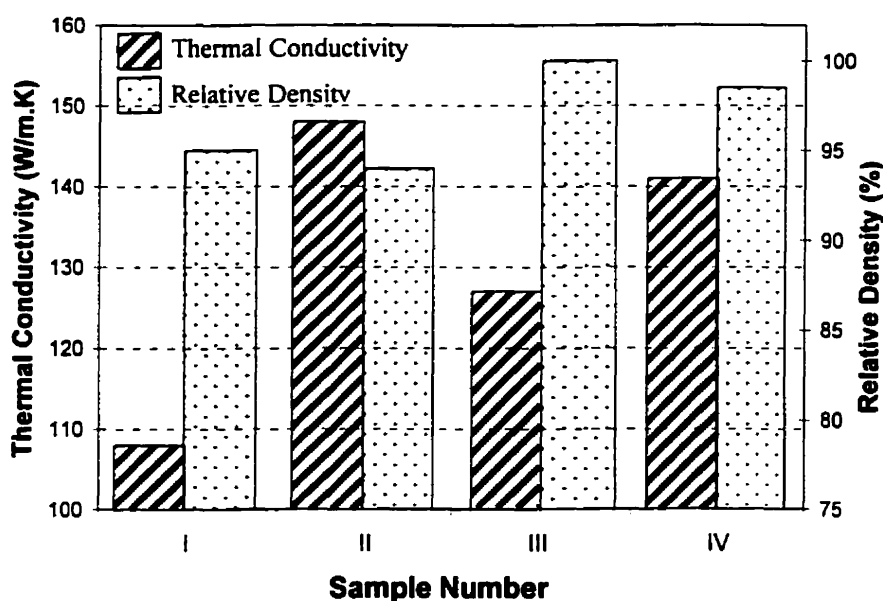


Figure 6-21: Variation in thermal conductivity with composition.

It was shown by the experimental work of Medraj *et al.* [107] that YAP wets the surface of AlN. Hence the presence of YAP phase will prevent the AlN-AlN surface contact. For this reason the thermal conductivity of the above samples varies according to the amount of YAP phase. As discussed above, compositions II, III and IV have 1.39, 2.95 and 1.84 wt% YAP, respectively, and the corresponding values of thermal conductivity, according to [19], are 148, 127 and 141 W/m.K, respectively. So higher YAP content is associated with lower thermal conductivity.

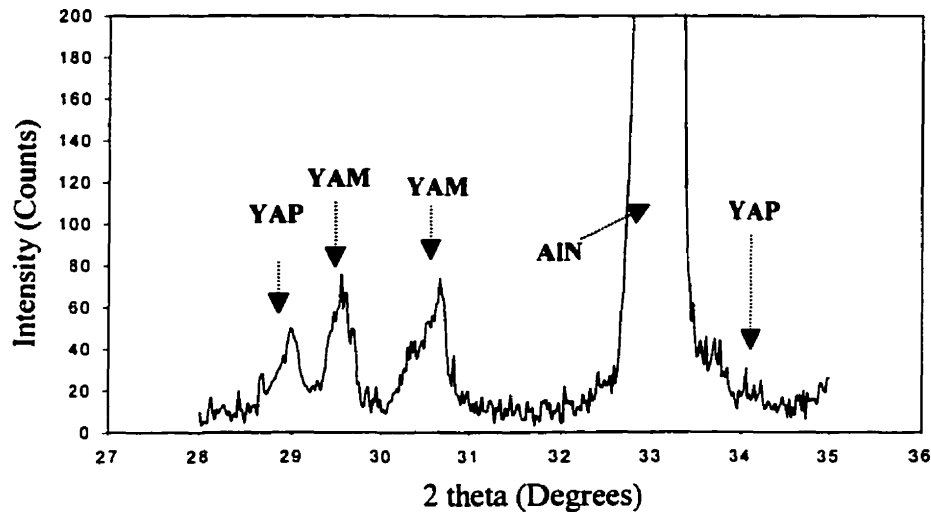


Figure 6-22: X-ray diffractogram of 5 wt% Y_2O_3 -added AlN sample sintered at 1900°C for 1 h [108].

Figure 6-22 shows X-ray patterns of AlN sample containing 5 wt% Y_2O_3 sintered at 1900°C for 1 h. Thermodynamic calculations for this sample are shown in the phase assemblage diagram (Figure 6-23).

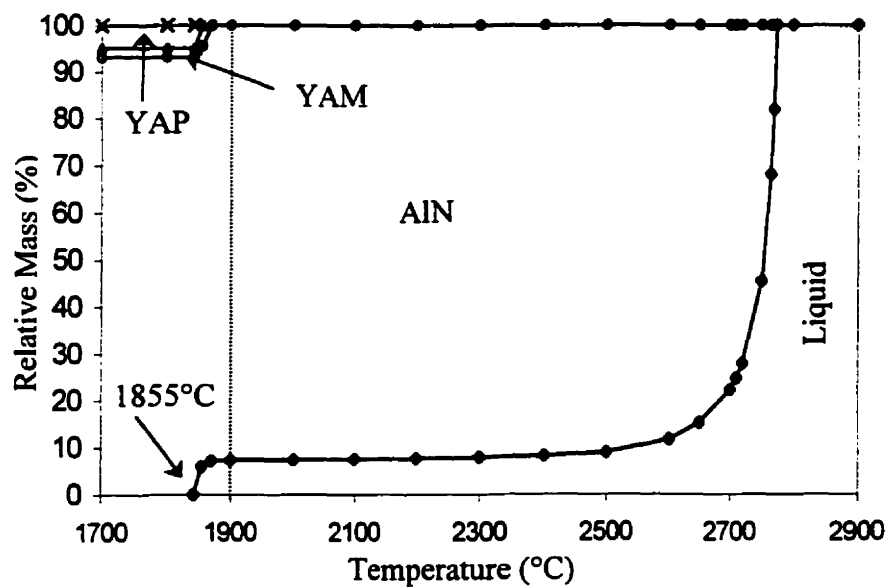


Figure 6-23: Phase assemblage of 5 wt% Y_2O_3 -added AlN sample.

Figure 6-23 shows that liquid starts forming at 1855°C for this sample and the phase composition at room temperature is AlN in addition to YAP and YAM as secondary phases. This agrees with the diffraction pattern of this sample shown in Figure 6-22.

In a very recent study Asai and Tkahashi [110] studied sintering of AlN with Y_2O_3 and CaO additives. They used 4 wt% Y_2O_3 and sintered it at 1800°C for 3 h in a nitrogen atmosphere. The room temperature X-ray diffraction pattern for this sample is shown in Figure 6-24. It can be seen that the grain boundary secondary phases are YAP and YAG.

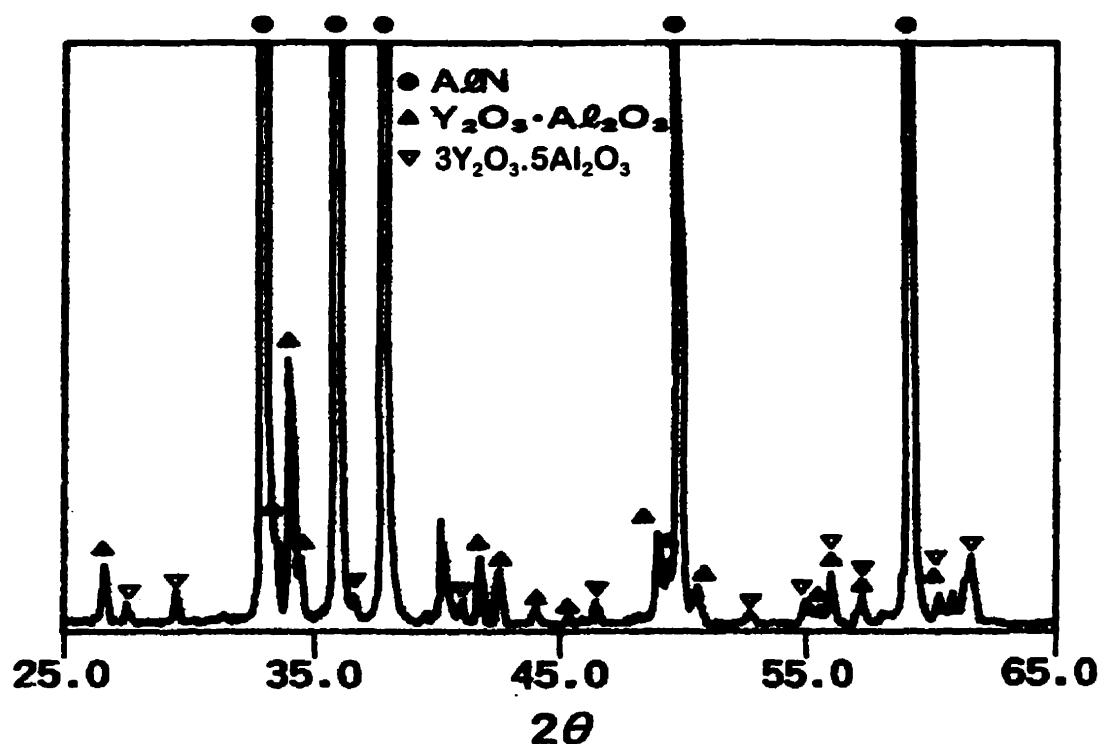


Figure 6-24: X-ray diffraction pattern of 4 wt% Y_2O_3 -added AlN sample sintered at 1800°C for 3 h.

The phase assemblage diagram for this sample is shown in Figure 6-25. It can be seen that at room temperature, 100 gm of overall material is composed of 94 g AlN, 4.871g YAP and 1.129 g YAG. This is consistent with the X-ray diffraction pattern in Figure 6-24, where YAP peaks are stronger than those of YAG. It can also be seen that even though the liquid starts forming at 1840°C for this sample, sintering at 1800°C for 3 h was enough to reach equilibrium for this sample.

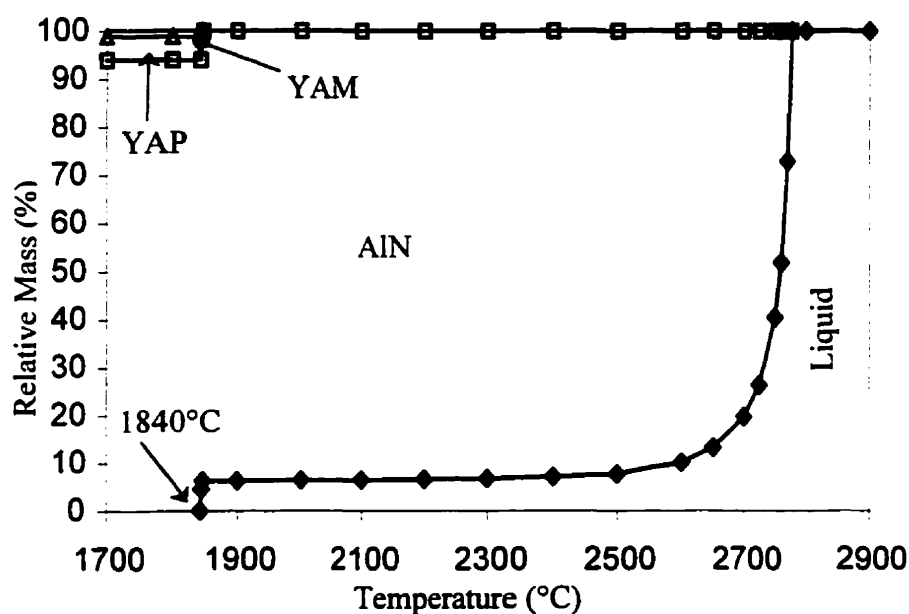


Figure 6-25: Phase assemblage of 4 wt% Y_2O_3 -added AlN sample.

Chapter 7:

MATERIALS, EQUIPMENT AND PROCEDURES

7.1 Materials

7.1.1 *AlN powder*

Only recently have high-purity, pretreated water-resistant AlN powders become available commercially [11]. AlN grade F supplied by Tokuyama Soda, Japan was used in this research. The impurities and their concentrations for this powder as received from Tokuyama Soda are shown in Table 7-1.

Table 7-1: Chemical analysis of AlN powder.

Impurity	Concentration
Oxygen	<0.9 wt%
Carbon	<400 ppm
Ca	<60 ppm
Fe	<10 ppm
Si	<15 ppm

The powder had a mean particle size of 0.3 μm and a specific surface area of 3.3 m^2/g . An SEM micrograph of the as received AlN powder is shown in Figure 7-1 and

shows that the particle size is consistent with manufacturing specifications. The particle shape is an equiaxed/spherical morphology.

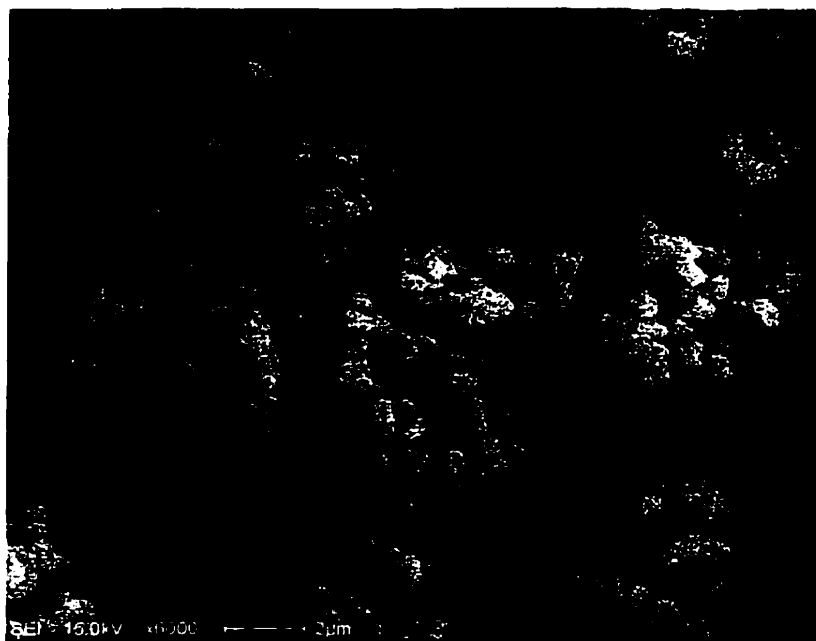


Figure 7-1: SEM micrograph of as received AlN powder.

7.1.2 Al_2O_3 powder

Aluminum oxide powder, A16-SG, with 99.8% purity was used. This powder was supplied by Alcoa Industrial Chemical Division. The chemical composition supplied by Alcoa is shown in Table 7-2. An SEM micrograph of the as received Al_2O_3 powder is shown in Figure 7-2. It can be seen that this powder had a wide size distribution. Figure 7-2(b) shows large Al_2O_3 particles containing fine agglomerates on the surface.

Table 7-2: Chemical analysis of Al_2O_3 powder.

Compound	Concentration
Al_2O_3	99.8
Na_2O	0.06
SiO_2	0.03
Fe_2O_3	0.02
CaO	0.03
B_2O_3	<0.003

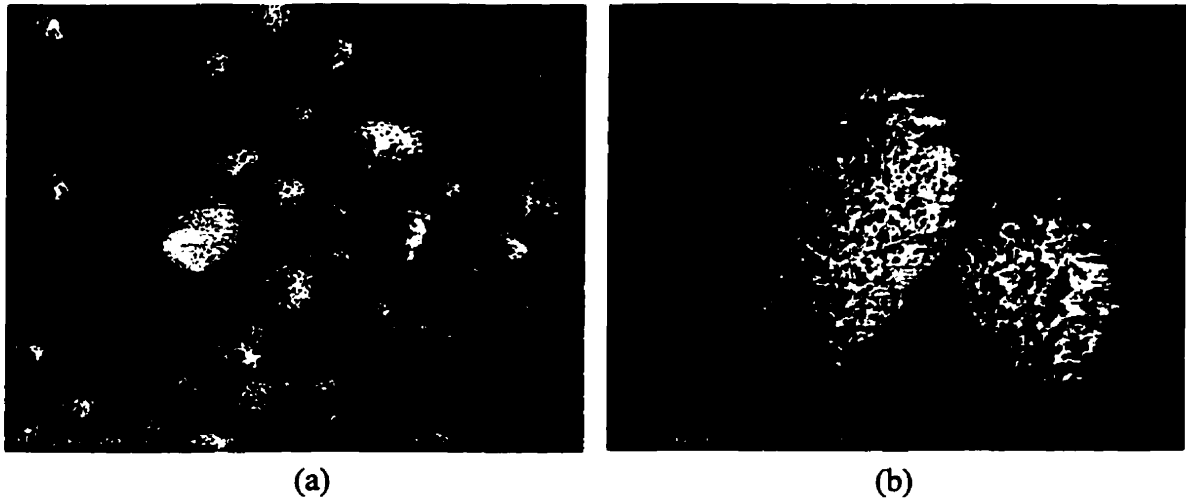


Figure 7-2: SEM micrograph of Al_2O_3 powder (a) x500 and (b) x2500.

7.1.3 Y_2O_3 Powder

Yttrium Oxide powder, Grade 5630X, supplied by Union Molycorp, U.S.A., with 99.99 purity, was used. The Y_2O_3 powder had a mean agglomerate size of $1.8\mu\text{m}$ and specific surface area of $33\text{ m}^2/\text{g}$. The chemical composition supplied by Union Molycorp of this powder is shown in Table 7-3. An SEM micrograph of the as received powder is shown in Figure 7-3. Given the particle size and the surface area, this powder clearly has a porous morphology.

Table 7-3: Chemical composition of Y_2O_3 powder.

Compound	Concentration
Y_2O_3	99.99%
CaO	< 2 ppm
SiO_2	< 25 ppm
Fe_2O_3	< 1 ppm
Na_2O	< 1 ppm
La_2O_3	2 ppm
NdO_3	4 ppm
Dy_2O_3	2 ppm
CeO_2	<1 ppm

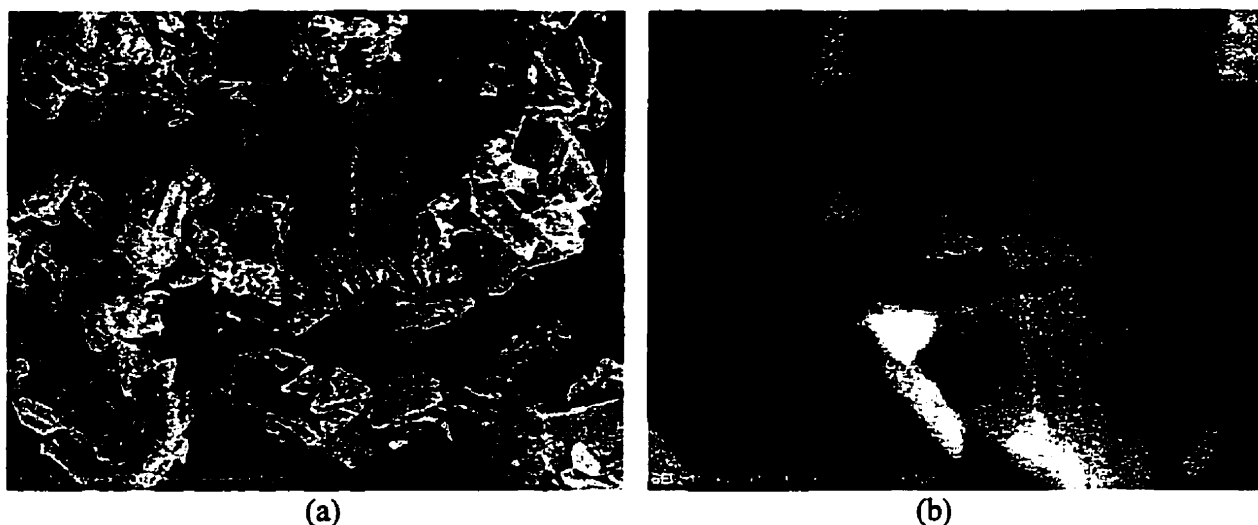


Figure 7-3: SEM micrograph of as received Y_2O_3 powder (a) x3300 (b) x17000.

7.2 Equipment

7.2.1 X-ray diffractometry

X-ray diffraction was conducted using an APD 1700, Philips, X-ray diffractometer. A schematic diagram is shown in Figure 7-4. It can be seen that this instrument consists of three basic parts: a source of X-ray radiation, specimen and the detector and counting equipment. This machine uses filtered $CuK\alpha$ radiation, at an accelerating voltage of 40 kV ($\pm 0.1\%$) and a beam current of 20 mA ($\pm 0.1\%$). The intensity and 2θ data were acquired and stored using a personal computer.

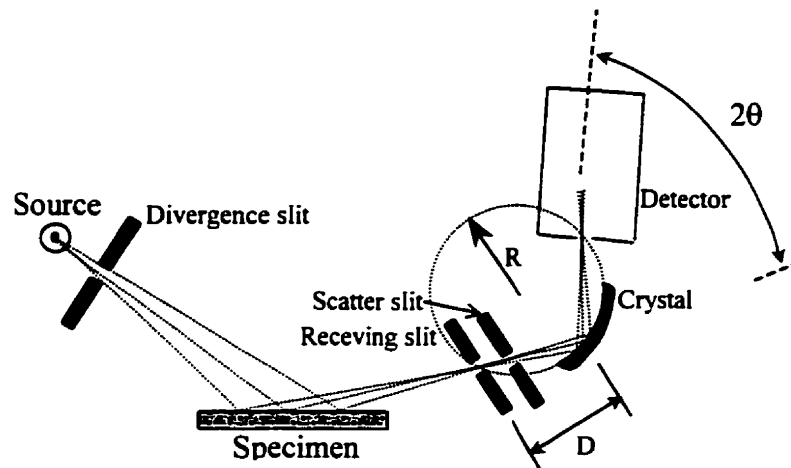


Figure 7-4: X-ray Diffractometer configuration.

Each component wavelength of a polychromatic beam of radiation falling onto a single crystal will be diffracted at a discrete angle, in accordance with Bragg's law. For powder diffractometry one needs monochromatic X-rays. The best way to achieve this is with a monochromator, which selects, by diffraction at a single crystal, one wavelength or a small wavelength band, like an analyzing crystal in a spectrometer. There are many physical forms of the crystal monochromator but among the most commonly used in powder diffractometry is the Johann type in the configuration shown in Figure 7-4. Here the crystal monochromator is placed between the specimen and the detector. The monochromator must be curved (focusing), see Figure 7-4. The incident and take-off angles in addition to the distance D , are adjusted to give the correct θ value for the d of the crystal, such that only the required wavelength can enter the detector [111,112].

7.2.2 Neutron Diffractometer

The major advantage of neutron diffraction compared to other diffraction techniques is the extraordinarily penetrating nature of the neutron, which leads to its use in measurements under special environments [83].

To determine the phase evolution in the $\text{AlN-Al}_2\text{O}_3\text{-Y}_2\text{O}_3$ system, neutron diffraction patterns were monitored *in situ* at elevated temperature using the DUALSPEC high-resolution powder diffractometer, C2, at the NRU reactor of Atomic Energy of Canada Limited (AECL), Chalk River Laboratories.

The diffractometer, shown in Figure 7-5, is an 800-channel position sensitive detector that spans 80° in scattering angle, 2θ . The wavelength, λ , of the neutron beam was calibrated by measuring the diffraction pattern of a standard powder of alumina, obtained from the National Institute of Standards and Technology. In this study, $\lambda=1.33(1) \text{ \AA}$, 2θ range of 8° to 88° and no collimation, was used.

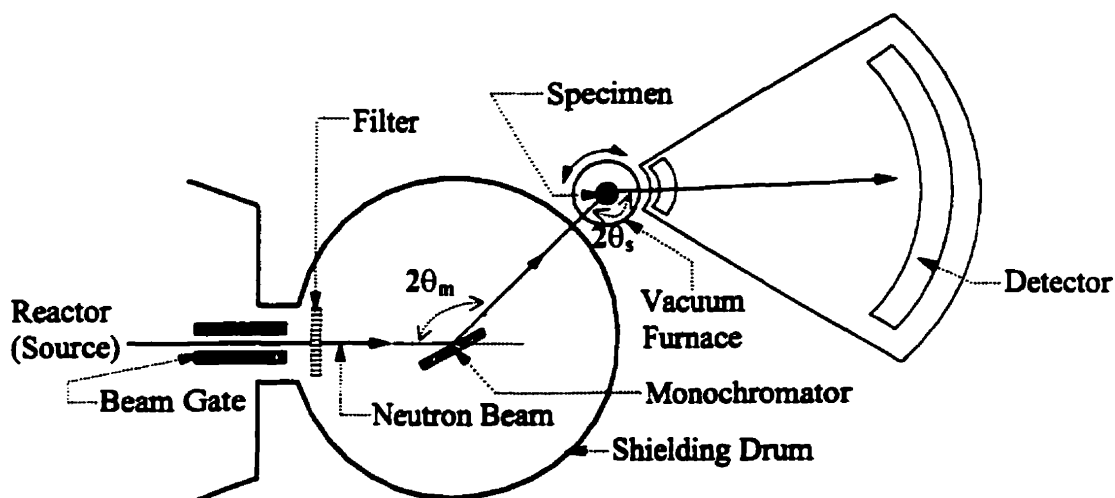


Figure 7-5: Neutron Diffractometer, C2, Chalk River Laboratories, $2\theta_m$: Scattering from monochromatic to select wavelength, $2\theta_s$: Scattering from sample.

The diffractometer was equipped with a tantalum-element vacuum furnace, (Figures 7-6 and 7-7) capable of reaching temperatures as high as 2000°C . The furnace programming and data acquisition system were fully computerized, allowing accurate temperature control and rapid data collection.

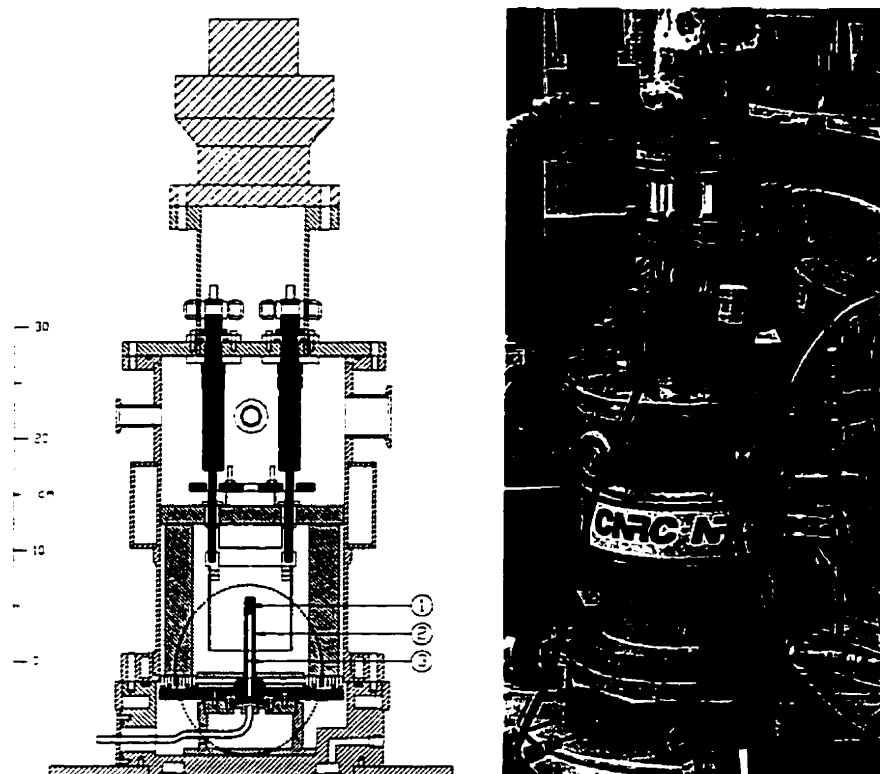


Figure 7-6: High temperature vacuum furnace, Chalk River Laboratories.

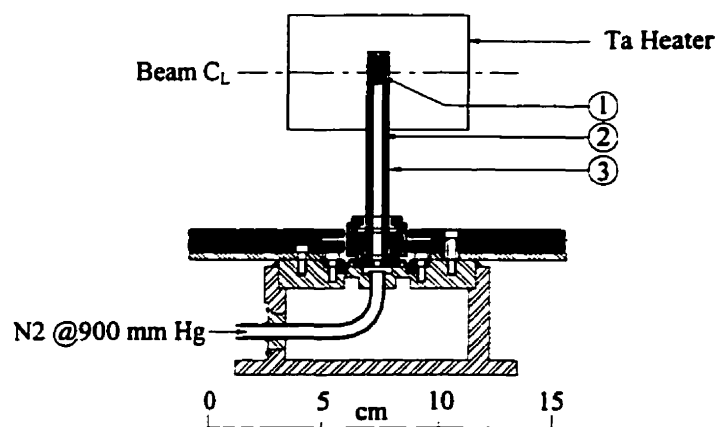


Figure 7-7: Detailed drawing of the circled parts in Figure 7-6; (1) sample capsule, (2) molybdenum sample support and (3) molybdenum pencil tube.

7.3 Experimental Procedures

The sintering behavior and the quality of the ceramic body are greatly influenced by the quality of the starting powder [49]. Fine unagglomerated powders with narrow size distribution, possessing the required chemical and phase purity were ensured throughout the course of the experimental work in this research.

7.3.1 X-ray diffraction experiments

The overall experimental approach of the X-ray diffraction experiments is summarized in the following flowchart.

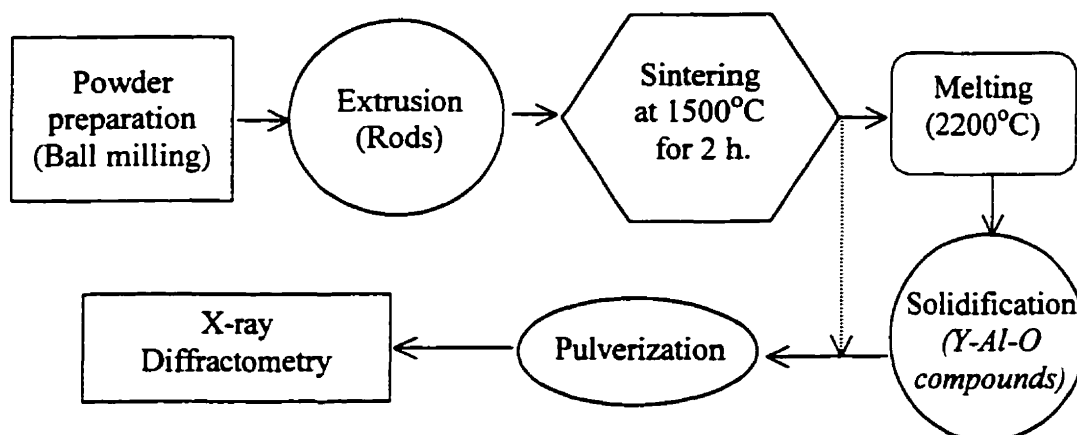


Figure 7-8: Flow diagram showing X-ray diffraction experimental procedure.

Nine different compositions were prepared using the stoichiometric ratios shown in Table 7-4 and Figure 7-9, in order to evaluate the calculated Al_2O_3 - Y_2O_3 phase diagram experimentally and determine the phase relations and reactions.

Table 7-4: Chemical composition and the expected phases of the studied samples.

Sample No.	Al_2O_3 mol%(wt%)	Composition
1	29% (15.57%)	E4
2	33.33% (18.42%)	YAM
3	43% (25.41%)	E3
4	50% (31.11%)	YAP
5	57.5% (37.92%)	E2
6	62.5% (42.94%)	YAG
7	70% (51.3%)	hypo E1
8	79% (62.94%)	E1
9	90% (80.25%)	hyper E1

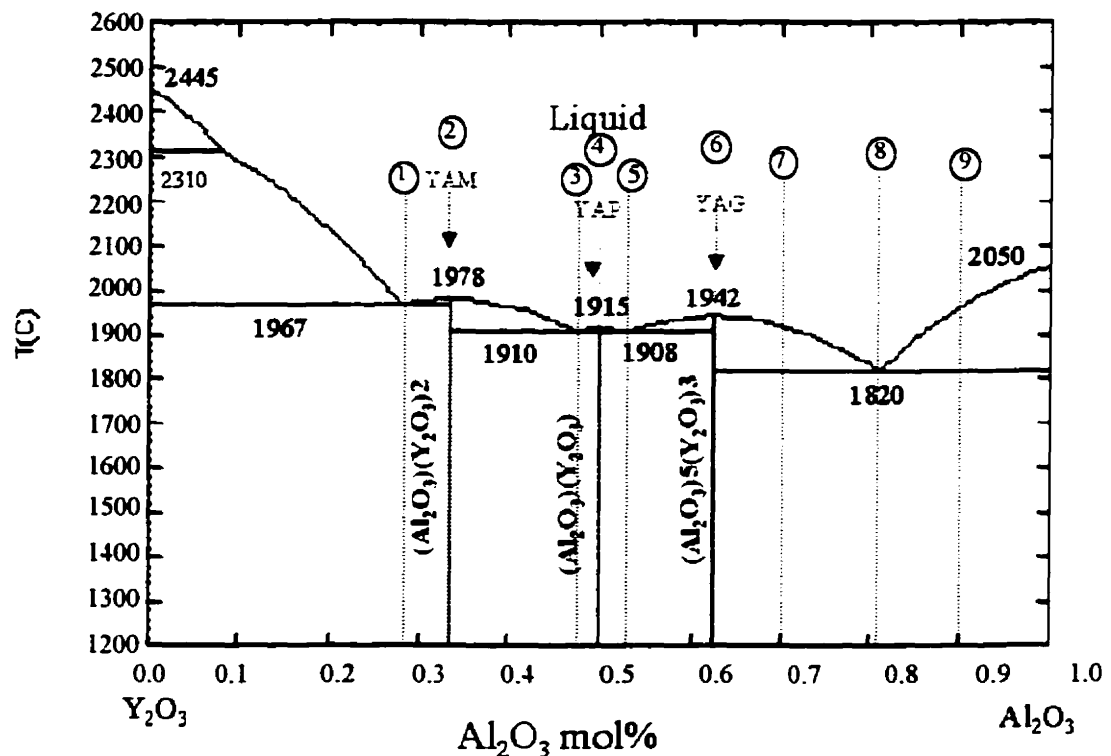


Figure 7-9: Calculated Al_2O_3 - Y_2O_3 phase diagram and the nine different compositions.

The premixed stoichiometric compositions were ball milled for 1 h using 4 mm alumina media and water. The resultant slurry was dried in a microwave oven to completely remove the water and then sieved to obtain a fine powder mixture. This powder was then mixed with water and 8 wt% of hydroxypropyl cellulose as a plasticizer and the mixture was extruded into 2.5 mm diameter rods. These rods were dried in air for 24 h, then sintered in air for 2 h at 1500°C at a heating rate of 10°C/min using a silicon carbide element, Blue M furnace. The rods were melted to form droplets at 2200°C using an oxyacetylene torch. The chemical analysis of Aguilar *et. al* [113] showed that there is no contamination or weight loss by using this technique for the melt extraction of Al_2O_3 - Y_2O_3 fibers.

The phase development was investigated using X-ray diffractometry, described in section 6-2-1. One of the sintered rods and a few droplets from each composition were

crushed individually into powder in order to determine the reaction at different stages. X-ray diffraction spectra were collected for the different samples at room temperature, after sintering at 1500°C and for the solidified droplets after melting with a scanning rate of 0.02 °/sec. The starting mixed powders and the resultant phases in the sintered rods and in the melted samples were identified using JCPDS-XRD patterns available in the database of the computer attached to the diffractometer.

7.3.2 Neutron diffraction experiments

AlN, Y₂O₃ and Al₂O₃ powders were mixed in various stoichiometric amounts. Table 7-5 and Figure 7-10 show the composition of these samples. The premixed compositions were ball milled in a plastic container for 24 h using 4 mm diameter Al₂O₃ media and reagent grade isopropanol with a solid to liquid ratio of 1:5, by volume.

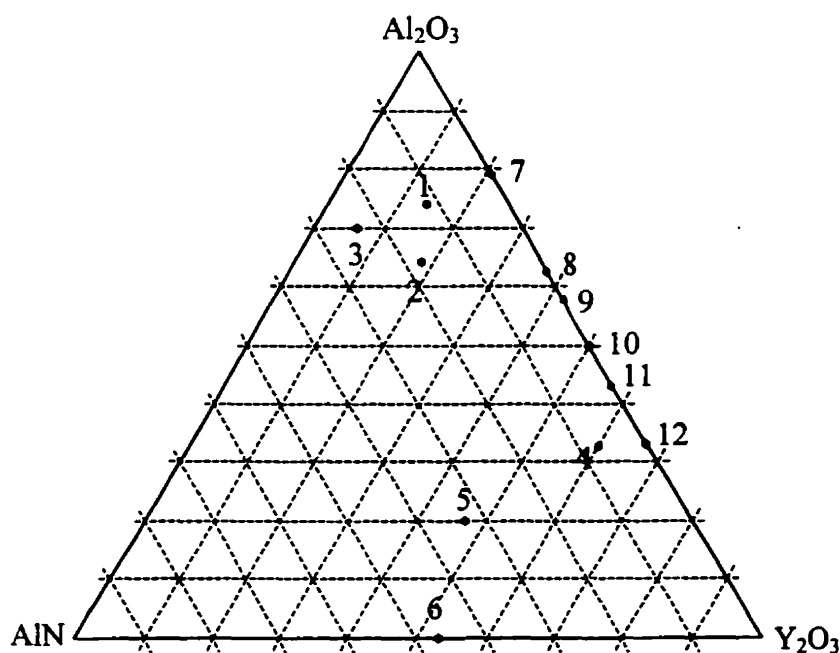


Figure 7-10: AlN-Al₂O₃-Y₂O₃ composition triangle with samples studied by neutron diffraction.

The mixtures were dried in a microwave oven to completely remove the isopropanol. After drying, the mixtures were granulated through a 60 µm mesh sieve.

Table 7-5: Chemical composition of the samples studied by neutron diffractometry.

Sample No.	AlN mol% (wt%)	Y ₂ O ₃ mol% (wt%)	Al ₂ O ₃ mol% (wt%)
1.	12 (4.392)	14 (28.23)	74 (67.377)
2.	17.5 (6.281)	18.5 (36.579)	64 (57.140)
3.	24 (10.381)	6 (14.298)	70 (75.32)
4.	7 (1.668)	60 (78.77)	33 (19.562)
5.	33 (9.737)	47 (75.781)	20 (14.444)
6.	47 (13.865)	53 (86.135)	0
7.	0	21 (37.06)	79 (62.94)
8.	0	37.5 (57.06)	62.5 (42.94)
9.	0	42.5 (62.077)	57.5 (37.923)
10.	0	50 (68.89)	50 (31.11)
11.	0	57 (74.59)	43 (25.41)
12.	0	66.67 (81.58)	33.33 (18.42)

A portion of each composition was encapsulated in molybdenum foil to prevent the powder from spreading in the sample chamber upon evacuating, and to protect the apparatus when the sample melts, Figure 7-11.

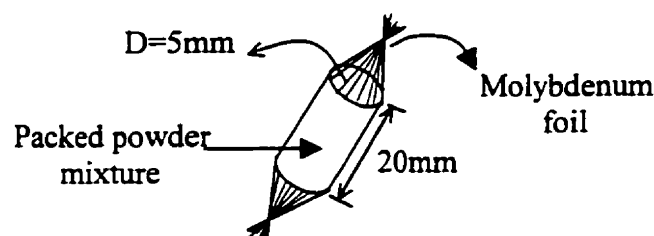


Figure 7-11: Sealed Mo container used to conduct the neutron diffraction experiments at high temperature.

After centering the furnace in the beam of the neutron diffractometer, the sample capsule was placed inside a molybdenum pencil tube, which is inside the furnace chamber. The aluminum furnace chamber was sealed, and the volume between the molybdenum tube and inside of the furnace chamber was evacuated to 10^{-8} atmosphere. A neutron diffraction spectrum for each sample was collected at room temperature to form the reference for any reactions taking place upon heating. AlN containing samples were heated while flowing nitrogen gas into the Mo pencil to prevent the decomposition

of AlN, whereas samples containing no AlN were heated with argon gas in the Mo pencil. According to the recent study of D'yachkov *et al.*, suppression of the dissociation of AlN and melting it is possible in a nitrogen pressure close to the atmospheric pressure [104].

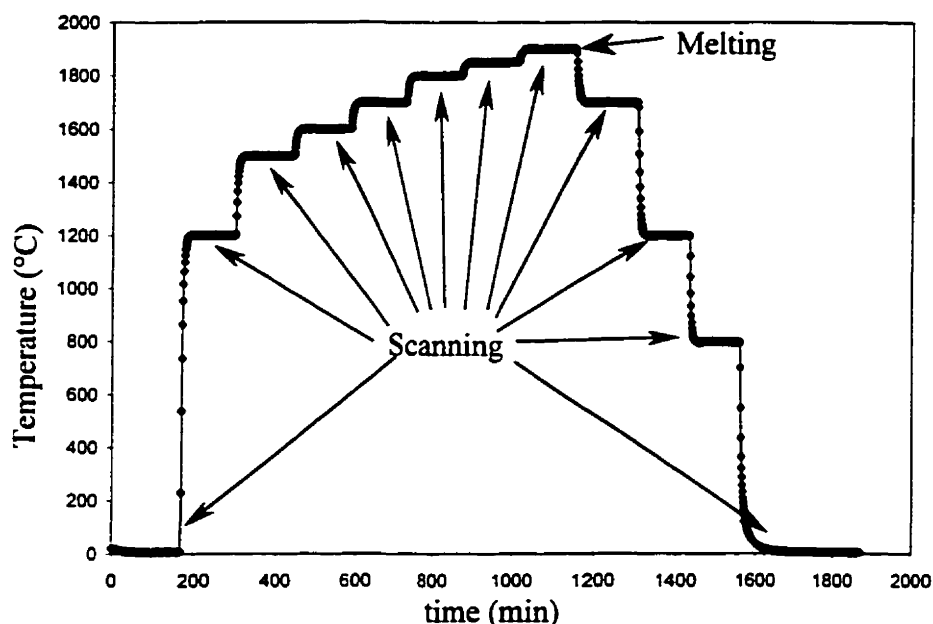


Figure 7-12: Heating and cooling cycle for neutron diffraction experiments.

The sample was observed *in situ* during heating and cooling as shown in Figure 7-12. Neutron diffraction spectra were collected at incremental intervals until the spectra displayed a loss of crystallinity (melting) or reached the maximum temperature of the apparatus (2000°C). Then cooling started and neutron spectra were collected at incremental cooling temperatures to observe the precipitation of crystalline phases.

Chapter 8:

PHASE EVOLUTION IN Al_2O_3 - Y_2O_3 AND AlN - Y_2O_3 SYSTEMS

In this chapter, the experimental results of Al_2O_3 - Y_2O_3 and AlN - Y_2O_3 systems will be discussed. Al_2O_3 - Y_2O_3 was investigated using room temperature X-ray and *in situ* high temperature neutron diffractometry. AlN - Y_2O_3 was studied using *in situ* high temperature neutron diffractometry. The experimental results will be compared with the thermodynamic findings in this chapter.

8.1 X-ray diffraction of Al_2O_3 - Y_2O_3 system

Experimental verification of the phase relationships, in Al_2O_3 - Y_2O_3 binary system, was performed using nine different Al_2O_3 - Y_2O_3 compositions, as shown in Figure 7-9. The phase relations in Al_2O_3 - Y_2O_3 system have been investigated at room temperature using powder X-ray diffraction for different stages of heat treatment. First it was carried out for the mixed starting powders in their stoichiometric ratio. This was done in order to have a baseline comparison to detect any change and phase development during the later stages of heat treatment. The patterns of the mixed powder are labeled with the letter (a) in the following diagrams.

Initially, a solid-state reaction of these powders was performed at 1500°C for 2 h. X-ray diffraction was conducted at room temperature and the patterns were labeled with the letter (b). However, it has been found that a solid-state reaction led to an incomplete

reaction. This indicated that a different experimental approach was required to bring about complete reaction, therefore, the samples were melted at $\sim 2200^\circ\text{C}$ using an oxyacetylene torch. The X-ray diffraction was performed on the crushed droplets for each composition and the resulting patterns were labeled with the letter (c). Aguilar *et. al* [113] used the same technique for the melt extraction of $\text{Al}_2\text{O}_3\text{-Y}_2\text{O}_3$ fibers. Their chemical analysis showed that there was no difference in the composition before and after extracting the fibers from the melt.

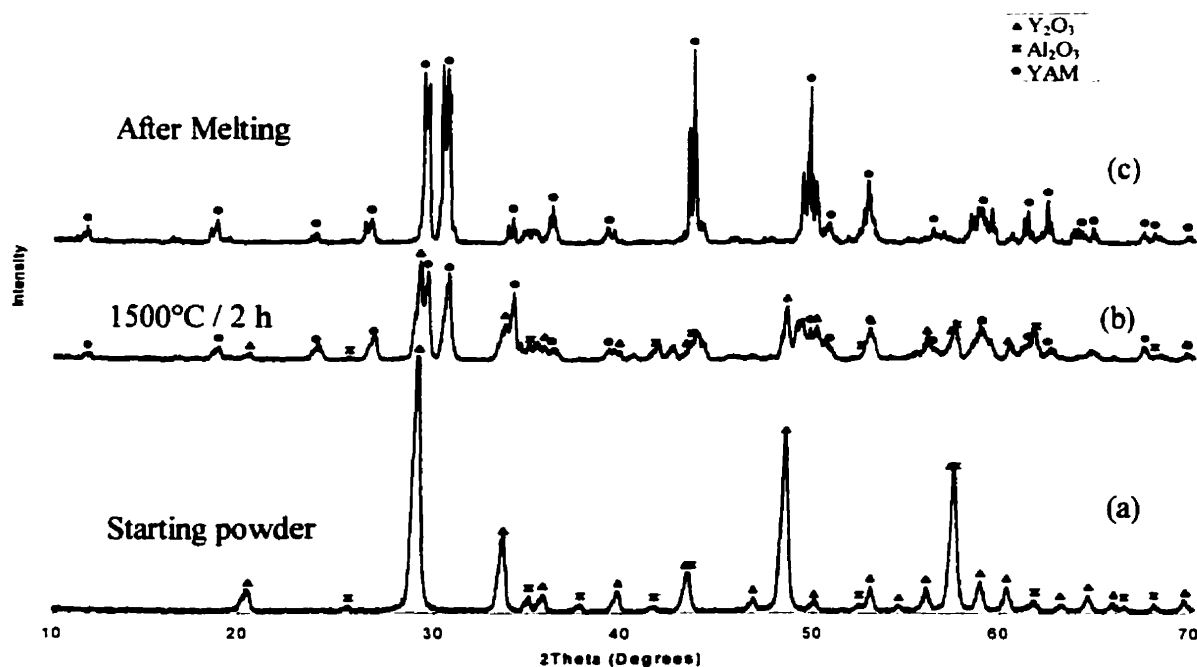


Figure 8-1: XRD patterns of sample 2 (YAM).

X-ray diffractograms of sample 2, (YAM composition) are shown in Figure 8-1, where Y_2O_3 peaks were indexed using JCPDS card 25-1200, Al_2O_3 peaks by JCPDS card 10-173 and Yttrium Aluminum Monoclinic (YAM) peaks by JCPDS card 34-368.

All the peaks in pattern (a) in Figure 8-1 are related to Y_2O_3 and Al_2O_3 . It can be seen that the high peaks are Y_2O_3 while the weaker ones correspond to Al_2O_3 . This is because X-rays interact with the electrons and yttrium has three times the number of

electrons of aluminum. The atomic number of yttrium is 39, whereas it is 13 for aluminum. The same trend was observed for all the other samples as shown in Figures 8-2 and 8-4 to 8-10.

Pattern (b) in Figure 8-1 shows peaks corresponding to Y_2O_3 and Al_2O_3 , as well as YAM, which is the expected phase according to the phase diagram. This indicates that reaction and formation of YAM takes place at 1500°C for 2 h but this reaction is incomplete. The same can be said for all the other compositions (i. e. patterns (b) show residual Al_2O_3 and Y_2O_3 for all the samples).

All the peaks in pattern (c) of Figure 8-1 correspond to the YAM phase without any residual reactants. This indicates that the starting powder reacted completely in the liquid state leading to the desired product being formed.

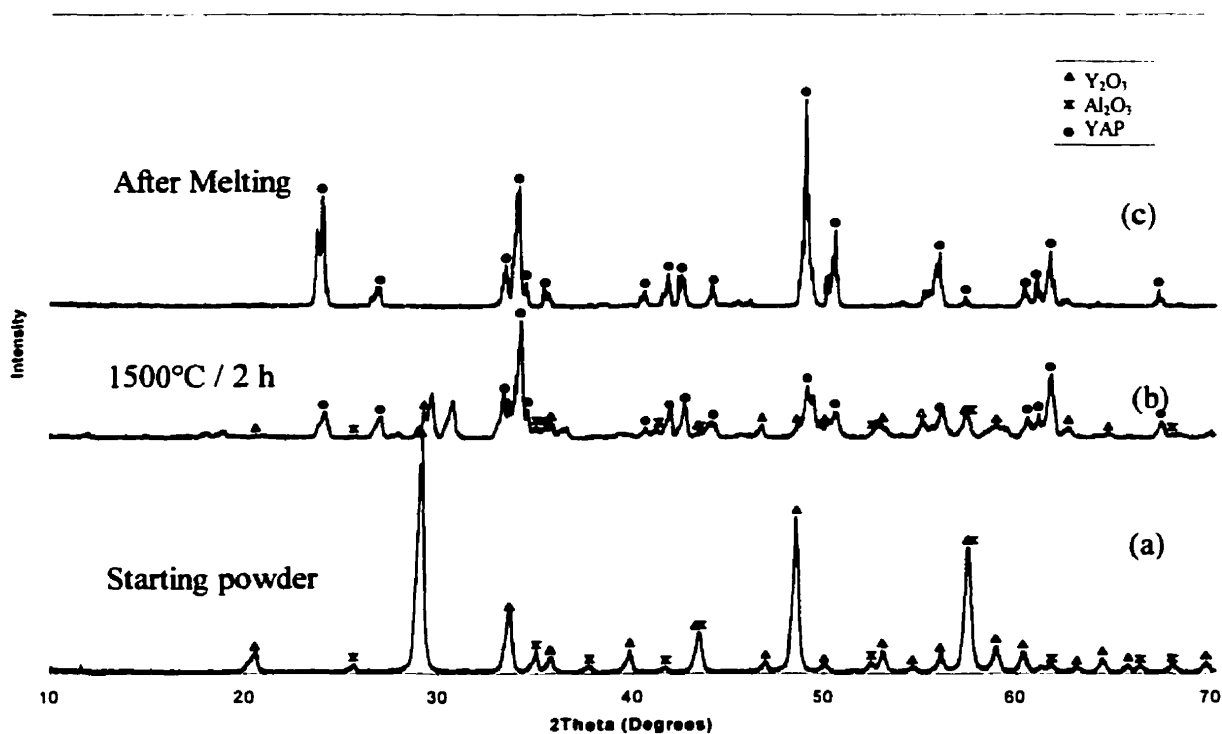


Figure 8-2: XRD patterns of sample 4 (YAP).

X-ray diffractograms of sample 4 (YAP composition) are shown in Figure 8-2, where yttrium aluminum perovskite (YAP) peaks were indexed by JCPDS card 33-41. This is the orthorhombic not the cubic structure mentioned in reference [50,114].

Pattern (c) of Figure 8-2 shows complete formation of YAP after melting. In order to observe stability and phase transformation of this compound, heat treatment of some droplets was done at 1550°C for 3 h. X-ray diffractograms of this compound before and after heat treatment are shown in Figure 8-3.

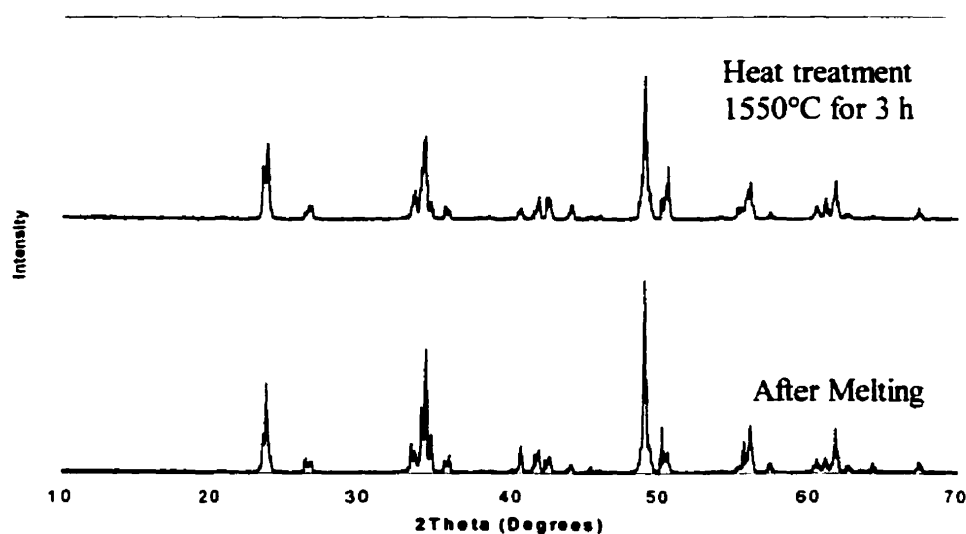


Figure 8-3: XRD patterns of YAP phase before and after heat treatment.

It can be clearly seen from Figure 8-3 that the two patterns belong to the same crystal structure. This means that orthorhombic YAP is stable at room temperature. Moreover pattern (c) of Figures 8-8 and 8-9, (representing E2 and E3 compositions) show orthorhombic YAP in conjunction with YAG and YAM, respectively, which is consistent with the phase diagram. This result is also supported by the neutron diffraction results as will be shown later in this chapter.

X-ray diffractograms of sample 6 (YAG composition) are shown in Figure 8-4, where yttrium aluminum garnet (YAG) peaks were indexed by JCPDS card 33-40.

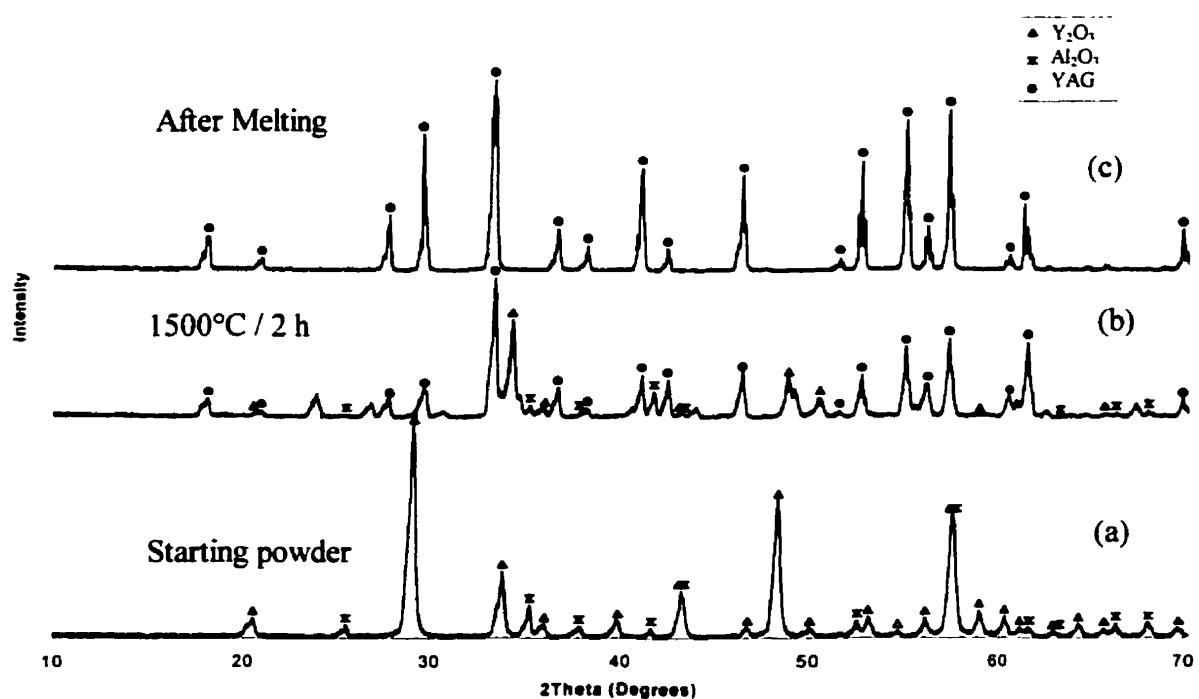


Figure 8-4: XRD patterns of sample 6 (YAG).

Pattern (b) in Figure 8-4 shows that not all the peaks are related to the YAG phase. This indicates that the formation of YAG starts at this temperature but the reaction is incomplete. However pattern (c) shows no residual reactants after melting.

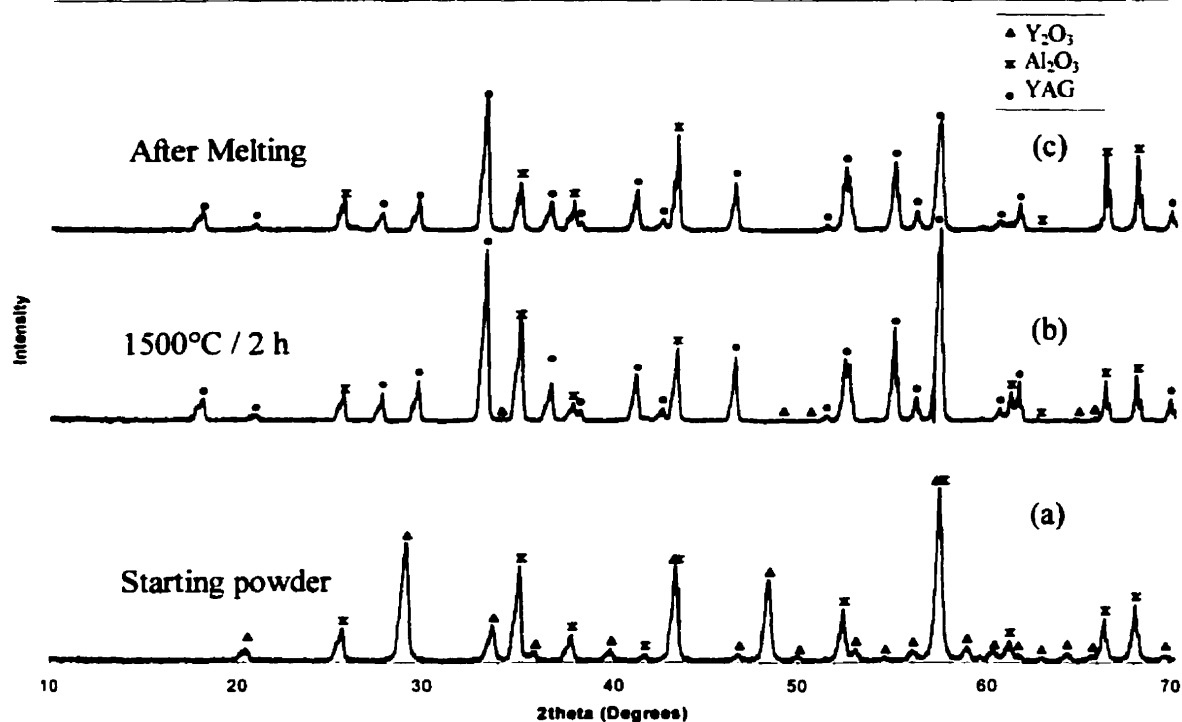


Figure 8-5: XRD patterns of sample 9 (hyper E1).

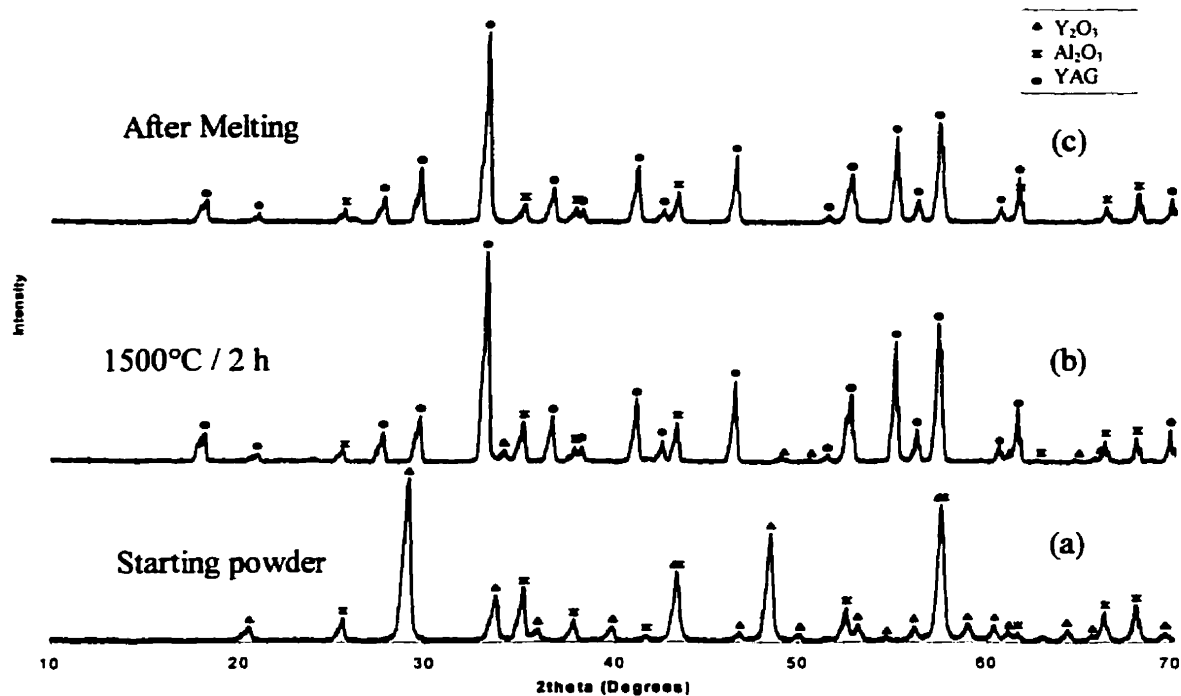


Figure 8-6: XRD patterns of sample 8 (E1).

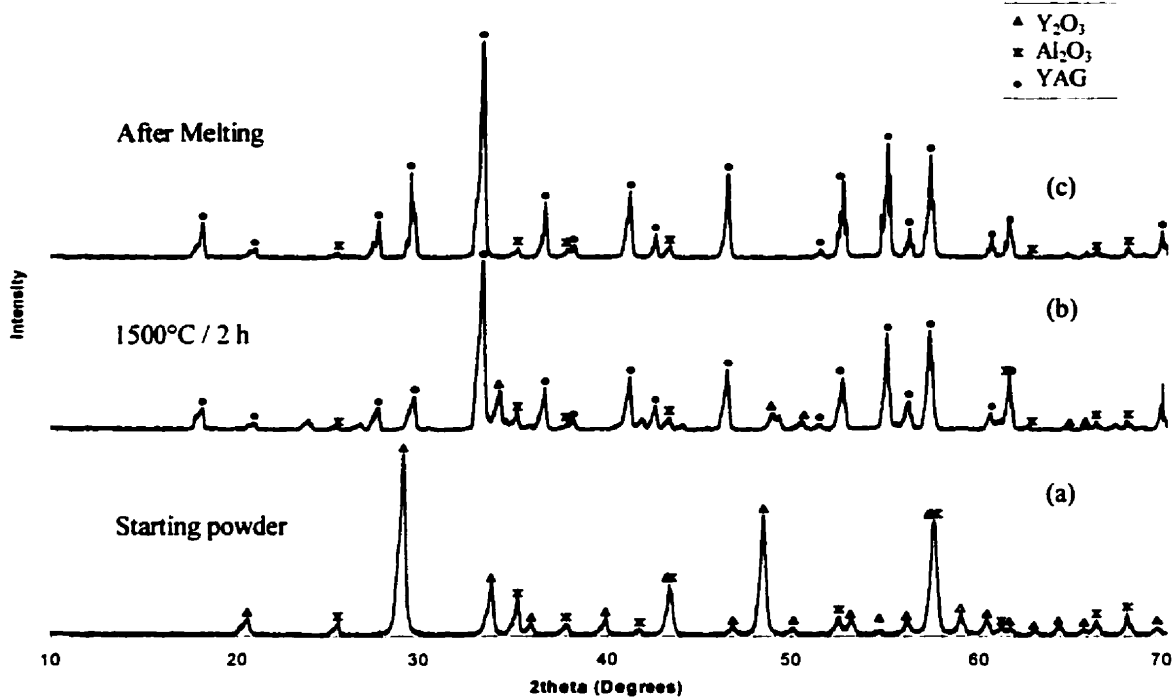


Figure 8-7: XRD patterns of sample 7 (hypo E1).

Figure 8-5 is for sample 9 (hyper E1 composition). Pattern (c) in this figure shows that YAG and Al_2O_3 are the stable phases after melting and solidification. The same thing can be said about Figures 8-6 and 8-7 (E1 and hypo E1, respectively) with differences in the relative intensities of YAG and Al_2O_3 peaks.

Comparing Figures 8-5 to 8-7 indicates that sample 9 has higher YAG peaks than both samples 8 and 7. Whereas, sample 8 has higher YAG peaks than those of sample 7. A reverse order for Al_2O_3 peaks can be observed for these three samples (i.e. sample 7 has the highest while sample 9 has the lowest relative intensity of Al_2O_3 peaks). These results obey the Lever Rule, exhibiting complete consistency with the calculated phase diagram (Figure 7-9).

Figure 8-8 revealed that sample 5, which represents the second eutectic point in the $\text{Al}_2\text{O}_3\text{-Y}_2\text{O}_3$ phase diagram, consists of YAG and YAP after melting. This is consistent with the calculated phase diagram (Figure 7-9).

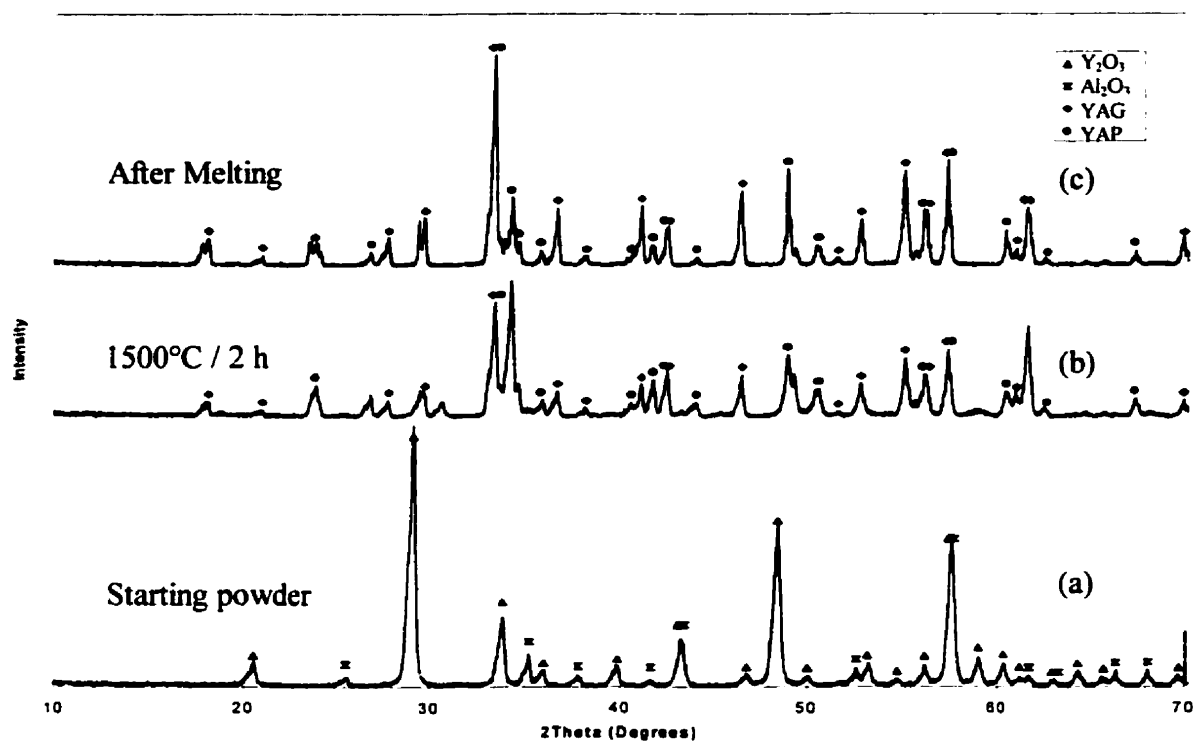


Figure 8-8: XRD patterns of sample 5 (E2).

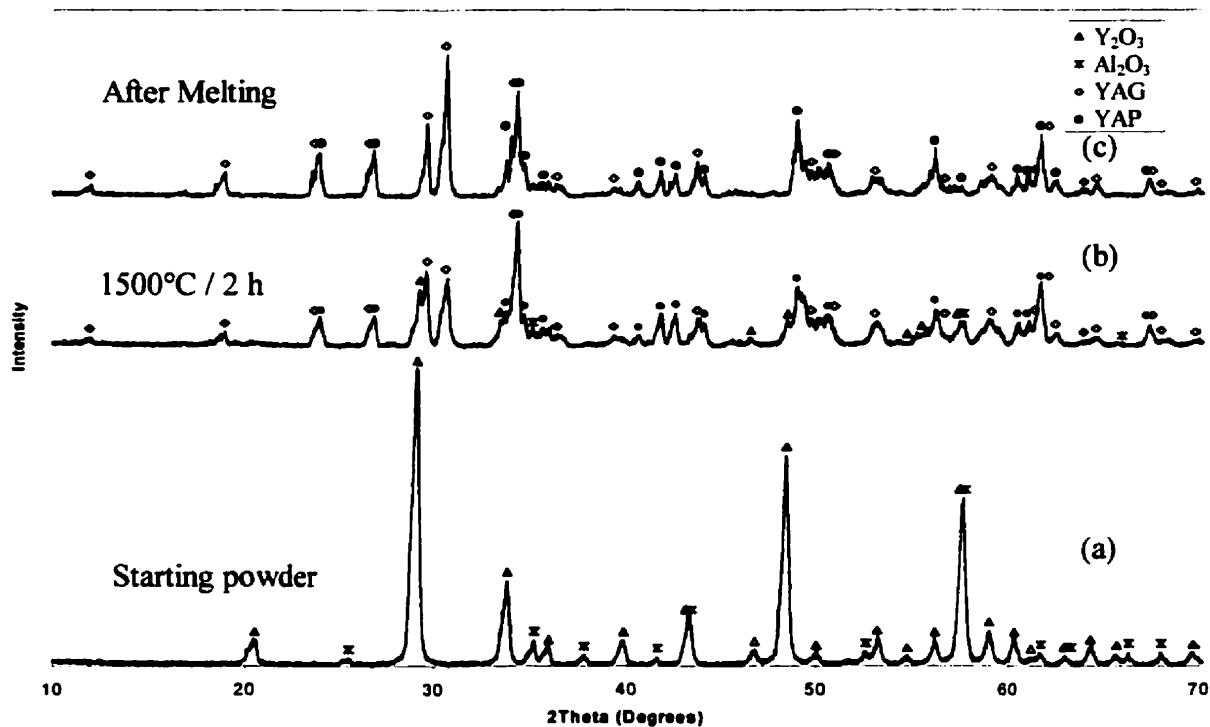


Figure 8-9: XRD patterns of sample 3 (E3).

Figure 8-9 is for the third eutectic point in $\text{Al}_2\text{O}_3\text{-Y}_2\text{O}_3$ system. Pattern (c) showed that complete reaction took place to produce YAP and YAM after melting. This is consistent with the $\text{Al}_2\text{O}_3\text{-Y}_2\text{O}_3$ calculated phase diagram.

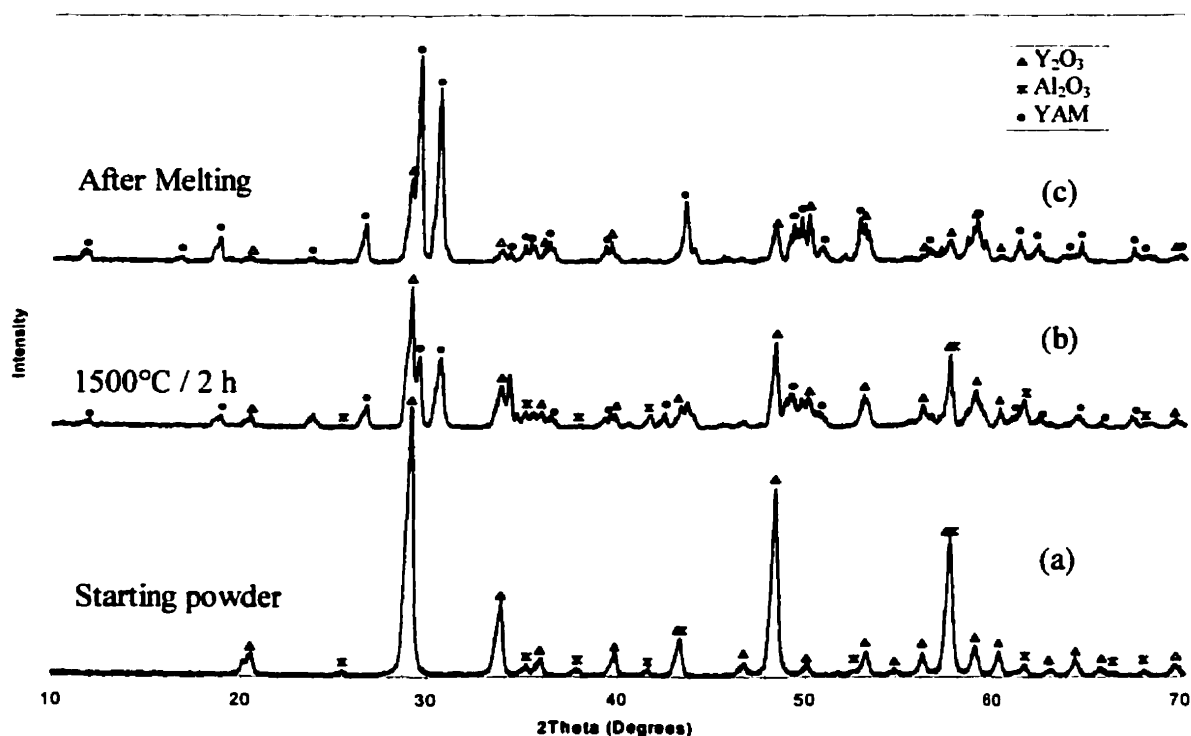


Figure 8-10: XRD patterns of sample 1 (E4).

Sample 1 is shown in Figure 8-10. Pattern (c) in this figure shows that YAM and Y_2O_3 are the stable phases after melting and solidification. This is again in complete agreement with the calculated phase diagram (Figure 7-9).

8.2 Neutron Diffraction Results

Unlike X-ray diffractometry, neutron diffractometers often use different wave lengths, λ . This implies that when neutron diffractometry is used for phase identification, a specific neutron diffraction pattern should be calculated for each phase in the system under investigation using the precise λ . In our case λ was $1.33(1)\text{\AA}$.

In order to calculate a neutron diffraction pattern, the crystal structure and the atoms positions in the unit cell must be known. The peak positions, 2θ , depend on the wavelength used and the lattice spacing, d , according to Bragg's law;

$$\sin 2\theta = \frac{\lambda}{2d} \quad \dots\dots\dots 8-1$$

Furthermore, any calculation of the intensity of a diffracted beam depends on the structure factor, which is determined by the arrangement of atoms within a unit cell. In other words the crystal structure and atom positions in the unit cell in addition to λ must be known in order to calculate a neutron diffraction pattern.

The calculation of the AlN neutron diffraction pattern will be demonstrated in this section, whereas, crystal structure description, lattice parameters, atoms positions in the unit cell and the corresponding calculated neutron diffraction pattern for the other phases are shown in appendix A.

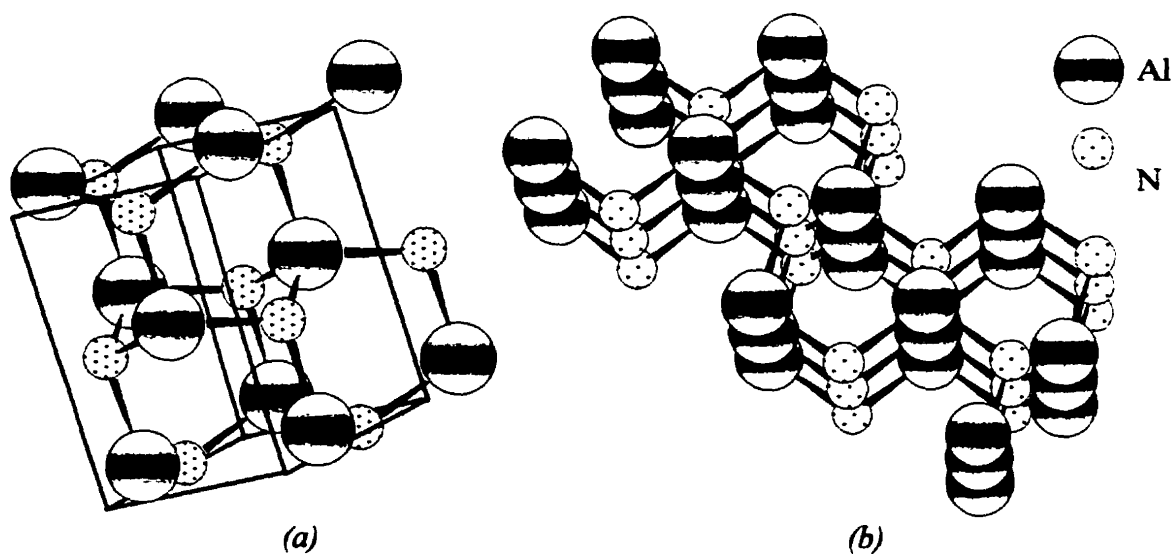


Figure 8-11: (a) Wurtzite structure of AlN. (b) Perspective view of the atoms arrangements of AlN.

AlN belongs to a class of diamond-like, adamantine, compounds (Figure 8-11 (b)) of which the physical properties such as thermal conductivity and thermal expansion are important factors relevant to the design of high-performance electronic packaging. For substrate application, high thermal conductivity and low thermal expansion are desirable. In the adamantine compounds, each atom is coordinated by four nearest neighbors forming a tetrahedron as shown in Figure 8-11 (a).

Table 8-1: Crystal Structure data of AlN [1,14,115].

Structure	Hexagonal		
Spacegroup	$P 6_3 m c$		
Spacegroup number	186		
Lattice parameter (Å)	a	b	c
	3.1120	3.1120	4.9780
Angles	α	β	γ
	90.00	90.00	120.00
Atoms in unit cell	4		

Crystal structure and lattice parameters of AlN are listed in Table 8-1. The positions of the atoms in the unit cell of AlN are shown in Table 8-2.

Table 8-2: Atoms positions in the unit cell of AlN [1,14,118].

Atom	Wyckoff position	x	y	z
Al	2b	0.3333	0.6667	1.0000
N	2b	0.3333	0.6667	0.6150

After gathering the required information from the literature, neutron diffraction patterns were calculated using the "PowderCell" program. AlN calculated neutron diffraction pattern is shown in Figure 8-15.

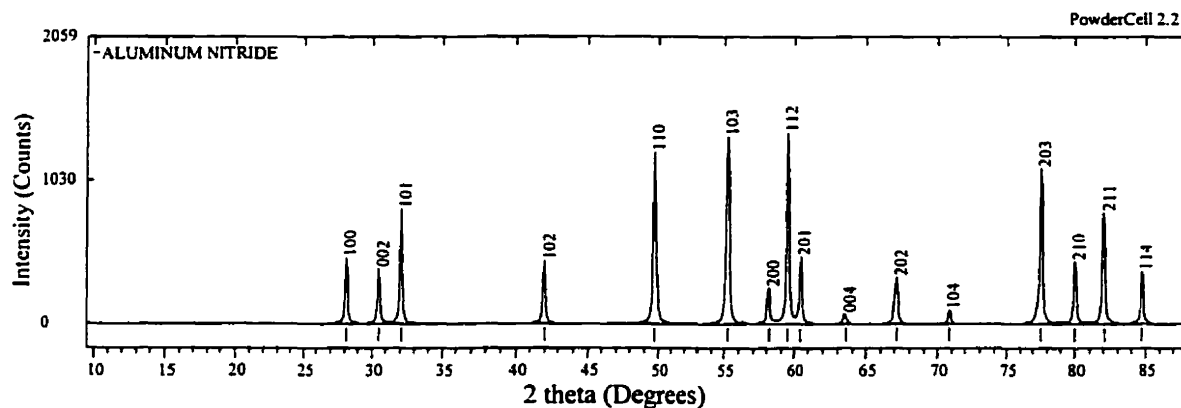


Figure 8-12: Calculated neutron diffraction pattern for AlN.

Since the furnace containing the sample was scanned (as mentioned earlier in the experimental procedure chapter) the acquired neutron diffraction spectra included peaks of the sample and those of the furnace. Correction of these spectra was achieved by subtracting the furnace peaks. For this purpose, neutron diffraction spectra were collected for the empty furnace at all the interested temperatures. The following example will be discussed in order to explain this technique.

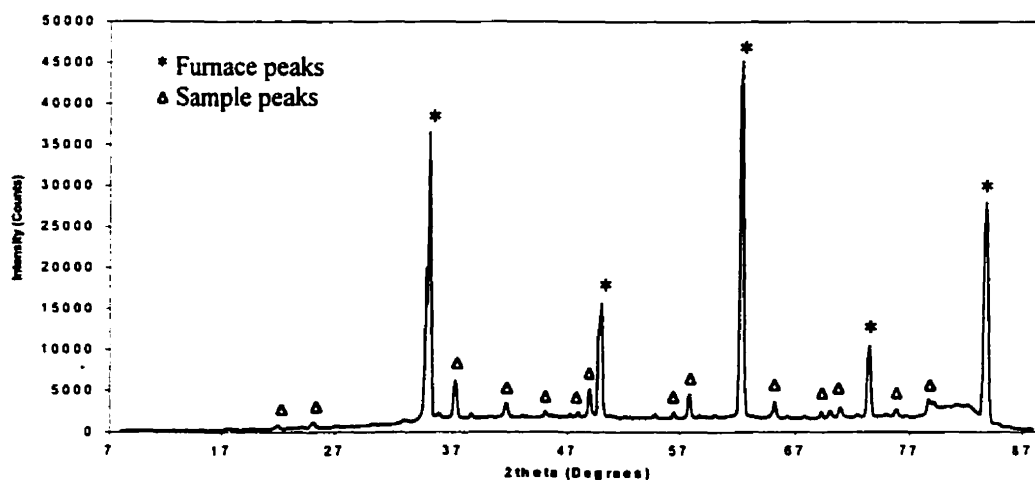


Figure 8-13: Neutron diffractogram of the furnace and a sample.

Figure 8-13 shows a spectrum of the environment (i.e. the sample and the surrounding furnace) of E1 composition at room temperature. The corresponding empty furnace spectrum is shown in Figure 8-14.

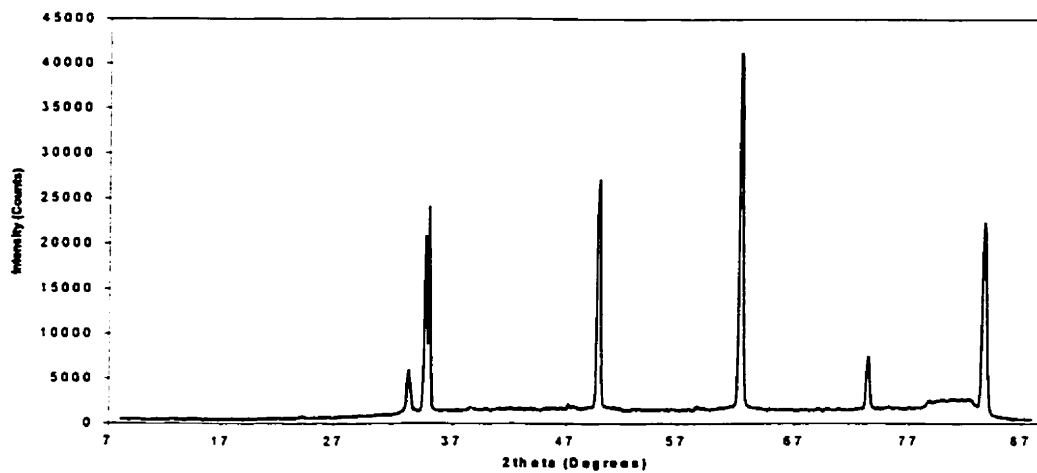


Figure 8-14: Neutron diffractogram of the blank furnace.

The pattern obtained after subtraction is shown in Figure 8-15, where the distinct peaks for different phases can be easily identified comparing with Figure 8-13.

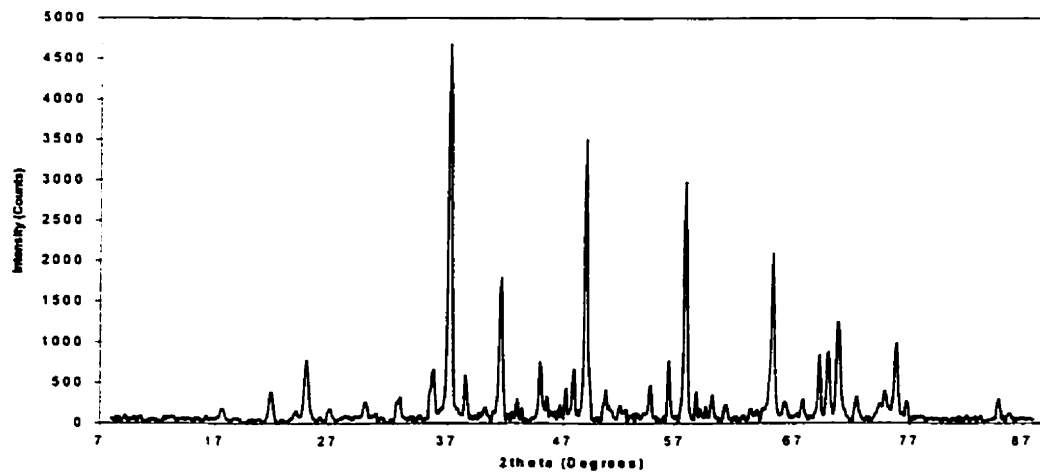


Figure 8-15: Neutron diffractogram after subtracting the pattern of the blank furnace.

8.2.1 Neutron Diffraction Results of $\text{Al}_2\text{O}_3\text{-Y}_2\text{O}_3$ Phase Diagram

To investigate the nature of the reaction between AlN surface oxide (Al_2O_3) and the sintering additive (Y_2O_3) during sintering, phase evolution in the $\text{Al}_2\text{O}_3\text{-Y}_2\text{O}_3$ system was studied *in situ* at elevated temperatures using neutron diffractometry. This was performed by monitoring the changes in the diffraction peaks and the diffraction angles relative to the room temperature pattern as a reference. The temperature was increased

incrementally in order to closely follow the evolution of the reactions. At each step the temperature was maintained for 120 min. to ensure that the reaction was complete. Several features are notable as heating progressed.

Diffraction patterns obtained during the heating and cooling cycles of each sample are shown in Figures 8-16 to 8-25. The patterns are shifted by a suitable offset for better comparison. The peaks are identified by markers as given in the legend of each figure, and will be discussed in this section. Comparison with the thermodynamic findings for $\text{Al}_2\text{O}_3\text{-Y}_2\text{O}_3$ phase diagram will be carried out at the end of this section.

Figure 8-16 illustrates the reaction of the E1 composition from room temperature until 1900°C . The main evolution in the diffraction pattern appears to be the gradual formation of the YAG phase, and the gradual reduction in the intensity of the Y_2O_3 diffraction peaks with the progression of heating. The reaction of Al_2O_3 and Y_2O_3 to produce YAG is clearly evident from the new diffraction peaks. These peaks can be seen first at 1200°C in addition to diffraction peaks for Al_2O_3 and Y_2O_3 with lower intensities than those at room temperature. Y_2O_3 diffraction peaks were not observed at 1500°C . This means all available Y_2O_3 was reacted to produce YAG upon heating from 1200°C to 1500°C . Neutron diffraction data were collected at higher temperature to detect the melting point of this composition. No changes can be seen in the patterns collected in the range of 1500°C to 1850°C . It can be seen from this figure that the sample lost crystallinity in the diffraction pattern collected at 1900°C . This means that the sample was melted between 1850°C and 1900°C .

YAG peaks were indexed as a cubic unit-cell (space group $\text{Ia}\bar{3}\text{d}$, $a = 12.016(3) \text{ \AA}$) using the calculated pattern in Appendix A-3, while Al_2O_3 peaks and Y_2O_3 peaks were identified using a rhombohedral unit-cell (space group $\text{R}\bar{3}\text{c}$, $a = 4.759(0) \text{ \AA}$ and $c = 12.992(0) \text{ \AA}$) and a cubic unit-cell (space group $\text{Ia}\bar{3}$, $a = 10.608(7) \text{ \AA}$), respectively. The calculated patterns for Al_2O_3 and Y_2O_3 are shown in Appendix A-1 and Appendix A-2.

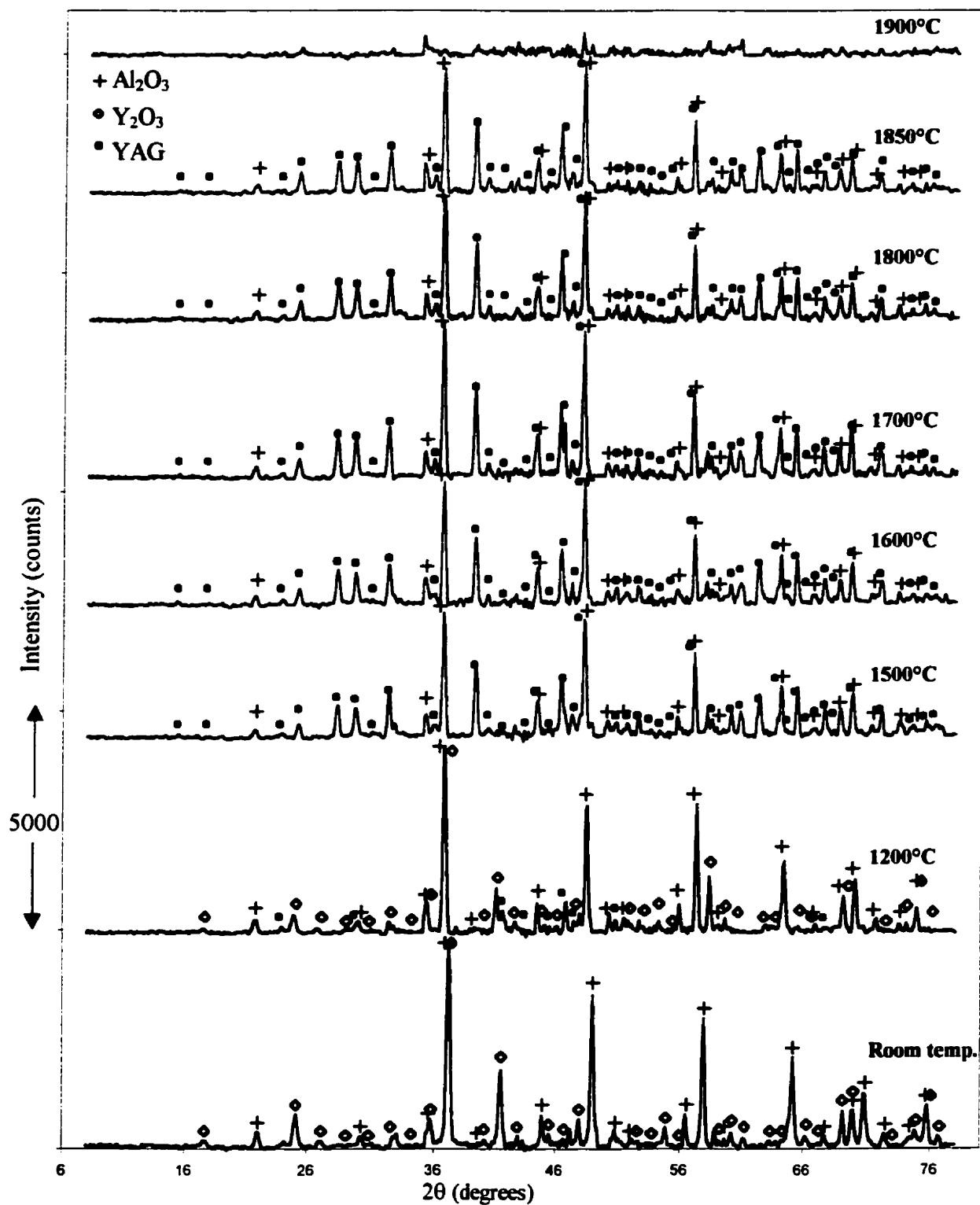


Figure 8-16: Neutron diffractograms during heating of E1 composition.

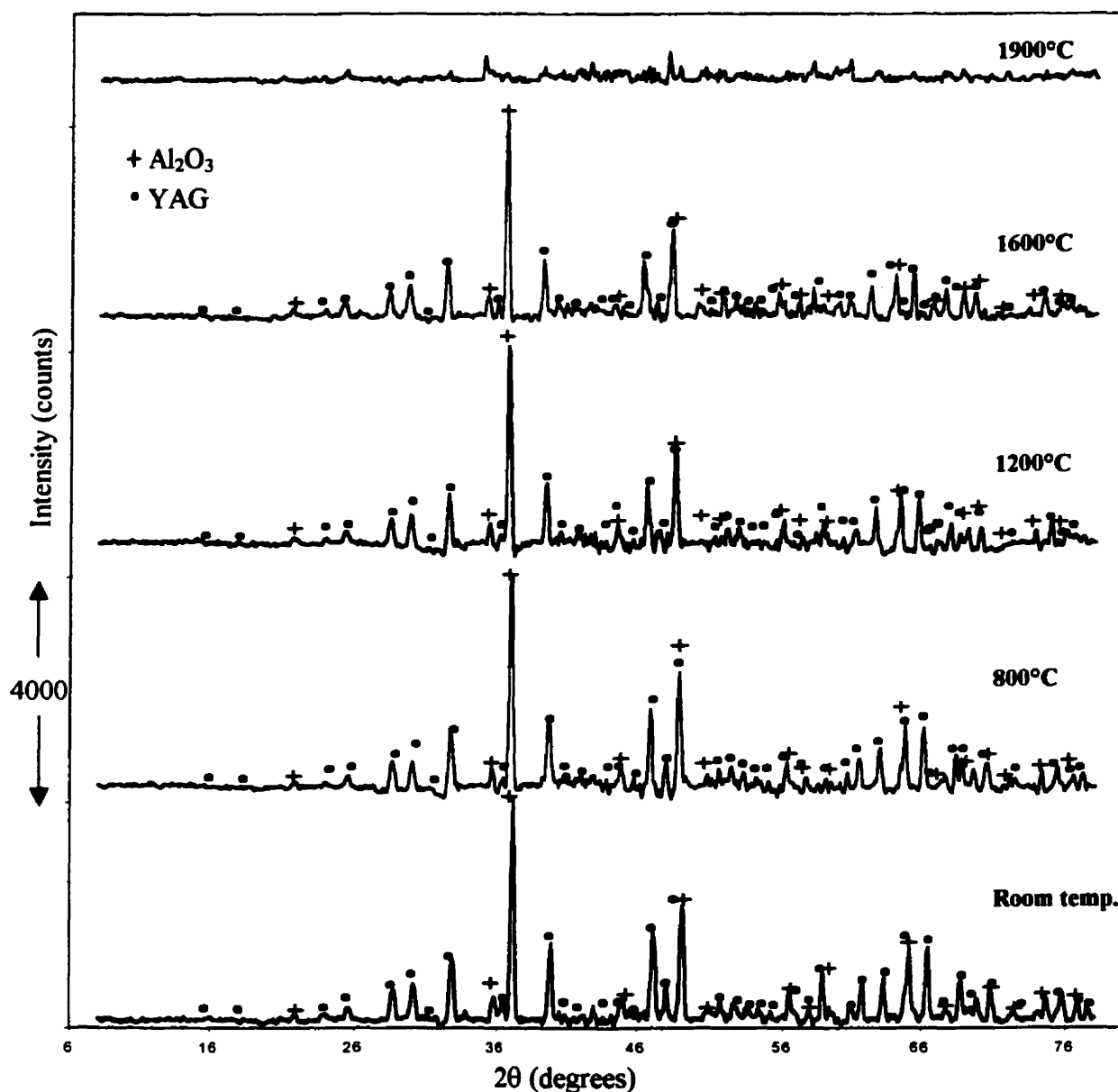


Figure 8-17: Neutron diffractograms during cooling of E1 composition.

Figure 8-17 shows the cooling cycle of sample 1, E1 composition. It can be seen that YAG and Al_2O_3 were fully crystallized at 1600°C. By cooling from this temperature to room temperature no difference in the collected diffraction pattern was noticed. This indicates that YAG and Al_2O_3 are the stable phases for E1 composition since crystallization occurred down to room temperature. This figure shows that the peaks

shifted to higher diffraction angle with decreasing the temperature. The same thing can be observed in Figure 8-16, where the peaks shifted to lower diffraction angle with increasing temperature, indicating a positive thermal expansion coefficient for both YAG and Al_2O_3 .

Heating and cooling of sample 2 which has YAG composition are presented in Figure 8-18 and 7-19. It can be seen from Figure 8-18 that a mixture of 62.5 mol% Al_2O_3 and 37.5 mol% Y_2O_3 produced a pure YAG phase at 1600°C. The first changes are already visible when comparing the neutron diffraction patterns of 1200°C with that at room temperature, where additional peaks, for example at 33° (2 θ) and 64° (2 θ), appear. These peaks continue to grow, whereas the peaks of Al_2O_3 and Y_2O_3 decay with increasing temperature up to 1600°C. For example, the (440) peak of Y_2O_3 at 41.5° (2 θ), which does not overlap with other peaks, is still present up to 1500°C but cannot be observed at 1600°C and higher. The same can be said about the (119) peak of Al_2O_3 at 65° (2 θ), which indicates that the reaction was completed between 1500°C and 1600°C.

The patterns are practically unchanged from 1600°C up to 1950°C, if peak shifts due to thermal expansion of the lattice, are neglected. The diffraction pattern collected at 2000°C in Figure 8-18 shows complete loss of crystallinity. This indicates that sample 2 melts between 1950°C and 2000°C.

The neutron diffraction patterns of the cooling sequence for sample 2 in Figure 8-19 show a full recrystallization of the YAG phase at 1600°C. The shift in the peaks to higher diffraction angles is due to the thermal contraction and can be seen when cooling from 1600°C to 1200°C and then to 800°C. Otherwise the patterns look very similar, which indicates that there is no phase transformation or decomposition of YAG upon cooling from its melt. Sample peaks could not be seen upon cooling to room temperature, which may be due to the shrinkage of the sample that removed it from the neutron beam path. Nevertheless, the cooling sequence of sample 1 showed YAG peaks after cooling to room temperature, which is sufficient evidence to indicate that YAG does not decompose in the temperature range of 800°C to room temperature upon cooling.

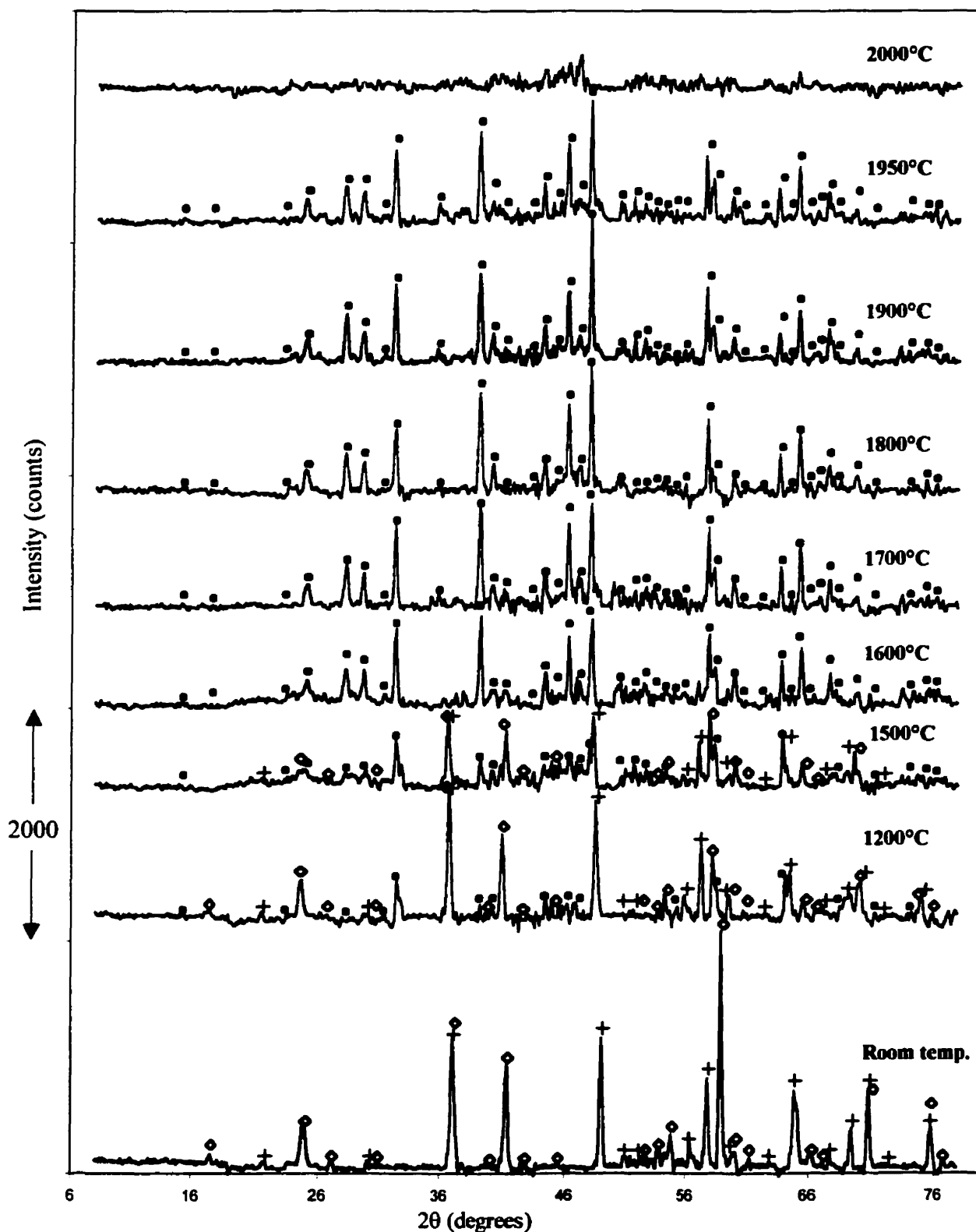


Figure 8-18: Neutron diffractograms during heating of YAG composition.

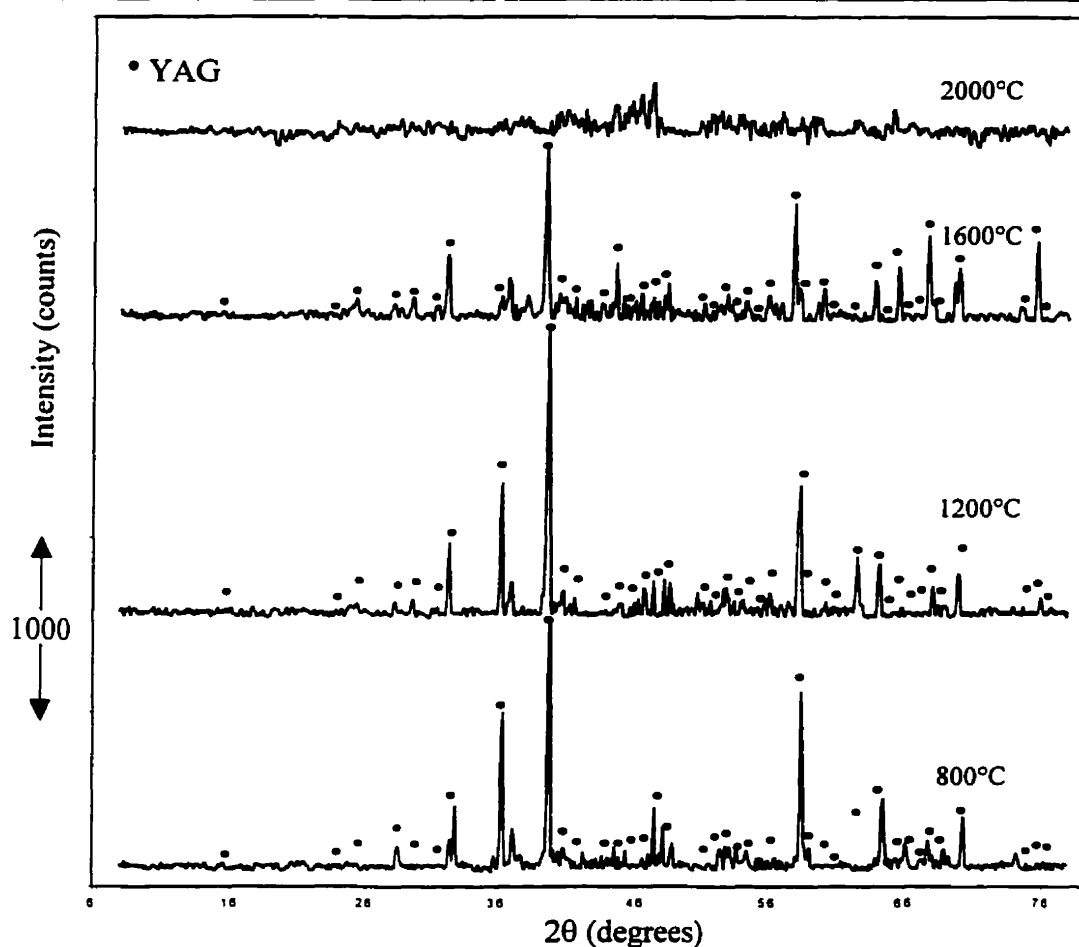


Figure 8-19: Neutron diffractograms during cooling of YAG composition

The development of the neutron diffraction pattern of sample 3, E2 composition, with increasing temperature up to 2000°C is shown in Figure 8-20.

Comparing the neutron diffraction patterns at 1200°C and that at room temperature shows that no additional peaks evolved at 1200°C. The first changes are visible when comparing patterns at 1500°C and 1200°C where additional peaks, for example (420) of YAG and (220) of YAP at 28° (2θ) and 35° (2θ) appear. This indicates that the reaction started in the temperature range of 1200°C to 1500°C.

At 1500°C significant proportions of both Al_2O_3 and Y_2O_3 are present, which are illustrated by, for example, the two overlapping peaks (413) of Y_2O_3 and (113) of Al_2O_3 at 37° (2θ), while there are no Al_2O_3 and Y_2O_3 traces visible at 1600°C. This indicates that the reaction was completed between 1500°C and 1600°C.

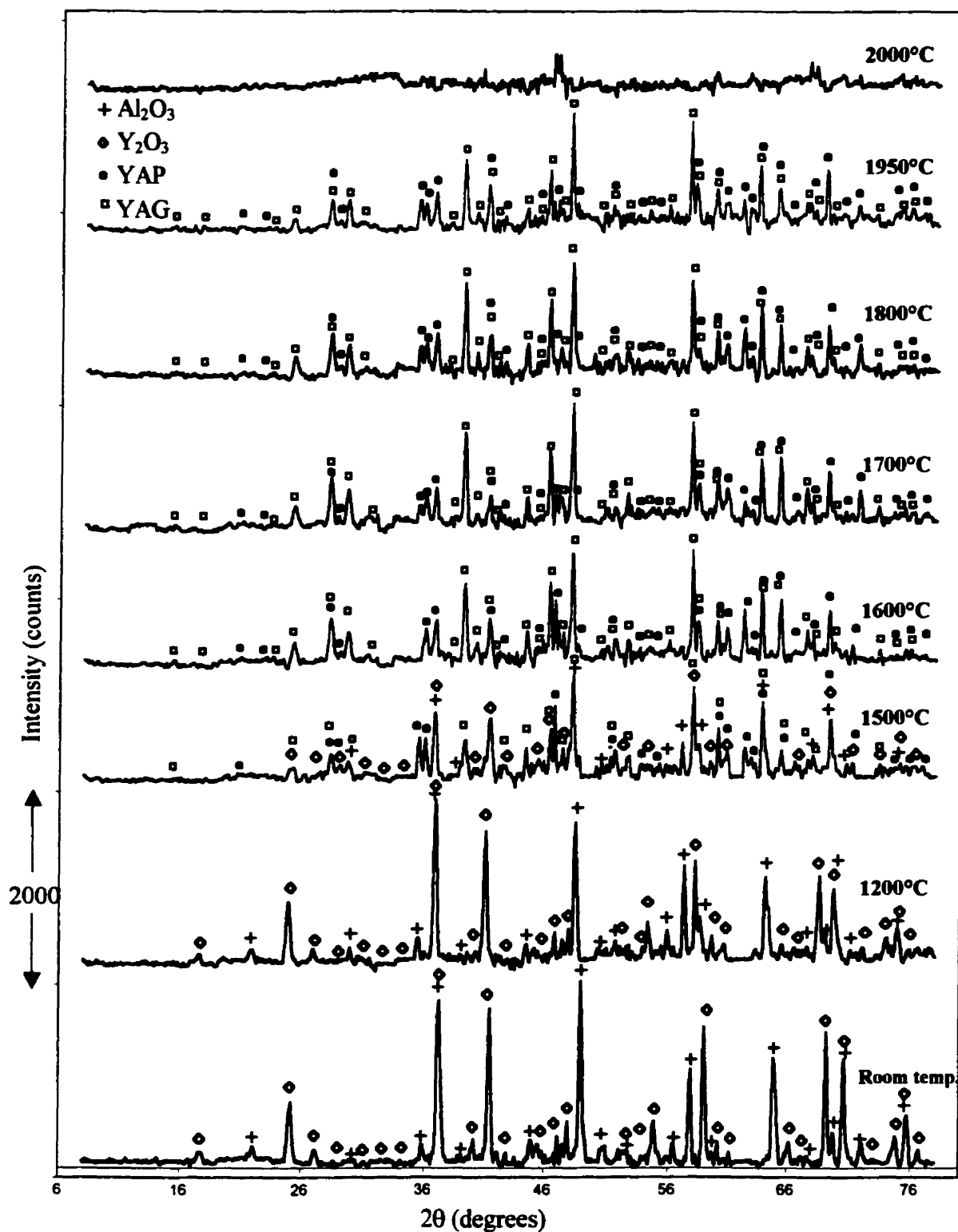


Figure 8-20: Neutron diffractograms during heating of E2 composition.

At 1600°C all the peaks correspond to YAG and YAP phases. YAP peaks were identified as orthorhombic unit-cell (space group $Pnma$, $a = 5.330(2)\text{\AA}$, $b = 7.375(2)\text{\AA}$ and $c = 5.180(2)\text{\AA}$) using the calculated pattern shown in Appendix A-4.

The patterns are unchanged up to 1950°C, if the shifts of reflections due to thermal expansion of the lattice are neglected. It can be seen from this figure that sample 3 was melted in the temperature range of 1950°C to 2000°C.

The neutron diffraction patterns of the cooling sequence of sample 3 are shown in Figure 8-21. This figure shows partial reconstruction of the YAP and the YAG phases, where some reflections (the ones at 2θ less than 36°) are missing at 1600°C. This is possibly caused by a deformation of some components of the furnace; for example, the heating element may have distorted at this high temperature to shield part of the diffracted beam.

By cooling to room temperature some difference in the peaks height was noticed. For example, YAP peak at 36° (2θ) lost height upon cooling. Whereas the shift in the peaks position is due to the thermal contraction as stated earlier in this section.

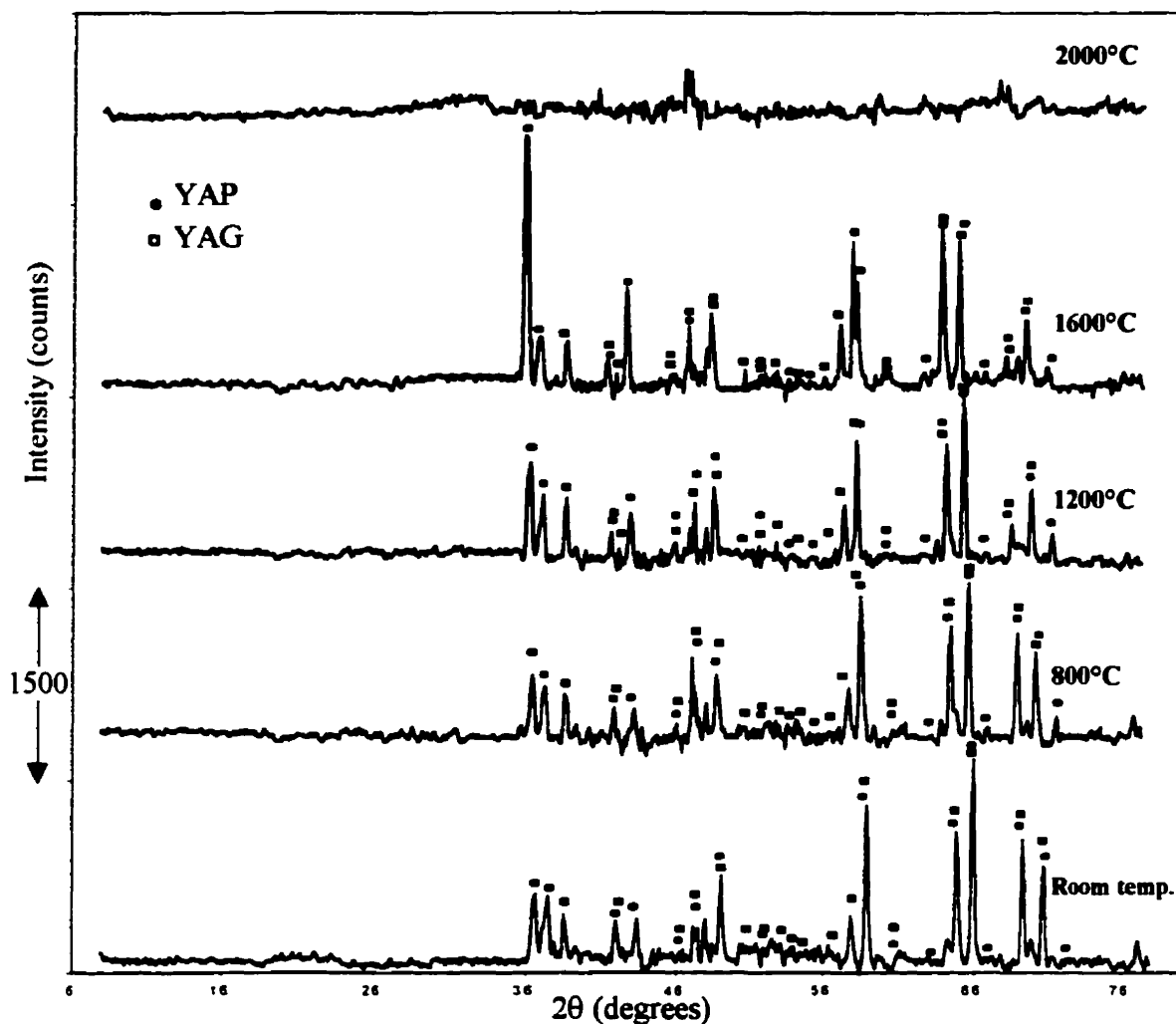


Figure 8-21: Neutron diffractograms during cooling of E2 composition.

The reaction process was different when starting with 50 mol% Al_2O_3 and 50 mol% Y_2O_3 or YAP composition. This was obvious when the collected spectra of this sample at different temperatures shown in Figure 8-22 were compared. The first changes were already visible by comparing the neutron diffraction patterns at 1500°C and 1200°C. The pattern at 1500°C clearly shows the elimination of the starting material peaks and the growth of new peaks. This phase was identified by the calculated pattern of YAP.

Following the reaction in later stages of heating shows that this mixture produced pure YAP only by 1800°C; since traces of Al_2O_3 and Y_2O_3 are still visible at 1600°C and 1700°C. Other evidence of incomplete reaction at 1700°C is the growth of (230) peak of YAP at 42° (2θ). It can be seen that this peak did not achieve its full height below 1800°C. Also, the decrease of the (400) YAP peak at 59° , which overlaps with (723) Y_2O_3 peak, proves indeed that some residual Y_2O_3 exists at 1700°C. Above 1800°C the patterns were unchanged except for a small shift in the peak positions due to the thermal expansion of YAP unit cell.

During the course of *in situ* high temperature neutron diffraction it was often difficult to reach 2000°C and maintain the furnace at such high temperature for more than a few minutes. Therefore the cooling cycle often began before melting took place. During the heating of this sample the furnace only reached 1900°C. Even though the melting was not achieved it was assured that the melting temperature of the sample is higher than 1900°C.

The neutron diffraction pattern of cooling for YAP is shown in Figure 8-23. During cooling from 1900°C to room temperature the patterns were practically unchanged. Therefore it is clear that, under these cooling conditions, the orthorhombic YAP phase the stable phase down to room temperature.

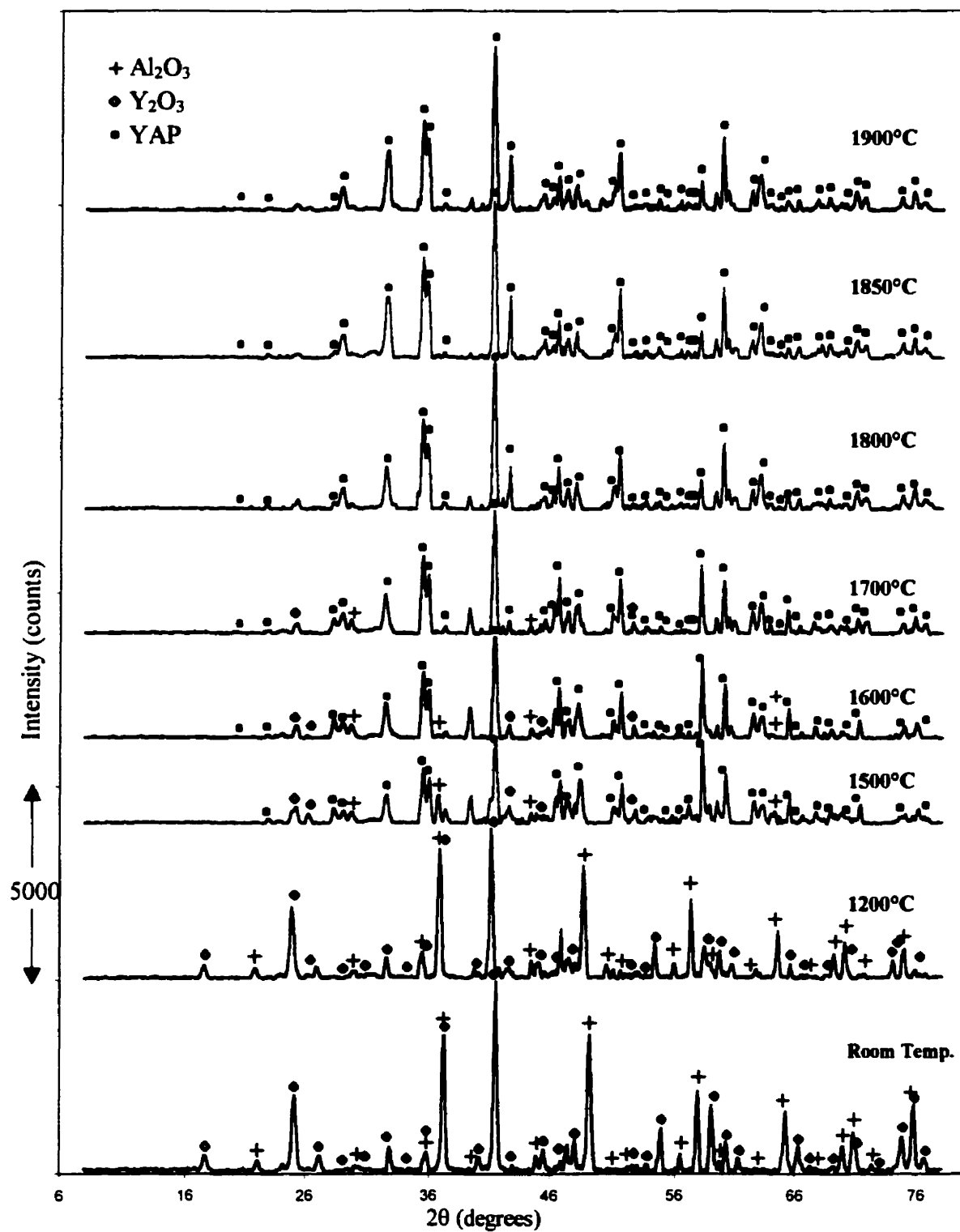


Figure 8-22: Neutron diffractograms during heating of YAP composition.

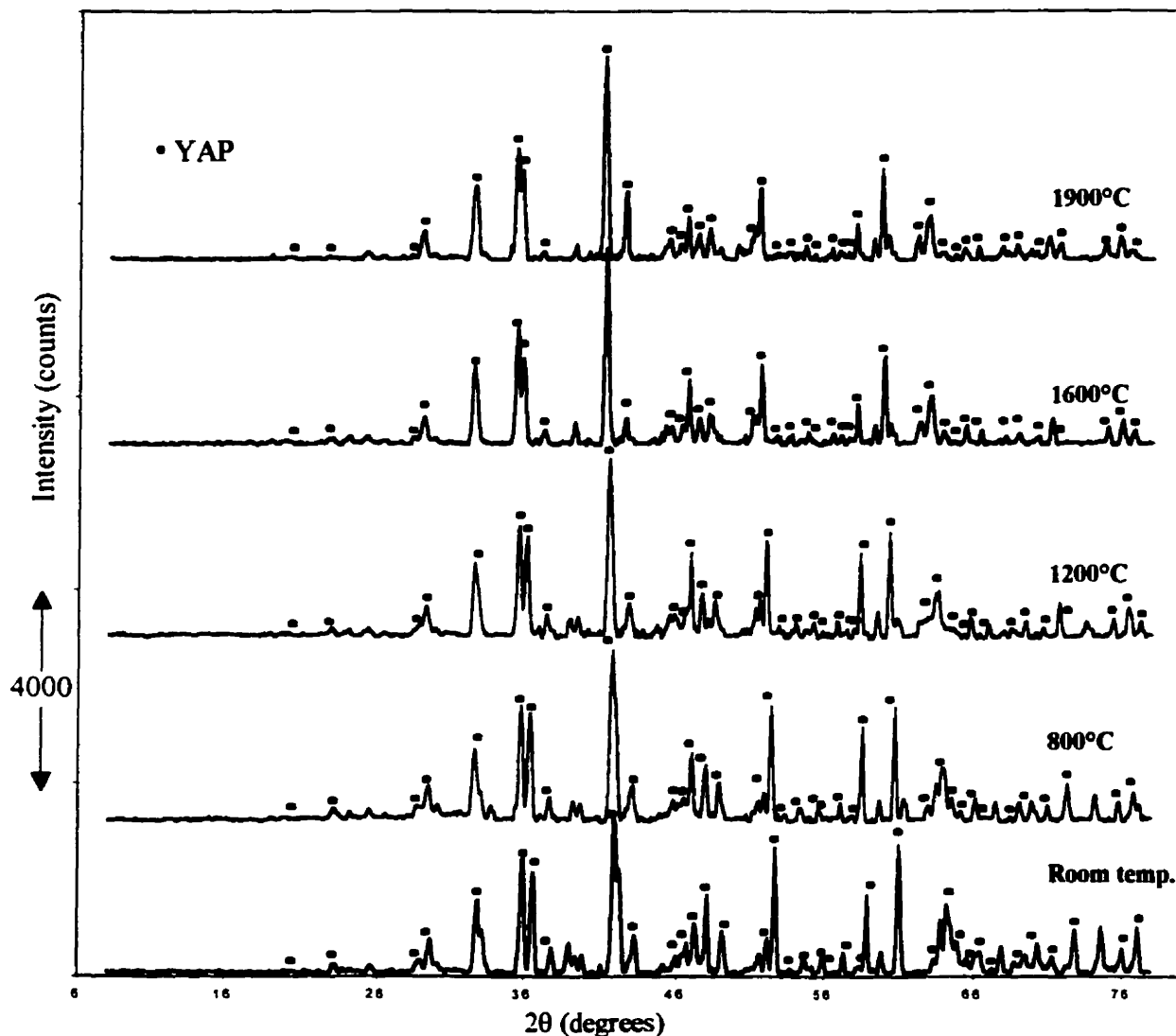


Figure 8-23: Neutron diffractograms during cooling of YAP composition.

The development of the neutron diffraction pattern with increasing temperature up to 1950°C for sample 5 (YAM composition) is shown in Figure 8-24. The first noticeable changes for this sample are observed by comparing the neutron diffraction patterns at 1200°C with that at room temperature. Additional peaks appear at 1200°C and although traces of YAM were seen at 1200°C, complete formation of YAM was not observed below 1800°C. This indicates that the reaction was completed in the temperature range of 1700°C to 1800°C. YAM peaks were identified according to the calculated pattern as

monoclinic (space group $P2_1/c$, $a = 7.4706(5)\text{\AA}$, $b = 10.535(6)\text{\AA}$, $c = 11.1941(8)\text{\AA}$, $\beta = 108.888^\circ(5)$) [53].

Patterns at 1800°C , 1900°C and 1950°C were similar and although the furnace reached 2000°C for this sample, due to technical problems, it was not possible to maintain the temperature for a long enough time to completely collect the pattern. So the cooling cycle started after remaining only 5 min at 2000°C . It can be seen that the sample is still crystalline at 1950°C . This indicates that the melting temperature of YAM is higher than 1950°C .

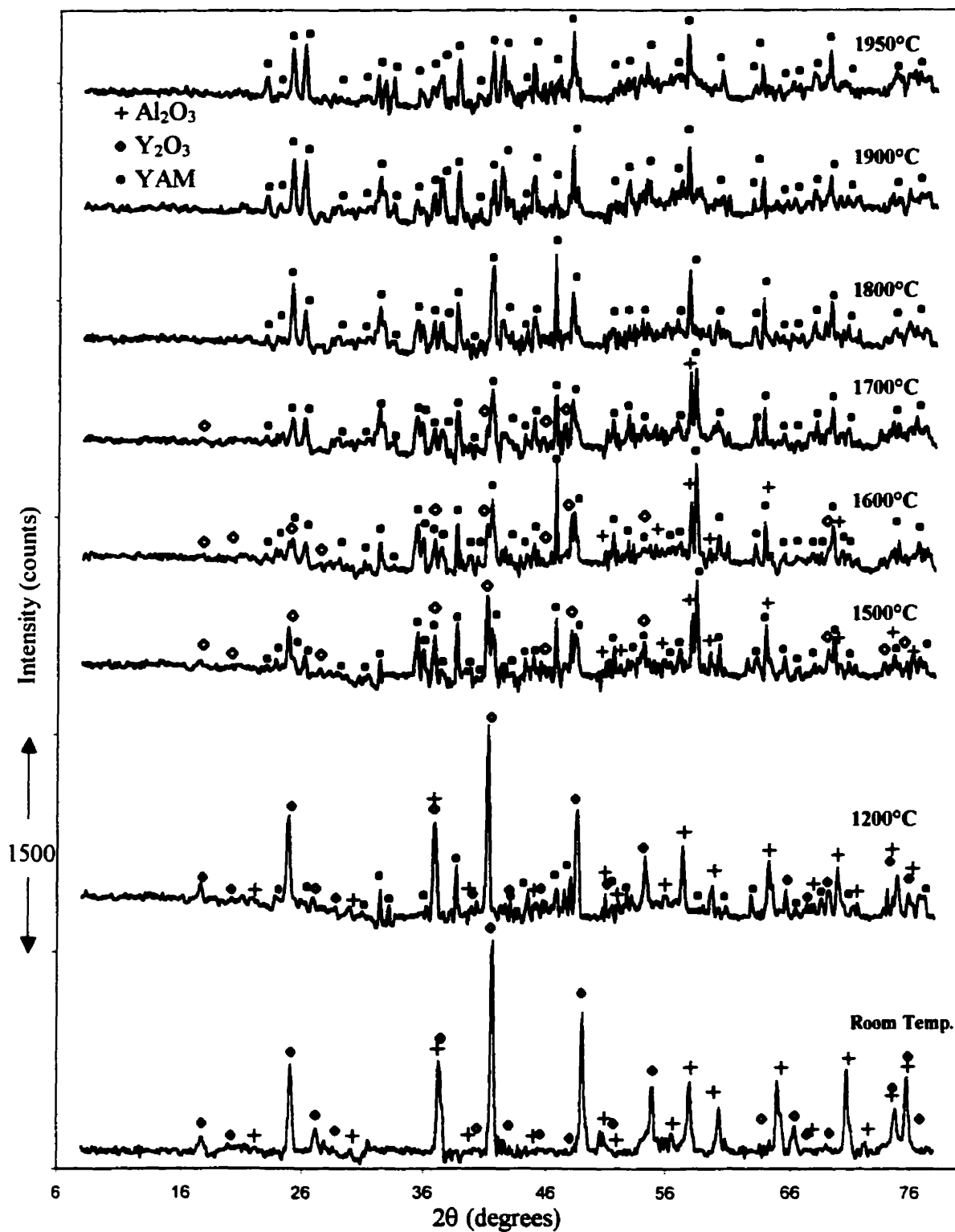


Figure 8-24: Neutron diffractograms of heating of YAM composition.

The neutron diffraction pattern of the cooling cycle for sample 5 (YAM composition) is shown in Figure 8-25. Upon cooling, the only occurrence is the shift in the peaks to higher diffraction angles due to the thermal contraction. Otherwise the patterns look very similar, confirming that under these cooling conditions YAM is a stable phase from 1950°C down to room temperature.

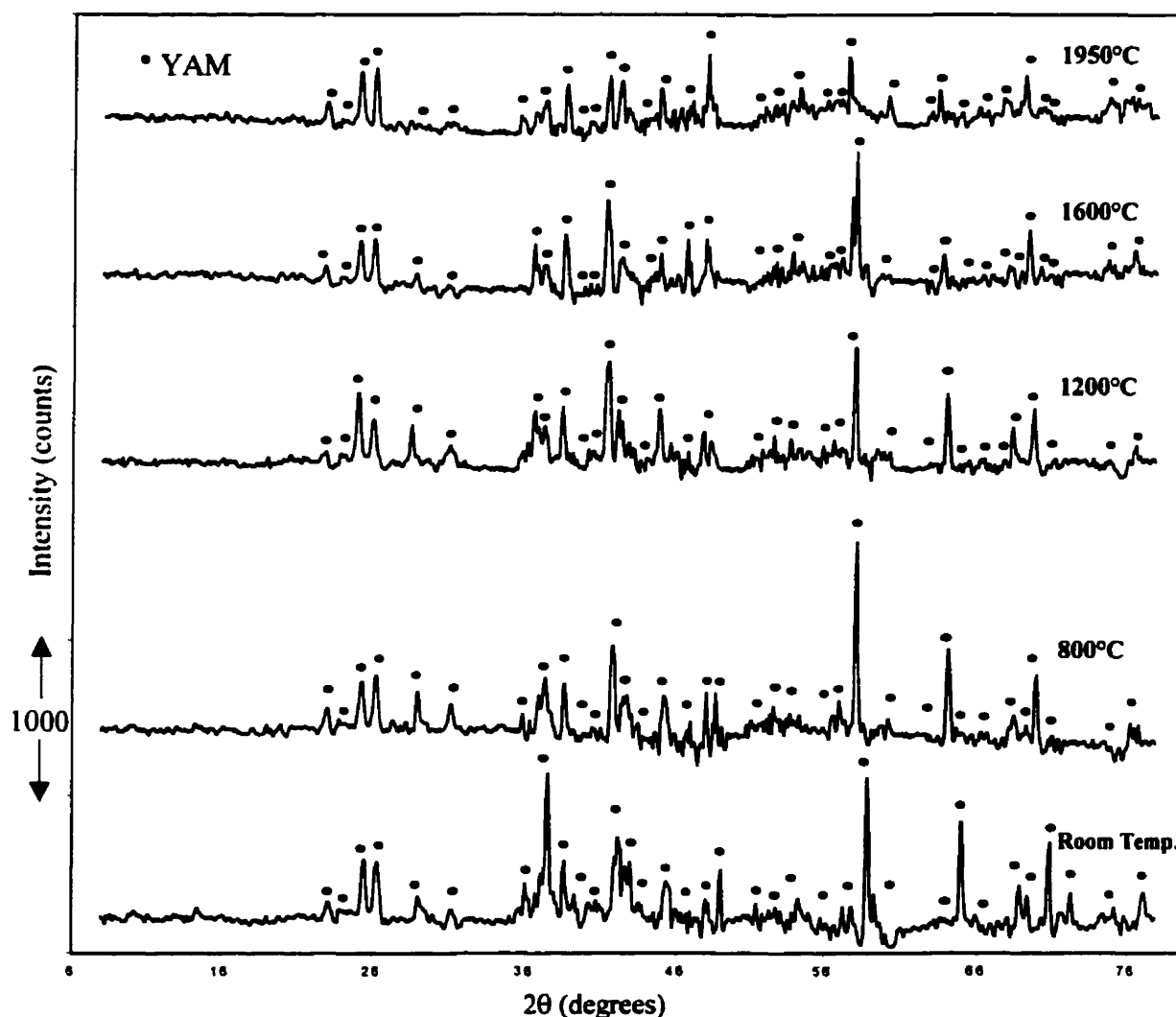


Figure 8-25: Neutron diffractograms during cooling of YAM composition.

Table 8-3: Summary of phase evolution for the Al_2O_3 - Y_2O_3 system.

Sample number	Neutron Diffraction Results				Thermodynamic Predictions	
	Reaction started (T_{rs})	Reaction finished (T_{re})	Melting temp. (T_m)	Phases obtained	Melting temp.	Stable phases
1	$T_{rs} < 1200^\circ C$	$1200^\circ C < T_{re} < 1500^\circ C$	$1850^\circ C < T_m < 1900^\circ C$	Al_2O_3 and YAG	$1820^\circ C$	Al_2O_3 and YAG
2	$T_{rs} < 1200^\circ C$	$1500^\circ C < T_{re} < 1600^\circ C$	$1950^\circ C < T_m < 2000^\circ C$	YAG	$1942^\circ C$	YAG
3	$1200^\circ C < T_{rs} < 1500^\circ C$	$1500^\circ C < T_{re} < 1600^\circ C$	$1950^\circ C < T_m < 2000^\circ C$	YAG and YAP	$1908^\circ C$	YAG and YAP
4	$1200^\circ C < T_{rs} < 1500^\circ C$	$1700^\circ C < T_{re} < 1800^\circ C$	$T_m > 1900^\circ C$	YAP	$1915^\circ C$	YAP
5	$T_{rs} < 1200^\circ C$	$1700^\circ C < T_{re} < 1800^\circ C$	$T_m > 1950^\circ C$	YAM	$1978^\circ C$	YAM

Table 8-3 summarizes the results of the neutron diffraction experiments and the thermodynamic findings for the Al_2O_3 - Y_2O_3 system. It can be seen that the phase evolution after heating and cooling for the different compositions are in complete agreement with the phases that resulted from the thermodynamic model. There is some discrepancy between the calculated melting temperature and those measured by neutron diffractometry. This discrepancy is due to the fact that the temperature was measured in a vacuum space between the heating element and the Mo pencil tube instead of measuring it right inside the Mo tube itself. This explains why the measured melting temperatures were always higher than the calculated ones, the latter are entirely consistent with the literature values.

8.2.2 Neutron Diffraction Results of AlN - Y_2O_3 Phase Diagram

High temperature *in situ* neutron diffraction experiments were conducted in order to study the phase relations in the calculated AlN - Y_2O_3 binary phase diagram (Figure 8-26). A sample of the eutectic composition, 47 mol% AlN , was prepared. Diffraction patterns obtained during heating and cooling of this sample are shown in Figures 8-27 and 8-28, respectively.

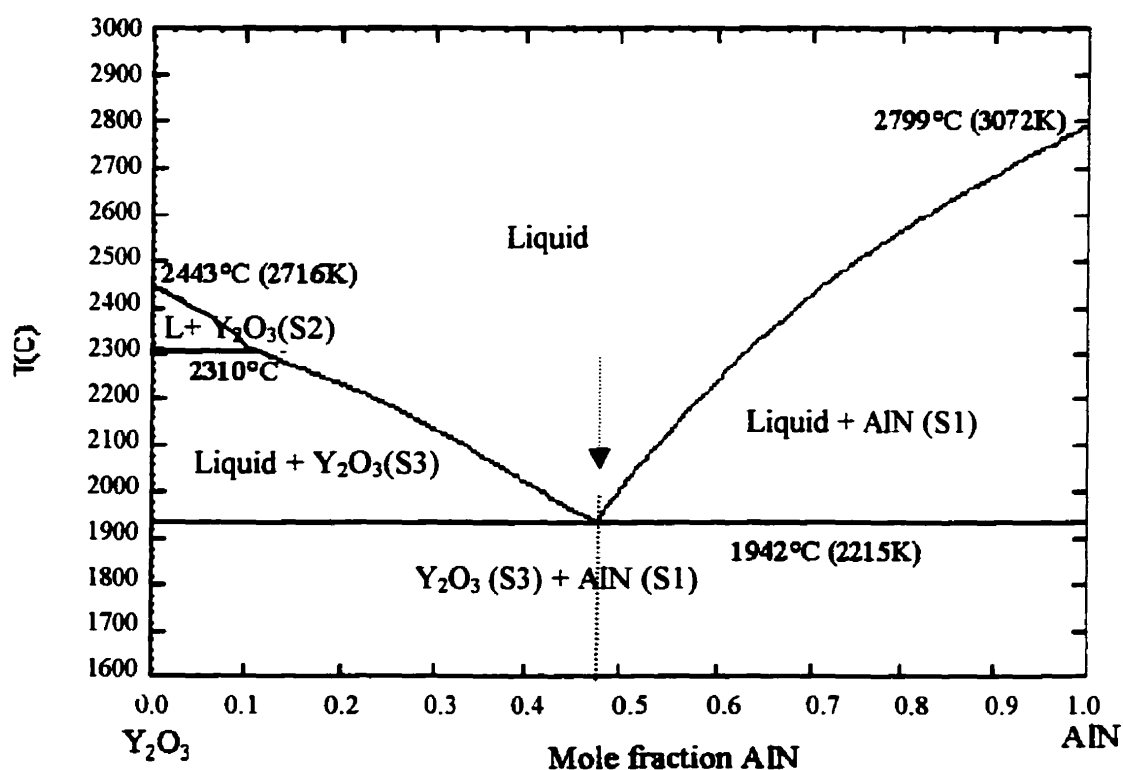


Figure 8-26: Calculated AlN - Y_2O_3 phase diagram with the investigated sample.

The development of the neutron diffraction pattern with increasing temperature up to the melting point is shown in Figure 8-27. The patterns are unchanged up to 1950°C except for the shift due to the lattice thermal expansion. AlN and Y_2O_3 are the only phases which exist from room temperature to melting. This means that no reaction takes place between AlN and Y_2O_3 during heating from room temperature till melting.

It can be seen from Figure 8-27 that this composition lost crystallinity in the diffraction pattern collected at 2000°C. This means that the melting point of this composition is between 1950°C and 2000°C.



Since melting occurred when the two solid phases were transformed into a liquid phase, this is a result of eutectic reaction. Moreover the melting temperature is lower than the melting point of both AlN, $2797 \pm 100^\circ\text{C}$ [104], and Y_2O_3 , $2439 \pm 12^\circ\text{C}$ [102], showing that 47 mol% AlN is the eutectic composition for this binary system. The calculated eutectic temperature of AlN- Y_2O_3 is 1942°C and the difference is due to the fact that the measured temperature is higher than the actual one as pointed out earlier.

AlN peaks were indexed as a hexagonal unit-cell (space group $P6_3mc$, $a = 3.112(0) \text{ \AA}$ and $c = 4.978(0) \text{ \AA}$) using the calculated pattern discussed in section 8-2. Y_2O_3 peaks were identified as described in section 8-2-1.

Neutron diffraction patterns collected during cooling of this sample are shown in Figure 8-28. It can be seen that AlN and Y_2O_3 were completely crystallized by cooling to 1900°C . Hence Y_2O_3 and AlN are the products of the eutectic reaction, when the opposite reaction of equation 8-2 occurs upon cooling. AlN and Y_2O_3 are the only phases that exist for this system down to room temperature. This proves that the phase relation between AlN and Y_2O_3 can be described by a simple binary eutectic phase diagram and there is no reaction or mutual solubility between these two solids. This fact, coupled with the measured eutectic temperature, are in complete agreement with the calculated phase diagram for this system.

It can be seen from Figure 8-28 that the height of (440) Y_2O_3 peak at $41.5^\circ (2\theta)$ increases with decreasing temperature from 1750°C to room temperature. On the other hand the calculated neutron diffraction pattern of Y_2O_3 , presented in Appendix A-2, shows that this is the strongest peak for Y_2O_3 . This indicates better crystallization of the Y_2O_3 phase upon cooling which has (440) as a preferred direction. AlN peaks remain unchanged during solidification to room temperature.

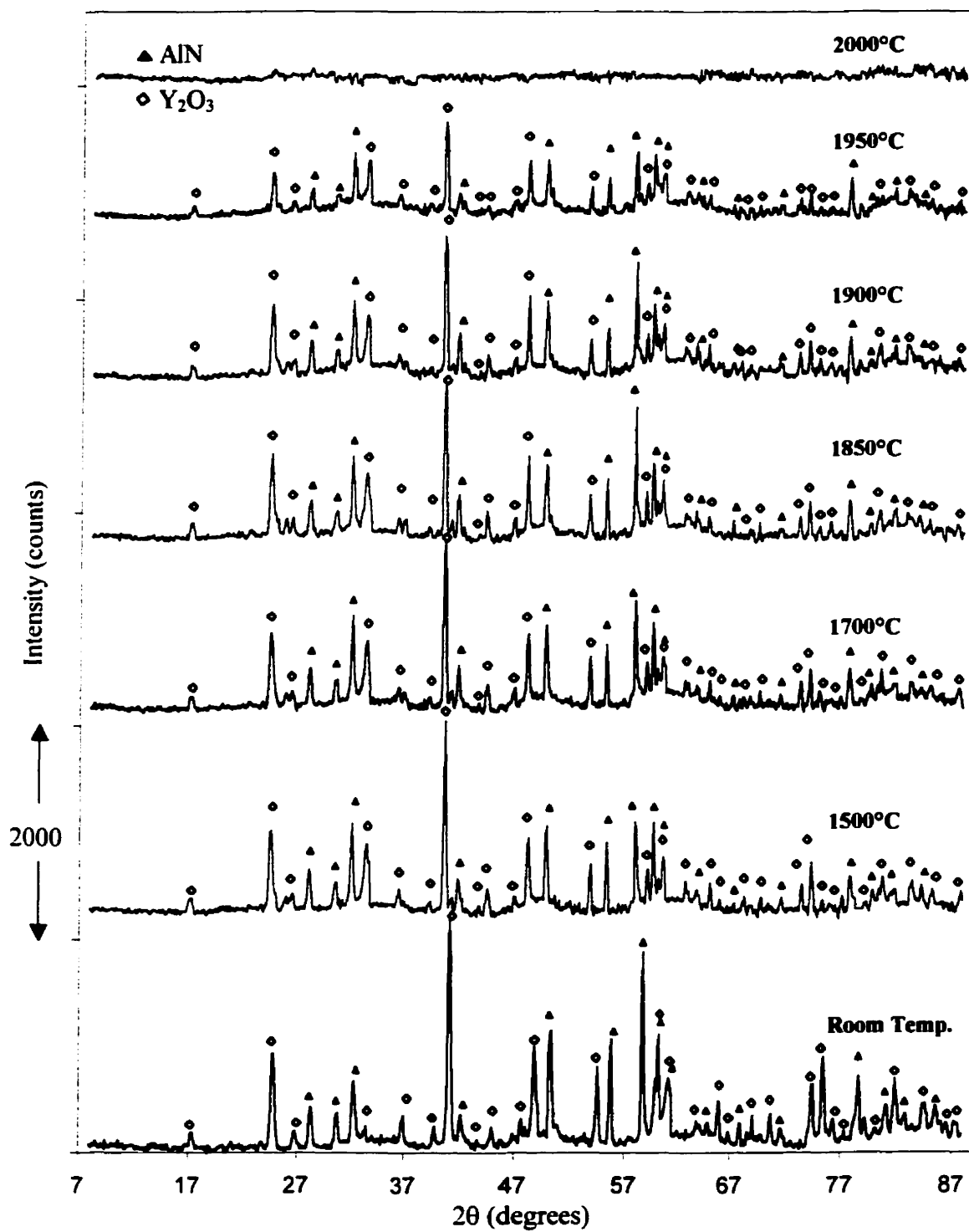


Figure 8-27: Neutron diffractograms during heating of $\text{AlN-Y}_2\text{O}_3$ eutectic composition.

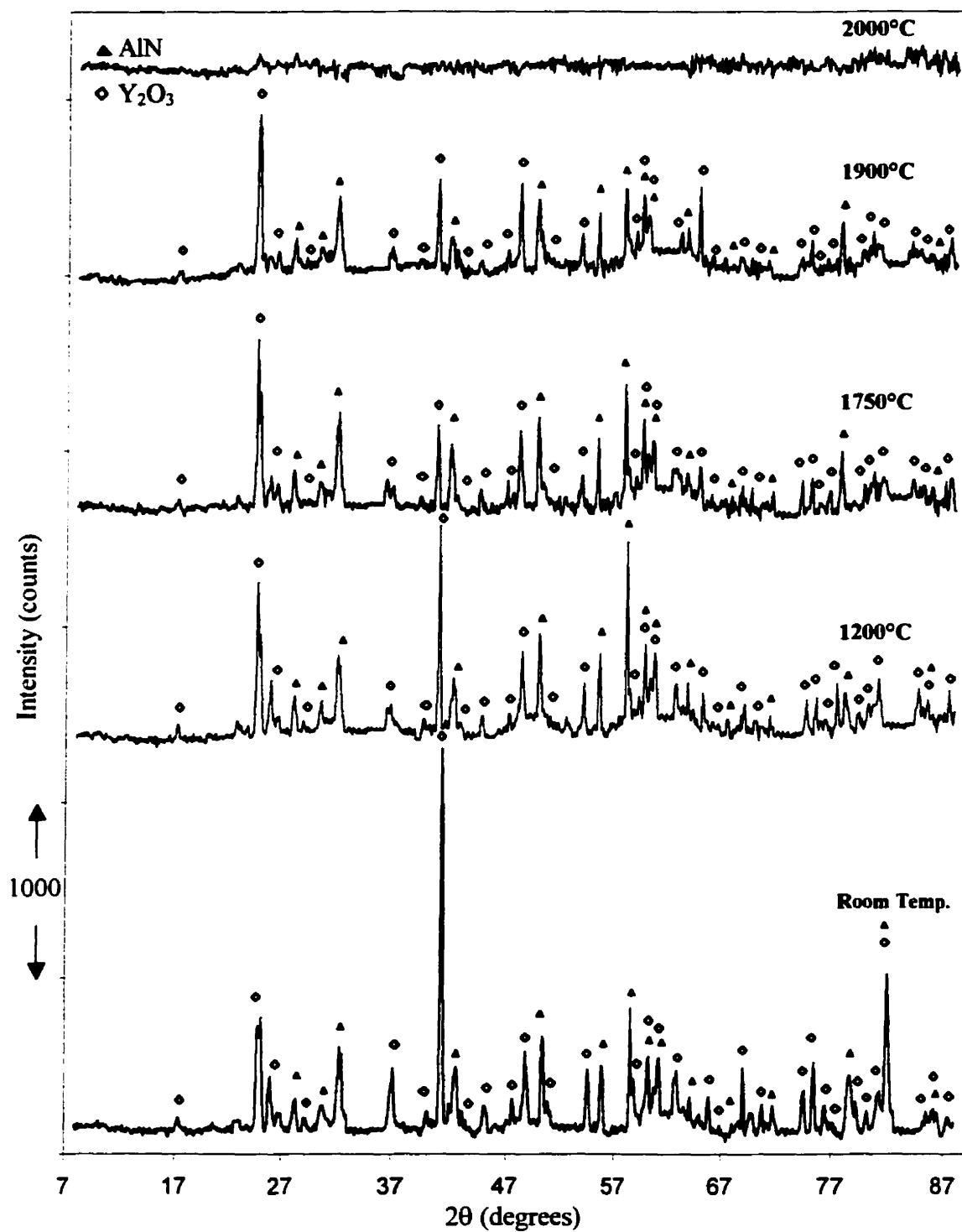


Figure 8-28: Neutron diffractograms during cooling of AlN - Y_2O_3 eutectic composition.

Chapter 9:

HIGH TEMPERATURE NEUTRON DIFFRACTION OF $\text{AlN-Al}_2\text{O}_3\text{-Y}_2\text{O}_3$ TERNARY SYSTEM

In this chapter the experimental investigation of the $\text{AlN-Al}_2\text{O}_3\text{-Y}_2\text{O}_3$ ternary system will be discussed. Five different ternary samples, with compositions listed in Table 9-1, were studied *in situ* at elevated temperatures by neutron diffractometry. These compositions along with the $\text{AlN-Al}_2\text{O}_3\text{-Y}_2\text{O}_3$ isothermal sections calculated at different temperatures are shown in Figure 9-1. It can be seen from this figure that these compositions were selected carefully to be close to the phase boundaries in order to critically verify the thermodynamic findings.

Table 9-1: The chemical composition of the studied samples.

Sample No.	Composition (mol%)		
	AlN	Al_2O_3	Y_2O_3
1	12	74	14
2	17.5	64	18.5
3	24	70	6
4	7	33	60
5	33	20	47

In situ neutron diffraction was performed during heating and cooling of these samples by monitoring the changes in the diffraction peaks and the diffraction angles.

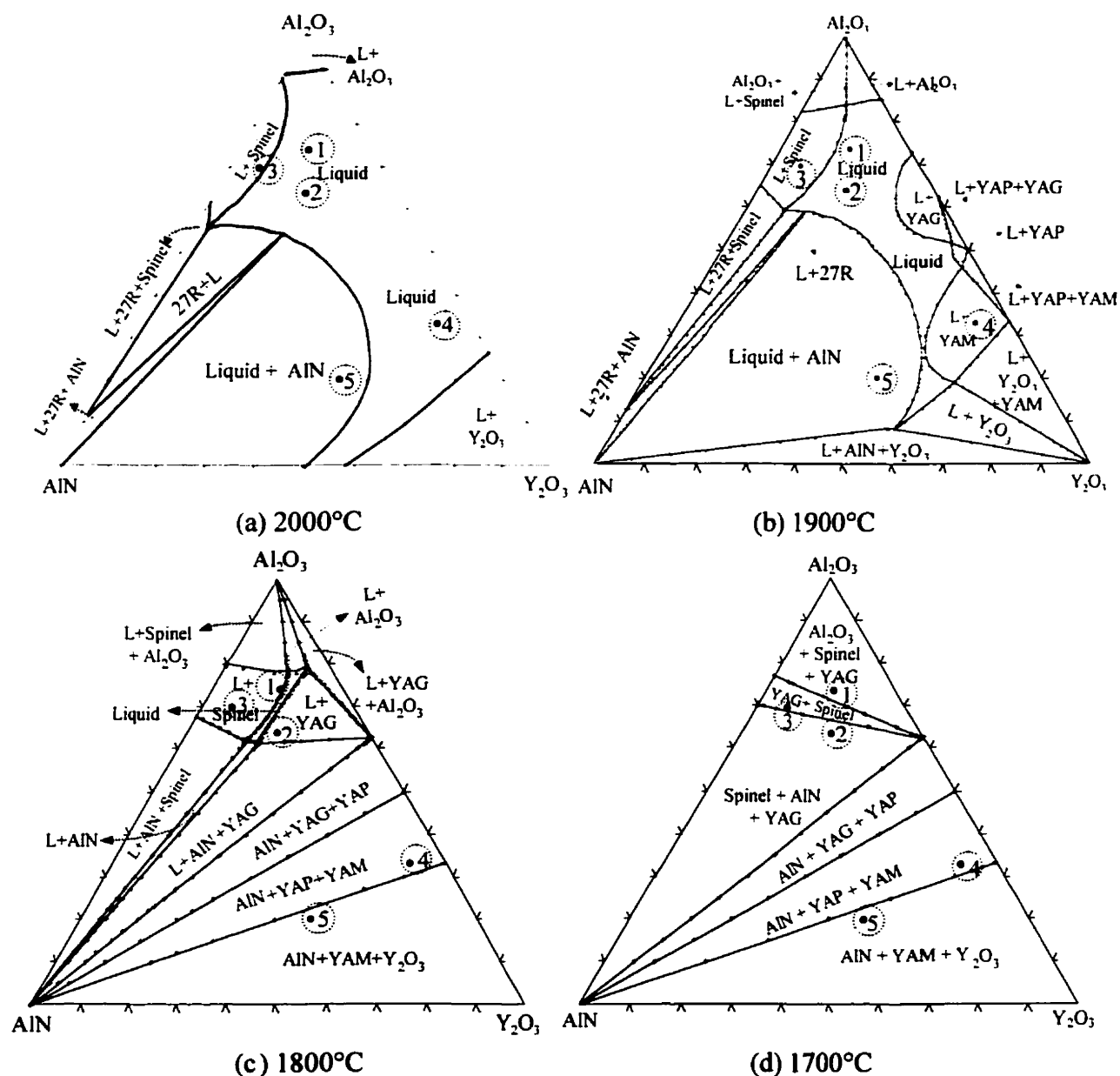


Figure 9-1: $\text{AlN-Al}_2\text{O}_3\text{-Y}_2\text{O}_3$ isothermal sections at different temperatures with the five investigated ternary compositions.

The evolution of the reactions was followed by increasing the temperature incrementally, and maintaining it for 120 min. to ensure that the reaction was complete. Also cooling was carried out incrementally to detect the crystallization as well as the

stability of each phase. Heating and cooling profiles were determined for each sample according to critical points, which were predicted by the thermodynamic calculations.

Diffraction patterns obtained during heating and cooling of each sample are shown in the following figures. The patterns are shifted by a suitable offset for better comparison. The peaks are identified by markers as given in the legend of each figure, and will be discussed and compared with the thermodynamic findings in this chapter. The effect of thermal expansion was observed in all the samples when the peaks shifted to lower and higher diffraction angles due to heating and cooling, respectively.

Spinel peaks were indexed as a cubic unit-cell (space group $\text{Fd}\bar{3}\text{m}$, $a = 7.9435(2)\text{\AA}$) using the calculated pattern shown in Appendix A-6. AlN peaks were identified as a hexagonal unit-cell (space group $\text{P6}_3\text{mc}$, $a = 3.112(0)\text{\AA}$ and $c = 4.978(0)\text{\AA}$) using the calculated pattern demonstrated in section 8-2, while Al_2O_3 , Y_2O_3 , YAG, YAP and YAM were identified as discussed in section 8-2-1.

Ternary isothermal sections show the phases in equilibrium at certain temperatures, but they do not show the relative amount of each phase, the formation, the melting and/or the decomposition temperature of these phases. Whereas the *in situ* neutron diffraction experiments reveal results about formation, decomposition and melting of the phases. Hence, the relative mass of each phase versus temperature is drawn, for the compositions in question, and compared with the results of neutron diffraction experiments.

9.1 Composition 1

The reaction of this composition (12 mol% AlN, 74 mol% Al_2O_3 and 14 mol% Y_2O_3) during heating the sample from room temperature until 1900°C is illustrated in Figure 9-2. Increasing the temperature to 1200°C did not introduce any change in the neutron diffraction pattern collected at this temperature. This indicated that no reaction took place in this temperature range. The first changes were visible when comparing the

neutron diffraction patterns at 1200°C and those at 1700°C, where additional peaks appear. The new peaks were found to belong to YAG and spinel phases. Unlike Al_2O_3 diffraction peaks, Y_2O_3 peaks were not observed at 1700°C indicating that all the 14 mol% Y_2O_3 reacted to produce YAG phase, whereas residual Al_2O_3 shows incomplete reaction to form spinel. This is consistent with the ternary phase diagram shown in Figure 9-1 (d) where composition 1 lies in the three-phase-region of Al_2O_3 , spinel and YAG. Cheng *et al.* also observed an incomplete reaction between Al_2O_3 and AlN at 1650°C for 6 h. They noticed an increase in the amount of spinel with increasing time from 60 min. to 6 h [119] Moreover, Yawei *et al.* [105] concluded that it is difficult to produce spinel by reaction sintering below 1650°C.

Upon heating from 1700°C to 1800°C, no difference in the collected diffraction pattern could be noticed. Neutron diffraction patterns were collected at higher temperatures to detect the liquid formation and melting of this sample. At 1850°C YAG peaks were not observed, whereas spinel peaks were present. Since no other peaks were present at this temperature, it can be concluded that liquid formation started between 1800°C to 1850°C. This is consistent with the isothermal section calculated at 1800°C shown by Figure 9-1(c).

It can be seen from Figure 9-2 that this composition lost crystallinity in the diffraction pattern collected at 1900°C. This shows that the sample melted in the temperature range between 1850°C to 1900°C. This is consistent with the calculated isothermal section at 1900°C shown in Figure 9-1(b).

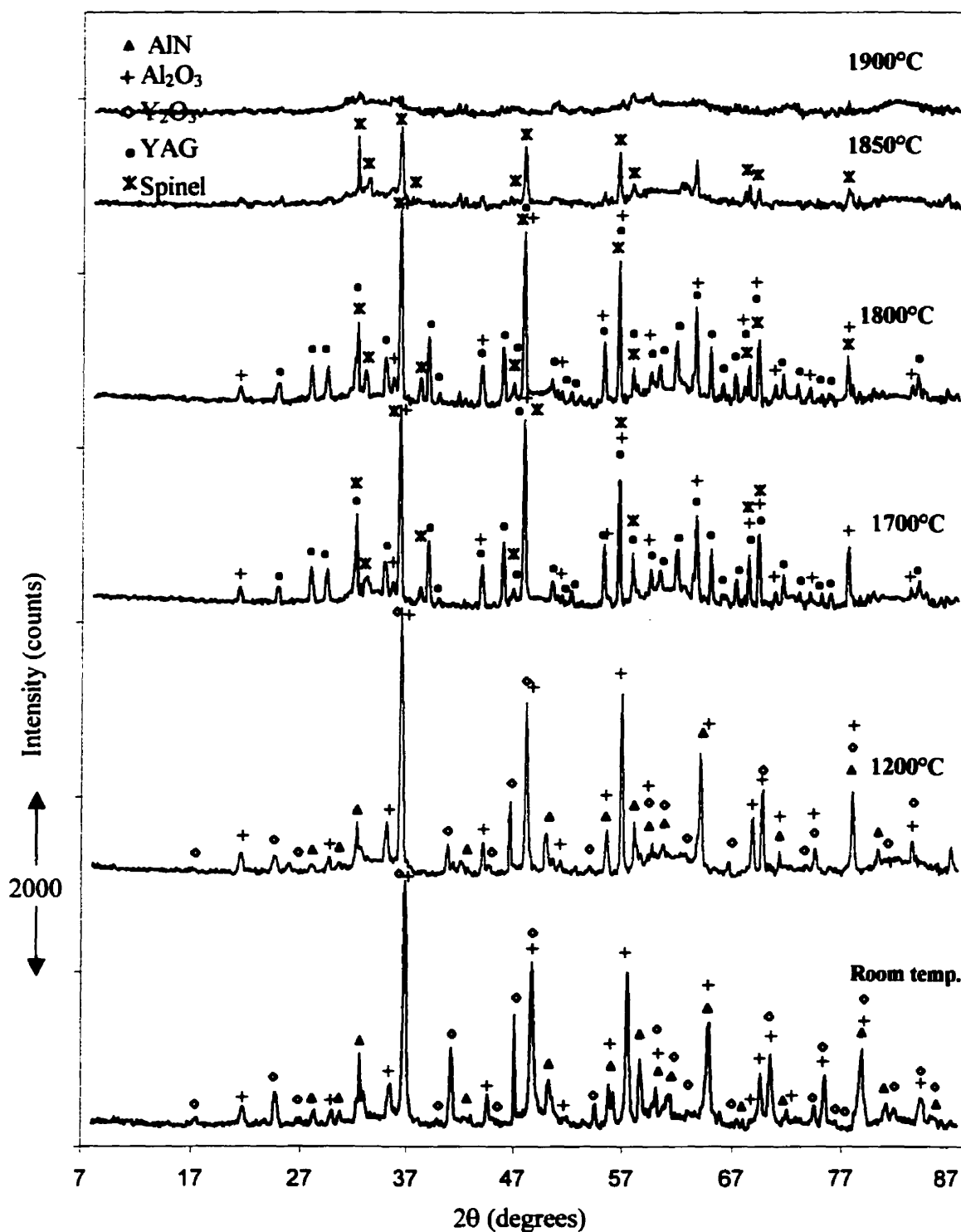


Figure 9-2: Neutron diffractograms during heating of composition 1 (12 mol% AlN, 74 mol% Al_2O_3 and 14 mol% Y_2O_3).

Figure 9-3 shows the cooling cycle for composition 1. It can be seen that spinel was fully crystallized at 1850°C, confirming that the liquidus point is in the temperature range of 1850°C to 1900°C. However the diffraction pattern collected at 1800°C did not show YAG peaks as in the 1800°C pattern collected during heating. This can be due to the following reasons: in general it was noticed that the peaks in the cooling cycle are weaker than those collected during heating, due to shrinkage of the sample at the melting point, also, the background of the patterns collected during cooling was higher than of those collected during the heating cycle. In any case, YAG peaks were noticed to have lower counts than those of spinel phase. This may have contributed to the loss of YAG peaks in the background of the pattern at 1800°C. By cooling to 1400°C, decomposition of the spinel phase occurred. This is evident by the new peaks of AlN and Al₂O₃ detected at this temperature. YAG peaks were also observed in the diffraction pattern collected at 1400°C. The same phases were found in the diffraction patterns collected at 1000°C with higher counts of AlN and Al₂O₃ peaks indicating more decomposition of spinel phase upon cooling.

Comparing the pattern of 1000°C and that collected at room temperature revealed that they were similar. This sample was composed of AlN, YAG and Al₂O₃ at room temperature.

In order to have a complete understanding of the reaction for this composition from its melting point to low temperature, a continuous relationship between the relative mass of each phase and temperature was established using the phase assemblage diagrams (Figure 9-4). This diagram was calculated for all the investigated compositions and will be discussed in the following sections.

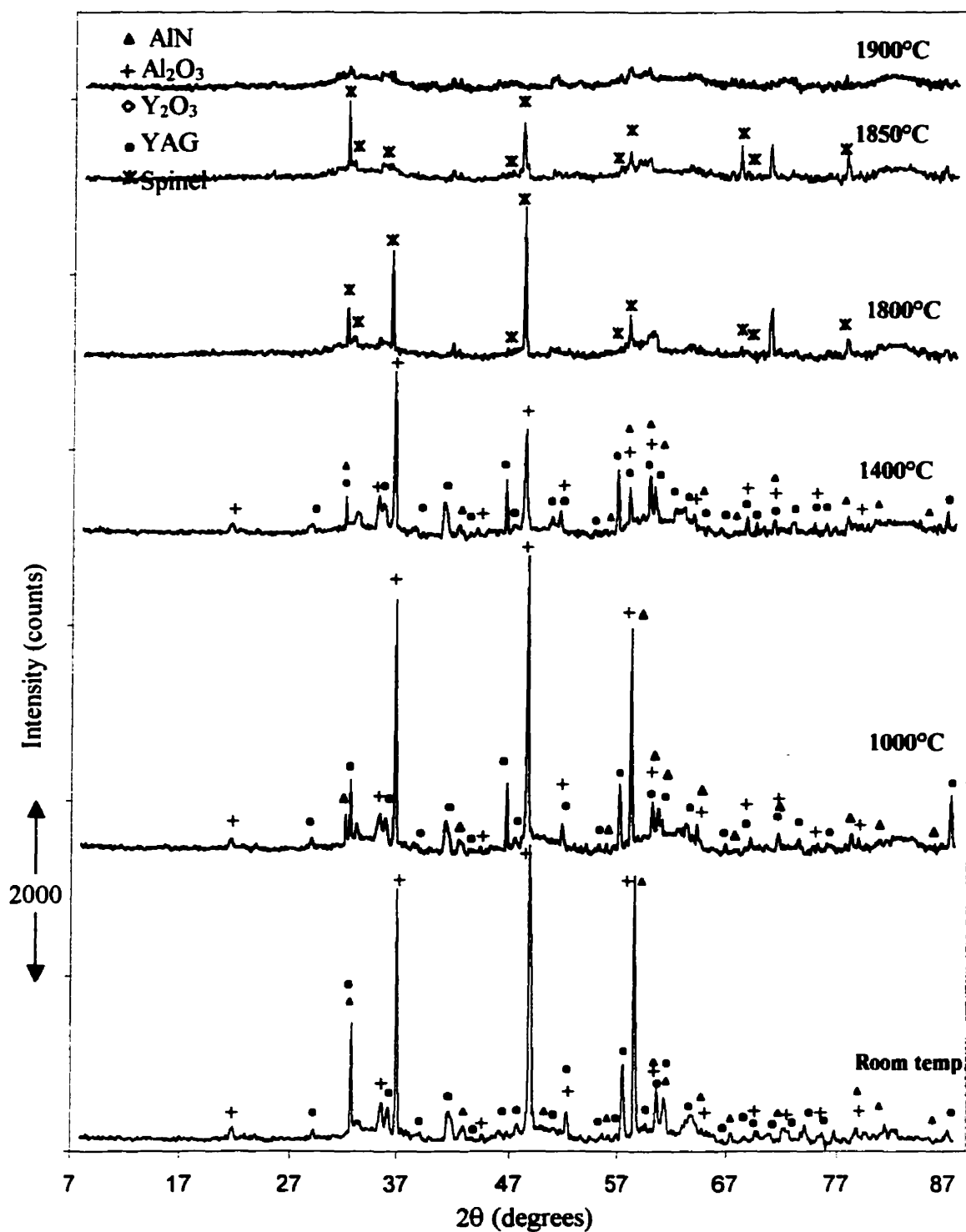


Figure 9-3: Neutron diffractograms during cooling of composition 1 (12 mol% AlN, 74 mol% Al_2O_3 and 14 mol% Y_2O_3).

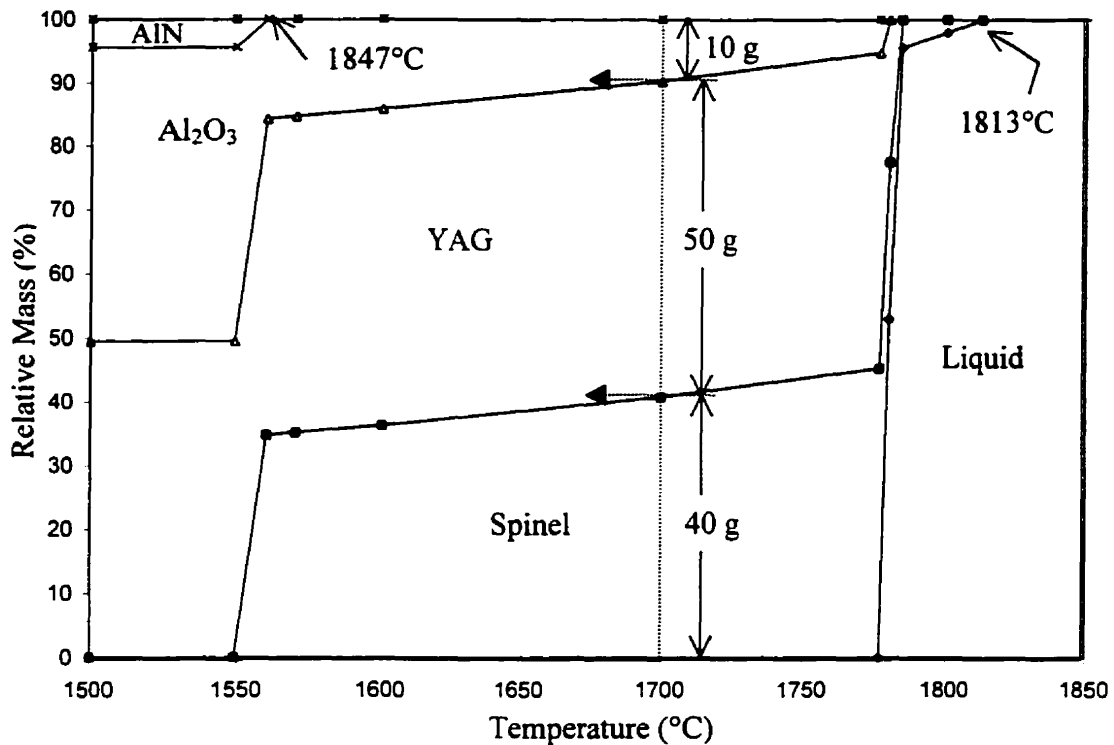


Figure 9-4: Phase assemblage diagram of composition 1 (12 mol% AlN, 74 mol% Al_2O_3 and 14 mol% Y_2O_3).

Figure 9-4 is calculated from the thermodynamic database of $\text{AlN-Al}_2\text{O}_3\text{-Y}_2\text{O}_3$, for a sample composition of 12 mol% AlN, 74 mol% Al_2O_3 and 14 mol% Y_2O_3 . The proportion of different phases can easily be read from this figure. For instance, at 1700°C, 100 g of the overall material consists of 40 g of spinel, 50 g of YAG and 10 g of Al_2O_3 . This is consistent with the neutron diffraction pattern collected at 1700°C of this composition (Figure 9-2) which shows that this sample was composed of spinel, YAG and Al_2O_3 .

Thermodynamic calculations showed that the liquidus point of this composition is 1815°C. However, melting was detected in the temperature range of 1850°C to 1900°C. This higher value is due to the fact that the sample temperature was monitored outside the molybdenum tube as mentioned earlier. This difference was noticed in all the samples. As a result, spinel and liquid were present at 1850°C in Figure 9-2, while spinel starts solidifying at 1815°C according to the thermodynamic calculations shown in Figure 9-4.

Figure 9-4 shows that by cooling the melt of (12 mol% AlN , 74 mol% Al_2O_3 and 14 mol% Y_2O_3) composition, spinel first starts to recrystallize followed by the crystallization of YAG and Al_2O_3 . This is in complete consistency with the neutron diffraction patterns collected during the cooling of this sample.

It can be seen from this figure that as the temperature decreased the proportion of spinel phase decreased until it decomposes at around 1550°C to give Al_2O_3 and AlN . This agrees with Figure 9-3, where AlN peaks were observed in the neutron diffraction pattern collected at 1400°C showing the decomposition of the spinel phase. One more important point can be deduced from this figure is that, around 1800°C , the proportion of solids increases rapidly with small decrease in temperature. This means that the composition is sensitive to small changes in the operating temperature.

9.2 Composition 2

Different types of reactions were obtained when starting with 17.5 mol% AlN 64 mol% Al_2O_3 and 18.5 mol% Y_2O_3 . This was obvious when the collected spectra of this composition at different temperatures (shown in Figure 9-5) were compared. The first changes are visible by comparing the neutron diffraction patterns collected at 1300°C with that at room temperature. The pattern at 1300°C clearly showed a reduction in the intensity of Y_2O_3 and Al_2O_3 peaks in addition to the growth of YAG peaks. No changes could be observed in AlN peaks by heating to 1300°C . YAG peaks continue to grow, whereas the peaks of Al_2O_3 and Y_2O_3 disappeared with increasing temperature up to 1600°C .

At 1600°C traces of AlN can be observed along with spinel and YAG phases. This agrees with what Williams *et al.* reported. They found that the reaction rate between AlN and Al_2O_3 to produce spinel was slow at temperatures below 1750°C [101]. The patterns collected in the temperature range of 1600°C to 1850°C look similar, except for the reduction in the intensity of AlN peaks with the progression of heating, indicating that the amount of AlN is decreasing with increasing temperature.

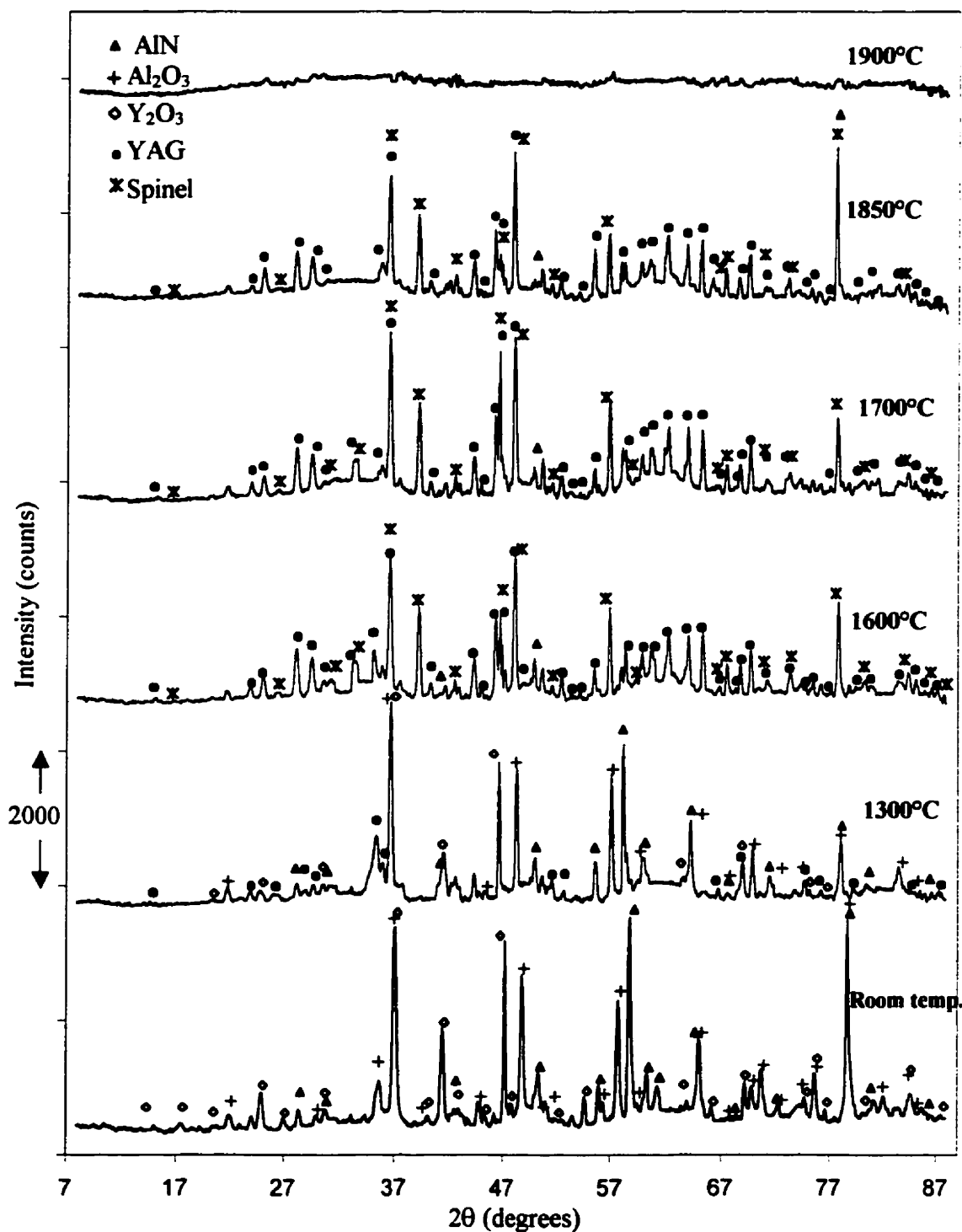


Figure 9-5: Neutron diffractograms during heating of composition 2 (17.5 mol% AlN 64 mol% Al₂O₃ and 18.5 mol% Y₂O₃).

The isothermal section in Figure 9-1 (c) shows that this composition should have liquid and YAG at 1800°C, whereas peaks for spinel were observed at 1850°C indicating that no decomposition of spinel took place during heating from 1700°C to 1850°C.

Figure 9-5 shows that the current composition lost crystallinity in the diffraction pattern collected at 1900°C. This indicates that the sample melted between 1850°C and 1900°C. This is in complete agreement with the isothermal section calculated at 1900°C Figure 9-1 (b), where this composition lies in the liquid region.

Figure 9-6 shows the cooling cycle of composition 1 (17.5 mol% AlN 64 mol% Al_2O_3 and 18.5 mol% Y_2O_3). It can be seen that YAG was fully crystallized by cooling to 1850°C. AlN or spinel peaks could not be observed at this temperature. This indicates that YAG and liquid are in equilibrium at 1850°C for this composition. By cooling to 1800°C spinel peaks appear. This means that spinel has crystallized in the temperature range of 1850°C to 1800°C.

No difference was noticed when the diffraction patterns collected during cooling to 1750°C, 1700°C and 1400°C were compared. AlN peaks could not be seen in these patterns because of its small quantity as it is shown in the assemblage diagram of this composition (Figure 9-7).

In addition to YAG and spinel peaks, Al_2O_3 and AlN peaks were observed upon cooling to room temperature. This shows the decomposition of the spinel phase to AlN and Al_2O_3 while cooling to a lower temperature than 1400°C. Since traces of spinel phase were observed at room temperature, incomplete decomposition occurred for the spinel of this sample. This might be due to the rapid cooling from 1400°C to room temperature without annealing at an intermediate temperature as in composition 1. Nevertheless, this agrees with Yawei *et al's* findings, when they annealed a sample with high spinel content in flowing nitrogen gas at 1550°C for 3 h. They found AlN, Al_2O_3 and spinel peaks at room temperature. The spinel powder used was produced at 1800°C [105].

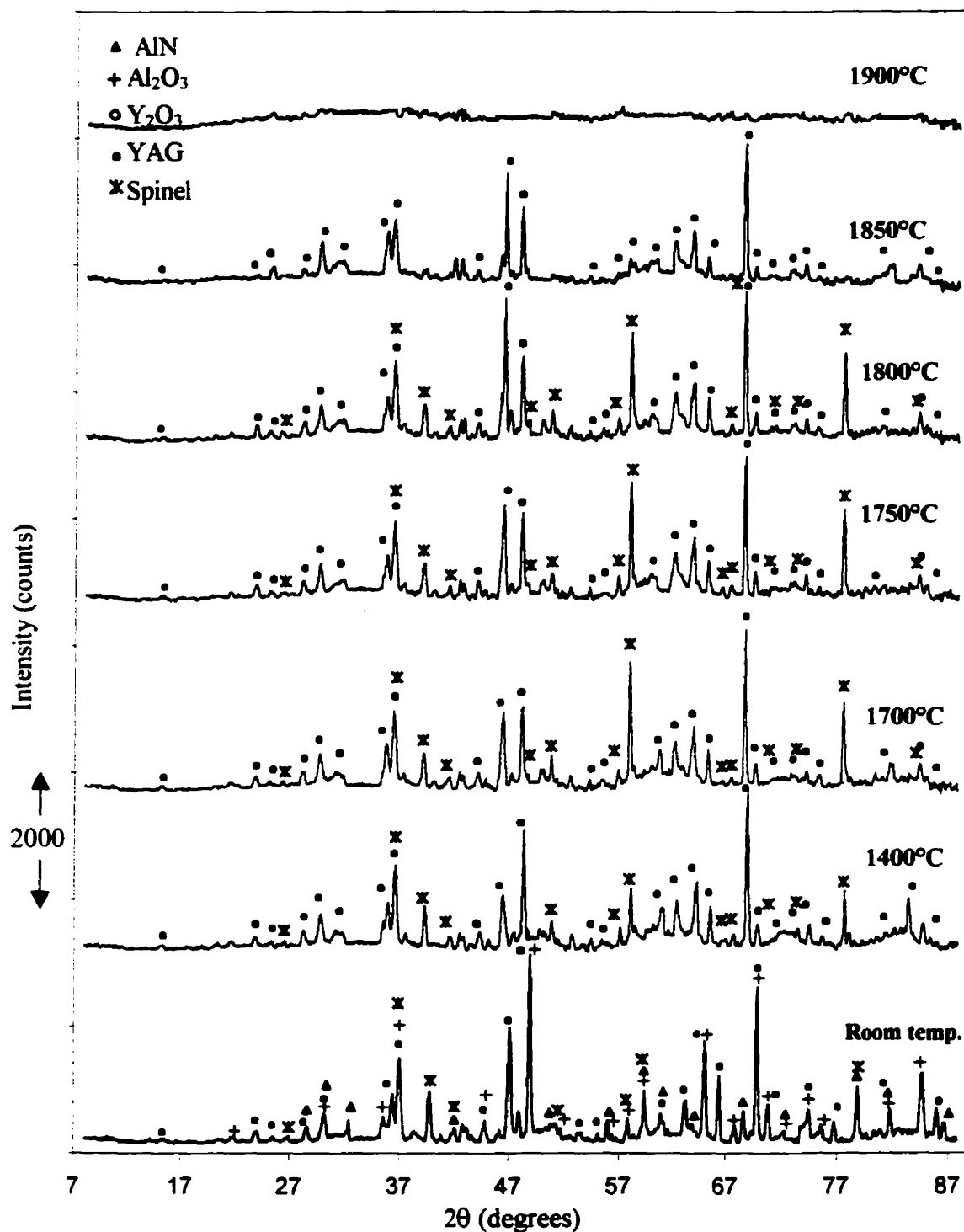


Figure 9-6: Neutron diffractograms during cooling of composition 2 (17.5 mol% AlN 64 mol% Al₂O₃ and 18.5 mol% Y₂O₃).

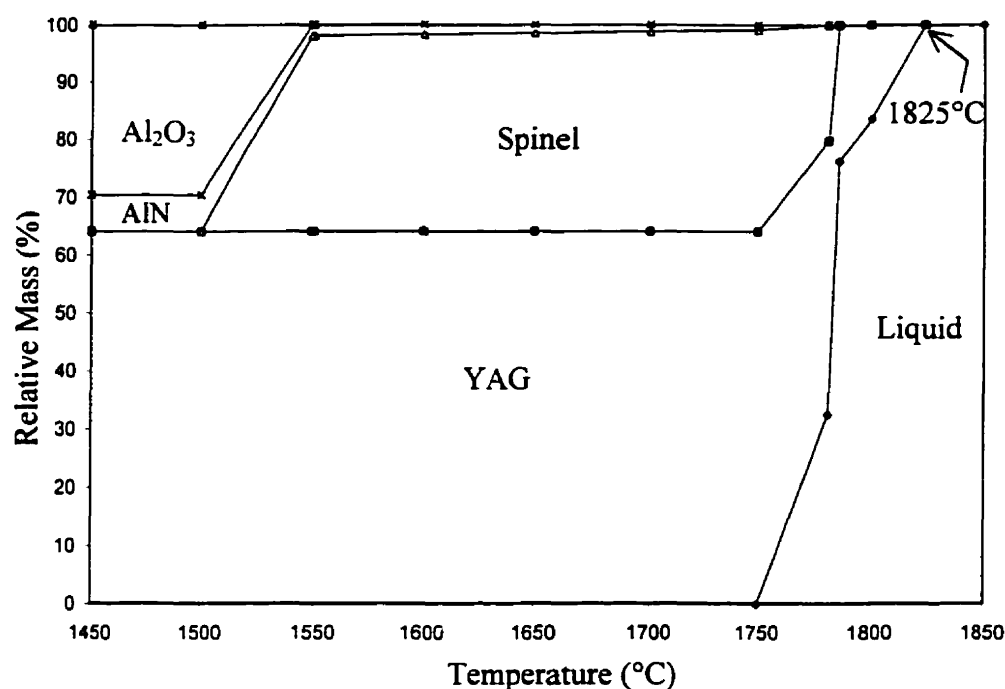


Figure 9-7: Phase assemblage diagram of composition 2 (17.5 mol% AlN 64 mol% Al_2O_3 and 18.5 mol% Y_2O_3).

The phase assemblage versus temperature of this composition is presented in Figure 9-7. It can be seen that the liquidus temperature of this composition is 1825°C, wherein the material melted in the temperature range of 1850°C to 1900°C. This difference is attributed to the temperature reading outside the molybdenum pencil tube as discussed before. Cooling this composition from its melt shows that YAG solidifies first and then spinel. This is completely consistent with the neutron diffraction results for the cooling of this composition shown in Figure 9-6.

Thermodynamic calculations show that spinel decomposes completely at around 1500°C, and at room temperature 100 g of overall material should consist of 64 g YAG 6 g AlN and 30 g Al_2O_3 , whereas, the neutron diffraction pattern collected during cooling of this composition indicated that decomposition starts at a temperature lower than 1400°C. In addition, incomplete decomposition occurred by cooling to room temperature leaving some residual spinel due to the high cooling rate (25°C/min) as shown in Figure 7-12.

9.3 Composition 3

The neutron diffraction patterns of heating and cooling of composition 3 are shown in Figures 8-8 and 8-9. It can be seen from Figure 9-8 that a mixture of 24 mol% AlN, 6 mol% Al_2O_3 and 70 mol% Y_2O_3 produced YAG and spinel phases at 1700°C. This is consistent with the isothermal section calculated at this temperature shown in Figure 9-1(d). As it is predicted by thermodynamics, this composition has liquid and spinel phases at 1900°C as well as at 2000°C (Figure 9-1(b) and (a)). Neutron diffraction patterns collected at these two temperatures are in agreement with the calculations.

The first changes are visible when comparing the neutron diffraction patterns at 1500°C with that at room temperature, where additional peaks of YAG phase appear. YAG peaks continue to grow with increasing temperature to 1700°C indicating incomplete formation of YAG phase at 1500°C. Also, AlN and Al_2O_3 were observed at 1500°C and disappeared at 1700°C to produce the spinel phase.

By heating to 1850°C, most of the YAG peaks were eliminated, however some weak peaks are still present suggesting that traces of the YAG phase are still present with the liquid and spinel phases at this temperature. YAG peaks appearing at this temperature may be due to of the kinetics of the reaction, where YAG phase appeared for sometime at the beginning of the two hour holding period, then when the reaction reached equilibrium its counts did not increase, and this is the reason behind observing only weak peaks at the diffraction angles of YAG's strong peaks. This can be supported by the neutron diffraction pattern collected at this temperature during cooling (Figure 9-9) where there are no YAG peaks.

Neutron diffraction pattern collected at 1900°C showed only spinel peaks, which indicated the formation of the liquid phase. Spinel peaks are weaker at 2000°C indicating less amount of spinel and more liquid phase. Since this pattern shows that there is a crystalline phase at this temperature, the liquidus point of this composition is higher than 2000°C.

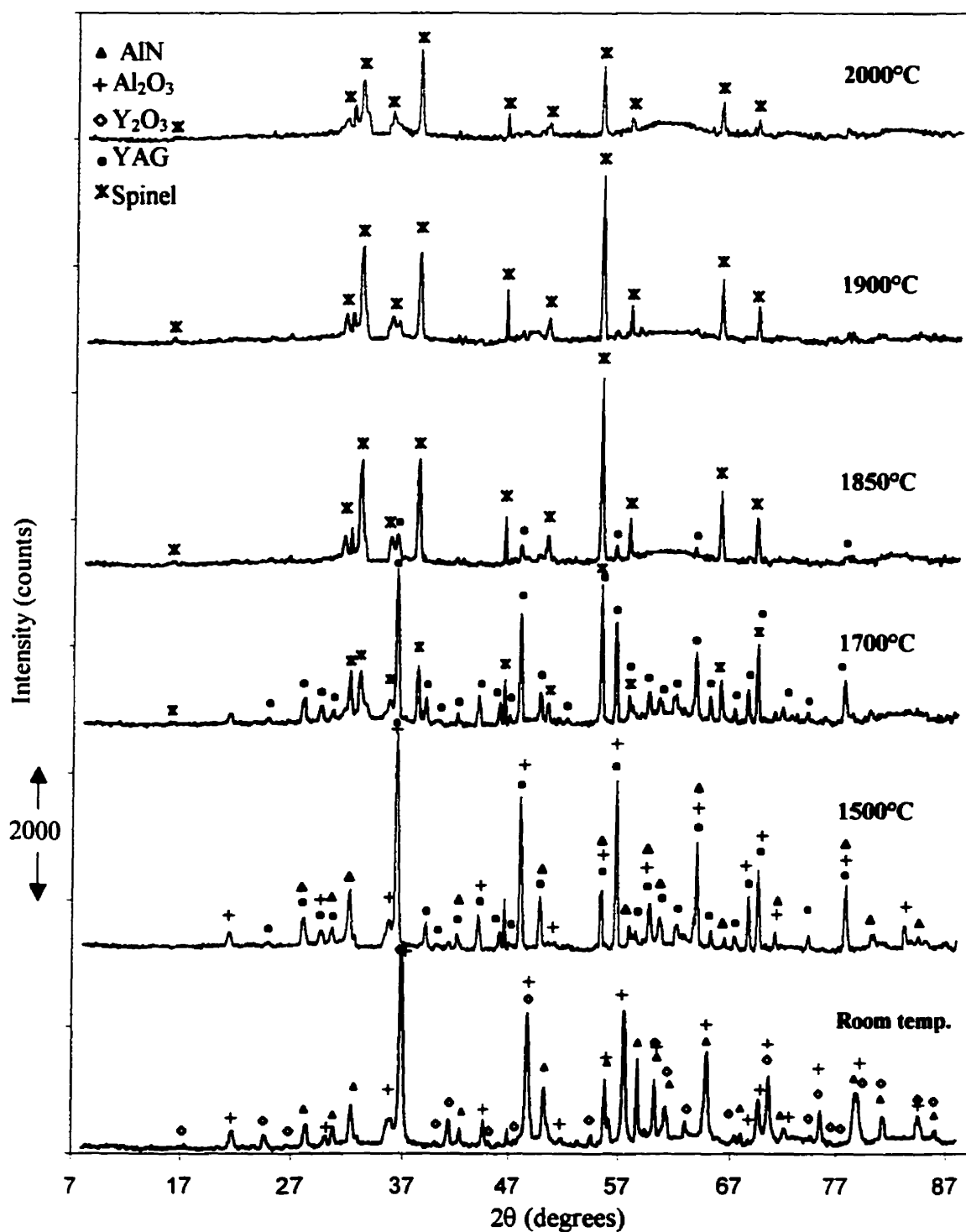


Figure 9-8: Neutron diffractograms during heating of composition 3 (24 mol% AlN 70 mol% Al₂O₃ and 6 mol% Y₂O₃).

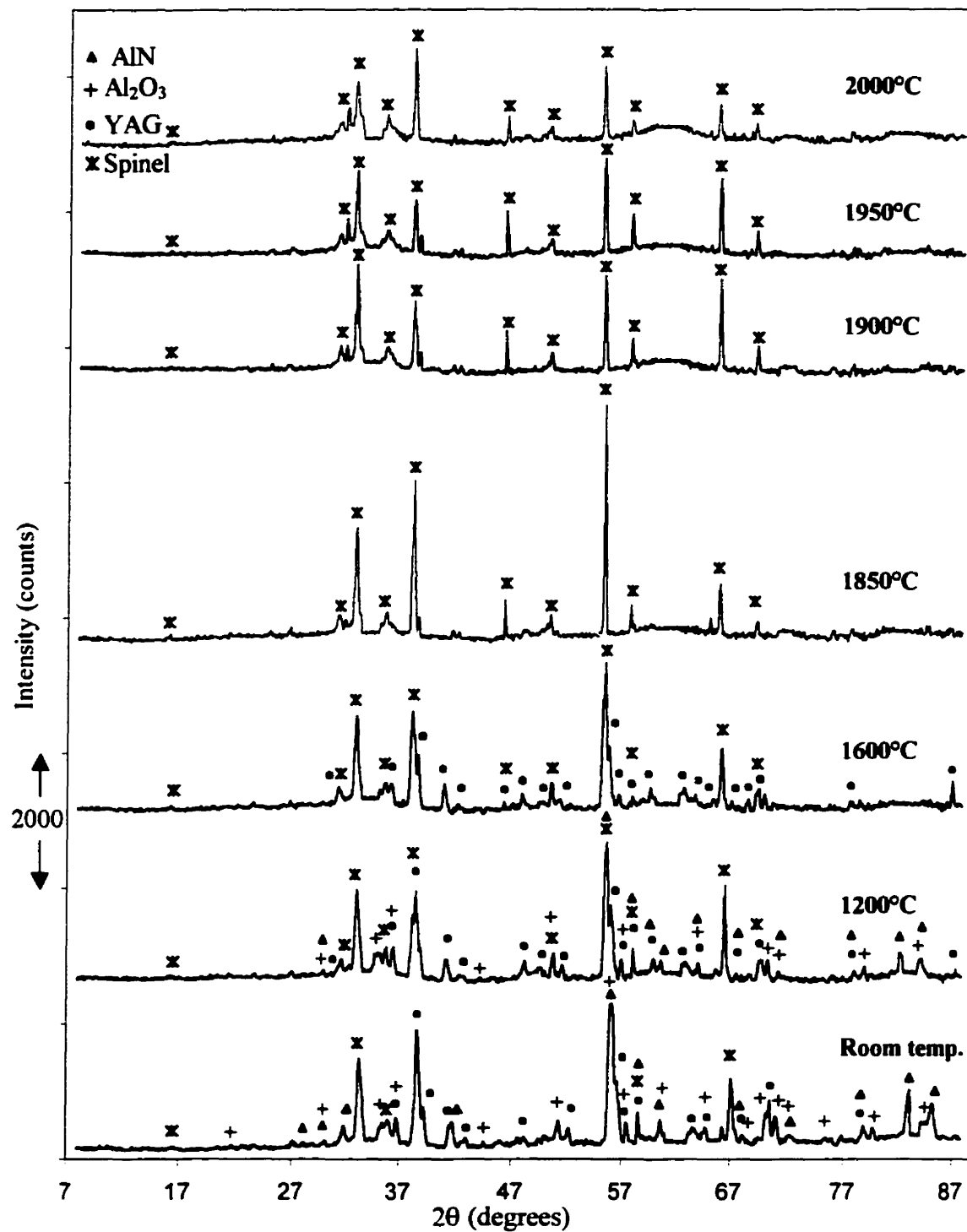


Figure 9-9: Neutron diffractograms during cooling of composition 3 (24 mol% AlN 70 mol% Al₂O₃ and 6 mol% Y₂O₃).

Figure 9-9 is for the neutron diffraction patterns collected during the cooling cycle of this composition. It can be seen from this figure that the spinel and liquid phases are present down to 1850°C. The spinel peak heights increase with decreasing temperature showing more crystallization. This is in complete agreement with the thermodynamic calculations presented in Figures 8-1(a), (b) and (c), where this composition consisted of liquid and spinel at 2000°C, 1900°C and 1800°C.

Upon cooling to 1600°C, YAG peaks were observed. This indicated that the YAG phase crystallized in the temperature range from 1850°C to 1600°C.

At 1200°C AlN and Al_2O_3 peaks were detected in addition to spinel and YAG. This shows that spinel decomposition occurred between 1600°C and 1200°C. Since spinel peaks were present, incomplete decomposition occurred by cooling to 1200°C.

The pattern collected at room temperature shows similar composition to that at 1200°C with higher AlN peaks and lower spinel peaks. This indicates more, but still, incomplete decomposition of spinel phase.

Figure 9-10 is calculated from the thermodynamic database constructed for $\text{AlN-Al}_2\text{O}_3\text{-Y}_2\text{O}_3$ ternary system for the composition 24 mol% AlN 70 mol% Al_2O_3 and 6 mol% Y_2O_3). It can be seen that the calculated liquidus point for this composition is 2030°C. This agrees with the results of neutron diffraction, where the sample was still diffracting at 2000°C, showing that melting takes place at higher temperature. From this figure, spinel starts precipitating then YAG at a lower temperature around 1800°C. This is in complete consistency with the neutron diffraction patterns collected during cooling of this composition shown in Figure 9-9, where spinel was the only solid phase down to 1850°C, then YAG started to precipitate below 1850°C and above 1600°C.

At 1600°C, 100 g of the overall material consists of 75g of spinel and 25 g of YAG. This is consistent with the pattern collected at 1600°C during cooling of this sample, Figure 9-9, which shows that this sample consists of spinel and YAG phases.

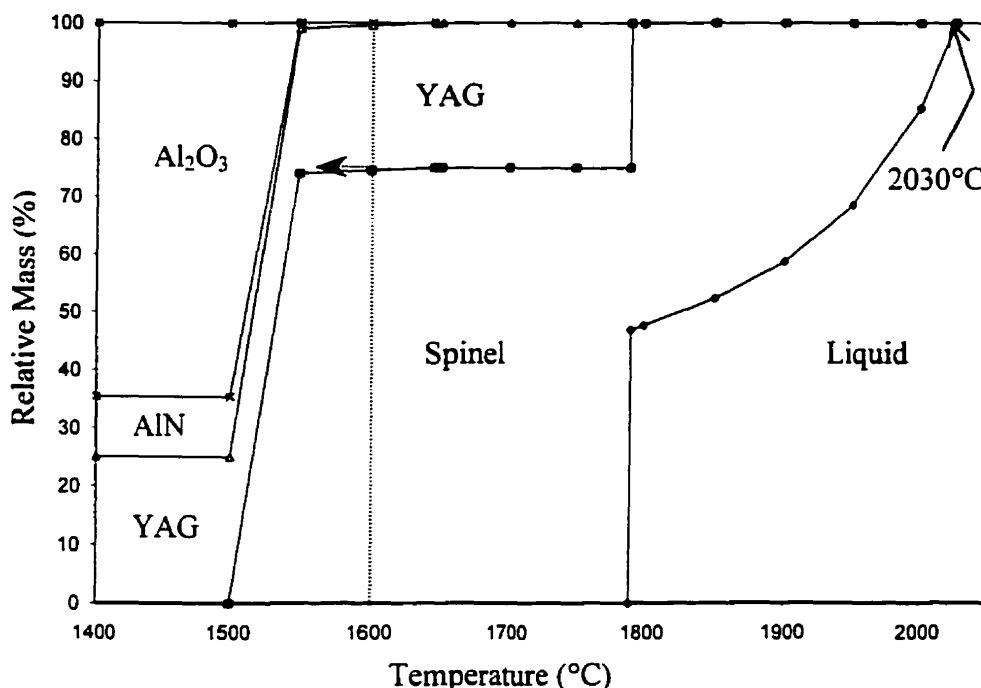


Figure 9-10: Phase assemblage diagram of composition 3 (24 mol% AlN 70 mol% Al_2O_3 and 6 mol% Y_2O_3).

Thermodynamic calculations show that spinel decomposes to Al_2O_3 and AlN completely below 1500°C for this composition. Whereas, the neutron diffraction results (Figure 9-9) show only partial decomposition of spinel of this composition, which starts in the temperature range 1200°C to 1600°C. This may be due to the high cooling rate, around 25°C/min, as shown in Figure 7-12.

9.4 Composition 4

The reaction was followed in this composition (7 mol% AlN 33 mol% Al_2O_3 and 60 mol% Y_2O_3) using the neutron diffraction patterns collected during the heating process to a temperature of 1850°C. It was not possible to pursue this experiment because the furnace failed before reaching 1900°C. However the development of the different phases could be followed up to 1850°C.

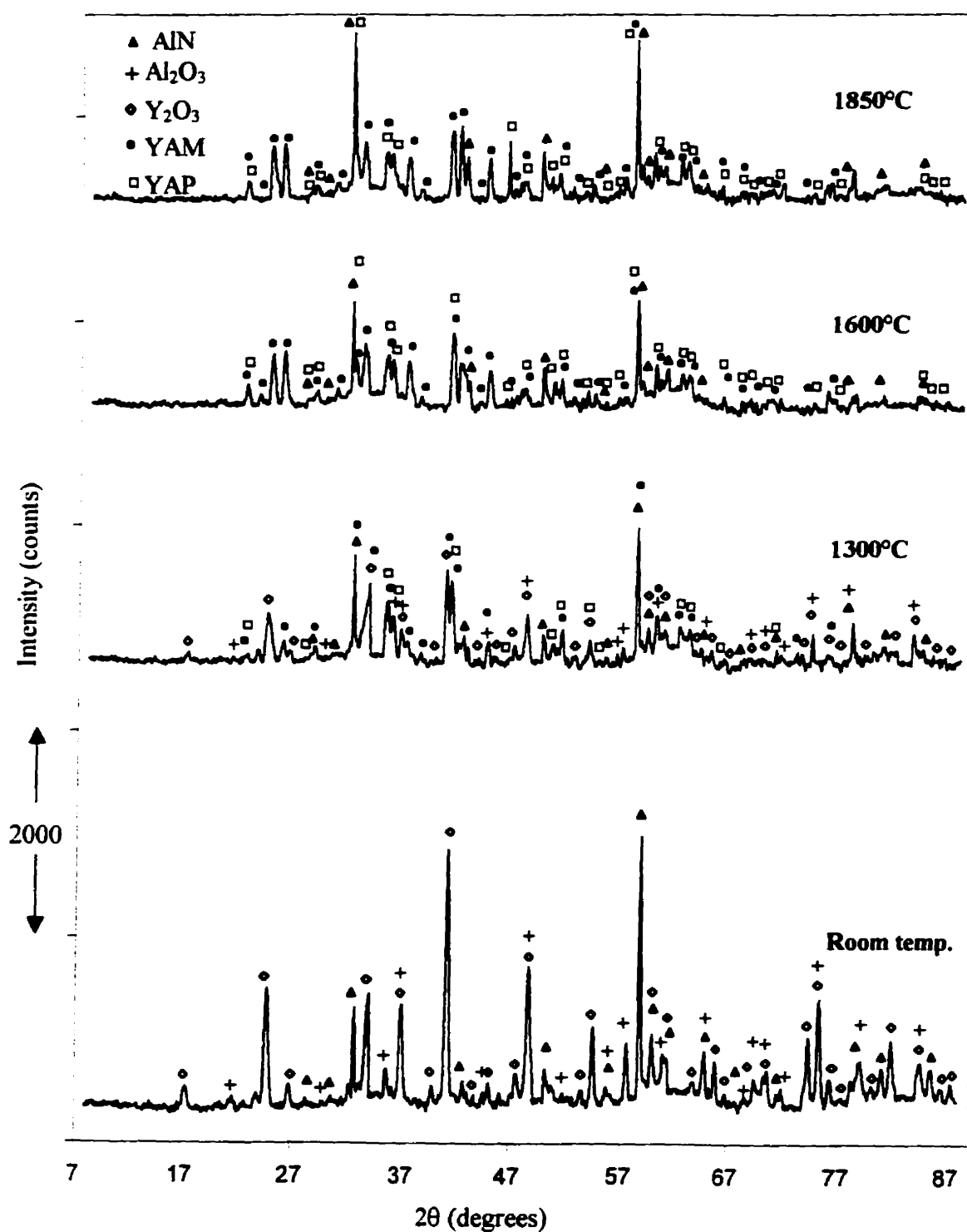


Figure 9-11: Neutron diffractograms during heating of composition 4 (7 mol% AlN 33 mol% Al_2O_3 and 60 mol% Y_2O_3).

Comparing the neutron diffraction pattern at 1300°C and that at room temperature showed that new additional peaks evolved at 1300°C. These peaks were identified as YAM and YAP phases. Al_2O_3 and Y_2O_3 peaks were observed at this temperature with lower peak heights, indicating incomplete formation of YAM and YAP, which started below 1300°C.

By heating to 1600°C there were no visible traces of Al_2O_3 and Y_2O_3 , while higher peaks for YAM and YAP phases were observed. This shows that the reaction to produce YAM and YAP phases was completed below 1600°C. The patterns are not changed at 1850°C and AlN peaks were observed in all the patterns collected up to this temperature, showing that AlN does not react with YAM nor with YAP. This is in complete agreement with the thermodynamic findings presented by the isothermal sections at 1800°C and 1700°C, shown in Figure 9-1 (c) and (d), where this composition lies in the three-phase-region, AlN, YAP and YAM.

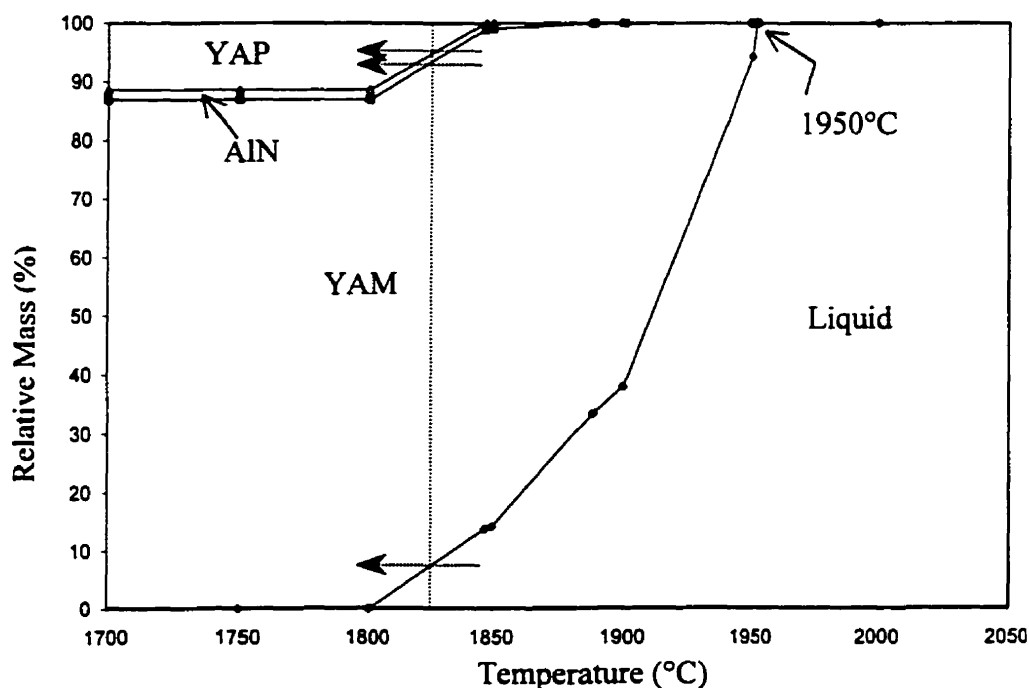


Figure 9-12: Phase assemblage diagram of composition 4 (7 mol% AlN 33 mol% Al_2O_3 and 60 mol% Y_2O_3).

Figure 9-12 is calculated for a sample consisting of 7 mol% AlN, 33 mol% Al_2O_3 and 60 mol% Y_2O_3 . The liquidus temperature of this composition was calculated to be 1952°C. The important point in this composition, as may be seen from Figure 9-12, is that the proportion of solid does not increase rapidly with decreasing temperature. This means that this sample is not sensitive to small changes in temperature. It can be seen from this figure that YAM is the first solid to precipitate upon cooling of this composition. It started crystallizing at 1952°C, whereas AlN and YAP started to precipitate at 1890°C and 1847°C, respectively.

According to the thermodynamic calculations, this composition should start forming a liquid above 1800°C. For example, at 1825°C, 100 g of overall material of this composition should consist of 8 g liquid, 85 g YAM, 2 g AlN and 5 g YAP. However, the liquid phase was not detected at 1850°C because of its small quantity and the fact that the measured sample temperature was lower than 1850°C when the pattern was acquired. For the same reasons the YAP phase was detected at this temperature.

9.5 Composition 5

The development of the neutron diffraction patterns with increasing temperature up to 2000°C for composition 5 (33 mol% AlN 20 mol% Al_2O_3 and 47 mol% Y_2O_3) is shown in Figure 9-13. Comparing the neutron diffraction patterns at 1200°C and that at room temperature shows that no additional peaks evolved at 1200°C. The first noticeable changes for this sample is observed by comparing the neutron diffraction patterns collected at 1500°C and 1200°C. Additional peaks of YAM phase appear, whereas no traces of Al_2O_3 were observed at 1500°C, indicating complete reaction and formation of the YAM phase. At this temperature significant amounts of AlN and Y_2O_3 were observed. Diffraction patterns of 1800°C and 1500°C are practically unchanged, proving that no reaction occurs between AlN with either YAM or Y_2O_3 . This agrees very well with the isothermal sections show in Figures 8-1(c) and (d) where this composition is in the three-phase-region AlN, YAM and Y_2O_3 at 1800°C and 1700°C, respectively.

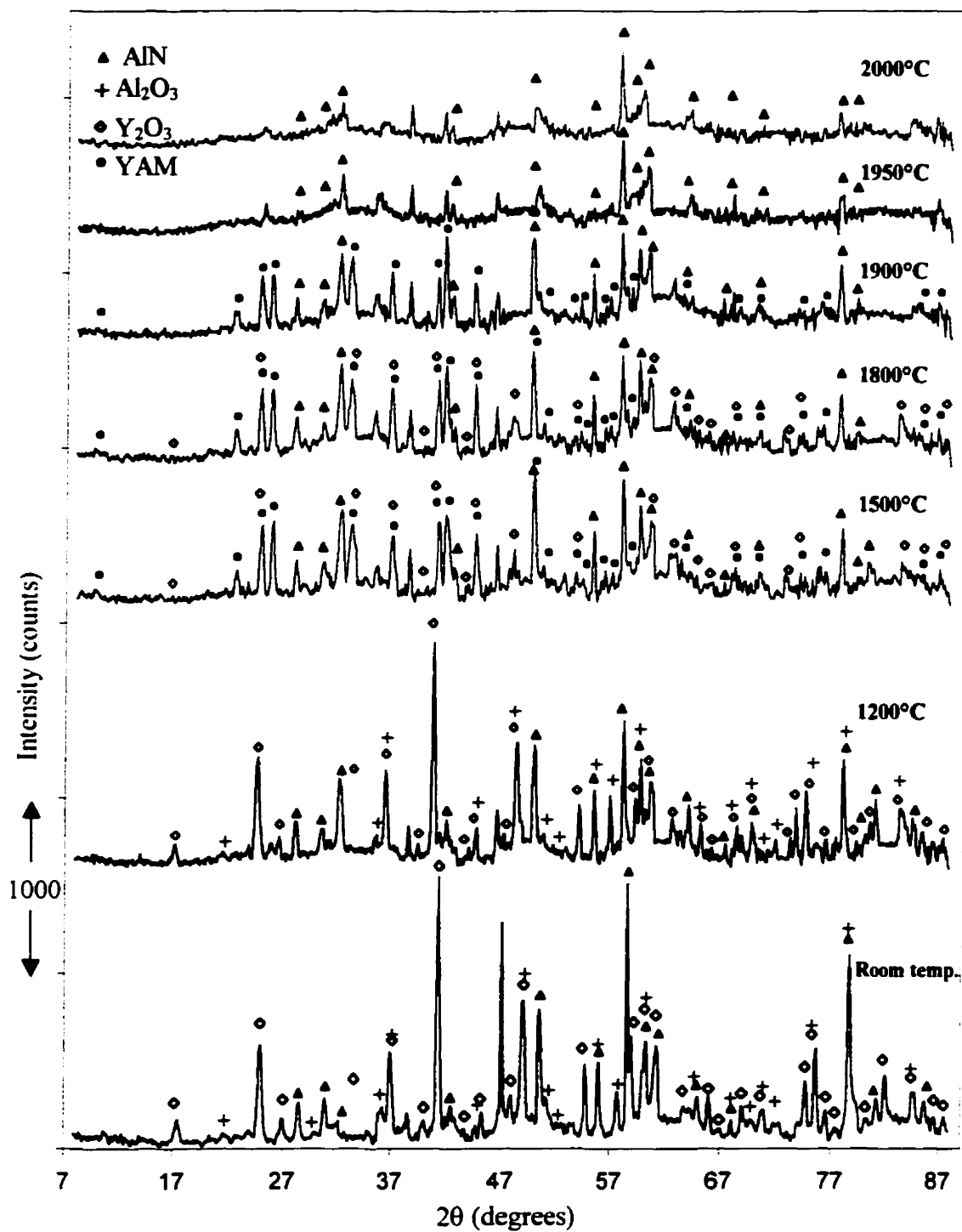


Figure 9-13: Neutron diffractograms during heating of composition 5 (33 mol% AlN 20 mol% Al_2O_3 and 47 mol% Y_2O_3).

By heating to 1900°C Y₂O₃ peaks were completely eliminated, unlike the YAM peaks, which were still present. But Figure 9-1(b) shows that this composition should have only AlN as solid phase in equilibrium with liquid. Since this figure is consistent with the neutron diffraction pattern collected at 1950°C, the discrepancy is due to the difference between the actual and the measured temperature which is estimated to be around 30°C.

Diffraction patterns collected at 1950°C and 2000°C were practically the same, where AlN and liquid phases were present at these temperatures. This is in complete agreement with the isothermal section calculated at 2000°C (Figure 9-1 (a)).

The neutron diffraction pattern of the cooling cycle for this composition is shown in Figure 9-14. By cooling from 2000°C to 1900°C, YAM peaks appear in addition to the already existing AlN peaks. This indicates that YAM started to recrystallize in the temperature range of 2000°C and 1900°C. Further cooling to 1850°C resulted in solidification of Y₂O₃ and because higher peaks of YAM and AlN is observed at this temperature, more precipitation of them occurred. The same phases were observed at 1600°C with a difference in their relative amounts. These results agree very well with the neutron diffraction patterns collected during heating of this composition and with the isothermal sections presented in Figure 9-1.

By cooling to 800°C and then to room temperature no difference was observed except the increase in the peak heights showing better crystallization with decreasing temperature. At room temperature this composition consisted of AlN, YAM and Y₂O₃.

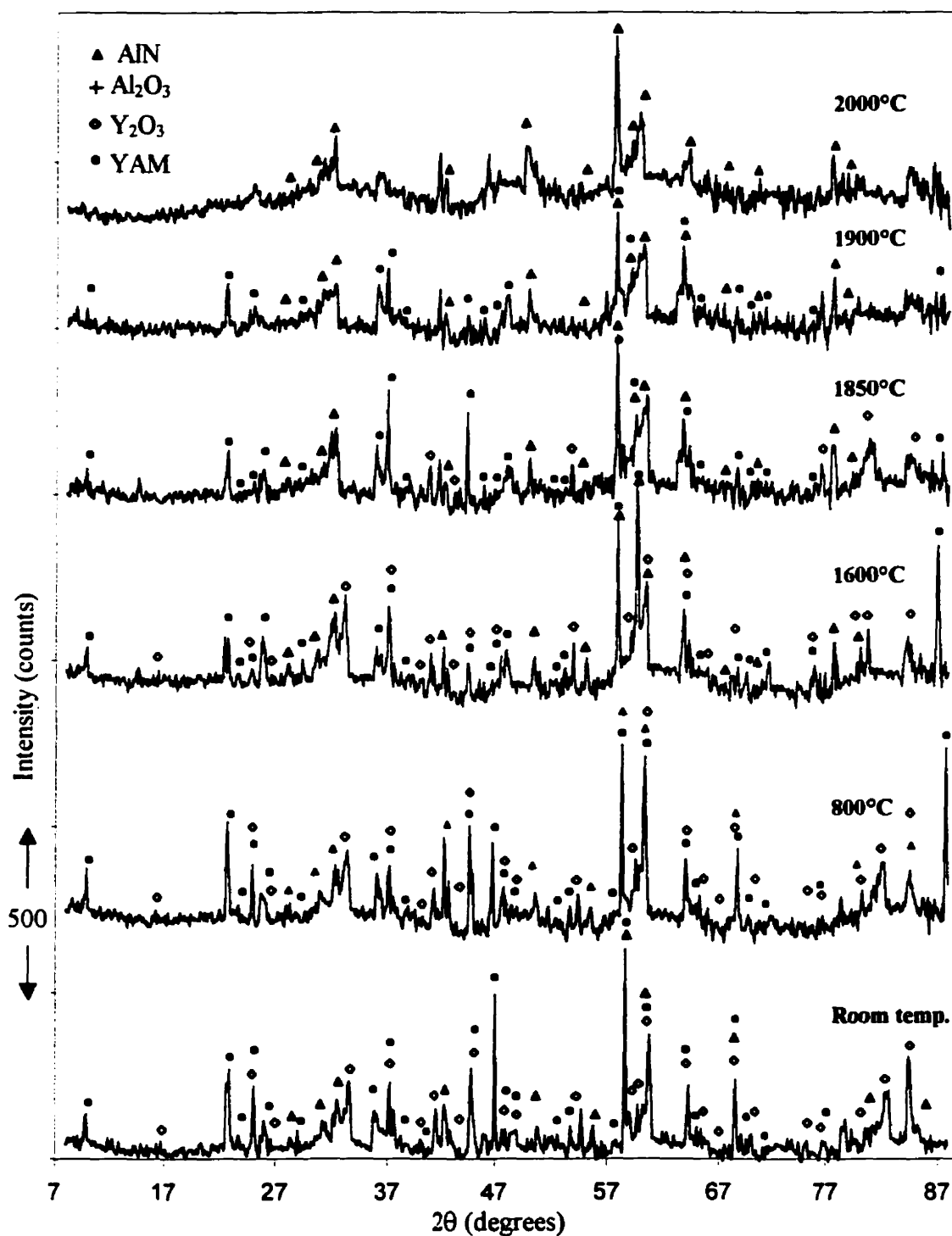


Figure 9-14: Neutron diffractograms during cooling of composition 5 (33 mol% AlN 20 mol% Al_2O_3 and 47 mol% Y_2O_3).

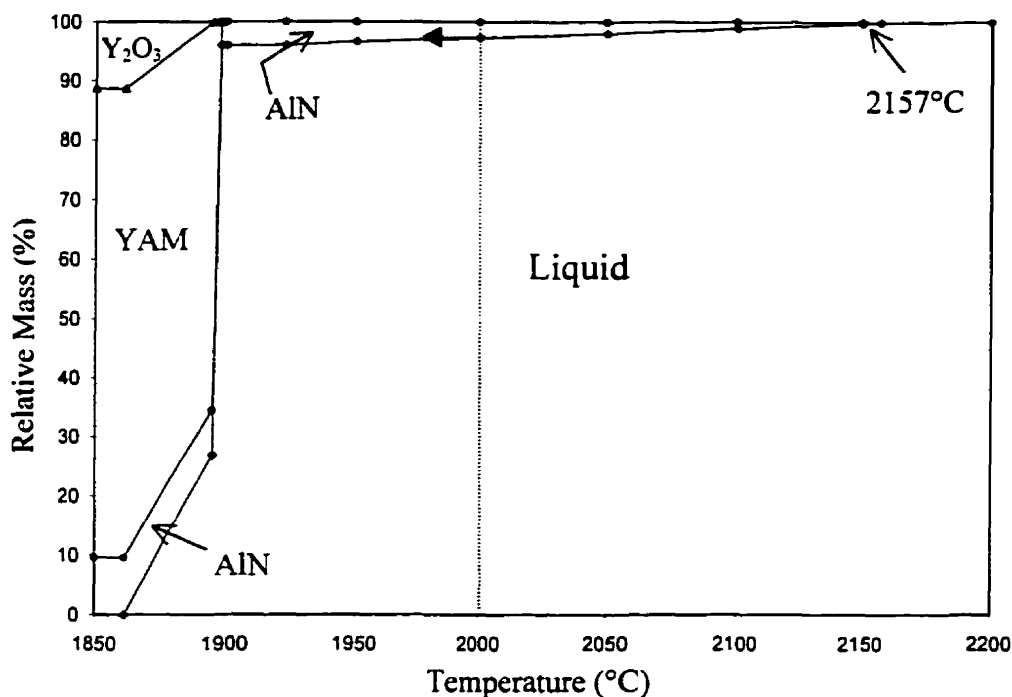


Figure 9-15: Phase assemblage diagram of composition 5 (33 mol% AlN 20 mol% Al_2O_3 and 47 mol% Y_2O_3).

Figure 9-15 is calculated for (33 mol% AlN 20 mol% Al_2O_3 and 47 mol% Y_2O_3) composition from the thermodynamic database of the $\text{AlN-Al}_2\text{O}_3\text{-Y}_2\text{O}_3$ system. Although this composition has a relatively high melting temperature of 2157°C, liquid starts forming at 1861°C, as can be seen from this figure.

Cooling a sample of this composition from its melt shows that the major phase will be liquid, down to 1898°C. Below this temperature the amount of solid increases rapidly. For instance: a 100 g of this sample will be composed of 97 g liquid and 3 g AlN at 2000°C. This agrees with the neutron diffraction pattern collected at this temperature, where AlN peaks were observed.

This Figure shows that Y_2O_3 starts to recrystallize below 1900°C, which is consistent with the neutron diffraction patterns collected during cooling of this sample at 1900°C and 1850°C (the latter showed Y_2O_3 peaks).

At room temperature a 100 g sample would be composed of 10 g AlN 78 g YAM and 12 g Y₂O₃. The room temperature pattern of Figure 9-14 showed these three phases with strong peaks of YAM phase confirming the thermodynamic calculations.

Chapter 10:

CONCLUSIONS, ORIGINAL CONTRIBUTIONS TO KNOWLEDGE AND SUGGESTIONS FOR FUTURE WORK

10.1 Conclusions

The present research was conducted to establish and investigate the equilibria in the AlN-Al₂O₃-Y₂O₃ ternary system and from the results the following conclusions can be drawn:

- Thermodynamic data for the three binary systems were evaluated simultaneously to obtain one set of self-consistent model coefficients for the Gibbs energy of all phases as functions of temperature and composition.
- The phase diagrams of the AlN-Al₂O₃-Y₂O₃ system were calculated based on the Redlich-Kister polynomial model. The three binary systems were first optimized, and then phase diagrams of the ternary system were calculated from the optimized model parameters.
- Very good predictions of the thermodynamic properties of the AlN-Al₂O₃-Y₂O₃ ternary system have been obtained with the polynomial model by using only

parameters from the binary system. Five ternary eutectic points occur in this system in the temperature range 1776°C and 1861°C.

- Calculated binary phase diagrams from the obtained thermodynamic parameters reproduce the experimental measured values from the literature very well.
- The optimized parameters of the spinel phase describe very closely the thermodynamic properties of this phase.
- An optimized self-consistent thermodynamic database has been developed with the computer system, F*A*C*T. This database can now be used to predict the phase relations and various thermodynamic properties in this three-component system, which represents sintering process of AlN.
- Thermodynamic modeling of the AlN-Al₂O₃-Y₂O₃ system provides an important basis for understanding the sintering behaviour of aluminum nitride, and explains the experimental results:
 - Samples with higher density have lower liquid formation temperature.
 - Thermal conductivity is related to the chemistry of the secondary phases.
 - Samples with residual Al₂O₃ and/or spinel have lower thermal conductivity.
 - Thermal conductivity decreases with the increasing amount of the YAP phase, because YAP wets the AlN surface and prevents AlN-AlN surface contact.
- High-purity YAG, YAP and YAM compounds have been produced successfully through a melt extraction technique.
- The calculated Al₂O₃-Y₂O₃ binary phase diagram was investigated using x-ray diffraction for nine different compositions. The calculated phase diagram is in excellent agreement with x-ray diffraction results.

- High temperature neutron diffractometry has permitted us to follow, in real time, the reactions involved in the Al_2O_3 - Y_2O_3 phase diagram, especially to determine the temperature range of each reaction, which would have been impossible to determine *ex situ*.
- Formation of the stoichiometric compounds in the Al_2O_3 - Y_2O_3 sub-system and their melting points were determined using high temperature neutron diffractometry as:
 - YAG phase starts forming below 1200°C and the reaction finishes between 1500°C and 1600°C . YAG melts in the temperature range of 1950°C to 2000°C .
 - YAP phase requires higher temperature to form when compared to YAG. It starts forming in the temperature range of 1200°C to 1500°C and finishes between 1700°C and 1800°C . YAP melts at a temperature higher than 1900°C .
 - And the reaction of YAM phase starts below 1200°C and finishes between 1700°C and 1800°C . So even though YAM started to form at lower temperatures than YAP, the reaction was completed in the same temperature range. YAM needed higher temperature than 1950°C to melt.
- Experimental investigation of the equilibria AlN - Y_2O_3 system was performed using *in situ* neutron diffractometry:
 - There is no reaction or mutual solubility between AlN and Y_2O_3 .
 - The equilibria in AlN - Y_2O_3 can be described as simple eutectic binary phase diagram.
 - The eutectic temperature is between 1950°C and 2000°C and the composition is 47 mol% AlN .
 - Experimental results are consistent with the thermodynamic findings of AlN - Y_2O_3 system.

- AlN-Al₂O₃-Y₂O₃ ternary phase diagram was investigated and verified experimentally using in situ neutron diffractometry:
 - Thermodynamic calculations of AlN-Al₂O₃-Y₂O₃ agree with the experimental results.
 - There is no reaction between AlN and YAG, YAP, YAM or Y₂O₃ which supports the thermodynamic findings.
 - Discrepancy between experimental results and thermodynamic calculations of spinel decomposition temperature was encountered. Nevertheless, spinel slow reaction and critical thermodynamic properties have been previously reported in the literature.

10.2 ORIGINAL CONTRIBUTIONS TO KNOWLEDGE

- AlN-Al₂O₃-Y₂O₃ ternary phase diagram was constructed for the first time in this work. This includes thermodynamic calculation of the equilibria in this system in addition to the experimental verification.
- High temperature *in situ* neutron diffraction investigation up to 2000°C was conducted for the first time in this work. This yielded to full understanding of the reaction and phase formation in AlN-Al₂O₃-Y₂O₃ ternary system during heating and crystallization of these phases during cooling.
- This is a first attempt to explain the sintering behaviour of AlN sintered with Y₂O₃ as an additive, using thermodynamic modeling of the AlN-Al₂O₃-Y₂O₃ ternary phase diagram.
- Unique dynamic determination of the formation and melting temperatures of the stoichiometric compounds in Al₂O₃-Y₂O₃ was established in this study.
- AlN-Y₂O₃ is thermodynamically modeled and experimentally verified *in situ* at high temperature for the first time in this research.

10.3 Suggestions for future work

- *In situ* high temperature is not restricted to the field of phase diagram elaboration. It should bring precise information on other processing techniques. Sintering processes of AlN or other ceramic materials can be continuously monitored at different working conditions. Using this technique will reveal important information such as: the temperature at which liquid formation initiates, the shrinkage rate, and the optimum time required for full densification.
- In this study, it was possible to produce pure YAG, YAP and YAM phases using the melt extraction technique. Since these compounds have applications in electronic industry, a complete study of establishing suitable processes for manufacturing modified compounds ready for electronic applications is required.
- High temperature differential thermal analysis (DTA) up to 2000°C should be used to study the equilibria in the AlN-Al₂O₃-Y₂O₃ ternary system. This technique provides measured thermodynamic data for different compositions from which thermodynamic properties such as enthalpy, entropy and heat capacity can be generated and an experimental phase diagram can be constructed.
- Implementing the methodology used throughout this research to other ceramic materials, especially when the equilibria phase diagram are lacking, such as in the case of Si₃N₄ and SiAlON.

References

1. T. B. Jackson, A. V. Virkar, K. L. More, R. B. Dinwiddie and R. A. Cutler, "High-Thermal Conductivity Aluminum Nitride Ceramics: The Effect of Thermodynamic, Kinetic, And Microstructure Factors", *J. Am. Ceram. Soc.*, 80[6], 1421-1435 (1997).
2. M. Sternitzke and G. Muller, "EELS Study of Oxygen Diffusion In Aluminum Nitride", *J. Am. Ceram. Soc.* 77[3], 737-742 (1994).
3. N. D. Kerness, T. Z. Hossain and S. C. McGuire, "Impurity Study of Alumina and Aluminum Nitride Ceramics: Microelectronics Packaging Applications", *Appl. Radial. Isot.*, 48[1], 5-9 (1997).
4. L. M. Sheppard, "Aluminum Nitride: a Versatile But Challenging Material", *Ceram. Bull.*, 69[11], 1801-1812 (1990).
5. "United States and Japan Cooperate on Aluminum Nitride Research", *J. Res. Natl. Inst. Stand. Technol.*, 101[6], 840 (1996).
6. N. Muraki, V. Sergo, G. Pezzotti, G. Katagiri, S. Meriani and T. Nishida, " Raman Piezo-Spectroscopic Behaviour of Aluminum Nitride", *Appl. Spectrosc.*, 51[11], 1761-1765 (1997).
7. F. Miyashiro, N. Iwase, A. Tsuge, F. Ueno, M. Nakahashi and T. Takahashi, "High Thermal Conductivity Aluminum Nitride Ceramic Substrate and Packages", *IEEE Transactions on Components, Hybrids, and Manufacturing Technology*, 13[2], 313-319 (1990).
8. Y. Baik and R. A. L. Drew, "Aluminum Nitride: Processing and Applications", *Key Eng. Mater.*, 122-124, 553-570 (1996).
9. R. Koba, J. Harris, R. Youngman, M. Mallinger and L. B. Max, "Aluminum-Nitride Packages Provide Consistent Performance", *Microwave and RF*, 156-166 (1997).

10. N. Kuramoto, H. Taniguchi and I. Aso, "Development of Translucent Aluminum Nitride Ceramics", *Ceram. Bull.*, 68[4], 883-887 (1989).
11. J. C. Nipko and C. K. Loong, "Phonon Excitations and Related Thermal Properties of Aluminum Nitride", *Phys. Rev. B*, 57[17], 10550-10554 (1998).
12. W. D. Callister, *Materials Science and Engineering: An Introduction*, John Wiley and Sons Inc., Reading, (1996).
13. Y. Yong, J. Lee, H. S. Kim and J. Y. Lee, "High Resolution Transmission Electron Microscopy Study on The Microstructures of Aluminum Nitride and Hydrogenated Aluminum Nitride Films Prepared by Radio Frequency Reactive Sputtering", *Appl. Phys. Lett.*, 71[11], 1489-1491 (1997).
14. E. Ruiz, S. Alvarez and P. Alemany, "Electronic Structure and Properties of AlN", *Phys. Rev. B*, 49[11], 7115-7123 (1994).
15. H. Kim and A. J. Moorhead, "Oxidation Behaviour and Flexural Strength of Aluminum Nitride Exposed to Air at Elevated Temperature", *J. Am. Ceram. Soc.* 77[4], 1037-1041 (1994).
16. V. Nicolaescu, G. Tardos and R. E. Riman, "Thermogravimetric Determination of Carbon, Nitrogen, and Oxygen in Aluminum Nitride", *J. Am. Ceram. Soc.* 77[9], 2265-2272 (1994).
17. K. Miwa and A. Fukumoto, "First-Principles Calculation Of The Structural, Electronic, And Vibrational Properties Of Gallium Nitride And Aluminum Nitride", *Phys. Rev. B*, 48[11], 7897-7902 (1993).
18. D. P. Dandekar, A. Abbate and J. Frankel, "Equation of State of Aluminum Nitride and Its Shock Response", *J. Appl. Phys.*, 76[7], 4077-4085 (1994).
19. Y. Baik, "Sintering of Aluminum Nitride with Y_2O_3 by Secondary Phase Composition Control", Ph.D. Thesis, McGill University, (1995).

20. P. S. de Baranda, A. K. Knudsen and E. Ruh, "Effect of CaO on the Thermal Conductivity of Aluminum Nitride", *J. Am. Ceram. Soc.* **76**[7], 1751-1760 (1993).
21. O. N. Grigoriyev, S. M. Kushnerenko, K. A. Plotnikov and W. Kreher, "Separation of Internal Strains and Lattice Distortion Caused By Oxygen Impurities in Aluminum Nitride", *Advances in x-ray analysis*, **38**, 479-487 (1995).
22. A. Tsuge, H. Inoue, M. Kasori and K. Shinozaki, "Raw Material Effect on AlN Powder Synthesis from Al₂O₃ Carbothermal Reduction", *J. Mater. Sci.*, **25**, 2359-2361 (1989).
23. J. W. McCauley and N. D. Corbin, "High Temperature Reactions and Microstructures in the Al₂O₃-AlN System", *Progress in Nitrogen Ceramics*, 111-118 (1983).
24. D. W. Richerson, *Modern Ceramic Engineering*, Marcel Dekker Inc., Reading, New York (1992).
25. M. Hirano, K. Kato, T. Isobe and T. Hirano, "Sintering and Characterization of Fully Dense Aluminum Nitride Ceramics", *J. Mater. Sci.*, **28**, 4725-4730 (1993).
26. P. S. de Baranda, A. K. Knudsen and E. Ruh, "Effect of Silica on the Thermal Conductivity of Aluminum Nitride", *J. Am. Ceram. Soc.* **76**[7], 1761-1771 (1993).
27. N. H. Kim, K. Komeya and T. Meguro, "Effect of Al₂O₃ Addition on Phase Reaction of AlN-Y₂O₃ System", *J. Mater. Sci.*, **31**[6], 1603-1608 (1996).
28. P. S. de Baranda, A. K. Knudsen and E. Ruh, "Effect of Ytria on the Thermal Conductivity of Aluminum Nitride", *J. Am. Ceram. Soc.* **77**[7], 1846-1850 (1994).
29. M. P. Borom, G. A. Slack and J. W. Szymaszek, "Thermal Conductivity of Commercial Aluminum Nitride", *Ceram. Bull.*, **51**[11], 852-856 (1972).
30. M. Kasori and F. Ueno, "Thermal Conductivity Improvement of YAG Added AlN Ceramics in the Grain Boundary Elimination Process", *J. Europ. Ceram. Soc.*, **15**, 435-443 (1995).

31. S. Loughin, R. H. French, W. Y. Ching, Y. N. Xu and G. A. Slack, "Electronic Structure of Aluminum Nitride: Theory and Experiment", *Appl. Phys. Lett.*, 63[9], 1182-1184 (1993).
32. J. Huang and J. Jih, "Investigation of SiC-AlN: Part II, Mechanical Properties", *J. Am. Ceram. Soc.* 79[5], 1262-1264 (1996).
33. W. Chen and G. Ravichadran, "Static and Dynamic Compressive Behavior of Aluminum Nitride Under Moderate Confinement", *J. Am. Ceram. Soc.* 79[3], 579-584 (1996).
34. H. L. Lu, W. F. Sommer, M. J. Borden, J. R. Tesmer and X. D. Wu, "The Microstructure and Properties of a Buried AlN Layer Produced by Nitrogen Implantation Into Pure Aluminum", *Thin Solid Films*, 229, 17-21 (1996).
35. E. Savrun, C. Toy and M. Sarikaya, "High Thermal Conductivity AlN Packages for High-Temperature Electronics", *Sienna Technical Report No. 974*, (1996).
36. M. Hundere and M. Einarsrud, "Microstructural Development in AlN (YF3) Ceramics", *J. Europ. Ceram. Soc.*, 17[7], 873-879 (1997).
37. L. Dumitrescu and B. Sundman, "A Thermodynamic Reassessment of the Si-Al-O-N System", *J. Euorp. Ceram. Soc.*, 15[3], 239-247 (1995).
38. W. D. Kingery, "Densification During Sintering in the Presence of a Liquid Phase. I. Theory", *J. Appl. Sci.*, 30[3], 301-306 (1959).
39. C. F. Chen, M. E. Perisse, A. F. Ramirez, N. P. Padture and H. M. Chan, "Effect of Grain Boundary Phase on the Thermal Conductivity of Aluminum Nitride Ceramic", *J. Matr. Sci.*, 29, 1595-1600 (1994).
40. M. Hotch, "Calculation of Ternary, Quaternary, and Higher-Order Phase Diagrams from Binary Diagrams and Binary Thermodynamic Data", *J. Phase Equilibria*, 14[6], 710-717 (1993).

41. J. Grobner, H. L. Lukas and F. Aldinger, "Thermodynamic Calculation of the Quasibinary Al_2O_3 - Y_2O_3 System and the Y-Al-O Ternary System", *Z. Metallkd.*, **87**[4], 268-273 (1996).
42. J. S. Abell, I. R. Harris, B. Cockayne and B. Lent, "An Investigation of Phase Stability in the Y_2O_3 - Al_2O_3 System", *J. Mater. Sci.*, [9], 527-537 (1974).
43. B. Cockayne, "The Uses and Enigmas of the Al_2O_3 - Y_2O_3 Phase System", *J. Less-Common Met.*, [114], 199-206 (1985).
44. T. Mah and M. D. Petry, "Eutectic Composition in the Psedobinary of $\text{Y}_4\text{Al}_2\text{O}_9$ and Y_2O_3 ", *J. Am. Ceram. Soc.*, **75**[7], 2006-2009 (1992).
45. Z. Jin and Q. Chen, "An Assessment of the $\text{AlO}_{1.5}$ - $\text{YO}_{1.5}$ System", *CALPHAD*, **1**[19], 69-79 (1995).
46. R. S. Hay, "Phase Transformation and Microstructure Evolution in Sol-Gel Derived Ytria-Alumina Garnet Films", *J. Mater. Res.*, **3**[8], 578-604 (1993).
47. R. S. Roth, *Phase Equilibria Diagrams: Phase Diagrams for Ceramics, Volume XI*, The American Ceramic Society, 107 (1995).
48. J. Grobner, U. Kolitsch, H. J. Seifert, S. G. Fries, H. L. Lukas and F. Aldinger, "Re-Assessment of the Y-O Binary System", *Z. Metallkd.*, [87], 88-91(1996).
49. K. T. Pillai, R. V. Kamat, V. N. Vaidya and D. D. Sood, "Synthesis of Yttrium Aluminium Garnet by the Glycerol Route", *J. Mater. Chem. Phys.*, [44], 255-260 (1996).
50. A. Maier and I. G. Savinova, "Melting Behavior and Crystal Growth of YAlO_3 ", *J. Inorg. Mater.*, **10**[32], 1078-1080 (1996).
51. H. Yamane, M. Omori and T. Hirai, "Twin Structure of $\text{Y}_4\text{Al}_2\text{O}_9$ ", *J. mater. sci. lett.*, [14], 561-563 (1995).

52. H. Yamane, M. Omori, A. Okubo and T. Hirai, "High-Temperature Phase Transition of $Y_4Al_2O_9$ ", *J. Am. Ceram. Soc.*, 76[9], 2382-2384 (1993).
53. H. Yamane, M. Omori and T. Hirai, "Thermogravimetry and Rietveld Analysis for the High-Temperature X-Ray Powder Diffraction Pattern of $Y_4Al_2O_9$ ", *J. mater. sci. lett.*, 7[14], 470-473 (1995).
54. G. Long and L. M. Foster, "Aluminum Nitride, a Refractory for Aluminum to 2000°C", *J. Am. Ceram. Soc.*, 42[2], 53-59 (1959).
55. Warshaw and R. Roy, "Stable and Metastable Equilibria in the Systems $Y_2O_3-Al_2O_3$ and $Gd_2O_3-Fe_2O_3$ ", *J. Am. Ceram. Soc.*, 9[42], 434-438 (1959).
56. N. A. Toropov, I. A. Bondar, F. Ya. Galadzhov, Kh. S. Nikhosyan and N. V. Vinogradova, "Phase Equilibria in the system Yttria-Alumina", *Izv. Akad. Nauk. SSSR, Ser. Khim.*, 7, 1158-1164 (1964).
57. J. L. Caslavsky and D. J. Viechnicki, "Melting Behaviour and Metastability of Yttrium Aluminium Garnet (YAG) and $YAlO_3$ Determined by Optical Differential Thermal Analysis", *J. Mat. Sci.*, [15], 1709-1718 (1980).
58. Bondar, L. N. Koroleva and E. T. Bezruk, "Physicochemical properties of Yttrium Aluminates and Gallates", *J. Inorg. Mater.*, [20], 214-218 (1984).
59. J. Lo, T. Tseng, "Phase Development and Activation Energy of the $Y_2O_3-Al_2O_3$ System by a Modified Sol-Gel Process", *Journal of Materials Chemistry and Physics*, [56], 56-62 (1998).
60. M. Gervais, S. Le Floch, J. C. Rifflet, J. Coutures and J. P. Coutures, "Effect of Melt Temperature on the Solidification Process of Liquid Garnets $Ln_3Al_5O_{12}$ ($Ln = Dy, Y,$ and Lu)", *J. Am. Ceram. Soc.*, 75[11], 3166-3168 (1992).
61. A. A. Maier and I. G. Savinova, "Melting Behaviour and Crystal Growth of $YAlO_3$ ", *Inorg. Mater.*, 32[10], 1078-1080 (1996).

62. L. Kaufman, F. Hayes and D. Birnie, "Calculation of Quasibinary and Quasiternary Oxynitride Systems-IV", *CALPHAD*, 3[5], 163-184 (1981).
63. P. Tabary and C. Servant, "Crystalline and Microstructure Study of the AlN-Al₂O₃ Section in the Al-N-O System; I. Polytypes and γ -AlON Spinel Phase", *J. Appl. Cryst.*, [32], 241-252 (1999).
64. N. D. Corbin, "State of the Art Aluminum Oxynitride Spinel: A Review", *J. Europ. Ceram. Soc.*, [5], 143-154 (1989).
65. C. Qiu and R. Metselaar, "Phase Relation in the Aluminum Carbide-Aluminum Nitride-Aluminum Oxide System", *J. Am. Ceram. Soc.* 80[8], 2013-2020 (1997).
66. J. W. McCauley and N. D. Corbin, "Phase Relations and Reaction Sintering of Transparent Cubic Aluminum Oxynitride Spinel (AlON)", *J. Am. Ceram. Soc.*, 62[9-10], 476-479 (1979).
67. H. Fukuyama, W. Nakao, M. Susa and K. Nagata, "New Synthetic Method of Forming Aluminum Oxynitride by Plasma Arc Melting", *J. Am. Ceram. Soc.*, 82[6], 1381-1387 (1999).
68. H. X. Williams, G. De With and R. Metselaar, "Neutron Diffraction of γ -Aluminium Oxynitride", *J. Mater. Sci. Lett.*, [12], 1470-1472 (1993).
69. H. X. Williams, M. M. R. M. Hendrix, R. Metselaar and G. De With "Thermodynamics of Alon I: Stability at Lower Temperatures", *J. Europ. Ceram. Soc.*, [10], 327-337 (1992).
70. M. Hillert and S. Jonsson, "Thermodynamic Calculation of Al-N-O System", *Z. Metallkd.*, [83], 714-719 (1992).
71. P. Tabary and C. Servant, "Thermodynamic Reassessment of the AlN-Al₂O₃ System", *CALPHAD*, 2[22], 179-201 (1998).

-
72. U. R. Kattner, "The Thermodynamic Modeling of Multicomponent Phase Equilibria", *JOM*, 49[12], 14-19 (1997).
73. J. Hertz, "Josiah Willard Gibbs and Teaching Thermodynamics of Materials (History)", *J. Phase Equilibria*, 5[13], 450-458 (1992).
74. J. W. Gibbs, "Graphical Methods in the Thermodynamics of Fluids", *Transactions of the Connecticut Academy II*, 309-342 (1873).
75. J. W. Gibbs, "Representation by Surfaces of the Thermodynamic of Properties and Substances", *Transactions of the Connecticut Academy II*, 382-404 (1873).
76. J. W. Gibbs, "On Equilibrium of Hetrogeneous Substances: I", *Transactions of the Connecticut Academy III*, 108-248 (1878).
77. J. W. Gibbs, "On Equilibrium of Hetrogeneous Substances: II", *Transactions of the Connecticut Academy III*, 343-524 (1878).
78. J. W. Gibbs, *The Scientific Papers of J. W. Willard Gibbs*, Dover Publication, New York, (1961).
79. J. J. Laar, *Z. Phys. Chem.*, [63], 216-253 (1908).
80. J. H. Hildebrand, "Solubility. XII. Regular Solutions", *J. Am. Ceram. Soc.*, [51], 66-80 (1929).
81. J. L. Meijering and H. K. Hardy, "Closed Miscibility Gaps in Ternary and Quaternary Regular Alloy Solutions", *Acta Metall.*, 4, 249-256 (1956).
82. J. L. Meijering, "Calculation of the Nickel-Chromium-Copper Phase Diagram from Binary Data", *Acta Metall.*, 5, 257-264 (1957).
83. R. E. Loehman, *Characterization of Ceramics*, Butter Worth – Heinemann, (1993).
84. M. Hillert, "Calculation of Phase Diagrams of Multicomponent Systems", *NATO ASI Series E Applies Science – Advanced Study Institute*, [276], 113-124, (1994).

85. H. L. Lukas, E. Th. Henig and B. Zimmermann, "Optimization of Phase Diagrams by a Least Squares Method Using Simultaneously Different Types of Data", *CALPHAD*, 3[1], 225-236 (1977).
86. Bergeron and Risbud, *Introduction to Phase Equilibria in Ceramics*, The American ceramic society, Inc. Reading, (1984).
87. D. A. Porter, K. E. Easterling, *Phase Transformations in Metals and Alloys*, Van Nostrand Reinhold Co. Ltd. England, Reading, (1983).
88. L. Li, Z. Tang, W. Sun and P. Wang, "Calculation of Phase Diagrams of Al_2O_3 - SiO_2 - R_2O_3 Systems", *Phys. Chem. Glasses*, 6[38], 323-326 (1997).
89. G. Eriksson and A. D. Pelton, "Critical Evaluation and Optimization of the Thermodynamic Properties and Phase Diagrams of the MnO - TiO_2 , FeO - TiO_2 , Ti_2O_3 - TiO_2 , Na_2O - TiO_2 and K_2O - TiO_2 systems", *Metall. Mater. Trans., B*, [24B], 795-805 (1993).
90. S. Degterov and A. D. Pelton, "Critical Evaluation and Optimization of the Thermodynamic Properties and Phase Diagrams of the CrO - Cr_2O_3 , CrO - Cr_2O_3 - Al_2O_3 and CrO - Cr_2O_3 - CaO Systems", *J. Phase Equilibria*, 6[17], 476-487 (1996).
91. C. W. Bale, A. D. Pelton and W. T. Thompson, *Facility for the Analysis of Chemical Thermodynamics*, McGill University/Ecole Polytechnique (1996).
92. C. W. Bale and A. D. Pelton, "Series Representations of the Thermodynamic Properties of Solutions", *Can. Metall. Q.*, 3[14], 213-219 (1975).
93. C. W. Bale and A. D. Pelton, "Optimization of Binary Thermodynamic and Phase Diagram Data", *Metall. Mater. Trans., B*, [14B], 77-83 (1983).
94. C. W. Bale and A. D. Pelton, "Coupled Phase Diagram and Thermodynamic Analysis of the 18 Binary Systems Formed Among Li_2CO_3 , K_2CO_3 , Na_2CO_3 , LiOH , KOH , NaOH , Li_2SO_4 , K_2SO_4 and Na_2SO_4 ", *CALPHAD*, 4[6], 253-278 (1982).

95. A. D. Pelton, M. Blander, M. T. Clavaguera-Mora, M. Hoch, L. Höglund, H. L. Lukas, P. Spencer and B. Sundman, "Thermodynamic Modeling of Solutions and Alloys", *CALPHAD*, 2[21], 155-170 (1997).
96. W. T. Thompson and B. R. Davis, "Computer Calculation of Phase Diagrams", *Microstructure Science*, [24], 3-9 (1996).
97. C. W. Bale and A. D. Pelton, "Mathematical Representation of Thermodynamic Properties in Binary Systems and Solution of Gibbs-Duhem Equation", *Metall. Trans.*, [5], 2323-2337 (1974).
98. C. W. Bale, "The Na-Rb (Sodium-Rubidium) System", *Bulletin of Alloy Phase Diagrams*, 3[3], 318-321 (1982).
99. E. Jak, S. Degterov, P. C. Hayes and A. D. Pelton, "Thermodynamic Modeling of Al_2O_3 - SiO_2 - CaO - FeO - Fe_2O_3 to Predict the Flux Requirements for Coal Ash Slags", *FEUL*, 1[77], 77-85 (1998).
100. Z. Fang and L. Chen, "A New Subregular Model and Theoretical Calculation of the Phase Diagram for a Binary System", *Phys. Stat. Sol. A, Appl. Res.*, 140[1], 109-117 (1993).
101. H. X. Willems, M. M. R. Hedrix, G. With and R. Metselaar, "Thermodynamics of Alon II: Phase Relations", *J. Europ. Ceram. Soc.*, [10], 339-346 (1992).
102. V. A. Lysenko, "Thermodynamic Calculation of the Yttrium-Oxygen Phase Diagram", *Inorg. Mater.*, 4[32], 392-396 (1996).
103. R. S. Hay, "Kinetics and Deformation During the Reaction of Yttrium-Aluminum Perovskite and Alumina to Yttrium-Aluminum Garnet", *J. Am. Ceram. Soc.*, 77[6], 1473-1485 (1994).
104. L. G. D'yachkov, L. A. Zhilyakov and A. V. Kostanovskii, "Experimental Instruments and Techniques - Melting of Aluminum Nitride at Atmospheric Nitrogen Pressure", *Tech. Phys.*, 45[7], 928-930 (2000).

105. L. Yawei, L. Nan and Y. Runzhang, "The Formation and Stability of γ -Aluminium Oxynitride Spinel in the Carbothermal Reduction and Reaction Sintering Processes", *J. Mat. Sci.*, [32], 979-982 (1997).
106. R. A. L. Drew, Y. Baik and M. Entezarian, "Effect of Y_2O_3 Content on Sintering of Aluminum Nitride", *Mater. Sci. Forum.*, [325-326], 249-254 (2000).
107. M. Medraj, M. Entezarian and R. A. L. Drew, "Wettability of Al_2O_3 - Y_2O_3 compounds on Aluminum Nitride and Their Role in Sintering", *Sintering 99 Conference Proceedings*, 307-312 (2000).
108. M. Zarinejad, *The Effect of Crystal Structure and Microstructural Evolution on the Thermal Conductivity of Y_2O_3 Sintered Aluminum*, Ph.D. Thesis, McGill University, (2001).
109. M. Faucher, "Refinement of the Y_2O_3 structure at 77K", *Acta Crystall. B*, 24, 1968-2006 (1982).
110. H. Asai and T. Takahashi, "Influence of the Grain Boundary Phase on the Mechanical Strength at Aluminum Nitride Substrates Surfaces", *IEEE trans. adv. packaging*, 23[3], 452-460 (2000).
111. R. Jenkins and J. L. de Vries, *An Introduction to X-ray powder diffractometry*, Second Edition, N. V. Philips Gloeilampenfabrieken, Holand.
112. B. D. Cullity, *Elements of X-ray Diffraction*, Second Edition, Addison-Wesley Publishing Company Inc., USA, (1978).
113. E. A. Aguillar and R. A. L. Drew, "Melt Extraction Processing of Structural Y_2O_3 - Al_2O_3 Fibers", *J. Europ. Ceram. Soc.*, 20, 1091-1098 (2000).
114. O. Yamaguchi, K. Matui and K. Shimizu, "Formation of $YAlO_3$ with Garnet Structure", *Ceram. Int.*, 11[3], 107-108 (1985).

115. T. Hahn, *International Tables for Crystallography: Volume A - Space Group Symmetry*, Third Edition, Kluwer Academic Publishers, (1992).
116. B. Burton, T. B. Chart, H. L. Lukas, A. D. Pelton, H. Seifert and P. Spencer, "Thermodynamic Models and Data for Pure Elements and Other Endmembers of Solutions", *CALPHAD*, 4[19], 537-553 (1995).
117. R. Subramanian, R. Diechmann, G. Eriksson and A. Pelton, "Model Calculations of Phase Stabilities of Oxide Solid Solutions in The Co-Fe-Mn-O System at 1200°C", *J. Phys. Chem. Solids*, 5[55], 391-404 (1994).
118. Powder Diffraction File, Card No. 76-0702 (Joint Committee on Powder Diffraction Standards, Swarthmore, PA, 1997).
119. J. Cheng, D. Agrawal and R. Roy, "Microwave Synthesis of Aluminum Oxynitride (ALON)", *J. mater. sci. lett.*, [18], 1989-1990 (1999).
120. D. R. F. West, *Ternary Equilibrium Diagrams*, McMillan and Company Ltd., London, (1965).
121. R. M. German, *Liquid phase sintering*, Plenum Press, New York, (1985).
122. H. Sawada, "Residual Electron Density Study of α - Aluminum Oxide Through Refinement of Experimental Atomic Scattering Factors", *Mater. Res. Bull.*, 29[2], 127-133 (1994).
123. Powder diffraction file, Card No. 10-0173 (Joint Committee on Powder Diffraction Standards, Swarthmore, PA, 1998).
124. M. A. Sichinava, V. P. Kobaykov and V. N. Taranovskaya, "High-Temperature Compatibility of Alumina/Yttria and Alumina/Scandia Ceramic Contacts", *J. Inorg. Mater.*, 9[35], 965-968 (1999).
125. R. M. German, *Liquid phase sintering*, Plenum Press, New York, (1985).

126. L. Kaufman and H. Bernestine, *Computer Calculation of Phase Diagrams with Special Reference to Refractory Metals*, New York: Academic Press, (1970).
127. M. E. Kipp and D. E. Grady, "Shock Phase Transformation and Release Properties of Aluminum Nitride", *J. De Physique IV*, 4[C8], 249-256 (1994).
128. Powder diffraction file, Card No. 83-0927 (Joint Committee on Powder Diffraction Standards, Swarthmore, PA, 1998).
129. E. Prince, "Neutron Diffraction Measurements on Yttrium-Iron and Yttrium-Aluminum Garnets", *Acta Crystall. B*, [24], 1968-2006 (1982).
130. A. D. Pelton, R. A. Sharma, "Thermodynamic Evaluation of Phase Equilibria in $\text{MCl}_3\text{-MF}_3\text{-MgCl}_2\text{-MgF}_2$ Systems Where $\text{M} = \text{La, Nd, Ce}$ ", *CALPHAD*, 2[20], 231-246 (1996).
131. G. Masing (Translated by B. A. Rogers), *Ternary Systems Introduction to the Theory of Three Component Systems*, Dover Publications, Inc. New York, (1960).
132. R. S. Hay, "Orientation Relationships and Interfaces Between Low Symmetry Phases in the Ytria-Alumina System", *Mat. Res. Soc. Symp. Proc.*, [357], 145-150 (1995).
133. R. Diehl and G. Grandtý G, "Crystal Structure of YAlO_3 , a promising laser material", *Mater. Res. Bull.*, 10, 85-90 (1975).
134. H. Yamane, K. Ogawara, M. Omori and T. Hirai, "Thermal Expansion and Athermal Phase Transition of $\text{Y}_4\text{Al}_2\text{O}_9$ Ceramics", *J. Am. Ceram. Soc.*, 78[5], 1230-1232 (1995).
135. A. D. Pelton, "Thermodynamic Databases and Equilibrium Calculations in Metallurgical Processes", *Pure Appl. Chem.*, 5[69], 969-978 (1997).
136. Herng Liu, D. C. Bertolet, J. W. Rogers. "The Surface Chemistry of Aluminum Nitride MOCVD on Alumina Using Trimethylaluminum and ammonia as Precursors", *Surf. Sci.*, 1[320], 146-160 (1995).
137. Guillo, P., Thesis No. 32-85, University of Limoges, France.

APPENDIX A

In order to calculate a neutron diffraction pattern, the crystal structure, as well as, the atoms positions in the unit cell must be known. Because the peak positions, 2θ , depend on the wavelength used and the spacing of the lattice planes, d . As summarized by Bragg's law:

$$\sin 2\theta = \frac{\lambda}{2d}$$

And any calculation of the intensity of a diffracted beam depends on the structure factor. The structure factor is determined by the arrangement of atoms within a unit cell. In other words crystal structure and atoms positions in the unit cell in addition to λ must be known to calculate neutron diffraction pattern.

Crystal structure description, lattice parameters, atoms positions in the unit cell and the corresponding calculated neutron diffraction pattern for the needed phases will be demonstrated in this appendix.

A-1 Neutron Diffraction Pattern Calculation of Al_2O_3

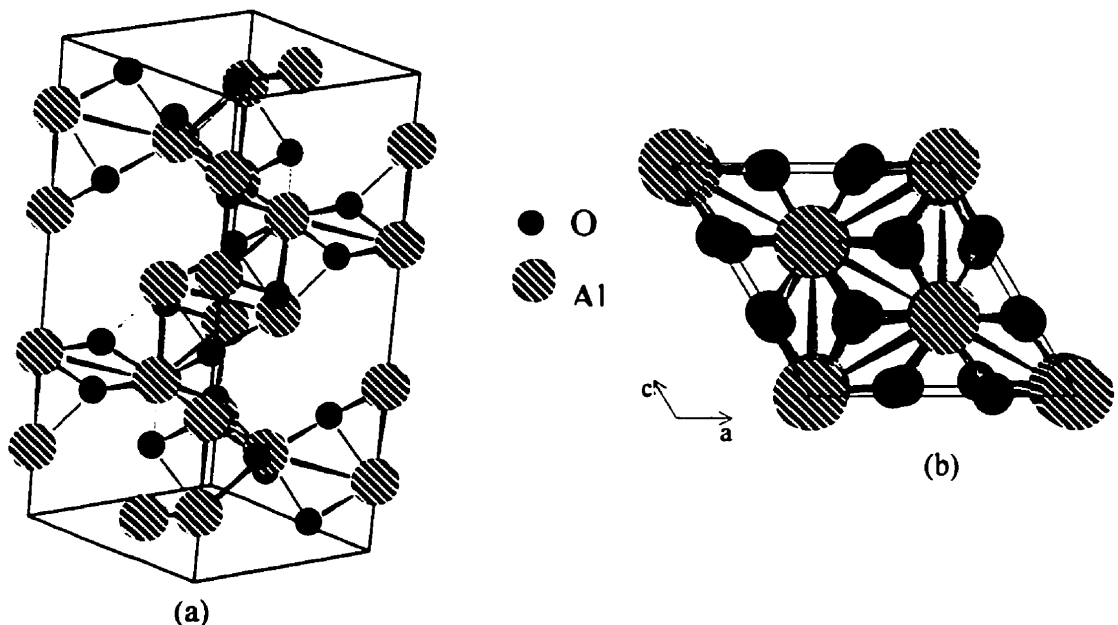


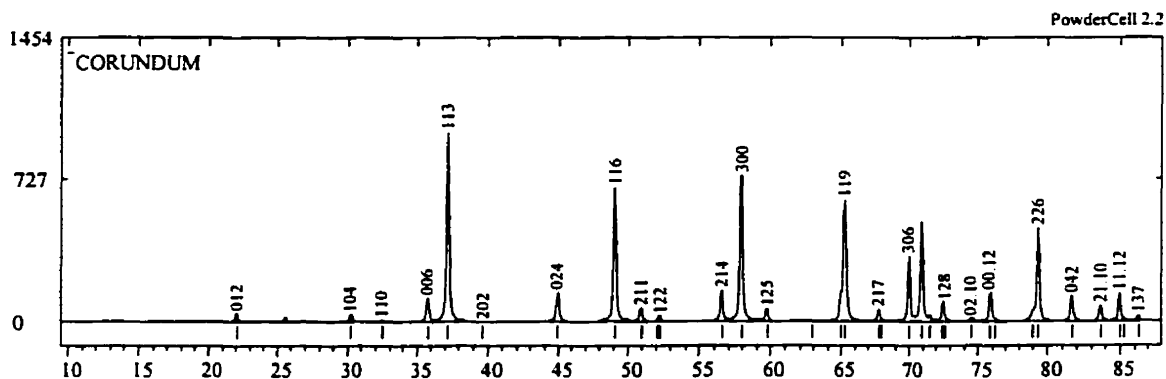
Figure A-1: (a) Al_2O_3 unit cell, (b) (001) projection.

Table A-1: Crystal Structure data of Al_2O_3 [122,123,124].

Structure	Corundum		
Spacegroup	R -3 2/c		
Spacegroup number	167		
Lattice parameter (Å)	a	b	c
	4.759(0)	4.759(0)	12.992(0)
Angles	α	β	γ
	90.00	90.00	120.00
Atoms in unit cell	30		

Table A-2: Atoms positions in the unit cell of Al_2O_3 [122].

Atom	Wyckoff position	x	y	z
Al	12c	0.0000	0.0000	0.8520
O	18e	0.3060	0.0000	0.2500

Figure A-2: Calculated neutron diffraction pattern for Al_2O_3 .

A-2 Neutron Diffraction Pattern Calculation of Y_2O_3

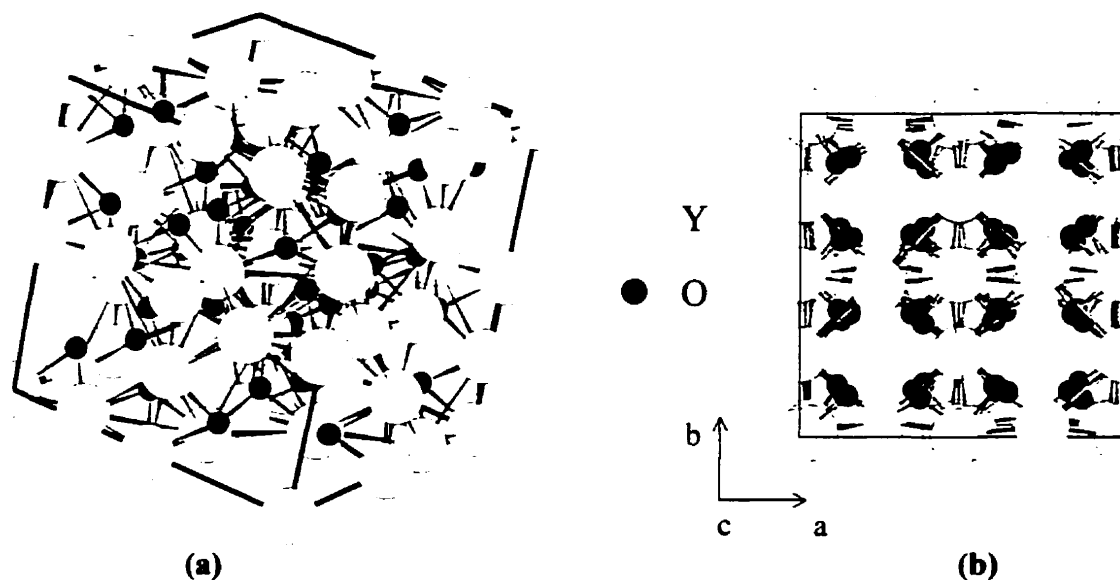


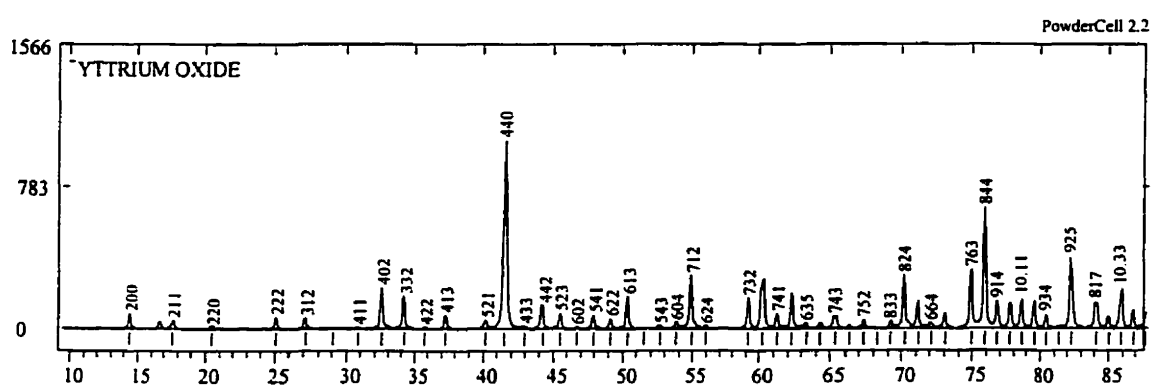
Figure A-3: (a) Unit cell of Y_2O_3 (b) (001) projection.

Table A-3: Crystal Structure data of Y_2O_3 [48,109,124,128].

Structure	Cubic		
Spacegroup	$I 2_1/a -3$		
Spacegroup number	206		
Lattice parameter (Å)	a	b	c
	10.608(7)	10.608(7)	10.608(7)
Angles	α	β	γ
	90.00	90.00	90.00
Atoms in unit cell	80		

Table A-4: Atoms positions in the unit cell of Y_2O_3 [109].

Atom	Wyckoff position	x	y	z
Y1	8a	0.0000	0.0000	0.0000
Y2	24d	0.9686	0.0000	0.2500
O	48e	0.3890	0.1500	0.37700

Figure A-4: Calculated neutron diffraction pattern for Y_2O_3 .

A-3 Neutron Diffraction Pattern Calculation of YAG

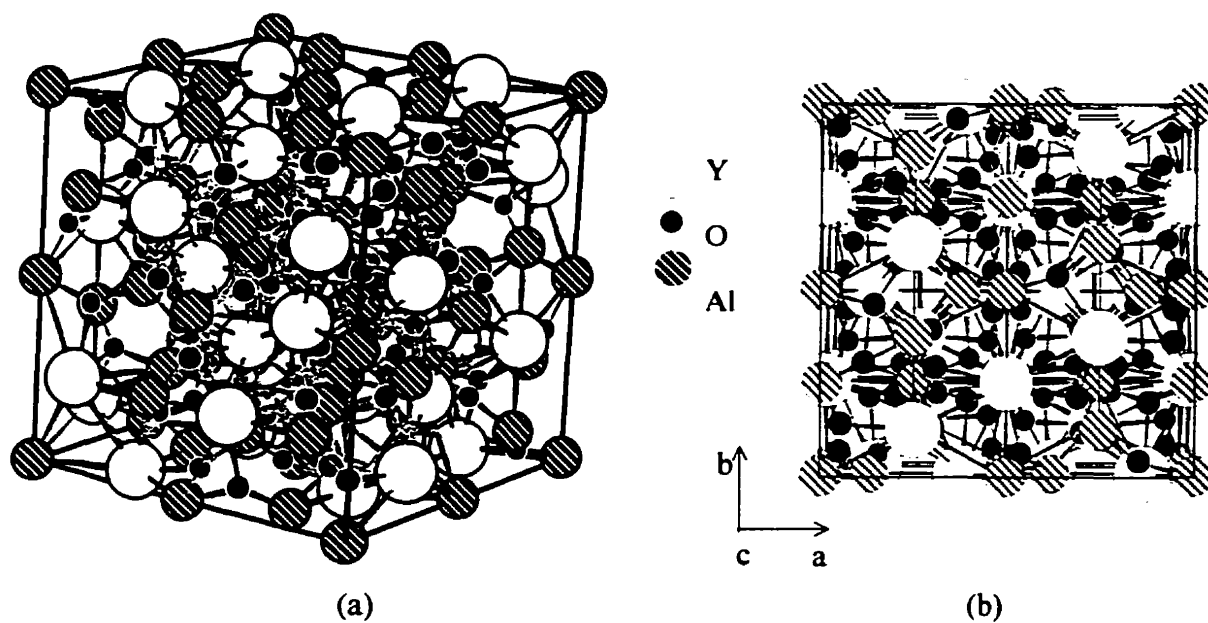


Figure A-5: (a) YAG unit cell (b) (001) projection.

Table A-5: Crystal Structure data of YAG [41,46,60].

Structure	Garnet		
Spacegroup	I 4 ₁ /a -3 2/d		
Spacegroup number	230		
Lattice parameter (Å)	a	b	c
	12.016(3)	12.016(3)	12.016(3)
Angles	α	β	γ
	90.00	90.00	90.00
Atoms in unit cell	160		

Table A-6: Atoms positions in the unit cell of YAG [129].

Atom	Wyckoff position	x	y	z
Y	16c	0.1250	0.0000	0.2500
Al1	16a	0.0000	0.0000	0.0000
Al2	24d	0.3750	0.0000	0.2500
O	24h	-0.0400	0.0550	0.1400

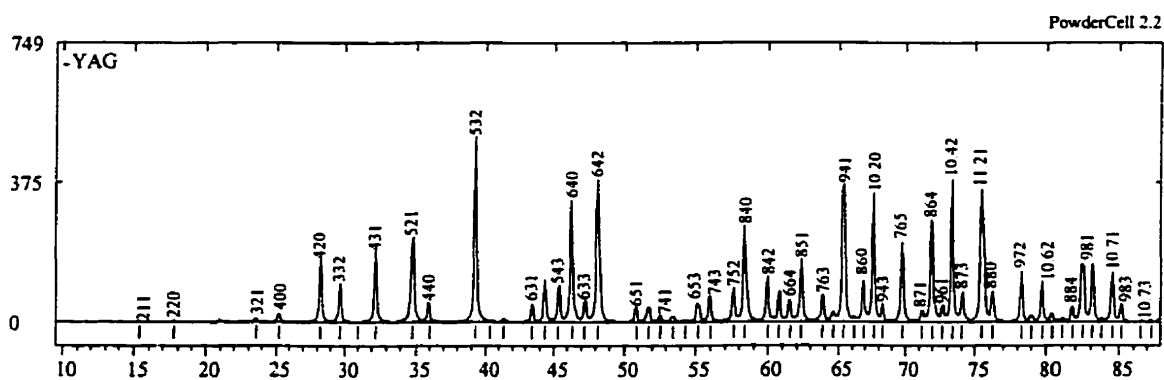


Figure A-6: Calculated neutron diffraction pattern for YAG.

A-4 Neutron Diffraction Pattern Calculation of YAP

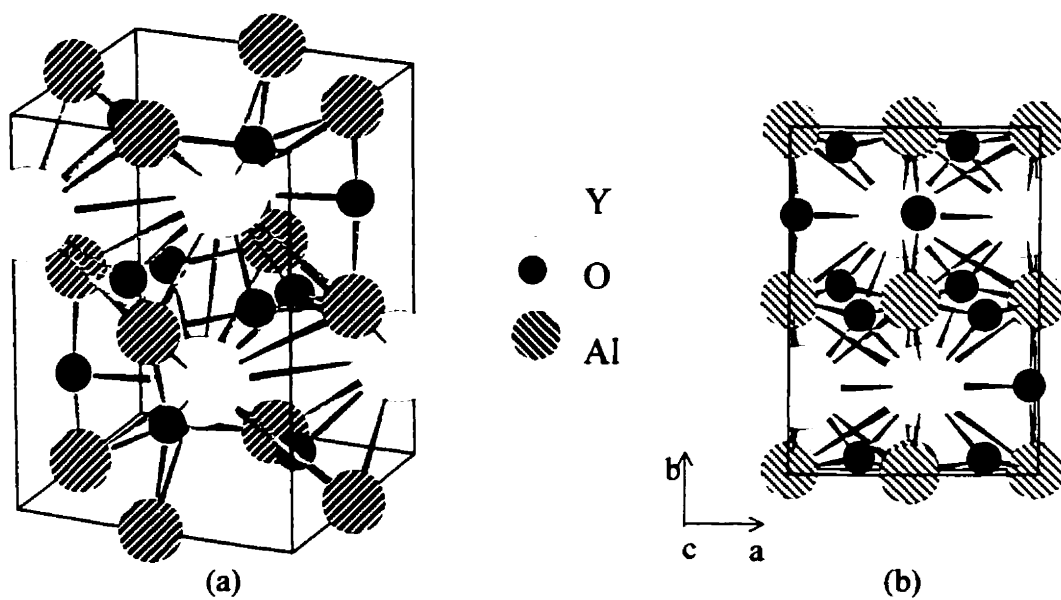


Table A-7: Crystal Structure data of YAP [41,103,132,133].

Structure	Orthorhombic		
Spacegroup	P n m a		
Spacegroup number	62		
Lattice parameter (Å)	a	b	c
	5.330(2)	7.375(2)	5.180(2)
Angles	α	β	γ
	90.00	90.00	90.00
Atoms in unit cell	20		

Table A-8: Atoms positions in the unit cell of YAP [133].

Atom	Wyckoff position	x	y	z
Y1	4c	0.5526	0.2500	0.5104
Al1	4b	0.0000	0.0000	0.5000
O1	4c	0.9750	0.2500	0.4140
O2	8d	0.2930	0.0440	0.7030

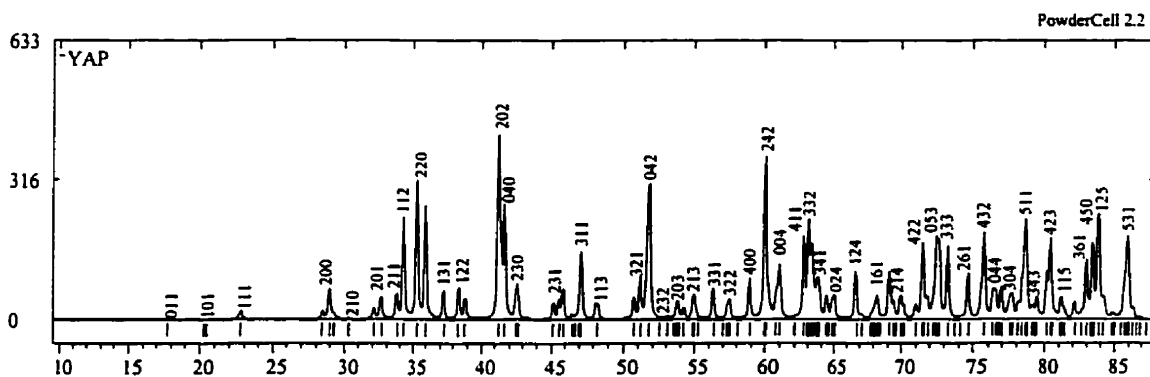


Figure A-8: Calculated neutron diffraction pattern for YAP.

A-5 Neutron Diffraction Pattern Calculation of YAM

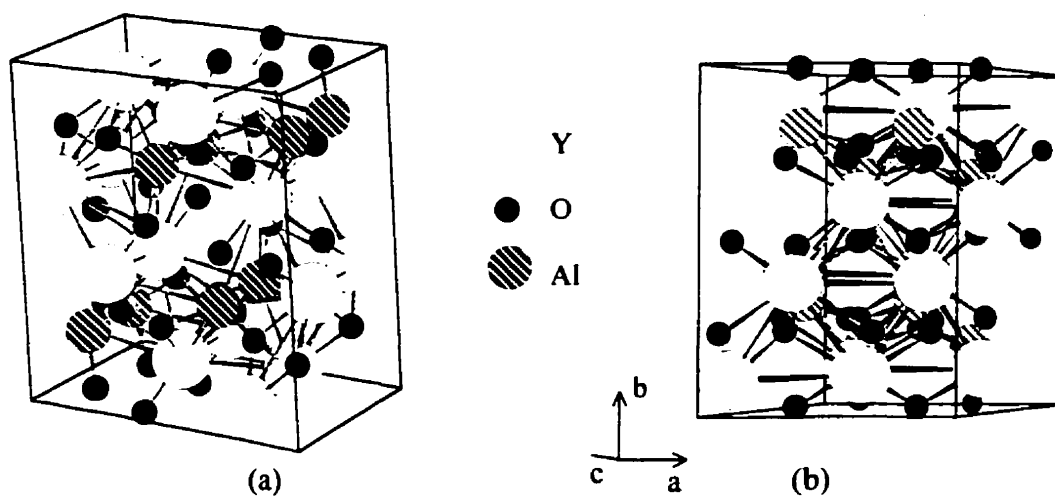


Figure A-9: (a) YAM unit cell, (b) (001) projection.

Table A-9: Crystal Structure data of YAM [51,53,132,134].

Structure	Monoclinic		
Spacegroup	P 1 2 ₁ /c 1		
Spacegroup number	14		
Lattice parameter (Å)	a	b	c
	7.4706(5)	10.535(6)	11.1941(8)
Angles	α	β	γ
	90.00	108.888(5)	90.00
Atoms in unit cell	60		

Table A-10: Atoms positions in the unit cell of YAM [53].

Atom	Wyckoff position	x	y	z
Y1	4e	0.5244	0.1080	0.7864
Y2	4e	0.0221	0.0944	0.8066
Y3	4e	0.3390	0.1206	0.4370
Y4	4e	0.8382	0.1206	0.4173
Al1	4e	0.2300	0.1820	0.1320
Al2	4e	0.6540	0.1810	0.1170
O1	4e	0.2150	0.0180	0.1560
O2	4e	0.6880	0.0050	0.1620
O3	4e	0.0830	0.0050	0.3940
O4	4e	0.5680	0.0060	0.4010
O5	4e	0.2230	0.2610	0.2640
O6	4e	0.0740	0.2310	0.9820
O7	4e	0.7820	0.2660	0.2450
O8	4e	0.6520	0.2370	0.9580
O9	4e	0.4290	0.2310	0.1110

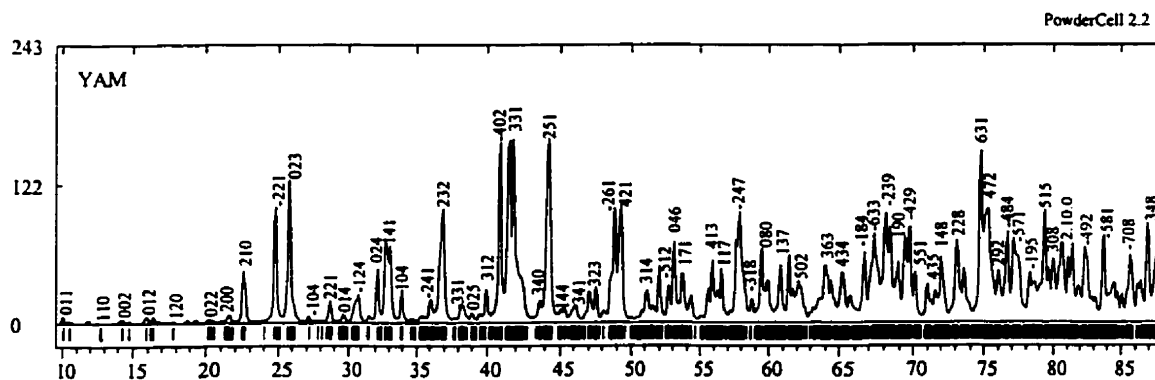


Figure A-10: Calculated neutron diffraction pattern for YAM.

A-6 Neutron Diffraction Pattern Calculation of Spinel

The lattice parameter of spinel varies with composition from 7.951Å (nitrogen-rich) to 7.938Å (oxygen-rich). Equation A-1 relates the lattice parameter of spinel to the bulk oxygen content of fully dense single phase spinel material as determined by Guillo [137]. For this reason and because nitrogen and oxygen atoms occupy the same sites, crystal structure of spinel was not drawn.

$$\text{\AA} = 7.914 + 0.117(X) \quad \text{.....A-1}$$

Where Å is lattice parameter in angstroms and X = 18 to 32 mol% AlN.

Table A-11: Crystal Structure data of spinel [64,68,115].

Structure	Cubic		
Spacegroup	F4 _{1/d} -3 2/m		
Spacegroup number	227		
Lattice parameter (Å)	a	b	c
	7.9526(5)	7.9526(5)	7.9526(5)
Angles	α	β	γ
	90.00	90.00	90.00
Atoms in unit cell	56		

Table A-12: Atoms positions in the unit cell of spinel [68,115].

Atom	Wyckoff position	x	y	z
Al1	8a	0.0000	0.0000	0.5104
Al2	16d	0.6250	0.6250	0.6250
O + N	32e	0.8688	0.8688	0.8688

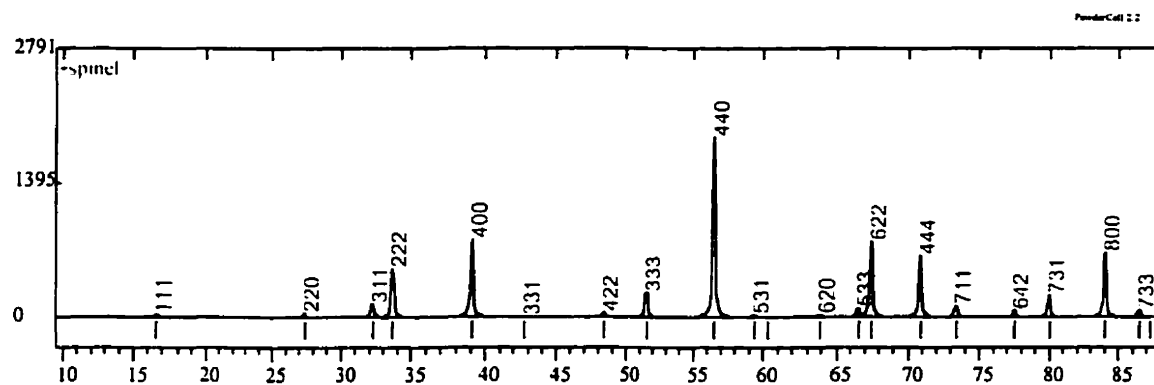


Figure A-11: Calculated neutron diffraction pattern for spinel when $a = 7.9526(5)$.

APPENDIX B

In order to ensure the stability of the compounds DTA of the YAG, YAP and YAM was performed at temperatures ranging from 400 to 1400°C with a heating rate of 10°C/min. DTA traces of heating and cooling of YAG, YAP and YAM phases will be discussed in this appendix.

B-1 Differential thermal analysis of YAG

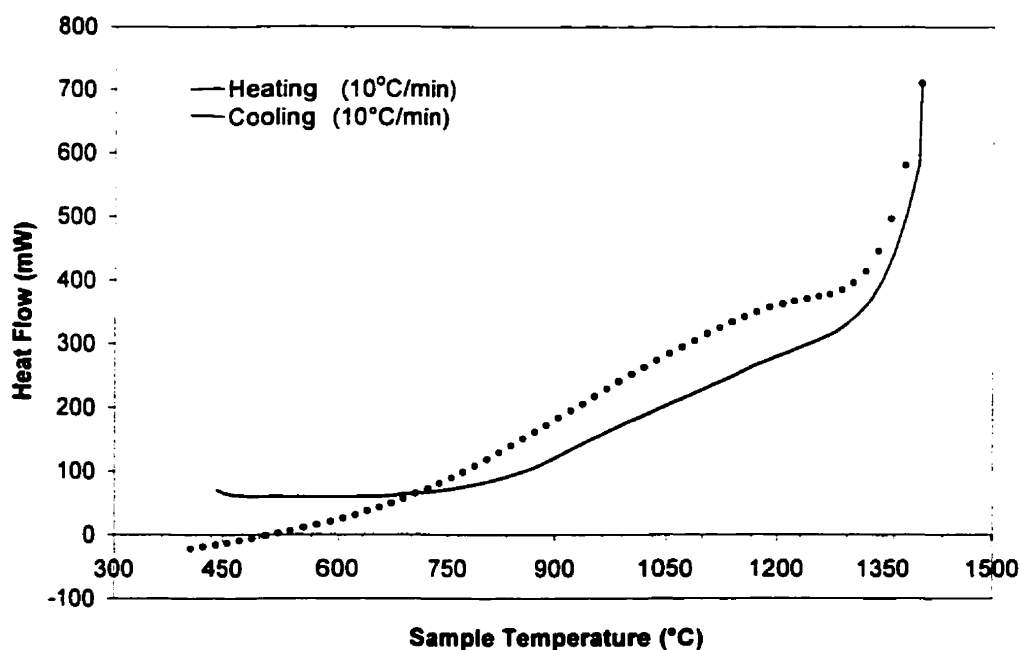


Figure B-12: DTA traces of cooling and heating of YAG phase.

It can be seen from the above figure that there are no peaks in the heating trace. This indicates that there is no phase transformation of YAG up to 1400°C. Also no furthermore peaks in the cooling trace were identified which means no decomposition of YAG occurred while cooling from 1400°C to room temperature. The same behaviour was observed for YAP and YAM.

B-2 Differential thermal analysis of YAP

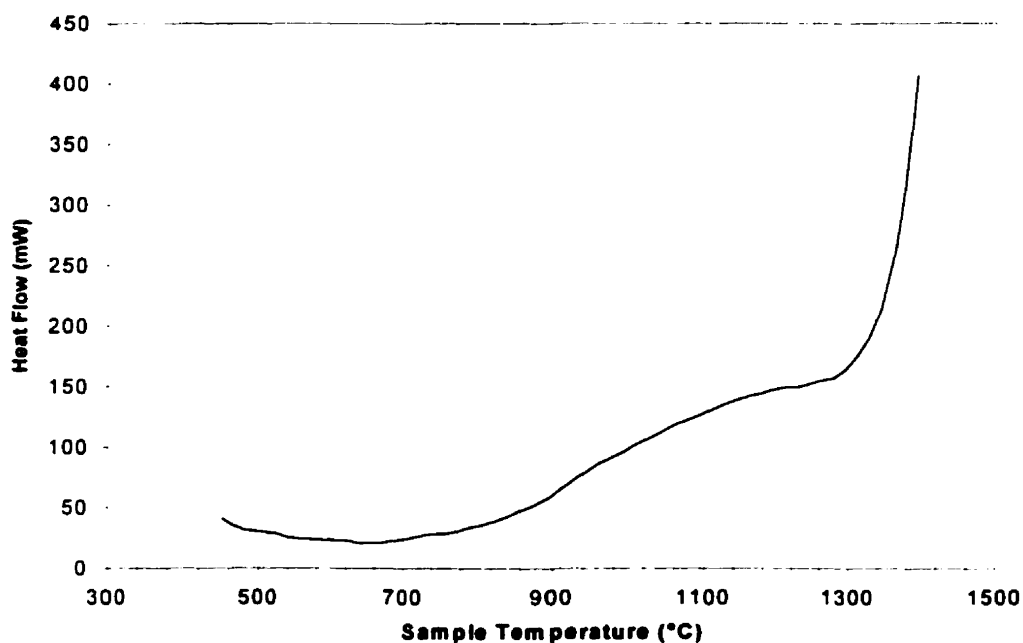


Figure B-2: DTA traces of heating of YAP phase.

B-3 Differential thermal analysis of YAM

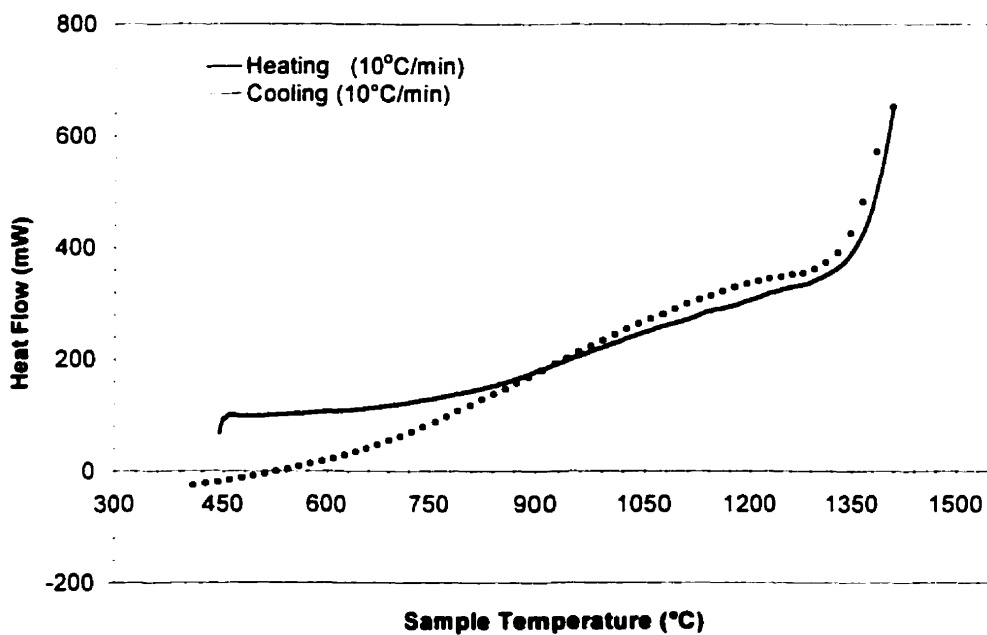


Figure B-3: DTA traces of cooling and heating of YAM phase.